The Effect Of Transition Metals On Amorphous Alloy Negative Electrode Materials For Lithium-Ion Batteries

by
Michael D. Fleischauer

Submitted in partial fulfillment of the
requirements for the degree of
Doctor of Philosophy

at

Dalhousie University
Halifax, Nova Scotia
November, 2005

Your file Votre référence
ISBN: 978-0-494-16697-0
Our file Notre référence
ISBN: 978-0-494-16697-0

DALHOUSIE UNIVERSITY

To comply with the Canadian Privacy Act the National Library of Canada has requested that the following pages be removed from this copy of the thesis:

Preliminary Pages

Examiners Signature Page (pii)

Dalhousie Library Copyright Agreement (piii)

Appendices

Copyright Releases (if applicable)

To my parents, my brother and my special lady friend.

Table of Contents

List of Tables viii

List of Figures ix

Abstract xix

List of Symbols xx

Acknowledgements xxiv

Chapter 1 Introduction 1

1.1 Li-Ion Batteries 1

1.2 Negative Electrode Materials 3

1.3 Combinatorial And High-Throughput Methods 7

1.4 Electrochemical Results 10

1.5 Macroscopic Atom Model 12

Chapter 2 Experimental Techniques 15

2.1 Thin Film Deposition 15

2.2 Structure Determination 23

2.2.1 X-Ray Diffraction 24

2.2.2 Mössbauer Effect Spectroscopy 28

2.2.3 Transmission Electron Microscopy 35

2.2.4 Differential Scanning Calorimetry 36

2.3 Composition And Mass Determination 38

2.4 Electrochemical Characterization 40

2.5 Automation 48

Chapter 3 Si-M (M = Cr+Ni, Fe, Mn) 51

3.1 Structural Characterization 54

3.2 Electrochemistry 60

Chapter 4 Al-M (M = Cr, Fe, Mn, Ni) **69**
4.1 Results 75
4.2 Discussion 81

Chapter 5 Al-Si **91**
5.1 Results 93

Chapter 6 Si-Al-M (M = Cr, Fe, Mn, Ni) **112**
6.1 Si-Al-Fe Binary Runs 115
6.2 Si-Al-M (M = Cr, Fe, Mn, Ni) Ternary Runs 126

Chapter 7 Conclusions And Future Work **146**

Bibliography **157**

Appendix A Macroscopic Atom Model Details **170**

Appendix B Mask Profile Calculation Routine **176**

Appendix C Tricks Of The Combinatorial Trade **178**
C.1 Thin Film Library Deposition 178
C.1.1 Defrost The Polycold 178
C.1.2 Vent The Chamber 179
C.1.3 Substrate / Mask Removal 179
C.1.4 Clean-Up 181
C.1.5 Loading The Chamber 182
C.2 Non-Photolithographic Substrate Preparation 185
C.2.1 Cu/Al Disks and Foil 185
C.2.2 DSC Pans 186
C.2.3 Kapton Film 187
C.2.4 Si Wafers 187
C.2.5 TEM Grids 188
C.3 Photolithography 188
C.4 Combinatorial Electrochemical Cell Assembly 191

Appendix D Copyright Releases 194
D.1 The Electrochemical Society, Inc. 194
D.2 IOP Publishing, Ltd. 195

List of Tables

Table 1.1 Theoretical room-temperature gravimetric and volumetric capacities of some elements that reversibly react with Li [15]. . . 3

Table 3.1 Brief summary of Si-M sputtering runs. 54

Table 3.2 Cycling parameters for the data presented in Figs. 3.6-3.10. . . 60

Table 4.1 Brief summary of Al-M sputtering runs. 74

Table 5.1 Brief summary of Al-Si sputtering runs. 93

Table 5.2 Atomic positions for $Al_2Li_{18}Si_6$ as determined by Spina *et al.* [137]. 108

Table 6.1 Brief summary of Si-Al-M sputtering runs. The range of x for all ternary runs was approximately from 0 to 1. 115

Table A.1 ΔH^{trans} values for those elements that undergo a gas-solid or semiconductor-metal transition [90]. 173

Table A.2 Fig. 2.4 from deBoer *et al.* [90]. 174

Table A.3 Fig. 2.28 from deBoer *et al.* [90]. 175

List of Figures

Figure 1.1 Schematic of a Li-ion cell undergoing charging. 2

Figure 1.2 An example of the fractal masking technique [64]. Grey areas are used to indicate those pixels blocked by a shadow mask during the deposition of starting material A, B, C or D. 8

Figure 1.3 Room temperature first discharge capacity of Si-Al-Mn as a function of composition. Dots are used to label the compositions investigated. The shaded region indicates compositions that can be prepared in an amorphous state by melt-spinning [46,47]. 11

Figure 1.4 Schematic of heat of formation of $(1-x)$ moles of AlLi and 1 mole of $Al_{1-x}M_x$ as a function of x. The thick line indicates the most stable Al alloy as a function of M content. A dashed line separates the region where the formation of AlLi is favorable from the region where $Al_{1-x}M_x$ will not react with Li. 14

Figure 2.1 Schematic of the sputtering processes. Wiring diagrams for RF and DC sputtering are shown to the left of the vacuum chamber. 16

Figure 2.2 Components of a magnetron sputtering source. 17

Figure 2.3 Layout of the sputtering machine substrate table. Reproduced by permission of The Electrochemical Society, Inc. [67]. 18

Figure 2.4 Deposition profile as a function of radius (solid line) when no mask is present. Dotted lines correspond to those in Figure 2.3. Thick dashed lines correspond to various deposition profiles. . 19

Figure 2.5 Vectors used in mask design calculation. The deposition profile with the mask in place is shown in the lower part of the figure. 20

Figure 2.6 Schematic of the process described in [80], which permits films with linear and orthogonal composition gradients to be deposited on a range of substrates. Only one substrate is shown for clarity. Colour variations are used to illustrate composition variations. 21

Figure 2.7 Layout of the substrates on the five substrate table for ternary deposition runs. Reproduced from [77] with the permission of IOP Publishing Ltd. 22

Figure 2.8 Layout of the substrates on the substrate table for binary deposition runs. 23

Figure 2.9 Schematic of x-ray diffraction. The extra path length of the lower incident ray (shown as the dotted line) must be an integral multiple of the incident beam wavelength for constructive interference to occur. 24

Figure 2.10 Schematic of method used in Inel CPS-120 for x-ray detection. 26

Figure 2.11 Schematic of Inel CPS-120 XRD set up. 27

Figure 2.12 Schematic energy distributions during emission and absorption. The shaded area corresponds to the overlap of both processes. Adapted from Figure 1.3 of [96]. 29

Figure 2.13 Decay scheme of ^{57}Co [96]. The two thick vertical arrows indicate the most common transitions. Energies and lifetimes (in brackets) are listed to the right of each state. Spin values are to the left of each state. 30

Figure 2.14 All possible nuclear transitions in ^{57}Fe. Cases a), b) and c) are related to the centre shift, the quadrupole splitting and the magnetic hyperfine interaction, respectively. 33

Figure 2.15 Schematic diagram of the high-throughput Mössbauer effect spectroscopy system (Courtesy J. McGraw). 34

Figure 2.16 Schematic diagram of a TEM. The shaded area indicates the range of possible electron paths. 36

Figure 2.17 Schematic diagram of possible features in DSC signals. 37

Figure 2.18 Sample differential capacity ($\frac{dQ}{dV} = \frac{dQ}{dt}\frac{dt}{dV}$) vs. voltage (rate of change of charge as a function of voltage, per unit mass) and gravimetric capacity (voltage as a function of charge per unit mass) plots. 41

Figure 2.19 Schematic of the 64-channel combinatorial electrochemical cell described in [67] and [77]. Reproduced from [77] with the permission of IOP Publishing Ltd. 42

Figure 2.20 Lead pattern for sixty-four channel combinatorial electrochemical cell. 32 electrical contacts on the left and right hand sides are spaced to interface with standard motherboard connectors. Materials under investigation are sputter-deposited on the sixty-four circular contact pads. Reproduced by permission of The Electrochemical Society, Inc. [83]. 44

Figure 2.21 'Binary' lead pattern on a 114 x 114 x 1 mm glass plate. Contact pads are positioned so that the distance between the centre of the contact pad and the centre of the substrate table is evenly incremented over the 76 mm span of the contact pads. 46

Figure 2.22 'Ternary' lead pattern on a 114 x 114 x 1 mm glass plate. Contact pads are positioned so that the distance between the centre of the contact pad and the centre of the substrate table is evenly incremented over the 76 mm span of the contact pads for both possible orientations of the substrate shown in Fig. 2.6. Reproduced from [77] with the permission of IOP Publishing Ltd. . 47

Figure 2.23 Current flow as a function of time. The cell is discharging at point 1. The voltage sweep direction changes from towards 0 V to towards 1.2 V at point 2. Although the voltage is increasing at points 3 and 4, the current is still negative, and the capacity is increasing. The capacity reaches a maximum at some point between 4 and 5. 49

Figure 3.1 Equilibrium phase diagrams for Si-Cr, Si-Fe, Si-Mn and Si-Ni (data from [115]). 53

Figure 3.2 XRD patterns for Si-Fe (grey) and Si-Mn (black) for 10, 25 and 40 at. % transition metal thin films deposited on a Si (100) wafer. Reproduced by permission of The Electrochemical Society, Inc. [86]. 55

Figure 3.3 Sample Mössbauer effect fits. Numbers in brackets refer to at. % Fe (in Si-Fe). Two humps in the centre difference plot suggest the fitting method is not ideal. 57

Figure 3.4 Isomer shift d (a), quadrupole splitting Δ (b) and site distribution σ (referenced to α-Fe) as a function of Fe content for the Si-Fe Mössbauer libraries listed in Table 3.1. Crosses, squares, diamonds and circles refer to data from sputtering runs spk022, spj045, spk088 and spl050, respectively. 58

Figure 3.5 TEM diffraction image of $Si_{0.55}Fe_{0.45}$. 59

Figure 3.6 64 dQ/dV vs. V plots collected simultaneously from 64 different compositions of Si-Cr-Ni using the methods described in Section 2.4. 62

Figure 3.7 dQ/dV vs.V plots for Si_xM_{1-x} for M = Mn (left column), Fe (middle column) and Cr + Ni (right column) for various values of x. The vertical scale is consistent across rows but varies from row to row. Solid (dashed) lines in the right column correspond to high Cr (Ni) and low Ni (Cr) content; the ratio of high:low is about 3:2 Reproduced by permission of The Electrochemical Society, Inc. [86].. 63

Figure 3.8 Capacity (mA h/g) vs. x in Si_xMn_{1-x}. The two sets of results are from separate sputtering runs (spj094, binary cell plates, and spj104, square cell plates). 64

Figure 3.9 Capacity (mA h/g) vs. x (Si content) in Si_xM_{1-x} (M = Mn, Fe, Cr + Ni). Data points for the range 50 to 70 at. % Si are shown on two vertical scales to emphasize the difference between Si-Mn and either Si-Fe or Si-Ni-Cr. The solid line was calculated using Eq. 3.1, which assumed a sample composition Si_xM_{1-x} is made up of a mole fraction of (2x-1) Si (nanoscale a-Si) and (2-2x) SiM (nanoscale SiM) for $0.5 \leq x \leq 1$. Reproduced by permission of The Electrochemical Society, Inc. [86]. 66

Figure 3.10 Capacity of $Si_x(Cr+Ni)_{1-x}$ as a function of cycling temperature. 67

Figure 4.1 Partial equilibrium phase diagrams for Al-Cr, Al-Fe, Al-Mn and Al-Ni (data from [115]). 70

Figure 4.2 Partial Fe-Li-Sn (a) and Al-Li-Fe (b) phase diagrams based on the macroscopic atom model. Reproduced by permission of The Electrochemical Society, Inc. [87]. 71

Figure 4.3 Schematic of heat of formation of (1-x) moles of AlLi and 1 mole of $Al_{1-x}M_x$ to illustrate the energetics of Reaction 2. The thick line indicates the most stable Al alloy as a function of M content. A dashed line separates the region where the formation of AlLi is favorable from the region where $Al_{1-x}M_x$ will not react with Li. Reproduced by permission of The Electrochemical Society, Inc. [87]. 72

Figure 4.4 dQ/dV vs. V for $Al_{0.95}Fe_{0.05}$ and $Al_{0.92}Fe_{0.08}$ at room temperature and 70 °C. Reproduced by permission of The Electrochemical Society, Inc. [87]. 75

Figure 4.5 Capacity vs. x for Al_xFe_{1-x}. The four regions labeled with roman numerals are discussed in the text. Dashed lines separate the regions. Reproduced by permission of The Electrochemical Society, Inc. [87]. 76

Figure 4.6 Voltage vs. capacity plots for selected low-Fe content Al_xFe_{1-x} alloys. Atomic percent Fe values for each plot are shown in brackets. Reproduced by permission of The Electrochemical Society, Inc. [87]. 77

Figure 4.7 XRD patterns for Al_xFe_{1-x} ($0 < x < 0.12$). Regions, corresponding to those shown in Figure 4.5, are marked. Reproduced by permission of The Electrochemical Society, Inc. [87]. 78

Figure 4.8 Mössbauer effect spectra collected from various Al_xFe_{1-x} alloys. at. % Fe values are provided for each panel. Circles, dashed lines and solid lines represent the raw data, site contributions and the total fit, respectively. Reproduced by permission of The Electrochemical Society, Inc. [87]. 79

Figure 4.9 $Area_{singlet}$ / $Area_{doublet}$ for the data shown in Figure 4.8 and that expected from a random distribution of Fe in Al. Reproduced by permission of The Electrochemical Society, Inc. [87]. 80

Figure 4.10 Unit cell of Al_6Mn [39]. Mn and Al atoms are dark and light grey, respectively. Reproduced by permission of The Electrochemical Society, Inc. [87]. 82

Figure 4.11 Schematic of $Al_{12}M_2$ in fcc (Al). M atoms are black. Al deactivated by the M atoms are dark grey and marked with a cross. Active Al atoms are light grey. Lines indicate the fcc unit cells. Reproduced by permission of The Electrochemical Society, Inc. [87]. 83

Figure 4.12 Capacity vs. x in Al_xFe_{1-x}. Crosses and squares indicate the maximum Li removal capacity during room temperature (4^{th} cycle) and 70 °C (6^{th} cycle, first four cycles at room temperature) cycling, respectively. The solid line indicates capacities predicted by the model described in the text. The non-equilibrium phase diagram as determined by XRD is provided for comparison. Reproduced by permission of The Electrochemical Society, Inc. [87]. 85

Figure 4.13 Summary of measured Al-M non-equilibrium phase diagrams. Results from Masui *et al.* for Al-Fe and Al-Ni [123], and Al-Cr and Al-Mn [124], are indicated by * and **, respectively. Reproduced by permission of The Electrochemical Society, Inc. [87]. 86

Figure 4.14 As in Figure 4.12 but for Al_xCr_{1-x}. Room temperature and 70 °C data corresponds to the second cycle and eighth cycle (cycles 1-3 at room temperature, cycles 4-6 at 50 °C, cycles 7-8 at 70 °C) of one cell, respectively. Reproduced by permission of The Electrochemical Society, Inc. [87]. 87

Figure 4.15 As in Figure 4.12 but for Al_xMn_{1-x}. Room temperature and 70 °C data corresponds to the fifth and third cycle of different cells cycled at the quoted temperature, respectively. Reproduced by permission of The Electrochemical Society, Inc. [87]. 88

Figure 4.16 As in Figure 4.12 but for Al_xNi_{1-x}. Room temperature and 70 °C data corresponds to the second and third cycle of different cells cycled at the quoted temperature, respectively. Reproduced by permission of The Electrochemical Society, Inc. [87]. 89

Figure 5.1 Al-Si equilibrium phase diagram (data from [115]). 92

Figure 5.2 XRD patterns for $Al_{1-x}Si_x$ ($0.07 < x < 0.97$). 94

Figure 5.3 (Al) (111) peak location as a function of composition for $Al_{1-x}Si_x$ ($0 \leq x \leq 35$). 95

Figure 5.4 Capacity of Si_xAl_{1-x} (mA h/g) as a function of composition (x). The nonequilibrium phase diagram as determined by XRD is also shown. 96

Figure 5.5 dQ/dV vs. V curves around 80 at. % Si. Grey and black curves were collected at 70 °C and room temperature, respectively. Compositions are indicated. 97

Figure 5.6 Capacity vs. composition for spl036 data set. Two cycling temperatures are shown, as well as the capacity predicted if 1 and 3.75 Li alloy with each Al and Si, respectively. 98

Figure 5.7 DSC curves of $Al_{1-x}Si_x$ ($61 < x < 94$). Atomic percent Si is indicated. Cycling parameters are listed in the text. 100

Figure 5.8 dQ/dV vs. V curves for compositions from 20 to 70 at. % Si. Grey and black curves were collected at 70 °C and room temperature, respectively. Compositions are indicated. See the text for cycle number / library information. 102

Figure 5.9 dQ/dV vs. V curves for $Al_{50}Si_{50}$ and $Al_{60}Si_{40}$. Numbers indicate cycle numbers. Cycles 1-3, 4-6 and 7-8 were cycled at room temperature, 50 °C and 70 °C, respectively. 103

Figure 5.10 Charge capacity between 0.9-1.2 V as a function of cycle number / temperature for spk002 data set. 104

Figure 5.11 1^{st}, 2^{nd}, 3^{rd} and 4^{th} charge capacity at room temperature (spk029). 105

Figure 5.12 Data shown in Figure 5.11 as a percentage of 1^{st} charge capacity. 106

Figure 5.13 Capacity retention of various Al-Si alloys at various temperatures. Cycles 1-3 were performed at room temperature. Cycles 4-6 and 7-8 were performed at 50 and 70 °C for all compositions except $Al_{0.30}Si_{0.70}$, where cycles 4-5 were performed at 70 °C. . 107

Figure 5.14 Charge capacity between 0.005-0.3 V as a function of composition for spk002 data set. 109

Figure 5.15 All reported Al-Li-Si ternary phases reported in the literature [135–137]. A solid line indicates the capacity expected if each Al and Si reacted with 1 and 3.75 Li, respectively. The dashed line indicates neutral compositions if charge transfer occurs between the atoms as in Zintl type phases [141] and Al, Li and Si have charges of +3, +1 and -4, respectively. 110

Figure 6.1 Al-Cr-Si equilibrium phases according to [39]. 113

Figure 6.2 Al-Fe-Si equilibrium phases according to [39] (circles) and [142] (triangles). 113

Figure 6.3 Al-Mn-Si equilibrium phases according to [39] (circles) and [143] (triangles). 114

Figure 6.4 Al-Ni-Si equilibrium phases according to [39] (circles) and [144, 145] (triangles). 114

Figure 6.5 Crosses and diamonds indicate the range of compositions tested for spl025 and spk091, respectively. The dashed lines are guides to the eye. Ternary Si-Al-Fe phases are reproduced from Figure 6.2. 116

Figure 6.6 XRD patterns for $(Al_{0.73}Si_{0.27})_{1-x}Fe_x$ $(0 \leq x \leq 0.2)$ (spk091). Numbers indicate at. % Fe. 116

Figure 6.7 Charge capacity (mA h/g) vs. x for $(Al_{0.73}Si_{0.27})_{1-x}Fe_x$ $(0 \leq x \leq 0.2)$ (spk091). 117

Figure 6.8 dQ/dV vs. V curves for various compositions of spk091. Black and grey curves were collected at room temperature (cycles 1-5) and 70 °C (cycles 6-8), respectively. Compositions are indicated. 118

Figure 6.9 Charge capacity between 0.52-0.8 V for $(Al_{0.73}Si_{0.27})_{1-x}Fe_x$ ($0 \leq x \leq 0.2$) (spk091). 119

Figure 6.10 dQ/dV vs. V curves for various compositions of spk091 collected at 70 °C showing the dissociation of the AlLiSi phase. Compositions are indicated. 120

Figure 6.11 6^{th} charge capacity between 0.9-1.2 V for the spk091 data set. 121

Figure 6.12 XRD patterns for $(Al_{0.31}Si_{0.69})_{1-x}Fe_x$ ($0 \leq x \leq 0.23$) (spl025). Numbers indicate at. % Fe. 122

Figure 6.13 Capacity (mA h/g) vs. x for $(Al_{0.31}Si_{0.69})_{1-x}Fe_x$ ($0 \leq x \leq 0.25$) (spl025). 122

Figure 6.14 dQ/dV vs. V curves for various compositions of spl025. Black and grey curves were collected at room temperature and 70 °C, respectively. Compositions are indicated. 124

Figure 6.15 Capacity as a function of Fe content spanning the range of Si:Al. The relative ratio of Si:Al is provided. 125

Figure 6.16 XRD patterns from Si-Al-Fe (spl036). Fe content increases from right to left. Compositions can be estimated from the numbers in Figure 6.17. 127

Figure 6.17 High and low Fe-content edges of spl036 composition range. Numbers correspond to those of Figure 6.16. 128

Figure 6.18 1^{st} charge capacity (mA h/g) as a function of composition for Al-Cr-Si cycled at room temperature. Dots indicate compositions used to form the contours. 129

Figure 6.19 1^{st} charge capacity (mA h/g) as a function of composition for Al-Fe-Si cycled at room temperature. Dots indicate compositions used to form the contours. 130

Figure 6.20 1^{st} charge capacity (mA h/g) as a function of composition for Al-Mn-Si cycled at room temperature. Dots indicate compositions used to form the contours. 131

Figure 6.21 1^{st} charge capacity (mA h/g) as a function of composition for Al-Ni-Si cycled at room temperature. Dots indicate compositions used to form the contours. 132

Figure 6.22 1^{st} charge capacity (mA h/g) as a function of composition for Al-Cr-Si cycled at 70 °C. Dots indicate compositions used to form the contours. 133

Figure 6.23 1^{st} charge capacity (mA h/g) as a function of composition for Al-Fe-Si cycled at 70 °C. Dots indicate compositions used to form the contours. 134

Figure 6.24 1^{st} charge capacity (mA h/g) as a function of composition for Al-Mn-Si cycled at 70 °C. Dots indicate compositions used to form the contours. 135

Figure 6.25 2^{nd} charge capacity (mA h/g) as a function of composition for Al-Ni-Si cycled at 70 °C. Dots indicate compositions used to form the contours. 136

Figure 6.26 Contour lines of 200 mA h/g for Si-Al-M (M = Cr, Fe, Mn, Ni) reproduced from Figures 6.22, 6.23, 6.24, and 6.25, respectively. 137

Figure 6.27 dQ/dV vs. V curves for various compositions approximately along $(Al_{0.22}Si_{0.78})_{1-x}Ni_x$. Black and grey curves were collected at room temperature and 70 °C, respectively. Compositions are indicated. 138

Figure 6.28 Formation range of $Li_{15}Si_4$ as determined by the presence of a peak in dQ/dV vs. V curves at 0.4 V on removal. Compositions with and without said peak are labeled with an 0 and X, respectively. The shaded region is a guide to the eye. 140

Figure 6.29 Formation range of $Al_2Li_{18}Si_6$ as determined by the presence of a peak in dQ/dV vs. V curves collected at 70 °C at 0.15 V on removal. Compositions with and without said peak are labeled with an 0 and X, respectively. The shaded region is a guide to the eye. 141

Figure 6.30 Formation range of AlLi as determined by the presence of a peak in dQ/dV vs. V curves between 0.5-0.7 V on removal. Compositions with and without said peak are labeled with an 0 and X, respectively. The shaded region is a guide to the eye. 142

Figure 6.31 Dissociation range of the AlLiSi phase as determined by the presence of a peak in dQ/dV vs. V curves collected at 70 °C between 1.0-1.2 V on removal. Compositions with and without said peak are labeled with an 0 and X, respectively. The shaded region is a guide to the eye. 143

Figure 6.32 Equilibrium binary (squares [115]) and ternary (circles [39]) Al-Cr-Si phases, and the 200 mA h/g line from Figure 6.26 extrapolated to 0 at. % Si according to Figure 4.14. 144

Figure 6.33 Equilibrium binary (squares [115]) and ternary (circles [39], triangles [142]) Al-Fe-Si phases, and the 200 mA h/g line from Figure 6.26 extrapolated to 0 at. % Si according to Figure 4.12. 144

Figure 6.34 Equilibrium binary (squares [115]) and ternary (circles [39], triangles [143]) Al-Mn-Si phases, and the 200 mA h/g line from Figure 6.26 extrapolated to 0 at. % Si according to Figure 4.15. 145

Figure 6.35 Equilibrium binary (squares [115]) and ternary (circles [39], triangles [144,145]) Al-Ni-Si phases, and the 200 mA h/g line from Figure 6.26 extrapolated to 0 at. % Si according to Figure 4.16. 145

Figure 7.1 1^{st} charge capacity as a function of composition for Si_xCo_{1-x} at room temperature (diamonds) and 70 °C (circles). Dashed and solid lines indicate the expected capacity if SiCo and Si_2Co are inactive. 148

Figure 7.2 XRD patterns of as-deposited (grey) and annealed to 400 °C in 45 seconds using a rapid thermal annealer (black) $Si_{0.60}Co_{0.40}$ and $Si_{0.45}Co_{0.55}$. 149

Figure 7.3 XRD patterns of annealed Si_xCo_{1-x}. 150

Figure 7.4 Capacity vs. potential plots of melt-spun $Al_{61}Si_{30}Ni_9$ and sputter deposited thin film $Al_{63}Si_{26}Ni_{10}$. 153

Figure B.1 Deposition profile opposite a target. 177

Figure B.2 Arc and angles used in mask design calculation. 177

Abstract

This work describes combinatorial investigations of high-capacity thin film negative electrode materials for Li-ion batteries. Amorphous alloy electrode materials are emphasized since they offer much better charge / discharge capacity retention than their crystalline counterparts. Various combinatorial and high-throughput methods, designed to deal with the experimental challenges posed by amorphous materials, are described.

The aim is to understand the electrochemistry of the Si-Al-M (M = transition metal such as Cr, Fe, Mn or Ni) system. Certain compositions of Si-Al-M can be mass produced as amorphous alloys, offer high capacities, and good capacity retention. Separate investigations of the Si-M, Al-M, and Al-Si systems were performed since the literature for each system is either conflicting or non-existent.

The electrochemical performance of Si-M can be explained by assuming the presence of active amorphous Si and inactive nanocrystalline SiM. Diffusion effects lower the observed capacity for compositions above 30 atomic percent M for all tested values of M except Mn.

Mössbauer and XRD measurements suggest that M atoms are not randomly distributed throughout Al-M samples, but instead occur in isolated and clustered sites. A phenomenological model based on the relative amounts of isolated and clustered sites is presented to explain the capacities of $Al_{1-x}M_x$ samples observed at room and elevated temperature. Interactions between Si, Al and Li complicate the electrochemistry of the Si-Al system. Measurements suggest the presence of AlLi, AlLiSi or $Al_3Li_7Si_4$, $Al_2Li_{18}Si_6$, and $Li_{15}Si_4$ in fully-lithiated films.

Capacities in the Si-Al-M system are dominated by the influence of Al-M and Si-M interactions at high Al and Si contents, respectively. Compositions with less than 80 atomic percent Si and more than 10-20 atomic percent M remained amorphous during Li insertion and removal and could be used as high capacity electrode materials. There is also some evidence all Si-Al-M equilibrium phases are inactive. Possible future research directions based on the insight gained during this research are provided.

List of Symbols

A	metal element in macroscopic atom model
A	peak area
a	volume contraction parameter
Å	Ångstrom, 0.1 nm
A_-/A_+	ratio of negative to positive peak areas
AC	alternating current
Ar^+	argon ion
at. %	atomic percent
$\vec{B}$	magnetic field
B	metal element in macroscopic model
B	XRD pattern peak width
$B(s)$	deposition profile
C/n	charge rate: full capacity C in n hours
C^i	mass percentage
ca.	circa
cc	cubic centimetre
c_i	molar concentration of element i
D	deposition
d	days
d	lattice spacing
δ	centre shift
Δ	quadrupole splitting
δ_1	coupling factor
DC	direct current
DEC	diethylene carbonate
°C	degrees Celsius
dia.	diameter
DOS	density of states

dQ/dV	differential capacity
DSC	differential scanning calorimetry
$\vec{E}$	electric field
E	energy
e^-	electron
EC	ethylene carbonate
EDS	energy-dispersive spectroscopy
eV	electron volt
eQ	nuclear quadrupole moment
f_A^B	degree to which atoms of element A surround atoms of element B
fcc	face-centred cubic
FWHM	full width at half maximum
Γ	Heisenberg linewidth
γ	adhesion energy
g	nuclear g-factor
ΔG	Gibbs free energy of formation
H	magnetic field at the nucleus
$\hbar$	Planck's constant divided by 2π
ΔH	enthalpy of formation
I	current
I	spin quantum number
I^i	integrated x-ray intensity
$\vec{J}$	deposition flux
$\mathbf{K}$, $\mathbf{k}$	scattering vector
K	bulk modulus
k_B	Boltzmann's constant
Kb	kilobyte
k^i	ratio of standard and sample x-ray intensities
L	grain thickness
λ	wavelength
Li^+	lithium ion

M	transition metal
M, m	mass
M	molarity
m	magnetic quantum number
MMA	multichannel microelectrode analyzer
μ_N	Bohr magneton
n	order of diffraction
N	north pole
n_{ws}	electron density at boundary of Wigner-Seitz cell
P	common oxidation state parameter
ϕ^*	electronic charge chemical potential
ψ	electron density
Q	capacity
Q	common oxidation state parameter
q, $\vec{q}$	distance, vector from centre of sputtering target to position on substrate
Q''	proportionality constant
R^*	compressibility of electron density parameter
R, r	radius
$\underline{\text{Rh}}^{57}\text{Co}$	^{57}Co diffused into Rh crystal
RF	radio frequency
RT	room temperature
rpm	revolution per minute
ΔS	entropy of formation
Σ	sum
σ	site distribution width
S	south pole
s	distance from the centre of the substrate table to the point of deposition
T	temperature (Kelvin)
t	time
θ	angle of incidence
TEM	transmission electron microscopy

UV	ultra-violet
V	molar volume
V, v	velocity
V	electric field gradient
VBF	Voigt-based fitting
WDS	wavelength-dispersive spectroscopy
Ω	resistance
ω	width of Gaussian
ω	frequency
x	magnification
x	composition variable
XRD	x-ray diffraction
y	composition variable
Z	nuclear charge
z	composition variable
ZAF	Z(atomic number)-Absorption-Fluorescence

Acknowledgements

Although I am the sole author, many people made significant contributions to this thesis. Prof. Jeff Dahn is the reason all this was possible. He conceived of and / or acquired the equipment, assembled a team of driven individuals, gave me freedom to explore without cutting me loose, asked for better explanations, and is still helping me to see the forest and the trees. Thanks.

Josh McGraw, Jessica Topple, and Richard Mar helped with sample fabrication and data collection. Their numerous specific contributions are noted throughout. I would also like to thank my committee members, Prof. Rich Dunlap and Prof. H. Jürgen Kreuzer, for guiding my attempts to convert a vast amount of data in to useful information. Dr. Mark Obrovac of 3M Co. provided a lot of valuable insight.

Dr. Tim Hatchard, Dr. David Stevens, Arman Bonakdarpour and Simon Trussler all played major roles in bringing our combinatorial methods to life. David Stevens wears many hats including chief programmer, computer administrator, and calm voice of reason. I can thank Dave, Dr. Brad Easton, and the rest of the Wendy's crew for many things, including my blood cholesterol. Dr. Junwei Jiang and Vincent Chevrier kept my heart pumping by providing energetic, but friendly, competition. May we be all be rich (in the broad sense) some day.

Kevin Whittingstall, Megan Saunders, Dr. Shane Beattie, Sue McWillams, Andrew Richardson and co. made Halifax a better place to live. That being said, I will finally move my very supportive home base from Fergus, ON to Edmonton, AB. Susan, Mom, Dad, John, you have no idea how much I appreciate you being there for me. Massa, you count too. The original motivation behind all of this was provided by my uncle, Ken Burns, who told me to "work hard, work smart" back in 1996.

Finally, I would like to thank the W.C. Sumner Foundation, Dalhousie and Prof. Jeff Dahn for financial support, as well as NSERC and the I.W. Killam Trust for substantial and continuing financial support.

Chapter 1

Introduction

Portable electronics powered by rechargeable batteries are changing the way we live. Batteries are collections of electrochemical cells, each of which allow ions to pass between two electrodes through an electrolyte. The corresponding electrons travel through an external circuit. Rechargeable batteries are able to transfer ions and electrons from one electrode to the other and back again ideally thousands of times. Typical rechargeable battery systems are based on a variety of chemistries, including lead-acid, nickel-cadmium, nickel-metal hydride, and the focus of this thesis, lithium-ion. Ions are transferred to and from the electrolyte using either an oxidation or reduction process. Since both electrode materials act as either an anode or cathode during charge and the opposite during discharge, electrode materials with a lower (higher) average potential relative to a reference potential (typically Li^+/Li) are referred to as negative (positive) electrodes.

1.1 Li-Ion Batteries

Li-ion rechargeable battery systems offer numerous advantages over other systems, including high energy density, excellent charge/discharge cycle life and low environmental impact. One of the main challenges in Li-ion battery development is to improve upon these advantages without increasing, or better yet by reducing, costs. A great deal of research focuses on improving the performance of rechargeable Li-ion batteries by improving the electrode materials. The charge capacity, rate capability, structure, composition, and thermal stability of an electrode material are some of the quantities of interest. Electrochemical testing is performed by controlling either the potential or current flow between the test material and a known electrode material, and measuring either the current flow or potential with time. One complete Li insertion / removal cycle, corresponding to charging and discharging, is known as a cycle.

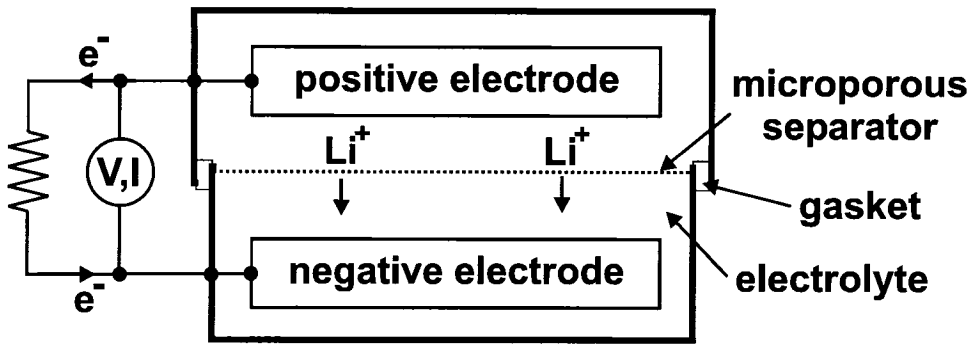

Figure 1.1: Schematic of a Li-ion cell undergoing charging.

A schematic of a Li-ion rechargeable cell is shown in Figure 1.1. Both electrodes are bathed in an electrolyte composed of Li salts (such as $LiPF_6$, $LiClO_4$ or $LiBC_4O_8$) dissolved in organic solvents (such as ethylene carbonate (EC), diethyl carbonate (DEC), dimethyl carbonate, among others, or some combination thereof). Each electrode is in electrical contact with one side of the cell casing. A gasket electrically isolates the cell casings and seals the cell. A microporous separator allows for the passage of Li^+ ions between electrodes when an external circuit is completed.

Early Li-based cells combined a Li metal negative electrode with Li salt dissolved in an liquid inorganic electrolyte (e.g. $LiAlCl_4$ in $SOCl_2$) [1], or a solid layered positive electrode such as TiS_2 [2]. Details of early electrode development are available in [3] and [4]. Upon repeated cycling, the Li metal electrode tends to form dendrites, which can puncture the microporous separator and short-circuit the cell. Scrosati *et al.* [5,6] were one of the first groups to demonstrate cells based on the 'rocking chair' concept with graphite negative electrodes. Li^+ ions 'rocked' between the positive and negative electrodes. Sony [7] introduced commercial cells based on this technology in 1990 using graphite negative and $LiCoO_2$ positive electrodes. Graphite and $LiCoO_2$ are still the predominant electrode materials after fifteen years of research and development. Graphite has a gravimetric / volumetric capacity of 350 mA h/g / 800 mA h/cc [1]. The gravimetric capacity of $LiCoO_2$ is lower than that of graphite (140 mA h/g) but the volumetric capacity is similar (700 mA h/cc) because of the higher density of $LiCoO_2$.

[1] mA h/g and mA h/cc are standard units of charge capacity, corresponding to the amount of charge stored per gram or cubic centimetre of pre-lithiated material.

$LiCoO_2$ is just one of the many $LiMO_2$ (M = transition metal) positive electrode materials under development. Co is toxic and expensive. Replacements such as $Li[Mn_xCo_{1-2x}Ni_x]O_2$ and $Li[Ni_xLi_{1/3-2x/3}Mn_{2/3-x/3}]O_2$ ($0 < x < 0.5$) are under investigation. See [8], [9], and associated references for details. Other positive electrode materials such as $LiFePO_4$ [10] and $LiMn_2O_4$ [11] offer advantages over $LiMO_2$ materials, such as improved safety, at the expense of lower capacity, power and/or cycle life. State of the art positive electrode materials are reviewed in [12]. Most positive electrode materials have theoretical capacities in the range of 100-200 mA h/g, leaving little room for dramatic capacity improvements over current commercial cells. Future work likely involves composite positive electrodes based on high capacity positive electrode materials held together with advanced binders (eg. [13]). Binders, electrolyte solvent / salt, and conductivity enhancements all play an important role in improving battery performance and safety but will not be discussed further. Instead, this thesis focuses on the dramatic capacity increases that can be realized with advanced negative electrode materials.

1.2 Negative Electrode Materials

Graphite has a theoretical capacity of 372 mA h/g. Li is stored between sheets of graphite at a ratio of one Li for every six carbons (LiC_6). The separation between graphite sheets changes by approximately 10% during Li insertion and removal. Graphite is inexpensive to manufacture, has a low average charge and discharge potential (all potentials are relative to Li^+/Li), can be cycled hundreds of times, and is relatively well understood. A review of graphitic carbon negative electrodes is available in [14].

element	grav. capacity	vol. capacity	Li:element ratio	avg. potential
Al	992 mA h/g	2680 mA h/cc	1:1 (LiAl)	0.3 V
C	372 mA h/g	840 mA h/cc	0.167:1 (LiC_6)	0.1 V
Sb	660 mA h/g	4420 mA h/cc	3:1 (Li_3Sb)	0.9 V
Si	3578 mA h/g	8483 mA h/cc	3.75:1 ($Li_{15}Si_4$)	0.4 V
Sn	992 mA h/g	7200 mA h/cc	4.4:1 ($Li_{22}Sn_5$)	0.5 V

Table 1.1: Theoretical room-temperature gravimetric and volumetric capacities of some elements that reversibly react with Li [15].

Table 1.1 lists just a few of the many materials that will reversibly react with Li. Other active materials, such as Pb and Ge, are not practical electrode materials for toxicity or cost reasons. Dey [16] performed a comprehensive survey of the reaction of Li with a variety of elements in 1971. More detailed studies on the reactions of Li with Al [17], Sb [18], Si [19] and Sn [20] were later reported.

Two conclusions can be reached from the data shown in Table 1.1. One, dramatic capacity increases (on both a gravimetric and volumetric basis) can be realized by replacing graphite with other elements. The second conclusion is more subtle. The energy density of a cell is based on capacity and the potential at which that capacity can be accessed. The cell potential is the difference between the potential of the positive and negative electrodes. Negative electrode materials with low average potentials are more desirable for high-energy density applications. Graphite has the lowest capacity but also the lowest average potential. There must therefore be some trade-off between capacity and average potential. Si offers the best combination of high capacity and low potential of the elements listed in Table 1.1.

The large capacities of Li alloys shown in Table 1.1 are also associated with large volume changes relative to those experienced by graphite. Fully-lithiated Si or Sn electrodes can expand to nearly four times their original size [21]. Large and uneven volume changes during Li insertion or removal lead to pulverization of the electrode material, a loss of electrical contact and therefore a loss in capacity. Poor capacity retention prevented high capacity alloy materials from being used commercially. Idota *et al.* of Fuji changed the nature of Li-ion negative electrode material research with their introduction of tin-based convertible oxides [22] with 600 mA h/g of reversible capacity and reasonable capacity retention. Li reacts with SnO_2 or other oxides during the first Li insertion to form a mixture of Li_2O and nanocrystalline Sn [23]. Li consumed in the production of Li_2O could not be extracted, which lead to a high irreversible capacity of up to 800 mA h/g. Courtney and Dahn demonstrated Sn tends to aggregate during extended cycling, leading to two phase regions, non-uniform volume expansion, and ultimately capacity fade [24]. Commercialization of batteries based on convertible oxide negative electrodes is still being attempted [25].

Variations of the active/less-active or inactive matrix concept [26] were introduced earlier by Huggins [27] and Yang *et al.* [28]. Absolute volume changes were sharply

reduced by dispersing small grains of active material in a porous metallic matrix produced during the first lithiation [28]. While this approach leads to better capacity retention, the inactive component reduces the capacity. Active material aggregation is also an issue. A review of negative electrode material development up to 1999 is available in [15].

A variety of other approaches have recently been attempted. Ferg *et al.* reported $Li_4Mn_5O_{12}$, $Li_4Ti_5O_{12}$, and $Li_2Mn_4O_9$ can be used as safer alternatives to graphite negative electrodes [29]. The increased safety came at the cost of a higher average potential (1.6 V vs 0.1 V) and low capacity (ca. 200 mA h/g). Poizot *et al.* realized much higher capacities (ca. 1000 mA h/g) and excellent capacity retention with transition metal oxides [30]. However, the high average potential (ca. 1.5 V) once again eliminates any high-energy density applications. Transition metal phosphides suggested by Souza *et al.* [31] offer high capacities (ca. 1000 mA h/g) and lower average potentials (ca. 0.5 V) but are plagued by poor capacity retention. Some authors have also doped graphite with various active elements such as Bi, Si and Sn (or coated said active elements with C) with mixed results [32, 33].

None of the negative electrode materials mentioned above are ideal from a capacity, average potential, capacity retention and production cost point of view. Beaulieu *et al.* [34] showed that amorphous alloys expand and contract uniformly during Li insertion and removal, eliminating uneven volume changes and a major source of capacity fade in high capacity materials. Amorphous Si-based electrodes should have high capacities, low average potentials, and excellent capacity retention. The main challenges involve producing amorphous Si in a cost-effective manner and keeping it amorphous during and after hundreds of cycles.

Li has long been known to alloy with Si [19]. However, the most Li-rich Li-Si room temperature phase was only recently determined by Obrovac and Christensen [35] and later confirmed by Hatchard and Dahn [36]. Numerous authors stuck to the idea that $Li_{22}Si_5$, the most Li-rich Li-Si phase at 415 °C, occurs at room temperature, despite measuring capacities of approximately 3500 mA h/g instead of the 4200 mA h/g expected for $Li_{22}Si_5$. $Li_{15}Si_4$ has a theoretical capacity of 3578 mA h/g. Obrovac and Christensen also confirmed the claims of Limthongkul *et al.* [37] that nanocrystalline Si and Li react to form amorphous Li_xSi during the first Li insertion. The formation of

amorphous Li_xSi may be facilitated by the complex, and dissimilar, crystal structures of the various Li-Si equilibrium phases [38,39]. A high capacity, low average potential material such as Si that becomes amorphous without any complicated fabrication steps seems to be an ideal electrode candidate. However, a transition is made between amorphous Li_xSi and crystalline $Li_{15}Si_4$ at approximately 50 mV during Li insertion [35]. Crystalline $Li_{15}Si_4$ converts back to amorphous Li_xSi at approximately 0.4 V during Li removal, but the two-phase region and non-uniform volume changes lead to capacity fade. Restrictions on electrode potential are undesirable from an engineering and energy density perspective.

Amorphous materials offer numerous experimental challenges related to fabrication and the lack of long-range crystallographic order. Amorphous materials form when the production of crystalline phases is hindered for thermodynamic or kinetic reasons. The atoms are not able to move to their crystalline sites before losing kinetic energy due to rapid quenching and / or complex crystallographic structures. The three empirical rules for amorphous systems are 1) multiple components 2) large differences in component element size and 3) negative heats of formation between the components [40]. More theoretical approaches to amorphous alloy formation are described in [41, 42] and [43]. Techniques to produce amorphous alloys, including mechanical milling, sputtering and rapid solidification from the melt, involve rapid quench rates, on the order of 1×10^6 to 1×10^9 K/s. The rapid quenching reduces the mobility of component elements and helps to produce structures without long range order. While sputtering, described in Section 2.1, is a very versatile experimental method, electricity costs inhibit industrial scale sputtered electrode production. A large number of materials systems with elements of interest (such as Al, Mg, Si, Sn, Zn, etc.) can be prepared in an amorphous state by melt-spinning. A short list includes Mg-Zn [44], Si-Al-M (M = Co [45–47], Cr [45–47], Fe [45–49], Mn [45–47,49,50], Ni [45–47]), Si-Al-Fe-M (M = Co, Cr, Ni) [51, 52], Si-Al-Fe-Ni-Cr [53] and Si-Al-Fe-Ni-Cr-Zr [53]. Multicomponent Si-based amorphous alloys are reviewed by Louzguine and Inoue in [54]. Many Al-based amorphous alloys exist (e.g. [55]), but are likely to have poor electrochemical performance in part because of the lower capacity of Al relative to Si.

Sony introduced the first commercial cell based on an amorphous alloy negative

electrode in early 2005. Nexelion negative electrodes are an amorphous mixture of Sn, Co, C and other unnamed elements (Ti and In) [56]. The reversible capacity is 450 mA h/g at an average potential of 0.5 V. Capacity retention is excellent for at least the first 800 cycles. The high degree of similarity between the Sn-Co-C alloy in the Nexelion cell and the Sn-Fe-C work of Mao *et al.* [26] published in 1999 suggests a significant time lag between discovery and commercial application. Si is the only element listed in Table 1.1 whose alloys are relatively unexplored. One can hope the development of Si-based amorphous alloys will proceed at a faster pace.

Beaulieu *et al.* determined certain compositions of amorphous Si-Sn offer capacities of up to 1600 mA h/g and good capacity retention [57]. Large capacities and good capacity retention were also observed for amorphous compositions of Si-Al-Sn [58]. However, both Si-Sn and Si-Al-Sn can only be produced in an amorphous state using expensive sputter-deposition methods. Details of the author's investigations of amorphous $Si_xAl_yMn_z$ $x + y + z = 1$ will be presented shortly. Subscripts are required to identify the precise composition of an amorphous alloy since crystalline phases (of known composition) are not present. Decimal subscripts are used to distinguish amorphous alloys from crystalline phases. Amorphous alloys can sometimes be produced over broad compositions ranges. This composition flexibility permits some optimization of various parameters such as capacity and conductivity, but increases the fabrication and characterization requirements dramatically. Tens to hundreds of samples would need to be fabricated and characterized to determine the electrochemical performance of only one of the amorphous material systems mentioned above. New experimental techniques, described in the following section, make investigations of the electrochemical performance of amorphous alloys practical.

1.3 Combinatorial And High-Throughput Methods

The main goal of combinatorial and high-throughput methods is to speed the materials discovery and optimization process. The cycle of sample fabrication, characterization and analysis for choice of future starting materials is repeated until satisfactory results are achieved. Significant improvements in data quality can also be realized by eliminating sample-to-sample variability.

Kennedy *et al.* [59] introduced the composition-spread technique in 1965. Two (or

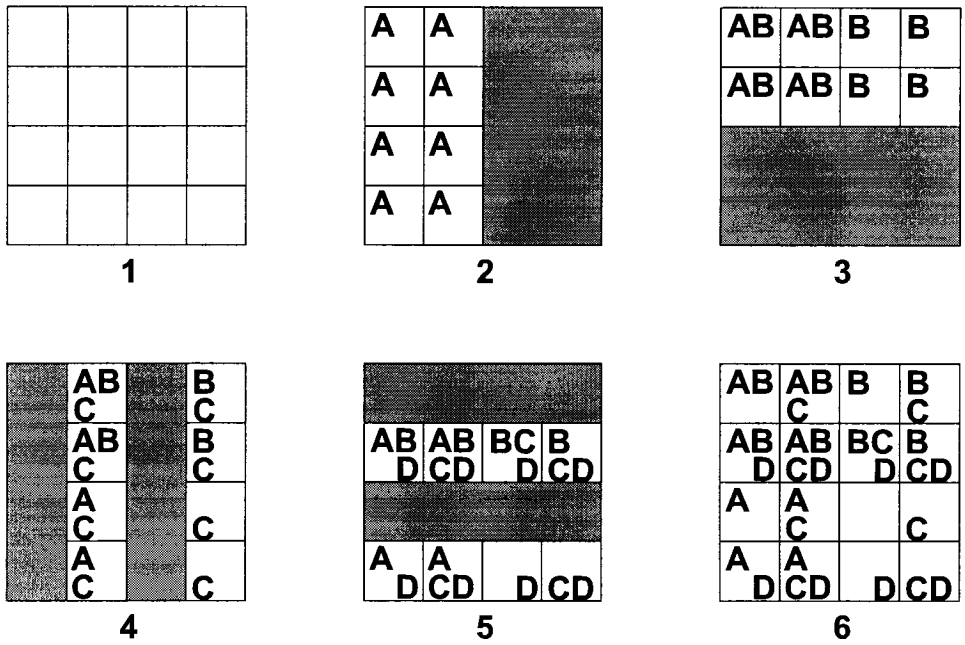

Figure 1.2: An example of the fractal masking technique [64]. Grey areas are used to indicate those pixels blocked by a shadow mask during the deposition of starting material A, B, C or D.

more) physical vapour deposition sources (eg. sputtering target, evaporation boat) are placed opposite a substrate. Composition variations can be produced since the flux on the substrate from each source varies with position. J.J. Hanak introduced the multiple-sample concept [60] in 1970, which combined high-throughput fabrication and testing methods. Combinatorial methods were then applied to pharmaceutical research and development (see [61] and references therein for details). Xiang, Schultz and co-workers at Symyx Technologies and the University of California ushered in the modern era of solid-state combinatorial materials science in 1995 with a landmark paper [62] and broad, but probably unenforceable, patents [63, 64].

Schultz *et al.* abandoned the simple composition-spread technique in favour of discrete pixels of material. Their two main fabrication techniques involve either electrochemical deposition of the test material or a complex physical vapour deposition method. A schematic of the fractal masking technique is shown in Figure 1.2 [64]. Many possible combinations of the starting materials can be produced by restricting the physical vapour deposition profile. Panel 1 of Fig. 1.2 depicts the bare substrate.

A mask is placed over the right half of the substrate in panel 2 so that starting material A is only deposited on pixels on the left half of the substrate. Similar steps are performed for certain columns and certain rows of pixels for starting materials B, C, and D in panels 2-5 of Fig. 1.2. Panel 6 shows that many possible combinations of A, B, C, and D were fabricated. Starting materials are mixed either with an annealing step or by depositing very thin (a few Å) layers and repeating the deposition process hundreds or thousands of times.

Warren *et al.* [63] devised a system whereby various starting materials are mixed in solution and then electrodeposited on to an electrical contact. This method is limited by expensive robotics and finding suitable salts / solvents for all desired materials. However, the idea of multiple (typically 64) electrodes on a single substrate can of considerable use. All 64 electrodes can be tested in a parallel or serial manner when the substrate is interfaced with a combinatorial electrochemical cell and a multi-channel potentiostat. This system is just one of many high-throughput electrochemical testing systems. Reddington *et al.* [65] introduced the combinatorial electrode array in 1998. Highly-reactive fuel cell catalysts were identified by acid-base fluorescence indicators. Sullivan *et al.* [66] extended this concept by attaching electrical leads to each pixel, which allowed for the current associated with each test electrode to be determined. Numerous combinatorial electrochemical cells have been designed since [67–71].

Watanabe *et al.* reported the first combinatorial investigation of Li-ion rechargeable battery electrode materials in 2001 [72]. Three other groups, including that of the author, presented combinatorial synthesis and testing methods at The Electrochemical Society sponsored meetings in 2002 [73–75]. Devenney *et al.* of Symyx are the only other researchers publishing accounts of combinatorial battery electrode development [76]. The groups of Wantanabe and Owen achieve composition variation by depositing solutions of various starting materials in wells, and then driving off the solvent. This approach is limited since only one sample of each composition is produced at a time. High-throughput testing is much more powerful if the various testing methods can be performed in parallel. These methods are also more suited to investigating positive electrode materials; amorphous solids are difficult to investigate when annealing steps are required. The costs associated with increasing the throughput rate of Wantanabe *et al.* are also prohibitive, as discussed in [77].

Composition-spread techniques are still used in high-throughput materials investigations (eg. [78–80]). The JPL group has the ability to deposit hundreds of complete microbatteries on a single substrate using a solid electrolyte and microfabrication facilities. While this approach is impressive, the very thin film / solid electrolyte approach is more suited to high-cost applications such as space exploration than standard commercial cells. The method of the Dahn group, described in [67] and [80], compares favorably with the other combinatorial electrode material investigations [77]. Briefly, films with up to two linear and orthogonal composition gradients can be deposited on multiple substrates, which permits fully parallel testing. Both negative (e.g. [81–83]) and positive [84] electrode materials have be investigated. Full details of the combinatorial infrastructure at Dalhousie University are provided in Chapter 2.

1.4 Electrochemical Results

Si-Al-Mn was the first material system to be investigated in the Dahn group using only combinatorial and high-throughput fabrication and characterization methods [83]. Si-Al-Mn is a promising negative electrode material since both Si and Al readily alloy with Li, and broad composition ranges can be prepared in an amorphous state by melt-spinning [46, 47]. The first discharge capacity of the Si-Al-Mn system is shown as Figure 1.3. The capacity varies smoothly from over 3000 mA h/g for nearly pure Si to 1000 mA h/g for nearly pure Al, as expected. Transition-metal content has a dramatic effect on capacity; 20 at. % Mn completely inactivates compositions with less than 50 at. % Si. Attempts were made to model the capacity as a function of composition, assuming one Mn atom inactivated either x Si atoms or y Al atoms [85]. This method prompted more thorough investigations of the Si-M [86], Al-M [87] and Al-Si systems. The general approach of this thesis is to apply lessons learned from investigations of the Si-M, Al-M and Al-Si systems to develop a phenomenological model for the capacity of the Si-Al-M system. Details of the author's investigations of the Si-M system are available in [86] and Chapter 3. Work on the Al-M system is reported in [87] and Chapter 4. Chapter 5 reports unpublished results from the Al-Si system. Investigations of Si-Al-M (M = Cr, Fe, Mn, Ni) are reported in Chapter 6.

Capacity determination is a major component of electrode characterization. It is

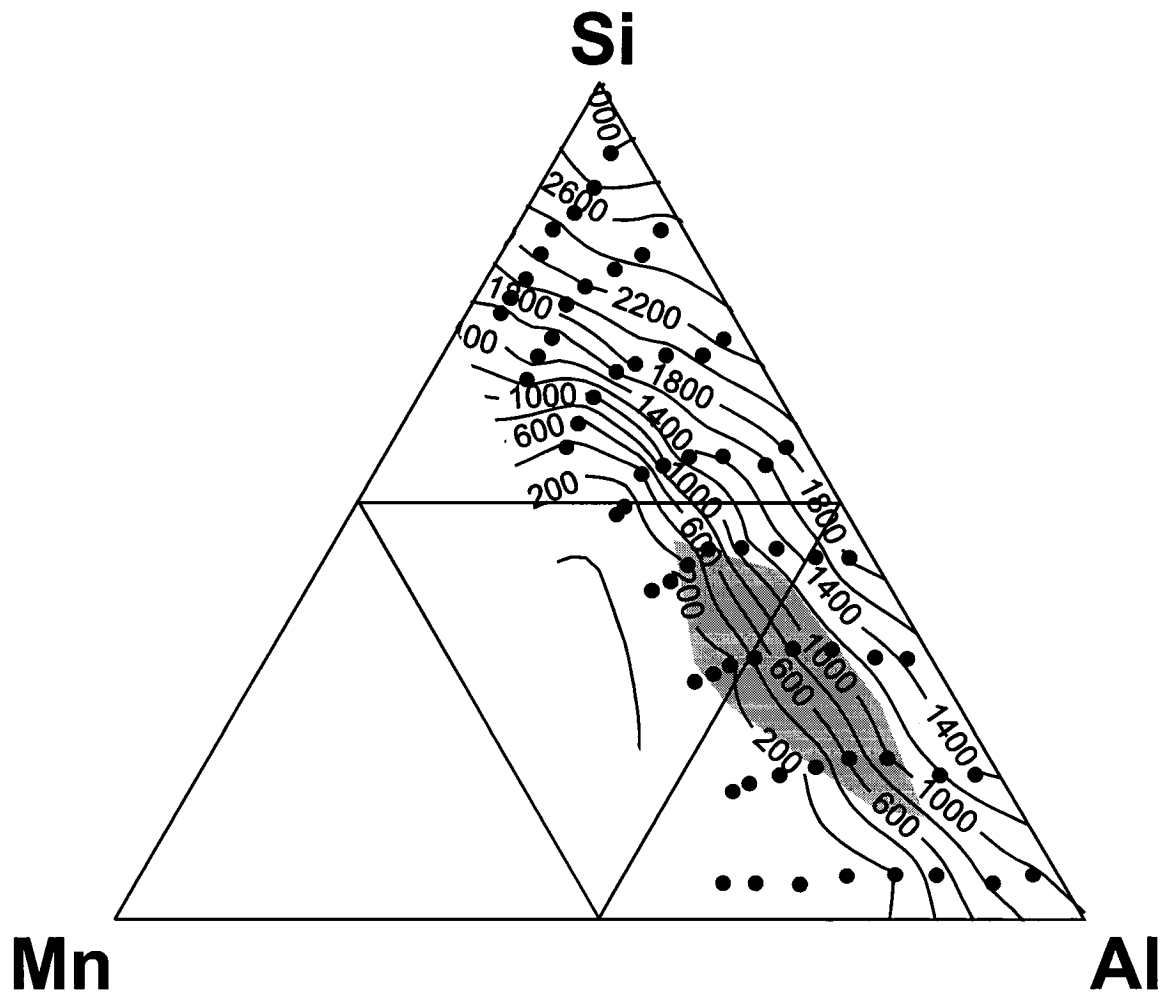

Figure 1.3: Room temperature first discharge capacity of Si-Al-Mn as a function of composition. Dots are used to label the compositions investigated. The shaded region indicates compositions that can be prepared in an amorphous state by melt-spinning [46, 47].

important to understand the difference between the fundamental capacity of a material, which depends only on the relevant phase diagram, and the observed capacity. The observed capacity is a result of the fundamental capacity and the rate at which the capacity is accessed. Our electrochemical cycling method, described in Section 2.4, cycles the test materials via potential control. This has the effect of setting the surface concentration of Li in the test material. Even though the thin film libraries are generally less than 1 μm thick, the Li concentration can vary a great deal from the surface to the back of the test material. Increasing the transition metal content seems to increase the concentration differential during cycling. Long periods of constant potential (generally at 5 mV) are often required to fully lithiate the test material. Periods of constant potential at 1.2 V are used to remove accessible Li from the test material.

Separating the effects of diffusion and composition is not a trivial problem. The broad range of compositions of interest adds additional complexities. The experimental techniques outlined in the following chapter rely heavily on combinatorial and high-throughput methodologies and computer automation to speed throughput. Structure, weight, composition, calorimetry, and electrochemical measurements can be performed on each thin film library.

1.5 Macroscopic Atom Model

Theory can sometimes provide results faster than any high-throughput experimental technique. Theoretical approaches are often used to gain insight to the physics of layered positive electrode materials. The group of Ceder *et al.* at M.I.T. has made significant contributions to the understanding of transition metal ordering in crystalline positive electrode materials and their equilibrium phase diagrams (e.g. [88,89]). Symmetry considerations and known Li bonding sites make such investigations feasible. Calculations based on amorphous materials would be complicated by the lack of symmetry, uncertain Li bonding sites, and complicated stoichiometries.

The macroscopic atom model of de Boer *et al.* [90] can be used to estimate the heat of formation of many binary metal systems. This information can then be used to screen for compositions whose reaction with Li is energetically favourable. The

Gibbs free energy of formation is given by

$$\Delta G^{for} = \Delta H^{for} - T\Delta S^{for}$$

where ΔH^{for} is the enthalpy of formation, T is the temperature (Kelvin) and ΔS^{for} is the entropy of formation. Reactions with negative free energy of formation will proceed; reactions with positive free energy of formation will not. de Boer *et al.* focus on estimating ΔH^{for} since entropy considerations are generally small for crystalline metallic alloys at room temperature [90].

The macroscopic atom model considers interactions between one atom of metal A surrounded by atoms of metal B. de Boer *et al.* assume the bulk of the interaction between atoms A and B can be described by the electron density at the boundary of the Wigner-Seitz cell n_{ws} and the electric charge chemical potential ϕ^*. Energy is required to remove discontinuities in electron density and released when two dissimilar metals are brought into contact. The heat of formation for a two-component alloy $A_{c_a}B_{c_b}$ where c_a and c_b are the molar concentrations of elements A and B is given by

$$\Delta H^{\text{for}}_{\text{calc}} = c_b\left(\Delta \bar{H}^{\text{interface}}_{\text{B in A}} + \Delta H^{\text{trans}}_{\text{B}}\right)$$

and

$$\frac{\Delta \bar{H}^{\text{interface}}_{\text{B in A}}}{V_{\text{B}}^{2/3}} = \frac{[-P(\Delta\phi^*)^2 + Q(\Delta n_{\text{WS}}^{1/3})^2 - R^*]}{(n_{\text{WS}}^{-1/3})_{\text{av}}}$$

where $\Delta\phi^*$ is the difference of work functions for elements A and B adjusted for experimental uncertainty. Δn_{ws} is the electron density at the boundary of the Wigner-Seitz cell and V_B is the molar volume of element B. ΔH_B^{trans} is only non-zero for those elements B, such as Si, that undergo a semiconductor-metal transition when alloying with a metal element A. P and Q are empirical parameters related to the most common oxidation state of elements A and B. R^* is a parameter related to the compressibility of electron density. All details and tables required to perform calculations with the macroscopic model are provided in Appendix A; full details of the model are available in Cohesion of Metals [90]. It should be noted that this model was developed for use with transition metal alloys but can be used for non-transition metal alloys with some success.

The application of the macroscopic model is far simpler than the equations on the previous pages. Consider the reaction

$$(1-x)\text{Li} + \text{Al}_{1-x}\text{M}_x \rightarrow (1-x)\text{AlLi} + x\text{M}.$$

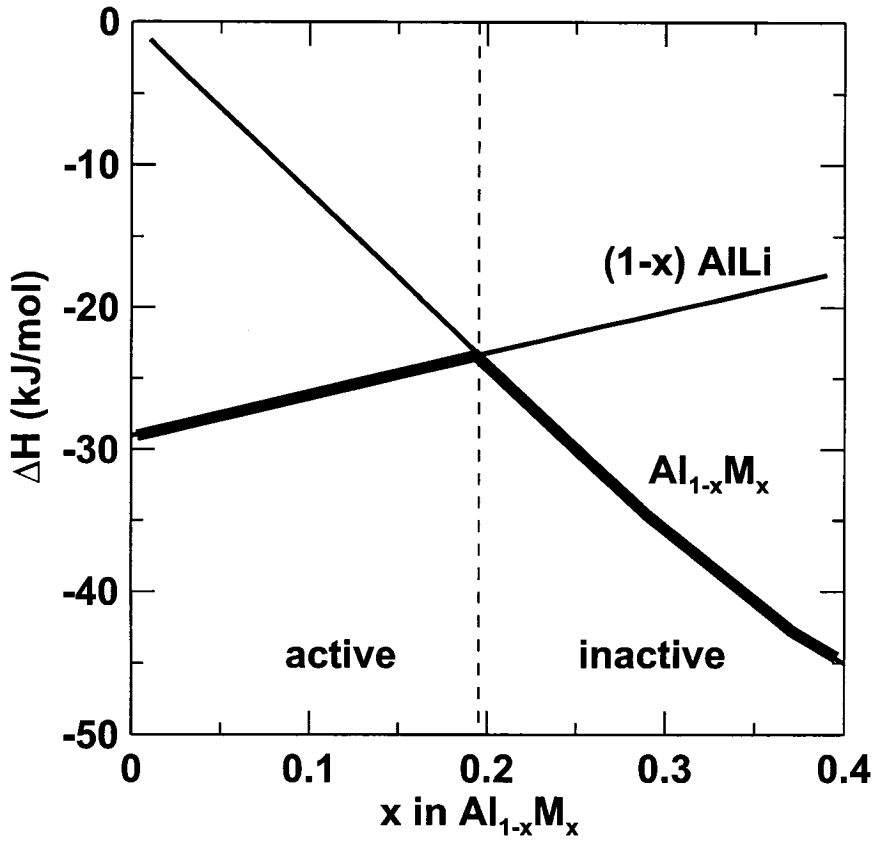

Figure 1.4: Schematic of heat of formation of $(1-x)$ moles of AlLi and 1 mole of $Al_{1-x}M_x$ as a function of x. The thick line indicates the most stable Al alloy as a function of M content. A dashed line separates the region where the formation of AlLi is favorable from the region where $Al_{1-x}M_x$ will not react with Li.

This reaction will only proceed if the heat of formation of $(1-x)$ moles of AlLi is more negative than that of 1 mole of $Al_{1-x}M_x$. Fig. 1.4 indicates this reaction will only proceed for compositions of $Al_{1-x}M_x$ with less than roughly 20 at. % M. The solid line of Fig. 1.4 indicates the most stable Al alloy as a function of composition.

Diagrams such as Fig. 1.4 could be used to speed combinatorial studies of advanced battery materials by limiting the range of compositions investigated. However, the large number of approximations and uncertainties present in the macroscopic model prevent it from being used for tasks such as composition optimization and structural understandings of electrode performance. Methods for the important task of electrode material fabrication and characterization will now be presented.

Chapter 2

Experimental Techniques

2.1 Thin Film Deposition

This thesis depends on the ability to fabricate and characterize a broad range of compositions simultaneously[1]. Sputter-deposition stands out from other physical vapour deposition techniques since it can be used to deposit elements, compounds, conductors, semi-conductors and insulators on any vacuum-compatible substrate. All thin film libraries described in this thesis were fabricated using a Corona Vacuum Systems VT-3 multi-target sputtering machine. The 61 cm diameter / 30.5 cm deep vacuum chamber is evacuated using a Varian 500 L/s turbo pump, which is backed by a roughing pump. Water vapour is removed from the chamber using a Polycold cryopump. Typical base pressures are in the low 10^{-7} torr range. Further details of this sputtering setup will be provided as the sputtering process is described.

Bombarding a target of source material with energetic ions can cause portions of the target to be removed by momentum transfer. A schematic of this process, known as sputtering, is shown in Fig. 2.1. A voltage is applied across the target and substrate, both of which are inside a high-vacuum chamber. The substrate and chamber are normally biased to ground. The target is negatively biased to hundreds of volts. Ions present in the vacuum chamber (due to cosmic rays etc.) accelerate to the substrate and target. At a sufficiently high voltage, the ions will collide with and ionize an inert gas introduced into the chamber. Collisions with inert gas atoms produce more ions, which in turn produce more collisions. A plasma soon forms between the target and substrate. Ionized inert gas atoms in the plasma accelerate toward the target. Electrons and target molecules are removed by momentum transfer when the gas ions strike the target. The ejected electrons then ionize more inert gas atoms as they travel through the plasma to the substrate or ground. Additional electrons are provided to the target by the power supply to conserve charge and drive

[1]Portions of this chapter first appeared in the author's M. Sc. Thesis [91]

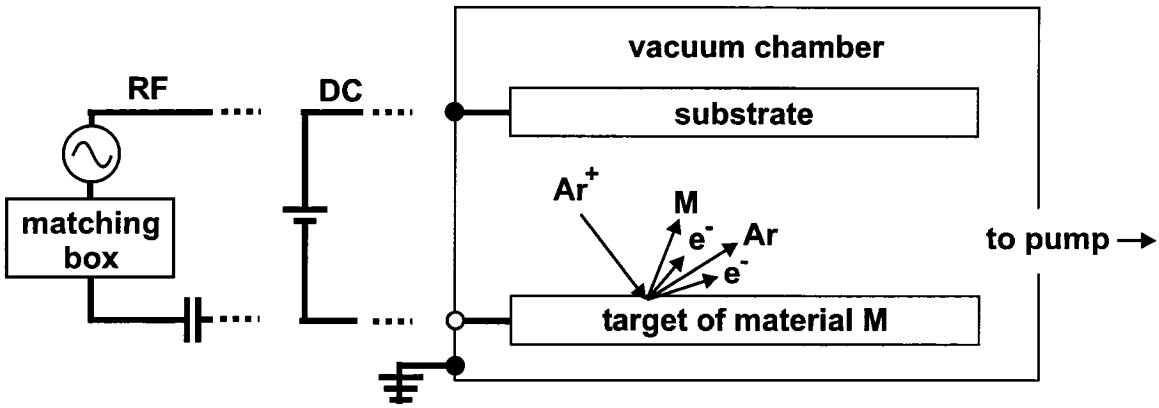

Figure 2.1: Schematic of the sputtering processes. Wiring diagrams for RF and DC sputtering are shown to the left of the vacuum chamber.

the process. The plasma is sustained by balancing the number of electrons emitted from the target with the number required to ionize enough gas atoms to cause the electrons to be emitted.

Electrically insulating materials can be sputtered if the target is capacitively coupled to an AC power supply. An impedence matching box is used to maximize the power transmission to the plasma. Tuning the impedance matching box results in a reflected power generally less than 10% of incident power. By convention, most AC sputtering systems operate at 13.6 MHz. Electrons flow in to the capacitor shown at the left of Figure 2.1 during the positive half of the voltage cycle. Current flow in to the capacitor during the negative half of the voltage cycle is much smaller since the ions are much heavier and therefore not as mobile. A negative target bias develops during the first few cycles since no net current can flow through the capacitor. Ar^+ ions respond to the bias voltage by striking the target and removing material. Electrons striking the target during the positive half of the voltage cycle prevent charge build-up [92]. Both the substrate and vacuum chamber are held at ground to prevent them from being sputtered.

It is difficult to sustain a plasma at low gas pressure since collisions between electrons and gas atoms are infrequent. Increasing the gas pressure produces more electron - gas atom collisions, but also affects the deposition rate and structure of the deposited film. The number of electron - gas atom collisions can be increased by increasing the electron drift path with crossed electric and magnetic fields. Concentric magnets placed underneath the target, shown in Figure 2.2, produce an $\vec{E} \times \vec{B}$ path

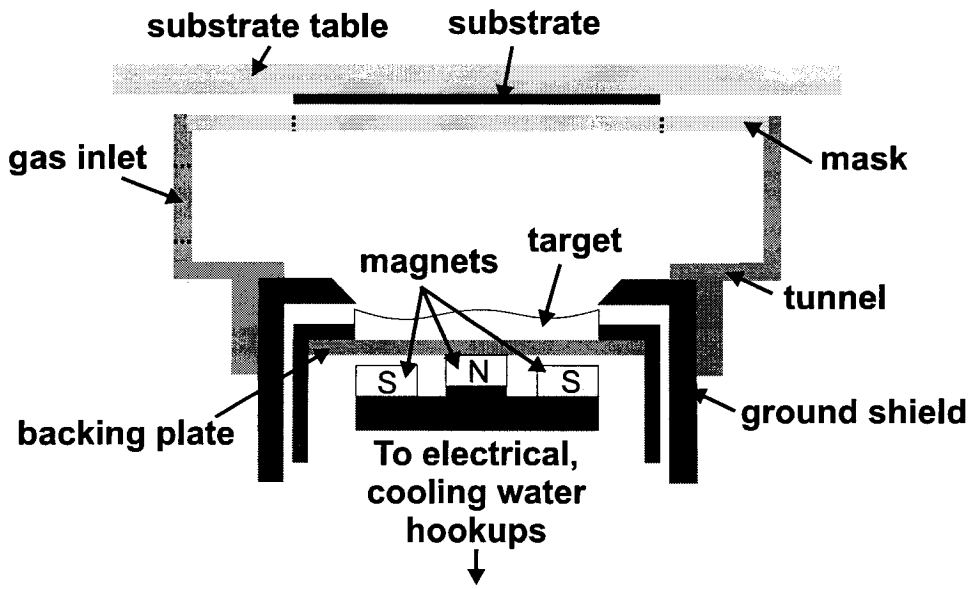

Figure 2.2: Components of a magnetron sputtering source.

that closes on itself when the electric field is normal to the target. A plasma can be formed in this region above the target with a gas pressure as low as a few tenths of a millitorr of Ar [93]. Magnetron sputtering allows for great flexibility in deposition rate and gas pressure for a given target material.

Each of the five magnetrons in the sputtering system uses a pair of Nd-Fe-B button and ring magnets. The button magnets are 1.9 cm in diameter. Ring magnets are 4.8 cm in outer diameter and are 7.6 mm wide. All magnets are 6 mm thick. The five magnetrons are separated by 60° on a 27.7 cm diameter circle concentric with the centre of the vacuum chamber. Four of the magnetrons are used for source material and the fifth is used for a plasma scrubber, which projects a plasma on to the substrates to remove various contaminants. Heat is removed from the target through the backing plate shown in Figure 2.2 by flowing water around the magnets. Water cooling the magnetrons prevents the target material from changing phase, and demagnetization of the magnets. The substrate table is also water-cooled to prevent substrate heating during sputter deposition.

The spatial extent of the plasma is limited by components surrounding the target (shown in Fig. 2.2) that restrict the gas and current flow. Gas pressure is controlled with a MKS M100B Mass-Flo controller and throttle valve on the turbo pump.

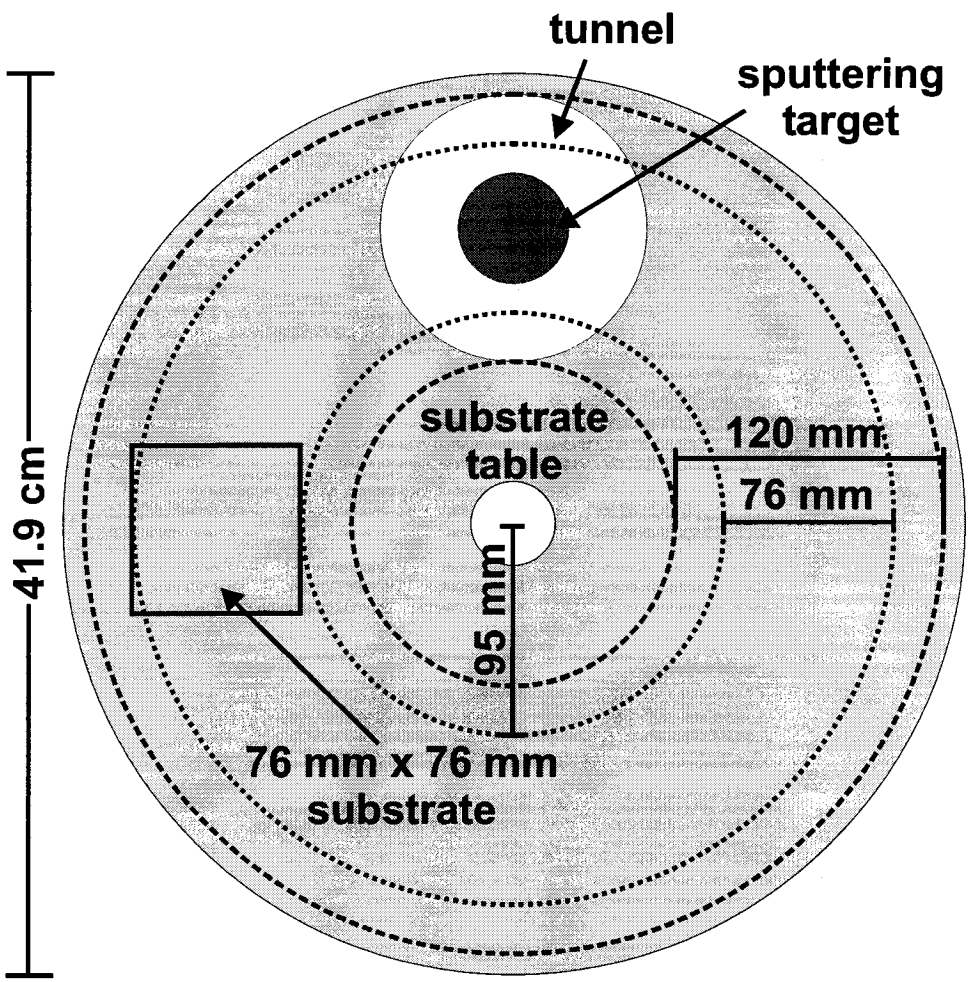

Figure 2.3: Layout of the sputtering machine substrate table. Reproduced by permission of The Electrochemical Society, Inc. [67].

Atoms or molecules ejected from the target coat all exposed surfaces. Most sputtering runs are performed with masks in place over each source material target. Thin films with composition gradients can be deposited on to the rotating substrate table if masks are used to vary the radial deposition profile of multiple source materials. Masks designed to produce deposition profiles that increase, decrease or are constant with radius can be combined with different targets to deposit a large range of compositions. If no mask is present, the deposition on a stationary substrate is highest directly opposite the centre of the target and diminishes with increasing distance from the target centre.

All substrates are mounted on a rotating substrate table, shown in Figure 2.3. The position of the target is noted with a dark grey circle. As the substrate table rotates

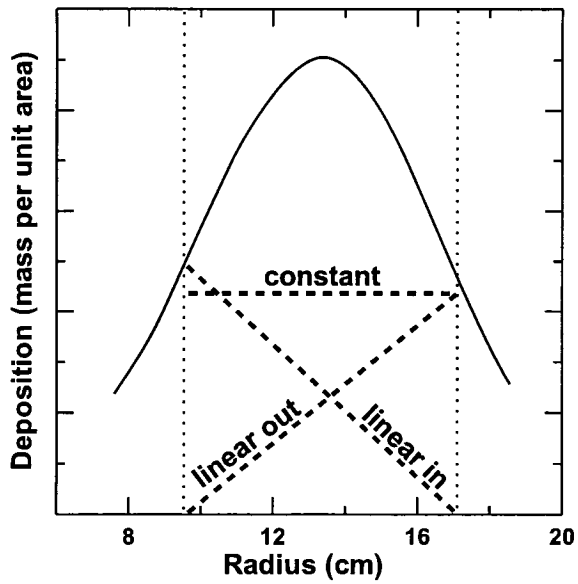

Figure 2.4: Deposition profile as a function of radius (solid line) when no mask is present. Dotted lines correspond to those in Figure 2.3. Thick dashed lines correspond to various deposition profiles.

underneath the target, a layer of varying thickness is deposited on the substrate. Deposition is limited to the area inside the two dashed lines in Figure 2.3 by the tunnel shown in Figure 2.2. Even though the two dotted lines shown in Figure 2.3 are evenly spaced from the target radius, the deposition rate is not the same because the deposition area goes as the radius squared. A plot of deposition (mass per unit area) as a function of radius is given as Figure 2.4.

It is possible to control the deposition profile by placing a mask over the tunnel to block portions of the flux. The thick dotted line in Figure 2.5 shows the profile for a mask that will produce a linear thickness variation (from r_1 to r_2) on a substrate rotating underneath the target. The mask opening varies with radius, and is largest at r_2. A small opening is present directly underneath the centre of the target to limit the deposition. Details of the mask profile calculation method are provided in Appendix B and [80]. Multiple masks were designed to vary the deposition profile over a 76 mm range, from 9.6 cm to 17.2 cm from the centre of the sputtering machine. Deposition profiles included constant, increasing from zero to maximum at 9.6 cm (referred to as 'linear in'), and from zero to maximum at 17.2 cm ('linear out').

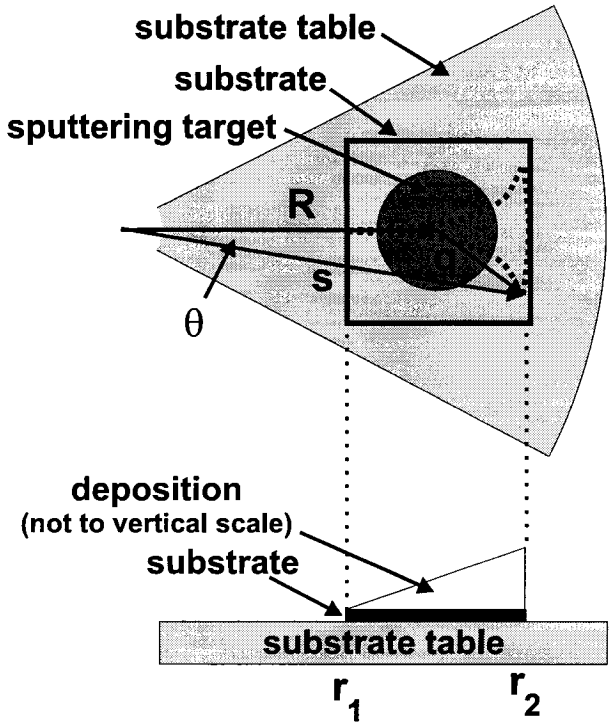

Figure 2.5: Vectors used in mask design calculation. The deposition profile with the mask in place is shown in the lower part of the figure.

Figures 2.6 a) through c) show a wedge of red[2] material that increases in intensity with radial distance being deposited on a substrate, followed by a wedge of blue material of decreasing intensity. One composition gradient is thus present in the deposited thin film library. A second, orthogonal, composition gradient is produced by rotating the substrate, mounted on a subtable, during the rotation of the substrate table, as shown in Figures 2.6 d) and e). The subtable is rotated back to its original position between Figures 2.6 f) and a), after the third wedge of material is deposited. The ability to fabricate identical thin film libraries containing linear and orthogonal composition gradients on multiple substrates is unique to this method. Layer thickness is typically on the order of a few Å, so the materials are intimately mixed. Approximately 10,000 substrate table rotations occur during the deposition of a 1 μm thick thin film library.

A variety of substrates appropriate for each characterization method are used.

[2]Colours, as opposed to shades, are used to indicate composition gradients. Two orthogonal composition gradients are present in the deposited film; this cannot be indicated using only one variable (shade). Colour versions of this figure are included where possible.

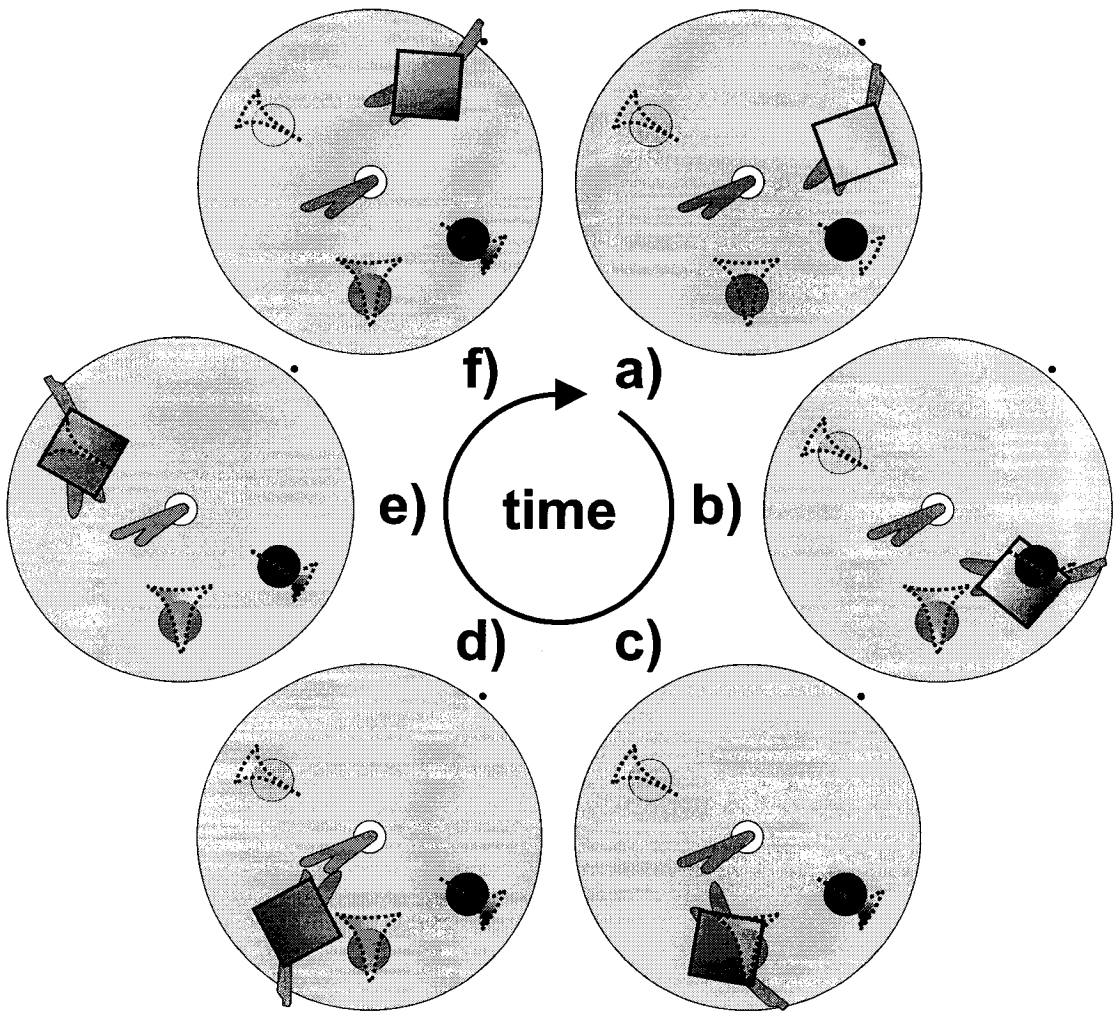

Figure 2.6: Schematic of the process described in [80], which permits films with linear and orthogonal composition gradients to be deposited on a range of substrates. Only one substrate is shown for clarity. Colour variations are used to illustrate composition variations.

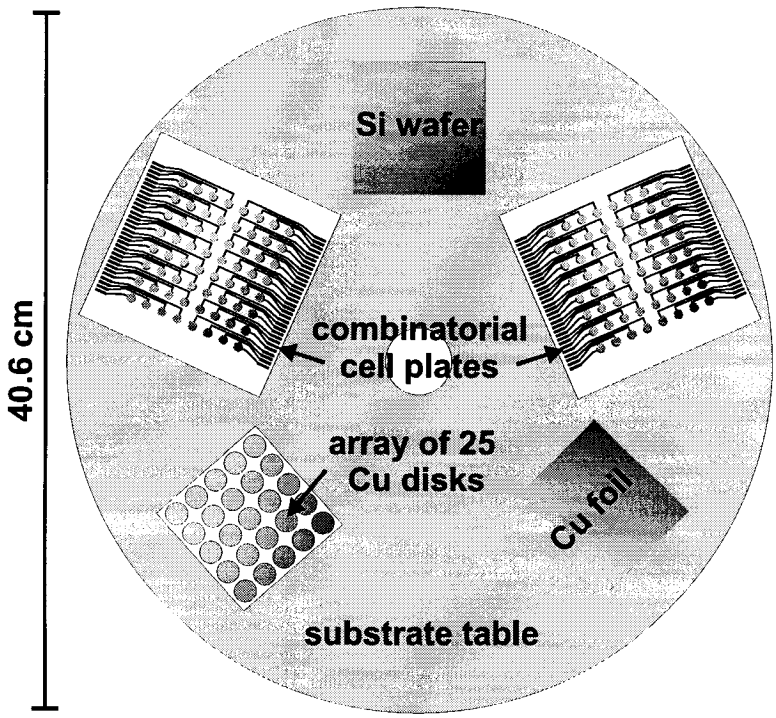

Figure 2.7: Layout of the substrates on the five substrate table for ternary deposition runs. Reproduced from [77] with the permission of IOP Publishing Ltd.

A typical substrate table load is shown in Figure 2.7. Only five 75 mm x 75 mm substrates can be loaded on to the substrate table at once due to space restrictions imposed by the rotating subtables. Tens of substrates can be loaded on substrate tables when only one composition gradient is desired. An example of this is provided as Fig. 2.8. The reader may refer to Fig. 2.3 for proper substrate position determination. Sputtering runs with one and two composition gradients are referred to as binary and ternary runs, respectively.

Many different types of substrates are indicated in Figures 2.7 and 2.8. The Si (100) wafer, kapton film and differential scanning calorimetry (DSC) pans are used for structure determination via x-ray diffraction, Mössbauer effect spectroscopy and differential scanning calorimetry, respectively. Cu foil is used as a substrate for both electron microprobe composition and mass determination since it is relatively inexpensive, conductive, durable, and not normally included in the thin film libraries. Twenty-five pre-weighed Cu disks are used for ternary runs; only 9 are required for binary runs. Al foil and disks can also be used, especially for positive electrode materials (Al does not react with Li at high potentials, Cu does not react with Li at

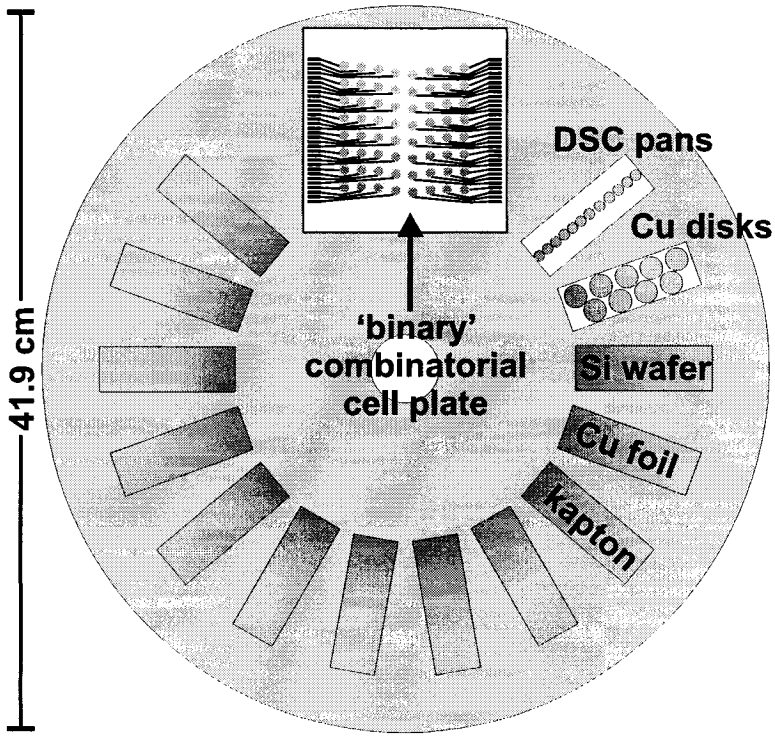

Figure 2.8: Layout of the substrates on the substrate table for binary deposition runs.

low potentials). Finally, combinatorial electrochemical cell plates are used for electrochemical testing. Any other vacuum-compatible material, such as transmission electron microscopy (TEM) grids, can replace any or all of the substrates when desired.

2.2 Structure Determination

The goal of this thesis is to understand the electrochemical performance of amorphous transition-metal alloys. It is therefore important to know the structure of the deposited thin films. Each of the four structure characterization methods described here provide different types of structural information. Peaks in x-ray diffraction (XRD) patterns are the result of constructive interference of x-rays scattered from electrons associated with nuclei on a periodic lattice. XRD is a powerful identification technique for crystalline samples but loses resolution when the periodic lattices are less than a few nm in size. Mössbauer effect spectroscopy probes the interaction of certain types of nuclei with the surrounding lattice on a smaller size scale. Insight to

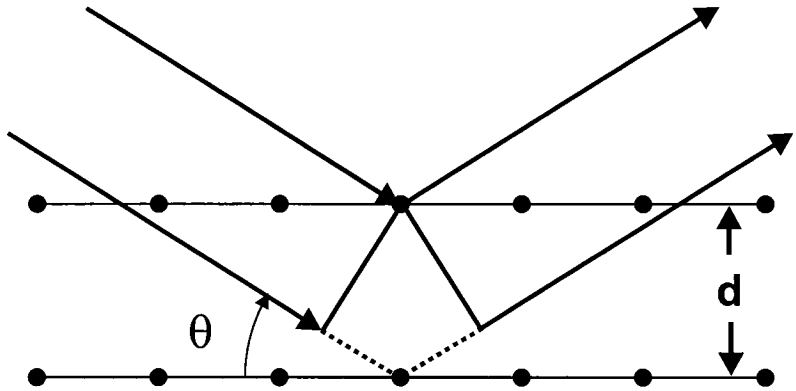

Figure 2.9: Schematic of x-ray diffraction. The extra path length of the lower incident ray (shown as the dotted line) must be an integral multiple of the incident beam wavelength for constructive interference to occur.

the microstructure of a sample can also be gained by directly imaging a very thin section of said sample using TEM, or alternatively, by looking for calorimetric changes in mg of material as a function of temperature using DSC. XRD is the only one of the four structural characterization techniques used for all materials systems investigated in this thesis for reasons of applicability, equipment access and sample throughput, and will now be described in detail.

2.2.1 X-Ray Diffraction

The basics of XRD can be understood by considering the interaction of two parallel x-rays incident on a regular array of atoms as shown in Fig. 2.9. The two x-rays are initially in phase. Both interact with the electrons of atoms, but the bottom x-ray must travel an additional distance of $d\sin\theta$ before doing so (where d is the distance between the top and bottom rows of atoms and θ is the angle of incidence). Constructive interference between the top and bottom x-rays will only be observed if the bottom x-ray travels an additional $d\sin\theta$ in a direction parallel to the top refracted x-ray and if the total extra distance $2d\sin\theta$ is an integral multiple of λ, the x-ray wavelength. This leads to the well-known Bragg Law,

$$n\lambda = 2d\sin\theta.$$

Multiple values of d are present in any particular crystalline material. The set of values of θ that leads to constructive interference can thus be used to identify material

composition and / or structure. Microscopic areas of the sample with constant interatomic distances and plane orientation, oriented in some random direction, are known as grains. Powder XRD is based on the assumption that there will be enough grains in a sample to permit all possible grain orientations. The x-rays will then constructively interfere if there is ever a plane spacing d that satisfies the Bragg equation.

XRD patterns can be collected in a number of ways. In some cases, the incident beam is fixed. The angle of incidence is varied by rotating the sample θ degrees. The detector is then positioned to measure the interference at 2θ degrees. Other XRD configurations are based on a fixed sample and rotating both the source and detector. In order to obtain a reasonable signal to noise ratio and angular resolution, the detector must collect data points for something on the order of five seconds every 0.05°. Typical scattering angles range from 10 to 80° and lead to scan times of a few hours. A variety of compositions, and possibly structures, are present in each thin film library. If 10 XRD patterns were collected along each composition gradient, a total of 100 XRD patterns would be required to characterize the structure of a ternary thin film library.

Those groups that have reported combinatorial structure data on electrode materials used curved, position sensitive x-ray detectors [81, 94]. Curved detectors collect the entire diffraction pattern of a particular material in a matter of minutes, not hours, and have been in use since 1983 [95]. An Inel CPS-120 curved, position sensitive detector coupled to a X-ray generator equipped with a Cu target X-ray tube was used to characterize the structure of binary and ternary thin film libraries. A monochromator is present in the incident beam path to limit the wavelengths striking the sample to Cu K_α. Additional XRD measurements were performed using a Siemens D5000 diffractometer equipped with a Cu target and Cu K_α monochromator. Details of D5000 experimental parameters will be presented in concert with the related results. One line of 10 points spaced at 7.5 mm is typically collected with the Inel instrument for binary libraries. Ternary libraries are characterized using a 10 x 10 grid spaced at 7.5 mm. Examples of this method are provided in [81] and [94].

Constructive x-ray interference is detected over a broad range of angles (approximately 10-110°) using the setup shown in Fig. 2.10. A mixture of Ar and ethane

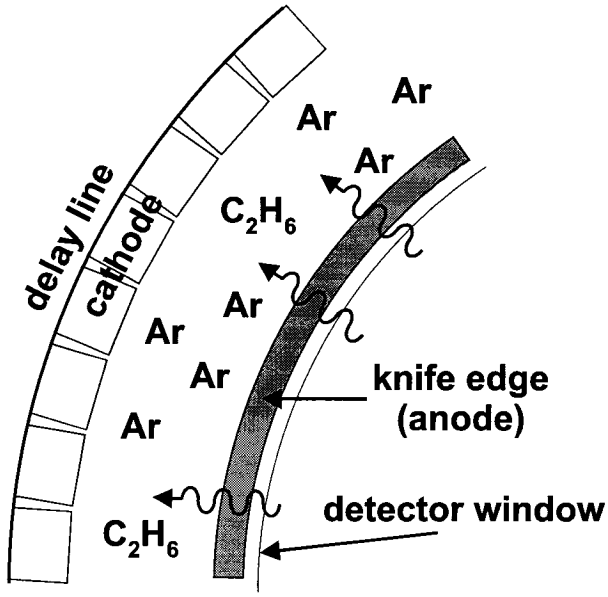

Figure 2.10: Schematic of method used in Inel CPS-120 for x-ray detection.

gas surrounds a blade (anode) and series of 4096 cathodes (only 8 are shown for simplicity). The potential of the anode is 9860 V below that of the cathode. Incident x-rays penetrate the detector window and ionize Ar to Ar^+, which is then quenched by the ethane gas. The electron freed from Ar ionizes other Ar atoms to produce a pulse of electrons accelerating toward the cathode. Detectors at both ends of a delay line are used to determine which cathode channel the current pulse originated from. Further details of detector operation are available in the original blade chamber paper by Ballon *et al.* [95].

The increased data collection rate of the Inel CPS-120 is offset by a decrease in peak position precision. Unlike rotating diffractometers, the scattering vector **K** is not constant, and varies as shown in Figure 2.11. The Inel system is calibrated by collecting the diffraction pattern of a known sample and fitting the peak positions as a function of channel number. Uncertainties in peak position also arise from incorrect sample height adjustment (as opposed to the fixed sample height of most diffractometers).

A high degree of precision in XRD peak position is not always required. As mentioned above, x-rays will constructively interfere only when there are crystal planes that satisfy the Bragg equation. No constructive interference will be observed if no

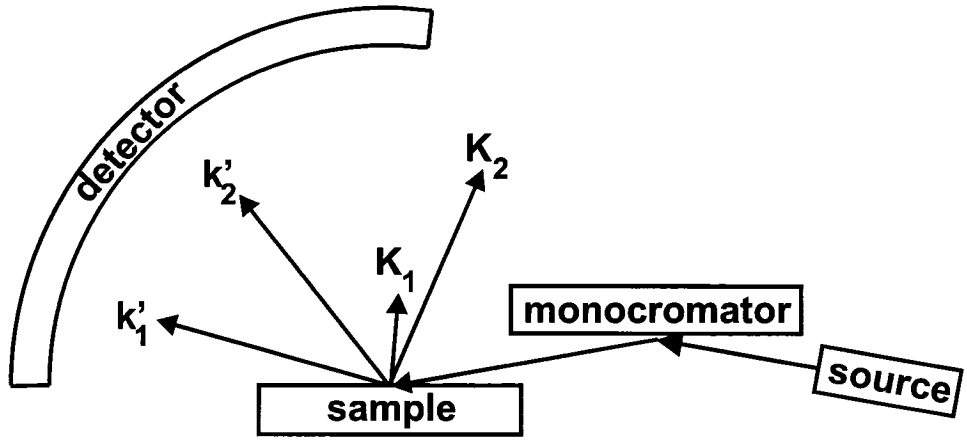

Figure 2.11: Schematic of Inel CPS-120 XRD set up.

crystalline planes are present, or if the planes are oriented in such a way that the Bragg condition is not met (i.e. the powder assumption does not hold). Many of the thin film libraries deposited on Si (100) wafers develop a preferred orientation (also known as 'texture'). However, preferred orientation is not a large concern for the Si and Al-based materials investigated in this thesis since sputter-deposited Si is almost always amorphous and crystalline Al has numerous intense peaks. Textured crystalline compositions without peaks in powder XRD patterns would be identified as crystalline based on other structural characterization methods. Truly amorphous samples do not have crystal planes *per se*, but atoms within amorphous samples are likely to have similar inter-atomic distances. XRD patterns of amorphous materials are identified by broad humps centered about the average inter-atomic distance (often the same as the crystalline inter-atomic distance).

It is clear peak width increases as grain size / long range order decreases. Grain size, L, can be estimated from the FWHM of a peak of width B located at scattering angle θ_B using

$$L = \frac{0.9\lambda}{B\cos\theta_B}, \tag{2.1}$$

which is known as the Scherrer equation. Peaks with a FWHM of 5° correspond to approximately 2 nm grains, and are difficult to distinguish from those associated with amorphous materials.

2.2.2 Mössbauer Effect Spectroscopy

Approximately 5 planes of atoms would be present in a 2 nm grain if the average plane spacing was 4 Å, and the grain could be considered nanocrystalline rather than amorphous. Mössbauer effect spectroscopy can be used for more precise identification of local structure. The Mössbauer effect refers to the recoilless emission of a γ-ray photon by an excited state nucleus. Consider an excited state nucleus of mass M moving at velocity V, as described in Chapter 1 of Greenwood and Gibb [96]. All velocities are taken to be along the direction of motion; the other velocity components are not affected so a full three dimensional treatment would yield the same result. The total energy E_t of the excited nucleus is given by

$$E_t = E + \frac{1}{2}MV^2$$

where E is the energy difference between the excited, E_e, and ground, E_g, states. After emission of a gamma ray of energy E_γ, the ground state nucleus will recoil at velocity v. The energy E_t can then be described as

$$E_t = E + \frac{1}{2}MV^2 = \frac{1}{2}M(V+v)^2 + E_\gamma.$$

Re-arranging the above expression leads to

$$\delta E = E - E_\gamma = 1/2Mv^2 + MvV = E_r + E_d \tag{2.2}$$

where the $\frac{1}{2}Mv^2$ and MvV terms can be identified as a recoil energy, E_r, and a Doppler shift term E_d related to thermal broadening, respectively. E_d can be better understood if the average kinetic energy $\overline{E_k}$ is identified as $\frac{1}{2}M\overline{V^2} \simeq k_BT$. This relationship can be rewritten as $(\overline{V^2})^{1/2} = \sqrt{2\overline{E_k}/M}$ and inserted in to an expression for the average thermal broadening $\overline{E_d}$ leading to

$$\overline{E_d} = Mv\sqrt{\overline{V^2}} = 2\sqrt{\overline{E_k}E_r}.$$

In essence, the gamma ray is lowered in energy by an amount equal to the recoil energy. In order for resonant absorption of the emitted gamma ray to occur at the absorber nucleus, the gamma ray must have an energy equal to the exited state energy E_e plus twice the recoil energy E_r. Line broadening related to the Heisenberg

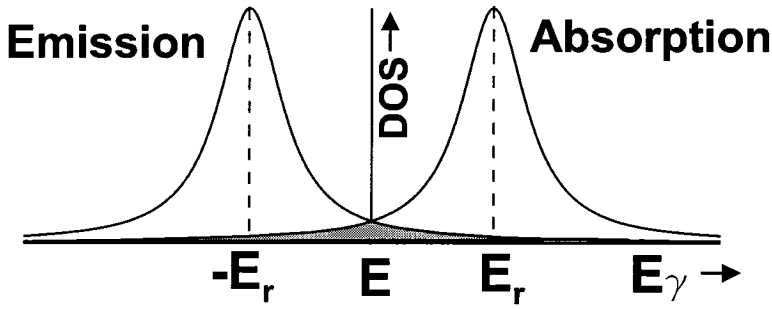

Figure 2.12: Schematic energy distributions during emission and absorption. The shaded area corresponds to the overlap of both processes. Adapted from Figure 1.3 of [96].

uncertainty principle and thermal effects is generally too small to produce significant source-absorber energy overlap, shown schematically in Figure 2.12.

The recoil energy of a single free nuclei given by

$$E_r = \frac{E_\gamma^2}{2Mc^2}$$

and is on the order of 10^{-1} to 10^{-4} eV [96]. This is not sufficient to cause the removal of nuclei from a crystal lattice, where bond energies are on the order of 1-10 eV. The other nuclei in a crystal must thus be considered when calculating the recoil energy. Nuclei in a crystal are free to vibrate. The recoil momentum of a nucleus can either contribute to the vibrational energy of the crystal or the entire crystal can recoil. Crystal vibrational energies are quantized in units of $\hbar\omega$, so not all recoil momentums will lead to changes in vibrational energy. For those cases where the momentum is transferred to the entire crystal, the recoil energy can be considered to be zero because of the very large mass of millions of nuclei. This establishes the necessary condition for recoilless absorption. Thermal broadening is also eliminated, since, according to Eq. 2.2, the thermal broadening is proportional to the square root of the recoil energy. This causes the emission and absorption peaks shown in Figure 2.12 to narrow and shift together, leading to significant emission / absorption overlap. It is interesting to note a transition on the order of tens of keV can be used to probe the nuclear environment with a resolution of approximately 1 part in 10^{12}.

Momentum is conserved in all cases mentioned above. A portion of the incident photons will contribute to the vibrational energy of the crystal and the remainder will contribute to the momentum of the crystal (i.e. have essentially zero recoil energy).

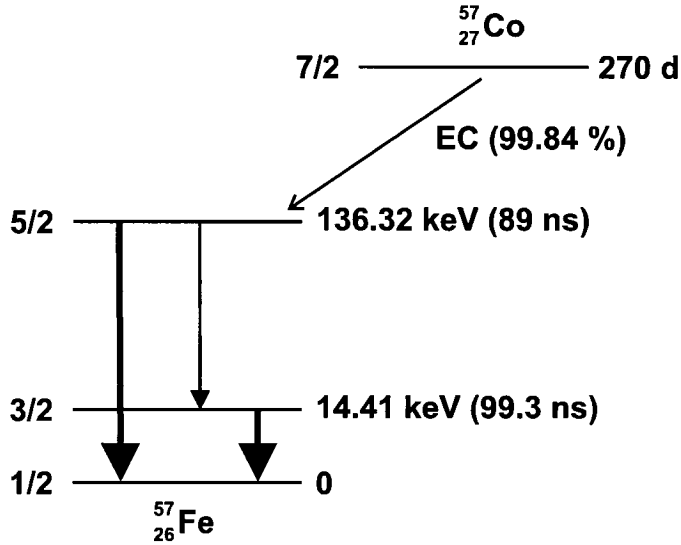

Figure 2.13: Decay scheme of ^{57}Co [96]. The two thick vertical arrows indicate the most common transitions. Energies and lifetimes (in brackets) are listed to the right of each state. Spin values are to the left of each state.

The average recoil-free fraction f has been shown to be given by

$$E_r = (1 - f)\hbar\omega,$$

as expected [97]. Expressions to calculate f based on the Einstein or Debye-Waller models are available in [96]. Briefly, f is proportional to $\exp(-E_r)$, so that f increases with increasing nuclide mass M and decreases with increasing E_γ. f can also be increased by performing experiments at low temperature. Additional details of the Einstein and Debye-Waller models are available in [96]. It is sufficient to know the recoil-free fraction is one of two significant factors considered when selecting the nuclide used for Mössbauer effect spectroscopy.

The other main restriction on nuclide selection is the availability of a supply of excited-state nuclei to produce incident photons, which essentially requires synchrotron access or the use of radioactive nuclei. The decay scheme for ^{57}Co is shown in Fig. 2.13. Mössbauer spectroscopy is often performed with ^{57}Fe because of the practical source material (^{57}Co has a half life of 270 days), the reasonable natural abundance of ^{57}Fe in bulk Fe (approximately 2 %) and the large number of Fe-containing materials of interest. Mössbauer source materials (eg. ^{57}Co) are typically diffused into an isotropic, non-magnetic host (eg. Rh) so that the source radiation is not magnetically split. Uncertainties in the absolute value of E_γ can be ignored since

all values quoted are energy differences between the source and absorber.

It does not make sense to have only one source energy when a range of absorber energies, corresponding to different interactions of the absorber nuclei with the surrounding lattice, are possible. Photons of suitable energy will be resonantly absorbed and then re-emitted over a solid angle of 4π. Energies where significant absorption occurs will therefore have lower transmission rates. The absorption rate can be approximated by

$$I(\epsilon) = \frac{\Gamma}{2\pi} \times \frac{1}{(\epsilon - E_\gamma)^2 + (\Gamma/2)^2}$$

where ϵ is a γ-ray of variable energy and Γ is the Heisenberg line width of the source material (according to $\Gamma = \hbar/t_{1/2}$ where $t_{1/2}$ is the half-life of the relevant transition). Absorption is therefore highest when the energy of the source and absorber is equal, as expected.

Incident γ-ray energies are varied by imparting a slight Doppler shift on the γ-ray frequency. The range of energies goes as $\epsilon = E_\gamma v/c$ where v is the source velocity. Velocities on the order of $\pm$ 5-7 mm/s are normally sufficient to scan the desired range of absorber energies for ^{57}Fe Mössbauer spectroscopy. The source is often operated in constant acceleration mode so that the velocity / γ-ray energy distribution is uniform over time. Velocity-energy calibration is performed by referencing all features to those found in α-Fe.

Hyperfine Interactions

Absorption spectra are the result of interactions between the absorber nucleus and its corresponding electrons, and interactions between the absorber atom and it surroundings. Mössbauer effect spectra from a source and absorber in identical chemical environments will consist of a Lorentzian function centred at E_γ (the emission and absorption curves of Figure 2.12 would overlap completely). Changes in the chemical environment of a electronic, crystallograpic or magnetic nature will have an impact on the absorption spectra. Three types of hyperfine interactions, known as the chemical isomer shift δ, the quadrupole splitting Δ, and the magnetic hyperfine interaction, can be present in any one spectra and used to identify the local (Fe) environment.

The chemical isomer shift δ is often referred to as the centre shift (they are equal at zero temperature). Transitions within the nuclei lead to variations in the nucleus

/ electron interaction by way of changes in nuclear size. Only s-shell electrons are involved in nucleus / electron interactions because of their non-zero density at the nucleus. However, all electrons within the atom can affect s-electron density. Chemical environments that lead to variations in s source / absorber electron density at the nucleus can therefore be detected. The isomer shift is given by

$$\delta = \frac{2}{3}\pi Z e^2 \Big\{ |\psi_s(0)_A|^2 - |\psi_s(0)_S|^2 \Big\} \Big\{ \langle R_e^2 \rangle - \langle R_g^2 \rangle \Big\}$$

where Z is the nuclear charge, $\psi_s(0)_{S,A}$ is the s electron density at the core of the source S or absorber A, and $R_{e,g}$ is the excited (e) or ground (g) state radius. Positive isomer shifts correspond to a lower s electron density in the absorber relative to the source for Fe (the opposite is true for Sn).

Centre shifts probe the electron density at the nucleus and therefore give some measure of the valence of the absorber atom. However, the dependence on spherically symmetric s-electron density prevents any discussion of asymmetric chemical environments. Many nuclei are present in electric field gradients (eg. non-cubic unit cells with more than one atom per unit cell). Nuclei with spin quantum numbers I greater than $\frac{1}{2}$ have a quadrupole moment and can interact with the electric field gradients. It is often assumed that the maximum electric field gradient V_{zz} is symmetric about the z axis of a nuclei. Electronic field gradients lift the degeneracy of I according to

$$\Delta = \frac{e^2 q Q}{4I(2I-1)}[3I_z^2 - I(I+1)]\left(1 + \frac{\eta^2}{2}\right)$$

where I is the total spin, I_z is the spin quantum state and eQ is the nuclear quadrupole moment (used to describe the charge deformation of the nuclide in question). $eq = V_{zz}$. η, defined as $\eta = (V_{xx} - V_{yy})/V_{zz}$, is used to describe situations not symmetric about the z axis. It is assumed $V_{zz} > V_{yy} > V_{xx}$ so that η ranges from 0 to 1. Splitting is observed for $I = \frac{3}{2}$ since $I_z = \pm\frac{3}{2}$ or $\pm\frac{1}{2}$. Spectra corresponding to a $I = \frac{3}{2}|\pm\frac{3}{2}\rangle$ to $I = \frac{1}{2}|\pm\frac{1}{2}\rangle$ or $I = \frac{3}{2}|\pm\frac{1}{2}\rangle$ to $I = \frac{1}{2}|\pm\frac{1}{2}\rangle$ transition will be offset from the energy of the γ-ray transition by $\pm e^2 qQ/4$, respectively. The centre shift of the resulting doublet is analogous to the chemical isomer shift.

The presence of magnetic fields can separate the energies of degenerate transitions further. This is known as as the nuclear Zeeman effect. Energy levels are split according to

$$E_m = -g\mu_N H m_I$$

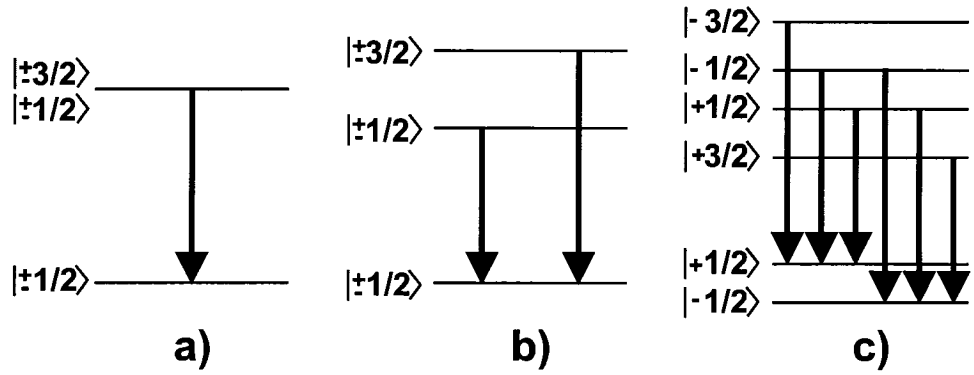

Figure 2.14: All possible nuclear transitions in ^{57}Fe. Cases a), b) and c) are related to the centre shift, the quadrupole splitting and the magnetic hyperfine interaction, respectively.

where g is the nuclear g-factor, μ_N is the nuclear magneton, H is the magnetic field at the nucleus and m_I is the magnetic quantum number with allowed values of $-I, -I+1, ..., +I$. The $|3/2\rangle$ level in ^{57}Fe is thus split in to four levels and the $|1/2\rangle$ level in ^{57}Fe is split in to two levels as shown in Fig. 2.14. All possible transitions corresponding to the centre shift and quadrupole splitting are indicated with arrows. Other transitions, such as from $|+3/2\rangle$ to $|-1/2\rangle$, are not allowed based on momentum considerations. Further details of all the hyperfine interactions are available in [96].

Mössbauer absorption spectra can include features related to atomic valence, electric field gradients and magnetic fields. The spectra features associated with these physical attributes are referred to as singlets, doublets and sextets, respectively. Multiple singlets etc. can be present in one spectrum. Determining the relative amount of ^{57}Fe associated with each site can be a complicated task, especially since a distribution of very similar sites is likely in disordered materials.

Rancourt and Ping developed the Voigt-based fitting (VBF) method to allow for the fitting of arbitrary lineshapes [98]. Briefly, VBF can be used to fit singlets, doublets and sextets where each feature is the result of a distribution of Fe sites. The two generalized sites are a quadrupole with a distribution of quadrupole splittings and magnetic sites with a distribution of magnetic splittings. Singlet sites can be modeled as quadrupole sites with zero average quadrupole splitting. Parameters such as the peak area A, peak area ratio A_+/A_- and δ_1, the coupling factor between the centre shift δ and the quadrupole splitting Δ such that $\delta = \delta_0 + \delta_1\Delta$ and those related

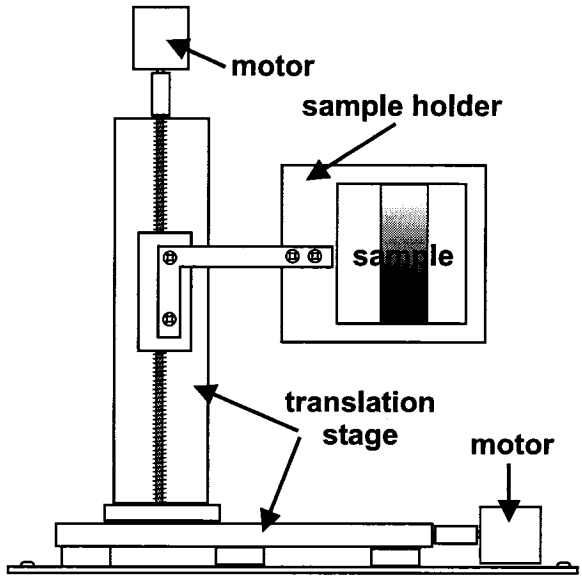

Figure 2.15: Schematic diagram of the high-throughput Mössbauer effect spectroscopy system (Courtesy J. McGraw).

to quadrupole distributions will be discussed when the need arises. Details of VBF analysis are available in [98] and [99].

Although the analysis can be complicated, Mössbauer effect spectroscopy is relatively easy to perform once all the equipment is set up. All Mössbauer spectra described in this thesis were collected using a $\underline{Rh}^{57}Co$ source and a Wissel System II spectrometer operating in constant acceleration mode. The velocity was calibrated using the spectra for room-temperature α-Fe as a reference. A Reuter-Stokes Kr-CO_2 proportional counter was used for γ-ray detection. Spectra with reasonable signal to noise ratios took on the order of hours to days to collect. McGraw and Dunlap developed a method to speed the Mössbauer effect characterisation of thin film libraries [100]. Samples are deposited on to numerous pieces of kapton foil as shown in Fig. 2.8. The kapton foils are then stacked on top of one another in order to increase absorber thickness (and overall absorption) and placed in the sample holder shown in Fig. 2.15. A lead aperture is used to limit the amount of the library exposed to the source radiation and detector. Apertures of 4 x 25.4 mm and 4 x 4 mm are used for binary and ternary films, respectively. The sample is then rastered past the aperture using software developed by J. McGraw. While this system does not directly increase the data collection rate, significant labour savings are realized by allowing

the instrument to operate for days or weeks on end without operator intervention.

Analysis of Mössbauer absorption spectra can be a challenging task. In general, one VBF site is assigned to each different type of Fe site within the material under investigation. Components corresponding to a second set of distributions can be justified for amorphous materials that are expected to have a larger variety of similar Fe sites. All spectra described in this thesis were fit by J. McGraw and R.A. Dunlap and confirmed by the author. Various computer programs written by the author to speed data processing and presentation are described in Section 2.5.

2.2.3 Transmission Electron Microscopy

Mössbauer effect spectroscopy can provide detailed insight on the local structure surrounding Mössbauer active elements such as Fe and Sn. Practical experiments are limited to only a few other elements of interest (e.g. I, Sb, Te)[3]. Transmission electron microscopy (TEM) can be used to probe the structure of any vacuum compatible material on the atomic scale.

The resolution of any microscope is limited by the wavelength of the illuminating radiation. Transmission electron microscopes use electrons accelerated to high energies to probe samples on the sub-nanometre scale. The de Broglie wavelength of an electron is given by $\lambda = h/m_e v$ where m_e is the mass and v is the (relativistic) velocity of the electron. A 100 keV electron has a de Broglie wavelength of approximately 4 pm. Practical resolutions are on the order of a few Å due to difficulties manipulating magnetic fields.

Fig. 2.16 depicts the basic components of a TEM. An electron gun biased to tens to hundreds of keV emits high energy electrons. The electron path is manipulated using magnetic lenses. A small aperture only permits those electrons deflected a small angle from vertical to strike the sample. Electrons in the incident beam interact with the atoms in the sample and are scattered. Thin (on the order of tens to a few hundred nm), conductive samples are required to allow for appreciable electron transmission through the sample. Those electrons not scattered a large amount are focused on to a projection screen or ccd camera using the objective lenses shown in Fig. 2.16 to form the bright field image. Areas with high atomic number atoms will appear

[3]based on the Mössbauer periodic table of the elements presented at www.mossbauer.org

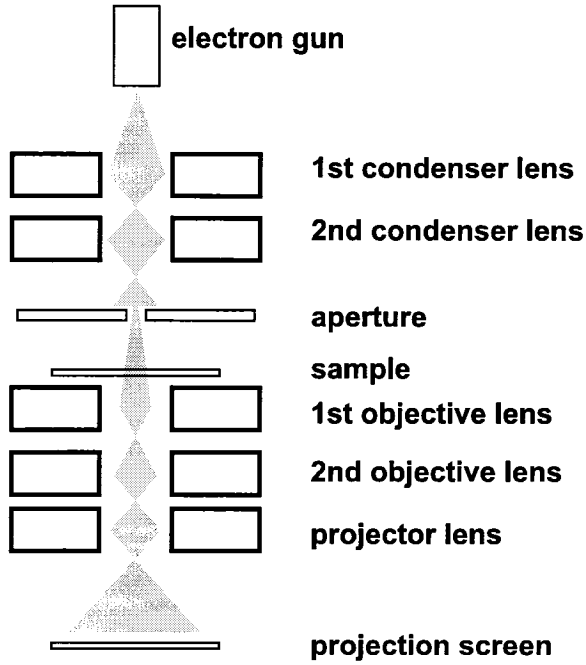

Figure 2.16: Schematic diagram of a TEM. The shaded area indicates the range of possible electron paths.

darker than areas with lower atomic number atoms because of the larger charge on the nucleus and therefore higher scattering rates. All TEM imaging was performed with the assistance of Prof. C. Bennett at Acadia University using a Philips EM301 100 kV TEM. Further details on TEM design and operation are available in [101].

2.2.4 Differential Scanning Calorimetry

X-ray diffraction, Mössbauer effect spectroscopy and transmission electron microscopy use interactions on the atomic or nuclear scale for structural characterization. Differential scanning calorimetry can be used to probe the (dis)order, and therefore structure, of a material without using electromagnetic radiation, nuclear transitions or high potentials.

All possible features in a DSC plot can be understood by considering a large number of balls dumped into a box. It is unlikely the balls are arranged in such a way as to maximize the packing density and minimize the potential energy. The balls will not move unless the box is shaken. Some balls will reposition themselves if the box is shaken hard enough. More intense shaking will cause the balls to order themselves

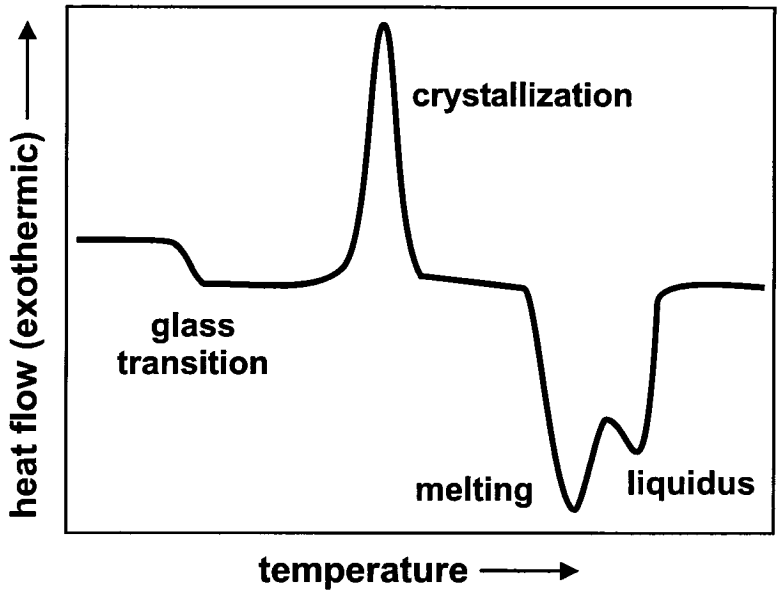

Figure 2.17: Schematic diagram of possible features in DSC signals.

in a way to maximize the packing density and minimize the potential energy. Balls will be thrown out of the box if it is shaken hard enough. The box will be destroyed if it is shaken too hard. The balls poured into the box represents the as-prepared sample. Shaking strength is analogous to sample temperature. Soft shaking of the box will likely cause the balls to oscillate within a small ranges of positions. Ball mobility can be increased by increasing the potential energy of a few balls (i.e. by raising them) so that the others can move around. This increase in mobility is known as a glass transition. The absorption of energy during a glass transition is shown as the dip in Figure 2.17. More intense shaking causing complete ordering of the balls corresponds to crystallization. Energy is released because of the lower potential energy. Very intense shaking corresponds to the melting and liquidus features shown in Fig. 2.17.

Scanning calorimetry is performed by heating a sample at a defined rate and measuring the heat flow in to or out of the sample. Differential scanning calorimetry measures the difference in heat flow between two sample holders, one of which contains the sample of interest. Approximately 0.05 mg of sample is sputter-deposited directly on to the DSC pans shown in Fig. 2.8. This is far below the 5-10 mg of sample typical of most DSC experiments but still allows for most features to be resolved. Twelve or forty nine DSC samples are produced for each binary or ternary run, respectively.

All DSC experiments were performed using a TA Instruments Q1000 DSC with a 49 sample autoloader. Samples are held at 50 °C for five minutes before the temperature is increased to 550 °C at a rate of 20 °C/minute. Two scans from 50 to 550 °C are performed for sputter-deposited samples. The second scan can be used as a baseline (if the sample under investigation does not re-melt) since slight variations in nominally identical sample and reference DSC pans lead to sample-to-sample baseline variability. The autoloader automatically changes samples after every two or three hour experiment until the series of experiments is finished. Methods to improve signal quality and autoloader operation are available in Appendix C.

2.3 Composition And Mass Determination

Four distinct structural characterization methods were described in the previous section. Compositional information can complement structural data and identify samples with no long-range order. Thin film library compositions were determined using a JEOL-8200 Superprobe electron microprobe for energy or wavelength dispersive spectroscopy (EDS and WDS, respectively). The microprope is equipped with a scanning x-y motion stage to permit composition determination on the same grid as the XRD samples.

Electron microprobe analysis works by bombarding a sample with high energy electrons to remove core electrons. Valance electrons replace the ejected core electrons and emit x-rays in the process. Each atom has characteristic x-ray energies which permit its identification. EDS is used for rapid detection of transition energy; WDS is required to distinguish between energetically similar transitions. Details of both processes are available in [102].

Energy measurements are performed with solid-state detectors based on Li-doped Si crystals. Incident x-ray photons generate electron-hole pairs as the photon loses energy. The electron-hole pairs are gathered and converted first in to a current and then a voltage pulse. Voltage readings are proportional to the energy of the incident photon. This technique is fast but suffers from limited energy resolution. In practice, it is very difficult to distinguish between neighbouring elements such as Fe, Co and Ni using EDS.

WDS increases the energy resolution at the expense of increased data collection

time. Wavelengths are measured using a variation of x-ray diffraction (described in Section 2.2.1). Various detector crystals of known lattice spacing d are rotated over a range of incident angle θ to span a broad range of wavelengths. Transmission through the detector crystal will be a maximum when d and θ satisfy the Bragg equation for the particular value of λ.

The relative proportion of elements in the sample is determined based on the relative intensities of the energy peaks. Each measurement is corrected by a Z(atomic number)-Absorption-Fluorescence (ZAF) factor. In addition, the x-ray intensity is compared to that obtained from a standard of known composition. Mass percentage calculations are performed using an iterative process. The initial assumption is that the mass percentage in the sample C^0_{sample} relative to the mass percentage in the standard $C^0_{standard}$ is given by

$$\frac{C^0_{sample}}{C^0_{standard}} = \frac{I^0_{sample}}{I^0_{standard}} = k^0$$

where I^0_{sample} and $I^0_{standard}$ are the integrated x-ray intensities of the sample and standard, respectively. k^0, the ratio of I^0_{sample} to $I^0_{standard}$, is then put in to

$$\frac{C^i_{sample}}{C^i_{standard}} = (ZAF)^i \frac{I^i_{sample}}{I^i_{standard}} = (ZAF)^i k^i$$

for $i = 0$. k^i is normalized after each iteration i and the process is repeated until C^i does not vary a large amount. Sometimes the collected spectra cannot be fit well, which results in an unusually high or low mass total. All mass totals less than 90% of expected were discarded. Scans with mass totals greater than 110% of expected were very rare.

Spectra are fit based on the inclusion of Cu, O and all deposited elements at each point. Cu is usually used as a substrate; small amounts of O are present at the surface of the Cu substrate and in the chamber, and can be incorporated in the film. Ar is incorporated in the films in such a small amount as to be negligible. The amount of, for example, x in $Si_xAl_yMn_{1-x-y}$ is determined by dividing the atomic percent of Si by the total atomic percent of Si, Al and Mn. The composition profiles of each material are then determined by creating contour plots of material (e.g. Si) as a function of position. Normal two-dimensional graphs are possible for binary libraries. Contour plots are important since the electrochemical data is not collected on the same grid as

the structural and compositional information. Interpolation between collected data points allows the various data collection routines to complement each other.

It is already apparent that vast amounts of data are generated in the process of investigating a material system. Contour plots of a particular variable, such as the amount of Si in a material, as a function of position are an effective way to simplify data processing. Contour plots of each starting material and mass as a function of position are generated for each ternary sputtering run. First or second-order equations are fit to mass and composition profiles for binary runs. Mass profiles are determined by weighing an array of Cu disks before and after deposition using a Cahn 29 electrobalance. Results from other substrates, such as the Si wafer or electrochemical cell plate shown in Figure 2.7, are then superimposed on the contour plots.

2.4 Electrochemical Characterization

Structure and composition play a large role in the electrochemical performance of a material. Figure 1.1 shows the basic operation of a Li-ion cell. The cell can be cycled by either supplying a fixed current and monitoring the voltage a function of time, or by sweeping the potential at a fixed rate and monitoring the required current. A typical plot of current vs. voltage is given as Figure 2.18(a). These plots are scaled to the voltage sweep rate and mass of electrode, leading to the units of mA h/g /V, and are referred to as differential capacity vs. voltage plots. One mA h (milliamp hour) corresponds to 3.6 Coulombs. The total charge (time integral of the current) of Figure 2.18(a) is given as Figure 2.18(b).

Peaks in Figure 2.18(a) indicate potentials where there is a large amount of charge being inserted or removed. This is because Li binding sites are available at these potentials. A single broad hump in differential capacity plots indicates a broad range of binding site energies. Phase changes appear in dQ/dV vs. V plots as a sharp peak since one phase (eg. AlLi) is growing at the expense of another (eg. Al) at a constant potential. The peak positions can vary as a function of sweep rate since there is a voltage drop, due to electrical resistance in the electrode leads and the internal impedance of the cell, that varies with current, and the current is changing. Lead resistances less than 10 Ω lead to voltage shifts ('overvoltages') of typically less

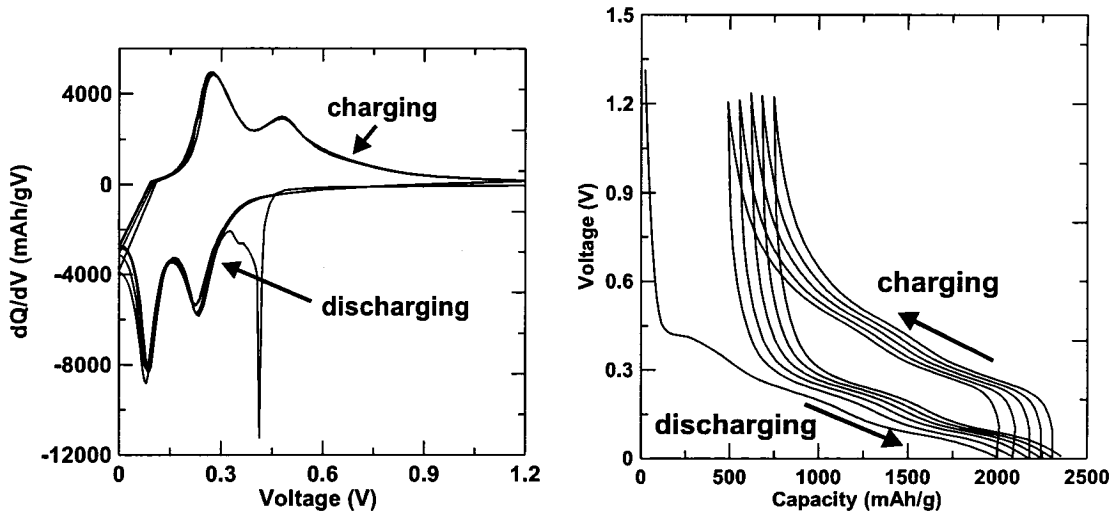

Figure 2.18: Sample differential capacity ($\frac{dQ}{dV} = \frac{dQ}{dt}\frac{dt}{dV}$) vs. voltage (rate of change of charge as a function of voltage, per unit mass) and gravimetric capacity (voltage as a function of charge per unit mass) plots.

than one mV. Internal impedances are on the order of 2 kΩ for the thin film Si-based electrode materials investigated using the cell hardware described in this thesis.

Many battery performance characteristics can be obtained from the plots shown in Figure 2.18. The first discharge capacity often corresponds to the maximum Li storage capacity of a material. Irreversible capacity is the difference in the first discharge (insertion) and charge (removal) capacities, i.e. the amount of Li remaining in the material. The irreversible capacity should be minimized for high-performance battery materials. Sputtered films tend to show lower irreversible capacity than bulk samples because the of the lower impact of diffusion on low-dimensional materials. Charge storage capacity as a function of cycle number is also of interest.

Electrochemical testing can be cumbersome because of the large number of sample preparation and data manipulation steps. A 64 channel combinatorial electrochemical cell, shown in Fig. 2.19, was designed to test the Li-ion electrochemistry of up to 64 different compositions in parallel. The cell design is an extension of the standard coin-type test cell hardware used in most research laboratories except the single test material is replaced by a 64-channel lead pattern on a glass plate. Examples of lead patterns are provided later in this chapter and in [63]. The glass plate extends outside the cell so electrical connections can be made to each electrode. This design is far

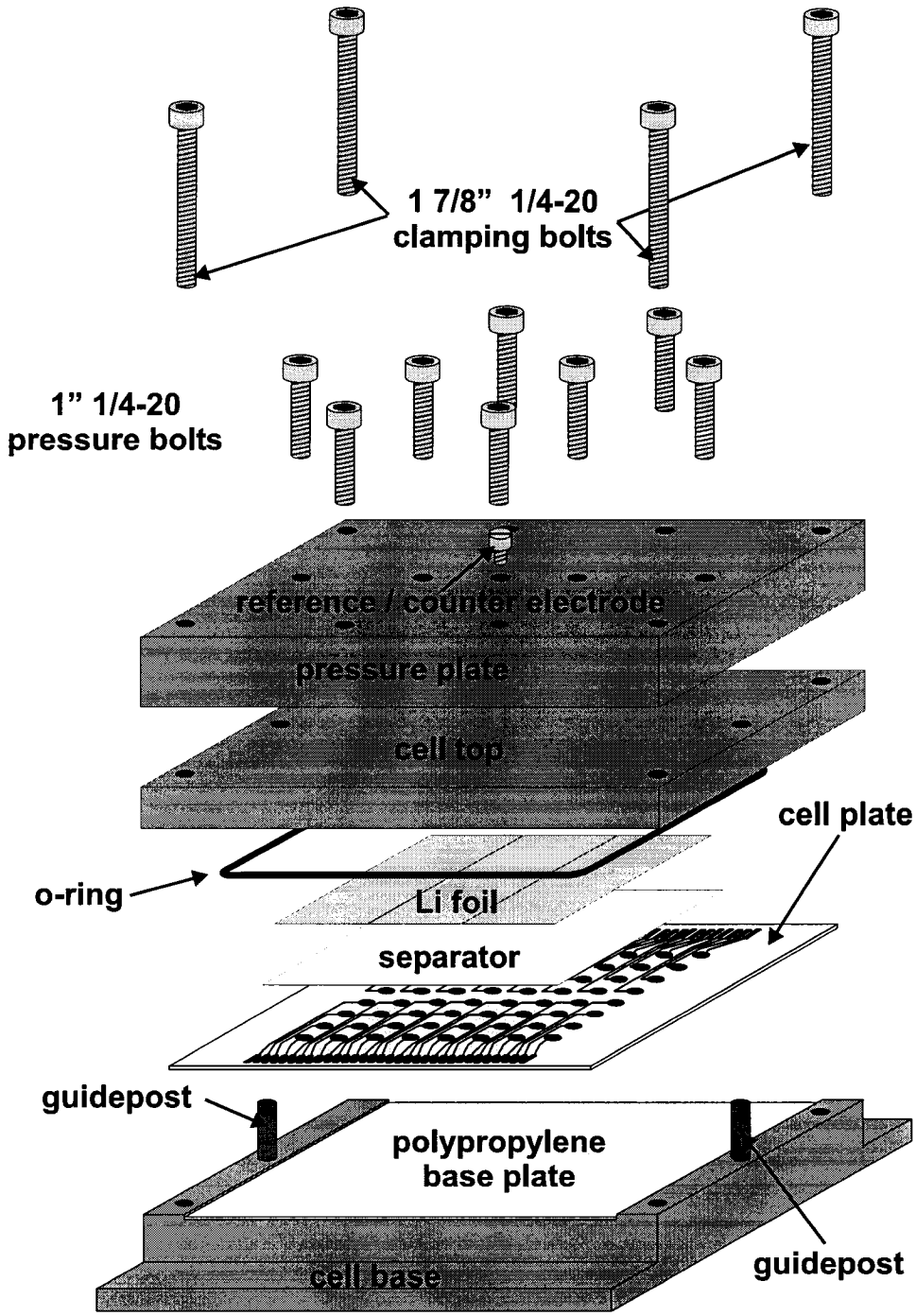

Figure 2.19: Schematic of the 64-channel combinatorial electrochemical cell described in [67] and [77]. Reproduced from [77] with the permission of IOP Publishing Ltd.

simpler than the microfabrication-based Li-ion battery electrode test cell described in [71]. Restrictions on cell design were strictly geometrical in nature. The only fundamental difference between the combinatorial electrochemical cell shown in Fig. 2.19 and coin-type test cells is the cycling method - the combinatorial electrochemical cell is cycled potentiodynamically and the coin cells are cycled galvanostatically. This difference is negligible with suitable sweep rate and current choices.

The pressure plate shown in Fig. 2.19 was added to the earlier combinatorial electrochemical cell design shown in Figure 4 of [67] to even out clamping pressure from the bolts and to act as a heat sink for elevated temperature cycling studies. Excellent sealing is required to prevent the evaporation of already volatile organic solvents at elevated temperatures. Results to date are mixed. The pressure plate can be used to apply pressures great enough to crack the glass cell plate, leading to incomplete electrical circuits. Cracks in glass cell plates also expose the Al base to the electrolyte, which then reacts. Ridges in Al base plates from previous exposure to electrolyte promote crack development in new glass plates when pressure is applied. A polypropylene liner was added to the base plate as shown in Fig. 2.19 to act as a barrier between electrolyte and the Al base in the event of cracked glass plates and to minimize the impact of contaminants on the bottom of the glass plate.

Torques of as little as 25 inch pounds can crack the glass plates if the o-ring does not evenly fill the o-ring groove. Efforts were made to improve o-ring fit by expanding the o-ring grove (now 0.150" deep and 0.113" wide). A further widening of the o-ring groove is probably in order. The author has also experimented with the amount of electrolyte: approximately 0.4 ml are required to completely wet the 80 x 76 mm separator shown in Fig 2.19. Any additional electrolyte could lead to gas pockets and uneven pressure distribution within the sealed area. The current cell assembly procedure involves tightening the four corner bolts to 20 inch-pounds in a star pattern and then repeating at 25 inch-pounds. The pressure plate bolts are then tightened finger tight followed by three rounds of 25 inch-pounds in a star pattern. Additional assembly details are available in Appendix C.

A VWR 1300 laboratory oven was purchased and special combinatorial cell - multichannel potentiostat connectors were designed to permit cycling at room temperature, 50 and 70 °C. Details of connector choice / testing are available in Appendix

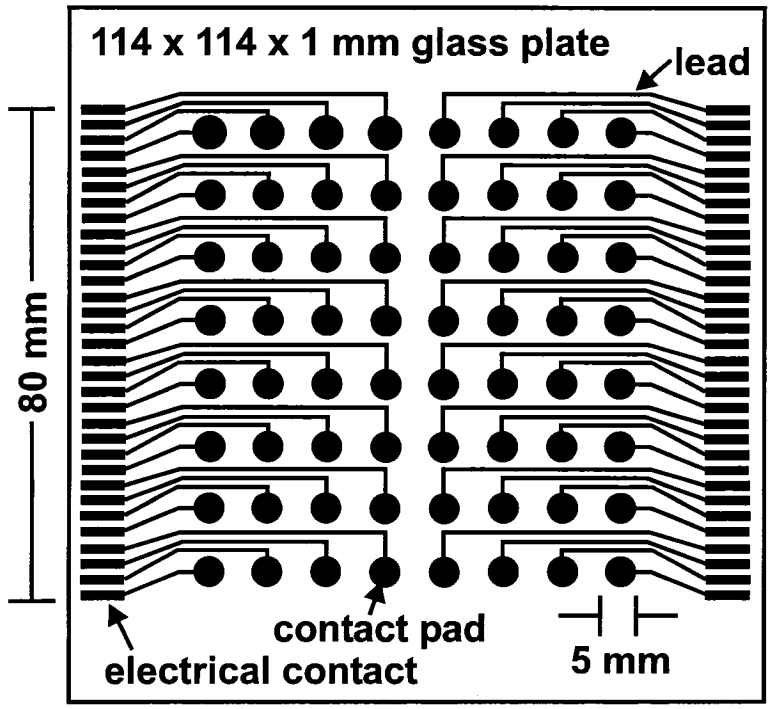

Figure 2.20: Lead pattern for sixty-four channel combinatorial electrochemical cell. 32 electrical contacts on the left and right hand sides are spaced to interface with standard motherboard connectors. Materials under investigation are sputter-deposited on the sixty-four circular contact pads. Reproduced by permission of The Electrochemical Society, Inc. [83].

C. Each connector is designed to interface with 32 of the 64 electrical contacts shown in Fig. 2.20. The lead pattern shown in Figure 2.20 allows for up to eight test points per horizontal or vertical composition gradient, which is a dramatic improvement over the coin cell method. The lead pattern is formed by sputtering Cu onto a frosted glass plate and then removing selected areas of the Cu with a photolithography process developed by G. Rockwell and later improved by J. Topple and the author. Frosted glass is used to promote good adhesion. Details of this process are available in reference [67] and Appendix C.

The materials under investigation are deposited only on the contact pads by sputtering through a mask. Thin Al plates were originally used to restrict the deposition profile. Gaps between the mask and the glass plate can allow the deposit to expand slightly beyond the boundaries of the contact pad. The mass of material deposited on to the 5 mm dia. contact pad is interpolated from masses determined on 1.3 cm dia. disks. Strict control on the area of deposited film is thus required for accurate

mass determination.

Photolithograpy is used to fabricate the lead pattern shown in Fig. 2.20 and can also be used to restrict the deposition profile[4]. Advantages include the virtual elimination of shadowing (the mask is approximately 3, rather than 800, μm thick) and flexibility in design. Disadvantages are related to the cost (about $3 per mask), chemical consumption and ca. 30 minutes of labour required for each plate. The masked cell plates are soaked in acetone to remove the photoresist; only film deposited on the contact pads remains. However, the acetone bath step and the corresponding air exposure prevents the use of this technique for air sensitive samples. In the end, all users should be familiar with both masking methods.

Mask design flexibility is very important. Fig. 2.3 depicts a square substrate on a rotating substrate table. Composition gradients are produced by controlling the radial deposition profile. The rows of contact pads shown in Fig. 2.20 (the so called 'square' lead pattern) are all a similar distance from the centre of the substrate table. The symmetry of the square lead pattern leads to only four distinct compositions per row. Only 32 distinct compositions, clumped in eight groups of 4, can be investigated at once. Contact pads on the 'binary' lead pattern (shown in Fig. 2.21) are evenly spaced from the centre of the substrate table over the 76 mm wide deposit and can therefore be used to investigate 64 distinct compositions. Masks required to produce the binary lead pattern and restrict the deposit cost approximately $4 to produce (two patterns each printed on two overhead transparancies). Details of the photolithographic masking process are available in Appendix C. A third lead pattern was developed for ternary deposition runs. The contact pad arrangement shown in Fig. 2.22 allows for each of the 64 contact pads to be evenly spaced over the deposition range during both orientations of the substrate shown in Fig. 2.6. 'Binary' or 'ternary' lead patterns can be used for the investigation of all but air sensitive materials (due to the approximately half-hour air exposure during the photoresist removal procedure) for improved data quality.

Combinatorial electrochemical cells are assembled with the cell plates using the method described above and cycled using a multichannel potentiostat. All combinatorial electrochemical cells (also known as 'combi cells') tested at elevated temperature

[4]The method of using photoresist to restrict the deposition profile was developed by J. Topple and the author.

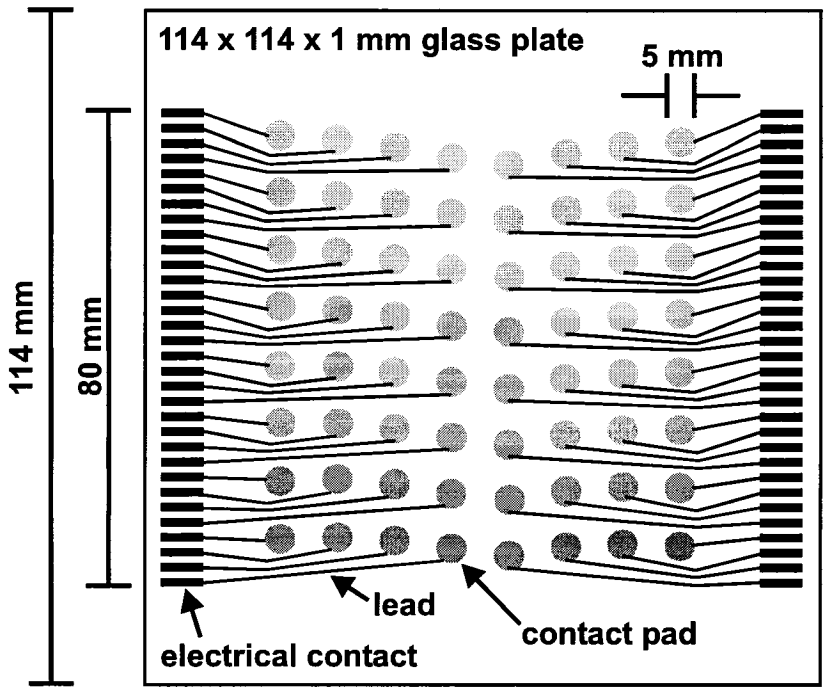

Figure 2.21: 'Binary' lead pattern on a 114 x 114 x 1 mm glass plate. Contact pads are positioned so that the distance between the centre of the contact pad and the centre of the substrate table is evenly incremented over the 76 mm span of the contact pads.

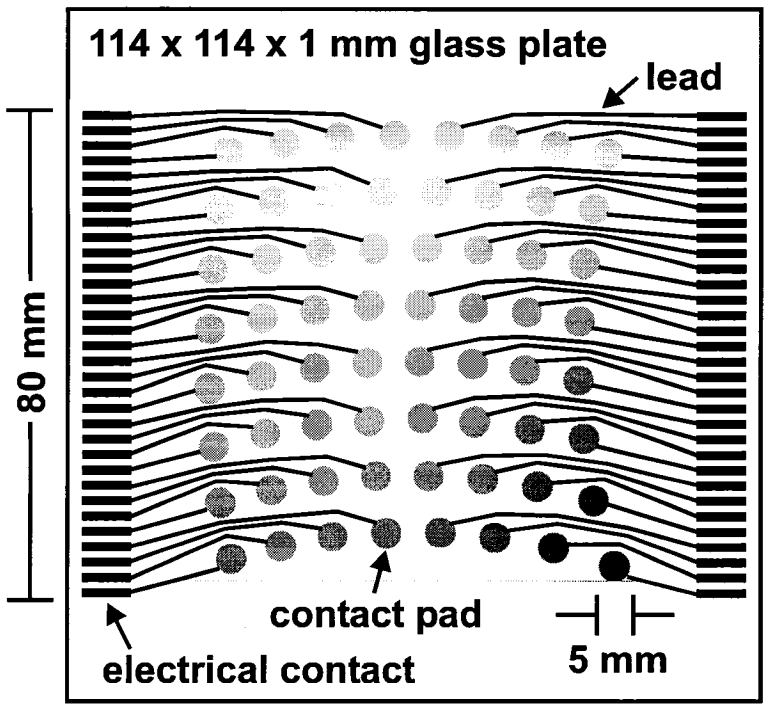

Figure 2.22: 'Ternary' lead pattern on a 114 x 114 x 1 mm glass plate. Contact pads are positioned so that the distance between the centre of the contact pad and the centre of the substrate table is evenly incremented over the 76 mm span of the contact pads for both possible orientations of the substrate shown in Fig. 2.6. Reproduced from [77] with the permission of IOP Publishing Ltd.

were cycled using a Scribner 900B Multichannel Microelectrode Analyser (MMA). A second system known as the 'Medusa' was developed by Cumyn *et al.* [103][5] and is used for room temperature testing. Cell potential is controlled using a Keithley 217 quad voltage source. Currents are determined by measuring the potential across a small fixed resistor using a 6.5 digit (22 bit) Keithley 2750 multimeter with multiplexer cards. Up to three combi cells can be cycled simultaneously.

2.5 Automation

The preceding sections described methods for combinatorial and high-throughput sample fabrication, structural characterization via XRD, DSC and Mössbauer effect spectroscopy, electron microprobe composition determination and electrochemical property measurement. High-throughput data processing is thus required to increase overall sample throughput. Over 300 data sets are produced for a typical sputtering run. Numerous computer programs were developed by the author to simplify data processing. `inel_dataconvert.exe` is used to combine the multiple `.ttx` files (converted from `.fdt` files) produced during each XRD experiment in to one `.ixd` file. `inel_fix.exe` should first be used to correct the number of scans stored in a `.fdt` file. The user should know the correct number of scans contained in the file based on notes in the lab book and the fact that each 4096 channel scan occupies approximately 17.7 Kb of disk space. `mossbauer_convert.exe` serves two purposes. First, multiple `.fit` files from a high-throughput Mössbauer effect spectroscopy experiment can be combined in to one `.cmf` file. `.lor` and `.vbf` fit parameter files can also be combined in to one `.csv` file to, for example, ease plotting the centre shift δ as a function of scan number or composition. The small amount of electron microprobe data processing required can be performed using `microprobe_convert.exe`.

The program `ta-convert.exe` was written by the author to combine the numerous files produced during a set of DSC experiments into one `.tas` file. Many data processing options were later added by V. Chevrier. Finally, the bulk of the electrochemical data processing can be performed using `electrochemical_convert.exe`. It

[5]Significant programming and hardware contributions were made by D. Stevens and T. Hatchard, respectively, after the publication of [103].

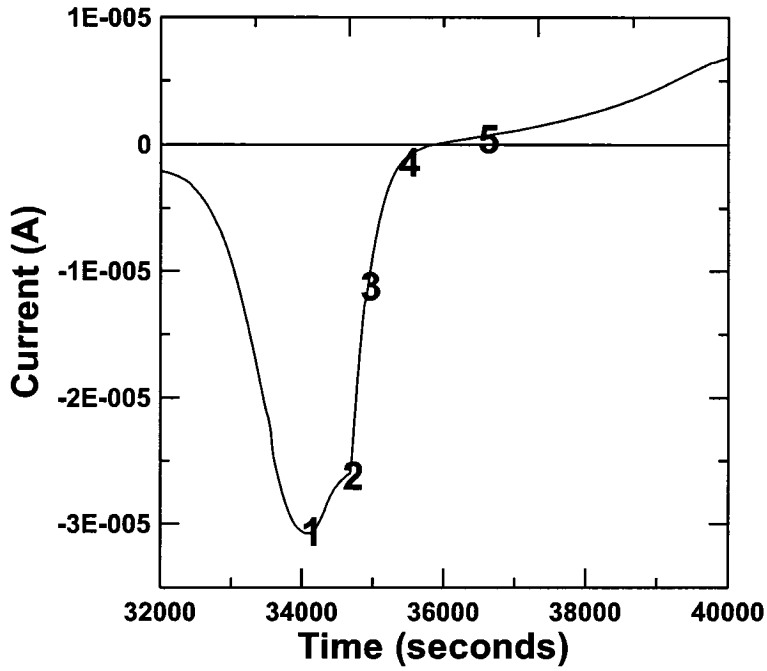

Figure 2.23: Current flow as a function of time. The cell is discharging at point 1. The voltage sweep direction changes from towards 0 V to towards 1.2 V at point 2. Although the voltage is increasing at points 3 and 4, the current is still negative, and the capacity is increasing. The capacity reaches a maximum at some point between 4 and 5.

is worth noting some of the features here. The performance of a battery electrode material can be quantified using three indicators: capacity, average voltage and capacity retention. Capacity calculations are more difficult than simply integrating the current as a function of time. The distinction between discharge (Li insertion) and discharge (Li removal) must be based on current flow rather than potential for cyclic voltammetry measurements. Complications arise for small currents when noise present in data from the Medusa or Scribner system changes a generally positive current negative, or vice versa. The solution is to compare the trailing average of an adjustable number of points to the previous local capacity maximum (or minimum). If the channel is discharging, the trailing capacity average will increase until the channel starts to charge. The maximum point in the trailing average is then the local maximum, which corresponds to some point between labels 4 and 5 in Figure 2.23. The opposite is true if the channel is initially charging. After the capacity calculation is performed, most other battery performance calculations are trivial. The average voltage can be

determined using

$$\left(\sum_{\text{start of (dis)charge}}^{\text{end of (dis)charge}} \text{current} \times \text{potential} \right) / \text{capacity}.$$

Cycle number is determined based on the number of capacity maxima and minima. By default, `.csv` spreadsheet files are produced for capacity as a function of channel number and cycle number in two different formats (one for database incorporation and one for rapid visualization). Voltage vs. capacity and differential capacity / current vs. voltage / time data is also written to the `.ecd` format.

The program `plot4.exe` acts as a common rapid visualization platform for the XRD (`.ixd`), Mössbauer (`.mcf`), DSC (`.tas`), and electrochemical (`.ecd`) data formats. The main feature of `plot4.exe` is the ability to display data sets in the same orientation they were collected in, i.e. an 8 x 8 grid for electrochemical data. Data sets can be selected for zoom, overlaid, displayed on linear or logarithmic scales, and most importantly, exported to publication quality graphs with the touch of a button. Subtle changes to the generated graphs (e.g. label frequency) are most easily performed using `grapher_convert.exe`. `plot4.exe` has been under development since October 2001; 28 upgrades have been performed to various versions (current version 1.24). Work is underway to expand the data handling capability of `plot4.exe` to various fuel-cell data sets being collected by others in Prof. Dahn's group.

A great deal of high-throughput instrumentation and methods have been described in this and the preceding four sections. Efforts were made to credit specific developments to the appropriate researchers. In general, the majority of the combinatorial infrastructure mentioned is the result of the efforts and ideas of Prof. Jeff Dahn, Dr. Tim Hatchard, Arman Bonakdarpour and the author. Significant contributions were also made by Dr. David Stevens, Jessica Topple, Prof. Kevin Hewitt, and Vivien Cumyn. The next four chapters detail the author's investigation of the Si-M (M = Cr+Ni, Fe, Mn), Al-M (M = Cr, Fe, Mn, Ni), Al-Si, and Si-Al-M (M = Cr, Fe, Mn, Ni) systems, and demonstrate the quantity and quality of data that can be produced using combinatorial and high-throughput methods.

Chapter 3

Si-M (M = Cr+Ni, Fe, Mn)

More electrochemical investigations have been performed on the Si-M system than the Al-M, Al-Si and Si-Al-M systems combined[1]. Researchers have looked at a variety of Si-M alloys, where M is an element that does not alloy with Li such as Co [104, 105], Cr [106], Fe [104, 107–110], Mn, Ni [35, 104, 110, 111], V [112], or Zr [113]. All of the Si-transition metal electrochemical investigations focused on the same basic idea: a combination of electrochemically active nanocrystalline or amorphous active material (Si) in an inert matrix (Si-M). It might seem reasonable to assume that all transition metals affect Si the same way, and therefore that the capacity of Si_xM_{1-x} would be independent of the variety of M. In fact, there is not even agreement in the literature for a particular combination of M and x. There are reports of transition metal silicides having capacities ranging from 60 to over 1000 mA h/g. Weydanz *et al.* reported capacities[2] in the range of 500-800 mA h/g for solid-state reactions of various ratios of Li to $CrSi_2$ [106]. Wang *et al.* reported a capacity of 1180 mA h/g for ball-milled NiSi and over 1000 mA h/g for a ball-milled mixture of Si and FeSi [110]. These capacities stand in contrast to the numerous reports of Si-M alloys with little to no capacity (50-200 mA h/g). Lee and Lee [109] obtained reversible capacities of ca. 150 and 100 mA h/g for ball-milled $Fe_{0.27}Si_{0.73}$ and $FeSi_2$, respectively. Dong *et al.* [107] declared $FeSi_2$ to be inactive since $FeSi_2$ x-ray diffraction peaks did not shift during Li insertion and removal. Huggins and co-workers [104] found capacities of 58, 60 and 198 mA h/g for $CoSi_2$, $FeSi_2$ and $NiSi_2$, respectively, and reported Li does not significantly react with various silicides at room temperature [114]. Kim *et al.* [105] reported very little electrochemical activity for sputtered $CoSi_{2.2}$.

More recently, Obrovac and Christensen [35] declared nickel and other transition metal silicides to be inactive, despite observing a capacity of ca. 850 mA h/g for

[1]Portions of this chapter first appeared in [86] and are reproduced with permission from The Electrochemical Society.

[2]capacity calculation based on fully-lithiated mass, not mass before lithiation

melt-spun $Si_{0.70}Ni_{0.30}$. If Si_2Ni were inactive, the capacity of approximately 1.2 moles of Li per mole of $Si_{0.70}Ni_{0.30}$ would be the result of Li reacting with only the remaining 0.10 moles of Si. The formation of inactive SiNi, rather than Si_2Ni, would leave 0.4 moles of Si free to react with Li. The ratio of Li/Si would then be 3, close to the theoretical room temperature limit (3.75 Li/Si).

Equilibrium phase diagrams for the Si-Fe, Si-Cr, Si-Mn and Si-Ni systems are provided in Figure 3.1. These diagrams can be used to estimate changes in local structure with composition for non-equilibrium sputtered thin films (i.e. the local structures of $Si_{0.67}M_{0.33}$ and Si_2M are not likely to be dramatically different). Si_2M is present in the phase diagrams for all values of M except Mn, where various Si-M phases with 63 at. % Si have instead been observed. SiM is present in all four phase diagrams. Excluding a single report [110], non-zero capacities have not been observed for Si-M alloys with more than 50 at. % M. Understanding the electrochemistry of the Si-M system therefore involves determining the electrochemical activity and / or presence of Si_2M and SiM.

The thermodynamics of the Si-M system is difficult to predict using the macroscopic atom model of de Boer *et al.* [90] for two reasons. One, all Si-M equilibrium phases of interest contain between 30 and 50 at. % M, which is outside the 0-20 or 80-100 at. % M range of highest model accuracy. As an example, the macroscopic atom model calculates a heat of formation of -52 kJ/mol for SiFe; -78 kJ/mol is measured experimentally [116]. Differences between experimental and macroscopic atom model calculations of 0-5 kJ/mol are typical over the range of highest accuracy mentioned above. Two, Si is one of the seven elements listed in Table A.1 that undergoes a semiconductor-metal or gaseous-solid transition and therefore has a non-zero ΔH^{trans} value (34 kJ/mol). This large offset can bias all calculations with low M content (the compositions of interest). For these reasons the macroscopic atom model will not be used to predict the electrochemical activity of alloys with high Si content.

Thin film libraries of Si-Cr-Ni, Si-Fe and Si-Mn were deposited on to a variety of substrates using the method described in Section 2.1 and [80]. Initial investigations involving two orthogonal composition gradients (Si-Cr-Ni) were replaced by binary two component runs (Si-Fe, Si-Mn) for clarity and ease of analysis. Multiple sputtering runs were performed over the course of this investigation. Table 3.1 lists the run

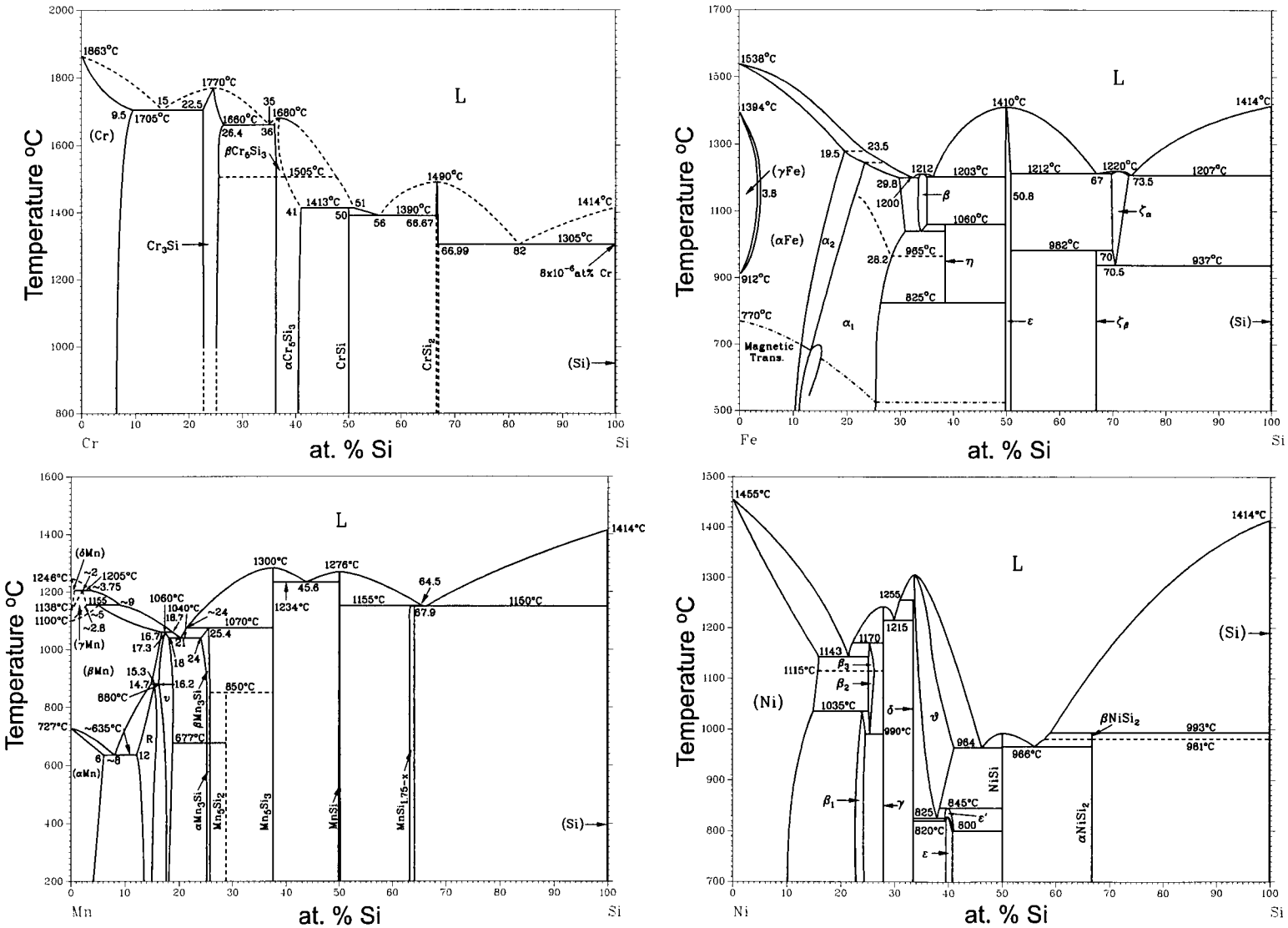

Figure 3.1: Equilibrium phase diagrams for Si-Cr, Si-Fe, Si-Mn and Si-Ni (data from [115]).

run label	elements	at. % M	thickness	focus
spi144	Si, Fe, Mn	$0 \leq x \leq 55$	0.6-1.7 μm	electrochemistry
spj043	Si, Cr, Ni	$0 \leq x \leq 60$	1.0-2.5 μm	electrochemistry
spj069	Si, Cr, Ni	$0 \leq x \leq 50$	1.3-2.0 μm	electrochemistry
spj091	Si, Fe	$0 \leq x \leq 50$	0.8-1.3 μm	electrochemistry
spj094	Si, Mn	$0 \leq x \leq 55$	1.1-2.2 μm	electrochemistry
spj104	Si, Mn	$0 \leq x \leq 55$	0.6-0.9 μm	electrochemistry
spj145	Si, Fe	$0 \leq x \leq 35$	0.4-0.7 μm	Mössbauer
spk022	Si, Fe	$40 \leq x \leq 55$	0.7-1.0 μm	Mössbauer
spk085	Si, Fe	$40 \leq x \leq 80$	0.2-0.7 μm	Mössbauer
spk088	Si, Fe	$0 \leq x \leq 25$	0.7-1.0 μm	Mössbauer
spl050	Si, Fe	$40 \leq x \leq 80$	0.5-0.7 μm	Mössbauer
spl097[4]	Si, Fe	$0 \leq x \leq 50$	10-20 nm	TEM

Table 3.1: Brief summary of Si-M sputtering runs.

label[3], constituent elements, range of transition metal content, thickness range, and characterization focus of each of the ten runs. Si was deposited using a power of either 130 W or 200 W net using a DC or RF power supply, respectively. Transition metals were deposited using a DC power supply set to 25-40 W. Fifty mm dia. by 6 mm thick targets of Si, Cr, Mn (99.9% purity, Pure Tech) were used. Ni and Fe targets were produced by stacking two 50 mm dia. disks cut from 0.7 mm thick sheets of Ni (99.5% purity, Aesar) and grade 1008 low carbon steel, respectively. Intimate mixing of Si and M was achieved by rotating the water-cooled substrate table at approximately 15 rpm. Thickness values (listed in Table 3.1) were calculated using the mass of material deposited on to 1.3 cm dia. Cu disks and a composition-dependent density. The density of $A_xB_yC_{1-x-y}$ was approximated using

$$\text{density}_{A_xB_yC_{1-x-y}} = \frac{(x)\cdot \text{mass}_{\text{mol. A}} + (y)\cdot \text{mass}_{\text{mol. B}} + (1-x-y)\cdot \text{mass}_{\text{mol. C}}}{(x)\cdot \text{vol.}_{\text{mol. A}} + (y)\cdot \text{vol.}_{\text{mol. B}} + (1-x-y)\cdot \text{vol.}_{\text{mol. C}}}.$$

3.1 Structural Characterization

Structural characterization of the libraries intended for electrochemical investigation listed in Table 3.1 was first performed using the Inel curved, position sensitive detector

[3]Sputtering runs are labeled according to the following method: 'sp' indicates the sputtering machine located in room B9 was used; the following four digits indicate the book (a=1, b=2, etc.) and page number the run details begin on.

[4]Composition and thickness values are estimates.

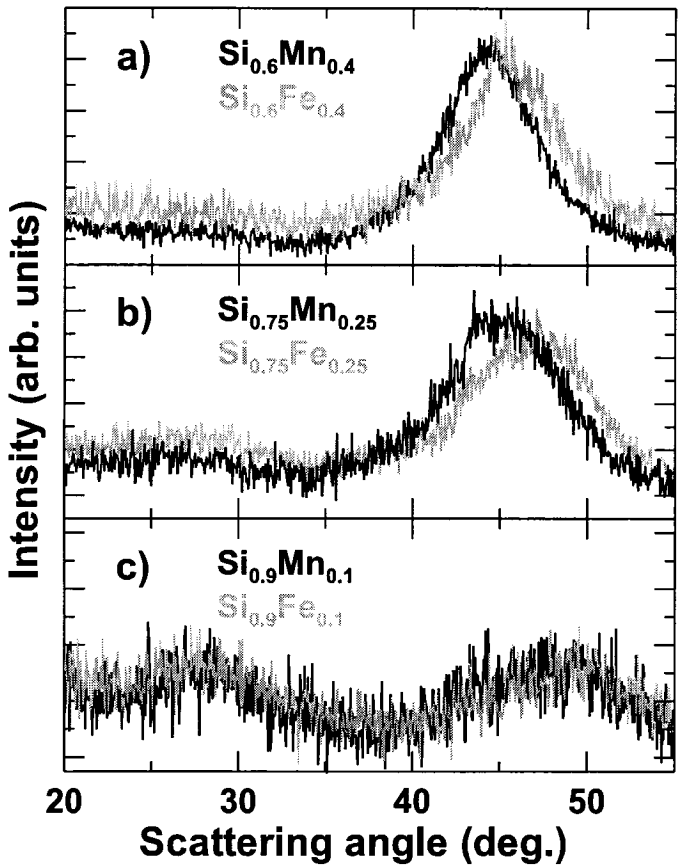

Figure 3.2: XRD patterns for Si-Fe (grey) and Si-Mn (black) for 10, 25 and 40 at.% transition metal thin films deposited on a Si (100) wafer. Reproduced by permission of The Electrochemical Society, Inc. [86].

described in Section 2.2.1. Diffraction pattern features present at high Fe compositions were masked by equipment artifacts related to the high count rates associated with Fe fluorescence. Diffraction patterns were then collected using the aforementioned Siemens D5000 in unlocked coupled mode. Diffractograms collected from 20 to 55° in scattering angle for three compositions in the Si-Mn and Si-Fe libraries are shown in Figure 3.2. The tube and detector started at 18 and 2°, respectively, to avoid detecting any peaks associated with the Si wafer. Divergence and anti-scattering slit widths were 0.5°. The beam spot size on the D5000 changes with angle of incidence, and varied from 1.3 to 0.5 cm^2. Compositions quoted in Figure 3.2 are therefore only approximate. No XRD data was collected for the Si-Cr-Ni system because the Si substrate fell off the substrate table during the deposition run.

The XRD patterns for $Si_{0.9}Mn_{0.1}$ and $Si_{0.9}Fe_{0.1}$ shown in Figure 3.2c contain broad

humps at 28 and 48°, which corresponds to amorphous Si and an unidentified amorphous or nanocrystalline phase. Increasing the transition metal content by 15 at. % decreases the hump at 28° and transforms the humps at 48° in to broad peaks at 45 and 47°, as shown in Figure 3.2b. The broad peaks at 45 and 47° sharpen and shift to lower angle, and the broad humps at 28° are eliminated when the transition metal content is increased an additional 15 at. % to 40 at. %, as shown in Figure 3.2a. The two peaks in Figure 3.2a at 44 and 45° can be associated with the strongest peaks of MnSi and FeSi, respectively. This peak width transforms to a grain size of about 2 nm via the Scherrer equation. The x-ray structural data suggests amorphous Si and nanocrystalline SiM phases co-exist and grow at the expense of each other (depending on composition).

Identification of a crystalline structure based entirely on a single, 5° wide peak, is highly speculative, especially when other phases such as pure Fe / Mn could lead to diffraction peaks at or near the same scattering angle. Mössbauer effect measurements were performed on the five Si-Fe libraries listed in Table 3.1 using the apparatus described in Section 2.2.2 and [100] to gain more structural insight. All Mössbauer spectra with less than 50 at. % Fe were fit to a Gaussian distribution of doublet sites using the Voigt-based fitting technique described in [98]. Spectra collected from samples with more than 50 at. % Fe were well fit by a distribution of magnetically split sextet sites, suggesting that a phase transition takes place at 50 at. % Fe. A Lorentzian FWHM of 0.12 mm/s was used for all fits. δ_1 was fixed at zero and A_-/A_+ was fixed at one, so that only the background, centre shift, area, Δ and σ were allowed to vary. Fits for three compositions of Si-Fe are shown in Figure 3.3.

Figure 3.4 summarizes the isomer shift δ, quadrupole splitting Δ and site distribution σ as a function of composition. The isomer shift decreases to 0.13 mm/s as the Fe content increases to 12 at. %, indicating higher s-electron density at the absorber (^{57}Fe) nucleus and therefore a higher average number of Fe-Fe nearest neighbours. Only a slight decrease in quadrupole splitting occurs over the same range so no major changes in the electric field gradient are occurring. Fe atoms are therefore incorporated in to an amorphous phase below 12 at. % Fe. Changes in isomer shift occur over the range of 12 to 50 at. % Fe. in three regions: a smooth increase is present from 12 to 25 at. % Fe, followed by some variation with sputtering run over the range 25-35 at. %

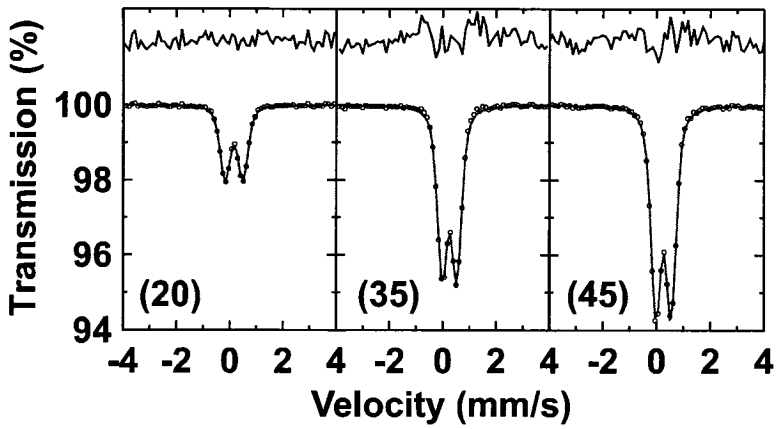

Figure 3.3: Sample Mössbauer effect fits. Numbers in brackets refer to at. % Fe (in Si-Fe). Two humps in the centre difference plot suggest the fitting method is not ideal.

Fe, and then a plateau at 0.26 mm/s over the range 35-50 at. % Fe. Quadrupole splitting data shown in Figure 3.4b follows a similar trend: a plateau at 0.66 mm/s over the range 12-25 at. % Fe, two sets of values from 25-35 at. % Fe, and then a plateau at 0.54 mm/s for 35-50 at. % Fe. These findings suggest the growth of nanocrystals containing Fe. The isomer shift and quadrupole splitting values measured near 50 at. % Fe (0.26 and 0.54 mm/s, respectively) are consistent with the known values for crystalline SiFe (0.28 and 0.50 mm/s, respectively) [117]. However, the isomer shift and quadrupole splitting values for the high-temperature α-Si_2Fe phase are identical within experimental uncertainty (0.27 and 0.49 mm/s, respectively) [117]. The appearance of plateaus over the range of 35-50 at. % Fe could also indicate co-existing α-Si_2 and SiFe at compositions with high Fe content, since metastable phases are sometimes produced during rapid-quench techniques such as sputter deposition.

All spectra were fit using a distribution of doublet sites. The distribution width σ as a function of Fe content is shown in Figure 3.4c. Variations of σ with sputtering run (for a given composition) are within experimental uncertainty. σ is relatively low for values at low and high Fe contents because the absorption spectra are dominated by either amorphous (low Fe) or nanocrystalline (high Fe) sites. Fits over the range 25-35, and especially 30-35, at. % Fe, would include significant contributions from both the amorphous and nanocrystalline phases. The signal to noise ratio was not sufficiently high enough to conclusively identify two separate spectral components, so the larger distribution of sites lead to a larger value of σ. Also, the fit to spectra

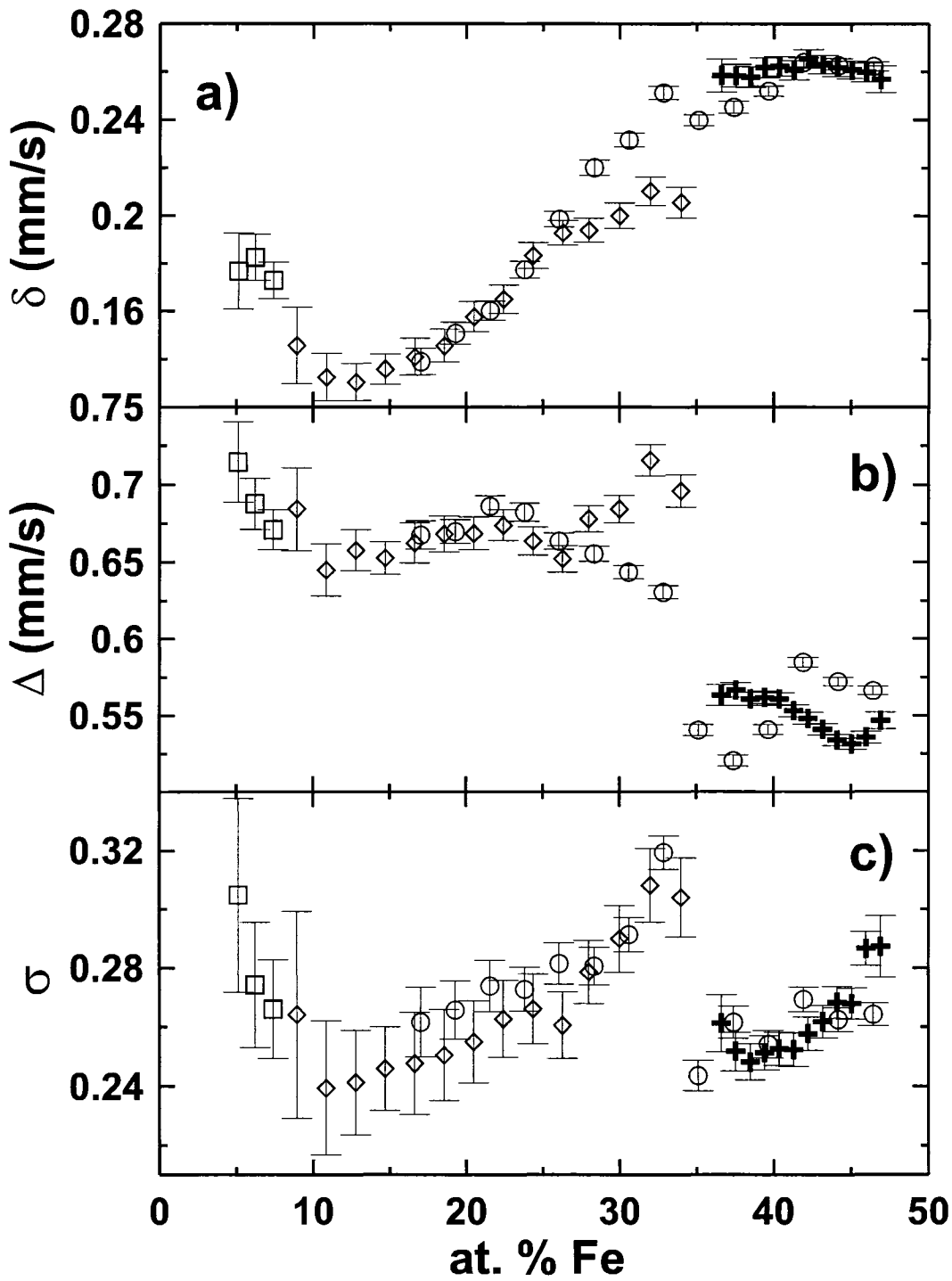

Figure 3.4: Isomer shift d (a), quadrupole splitting Δ (b) and site distribution σ (referenced to α-Fe) as a function of Fe content for the Si-Fe Mössbauer libraries listed in Table 3.1. Crosses, squares, diamonds and circles refer to data from sputtering runs spk022, spj045, spk088 and spl050, respectively.

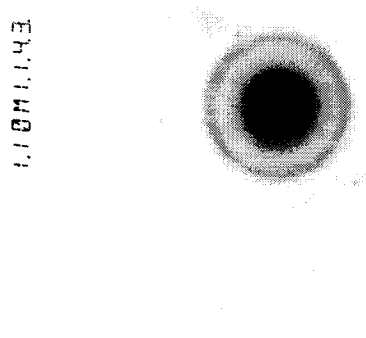

Figure 3.5: TEM diffraction image of $Si_{0.55}Fe_{0.45}$.

within this composition range lead to features in the difference plots shown in the centre of Figure 3.3. The peak in σ at 35 at.% Fe suggests a well ordered α-Si_2Fe phase is not present. Variations of δ and Δ with sputtering run over the range 25-35 at.% Fe may be the result of minor variations in deposition conditions (e.g. quench rate) with library position.

Mössbauer effect and x-ray diffraction results suggest co-existing nanocrystalline SiM and amorphous Si. It should be possible to 'see' the 2 nm SiM nanocrystals present at high Fe content, if they exist, using transmission electron microscopy (TEM). Very thin films (10-20 nm) of Si-Fe were deposited on two types of TEM grids with carbon support films purchased from pelcoint.com: 15-25 nm C films on 200 mesh grids and 3 nm C films on 400 mesh grids. Both types of C films were supported by a 60-70 nm thick layer of Formvar (polyvinyl formal, $(C_8H_{13}O_2)_x$). Attempts to remove the Formvar support layer using the instructions provided by the manufacturer were not successful for reasons still under investigation. The net result was thin films deposited on ultrathin C layer for high-resolution imaging were actually deposited on a rather thick 70-90 nm support layer. 'Low' resolution (e.g. 90,000 x magnification) images collected by Profs. Craig Bennett and Michael Robertson of Acadia University using a Philips CM30 TEM still provided useful information.

Figure 3.5 presents a diffraction image of the highest Fe-content sample produced (approximately $Si_{0.55}Fe_{0.45}$). Diffraction rings present in Figure 3.5 correspond to lattice spacings of 2.01 and 1.19 Å. α-Si_2Fe has strong diffraction peaks at d spacings

sputtering run	sweep rate	trickle discharge duration (@ 5 mV)	trickle charge duration (@ 1.2 V)
spj069-SiCrNi	0.01 mV/s	3 hours	1 hour
spj091-SiFe	0.02 mV/s	12 hours	1 hour
spj094-SiMn	0.0185 mV/s	12 hours	1 hour
spj104-SiMn	0.02 mV/s	12 hours	1 hour

Table 3.2: Cycling parameters for the data presented in Figs. 3.6-3.10.

of 5.2, 2.36, 1.9 and 1.86 Å. β-Si_2Fe has strong diffraction peaks at d spacings of 3.02, 2.40 and 1.83 Å. Finally, SiFe has strong diffraction peaks at d spacings of 3.17, 2.01, 1.83 and 1.20 Å. Diffraction rings associated with either form of Si_2Fe are not present; SiFe is the only logical Si-Fe phase present. XRD data could, and in retrospect should, have been collected at higher scattering angles to make this identification earlier. It is possible the ring corresponding to diffraction by the (110) plane of SiFe was 'washed out' by the very intense central beam. The lack of a ring at 1.83 Å, corresponding to the (211) plane of SiFe, is surprising considering the very polycrystalline nature of the sample. Nevertheless, this diffraction data eliminates the possibility of either form of Si_2Fe being present. Nanocrystalline areas can therefore be identified as SiFe.

Images of lower Fe-content samples were not attempted because of difficulties encountered in obtaining clear images of samples expected to contain the largest features (i.e. nanocrystalline SiFe) at high magnification (eg. 250,000x). Future TEM imaging will involve development of the Formvar removal procedure, or deposition on to ultrathin carbon films supported only by a lacey carbon film with no Formvar support layer. Thin films of SiFe will be used as the known standard for the technique development.

3.2 Electrochemistry

Three separate techniques were used to conclusively idendify the nanocrystalline component of the Si-Fe libraries as SiFe. It will become apparent that the same conclusion can be reached using only an electrochemical testing method.

Thin film libraries of Si-Cr-Ni, and Si-Mn and Si-Fe, were deposited on to the ternary and binary combinatorial cell plates described in Section 2.4. Cycling parameters are provided in Table 3.2. Figure 3.6 depicts 64 differential capacity vs. voltage

(dQ/dV vs. V) plots collected simultaneously from 64 different compositions of Si-Cr-Ni using the combinatorial electrochemical cells and cycling hardware described earlier.

Figures of the type of Figure 3.6 are useful for displaying general trends in data, but are too compact to allow for detailed analysis. It is clear from Figure 3.6 that a) the combinatorial methods described in Chapter 2 can be used to collect a large amount of data, b) transition metal content (which increases from bottom to top and right to left in Figure 3.6) has a large effect on capacity, and c) changes in dQ/dV vs. V plots with composition are mostly related to changes in magnitude rather than feature growth / disappearance.

Differential capacity vs potential plots for all three Si-M systems (Si-Cr-Ni, Si-Fe and Si-Mn) at various Si contents are shown as Figure 3.7. Si content increases from top to bottom, from 60 to 90 at. %. The vertical scale varies from row to row, but is consistent across each row. The solid and dashed curves shown in the upper right-hand corner correspond to $Cr_{0.25}Ni_{0.15}Si_{0.6}$ and $Cr_{0.15}Ni_{0.25}Si_{0.6}$, respectively. The same ratio of Cr:Ni is maintained for the solid and dashed curves for 70 and 80 at. % Si. Cr and Ni are assumed to be interchangeable due to the high degree of overlap between the solid and dashed curves. The relative heights of the differential capacity vs potential peaks at 0.3 and 0.5 V upon Li removal shown in the bottom row of Figure 3.7 (90 at. % Si) change because of different degrees of $Li_{15}Si_4$ crystallization, which is affected by many variables including film thickness and adhesion [36]. The high Si content curves range from completely amorphous (Si-Fe) to partially crystallized (Si-Mn). Plots for 70 and 80 at. % Si show curves characteristic of amorphous Si. All four transition metals lead to nearly identical differential capacity vs potential plots for 70 at. % Si. Investigations of subtle differences in voltage profile with transition metal content / variety are still underway.

The differential capacity vs potential plot for $Mn_{0.4}Si_{0.6}$ shown in Figure 3.7 is characteristic of amorphous Si but does not match the other plots with 60 at. % Si. Some clues to may be found in the equilibrium phase diagrams shown in Figure 3.1. As mentioned earlier, Si forms disilicides with Cr, Fe and Ni, but not Mn. Instead, there have been reports of at least four Si-Mn phases with close to 63 at. % Si (Mn_4Si_7, $Mn_{11}Si_{19}$, $Mn_{15}Si_{26}$ and $Mn_{27}Si_{47}$) [39]. Mn_6Si_7 (53 at. % Si) has been observed to

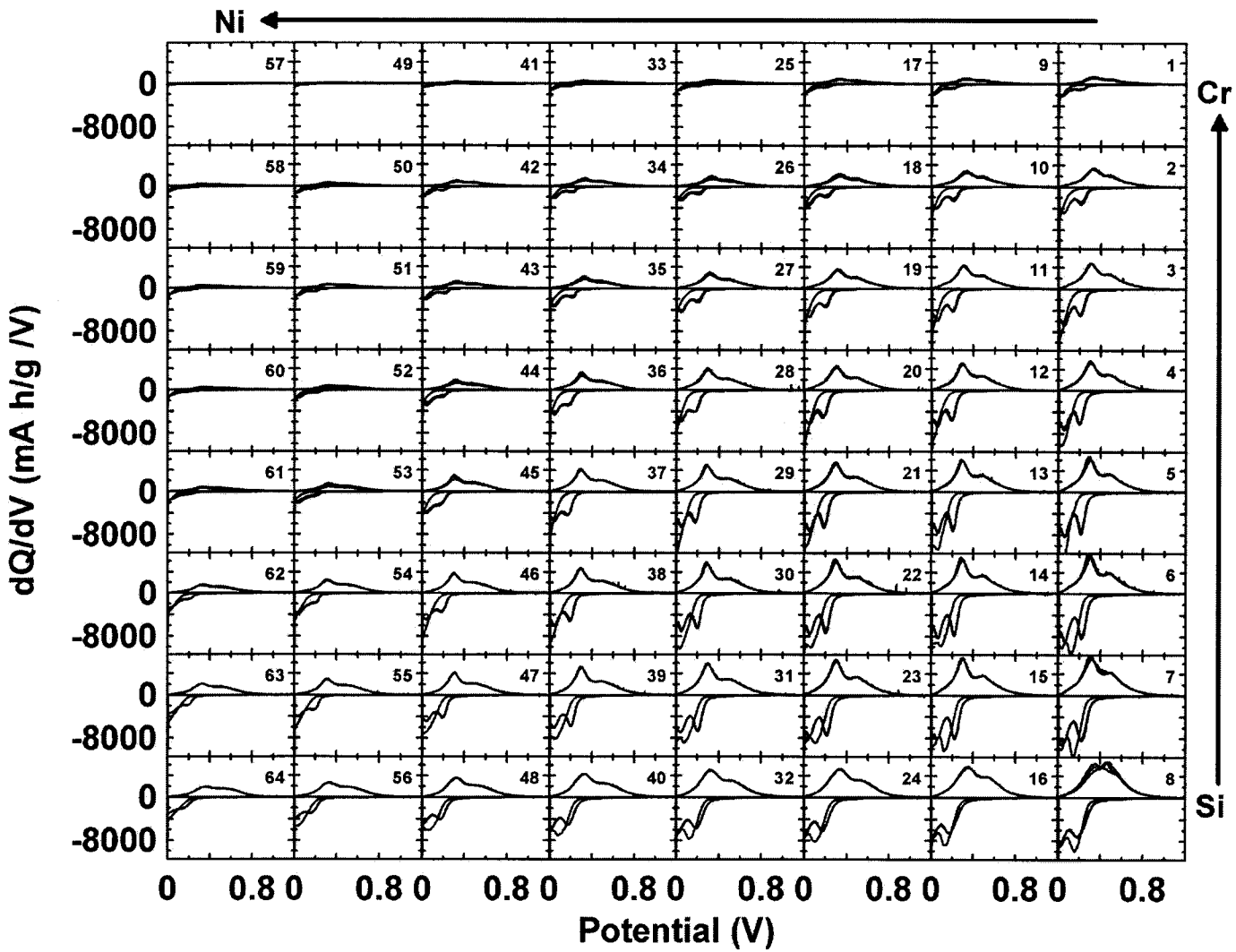

Figure 3.6: 64 dQ/dV vs. V plots collected simultaneously from 64 different compositions of Si-Cr-Ni using the methods described in Section 2.4.

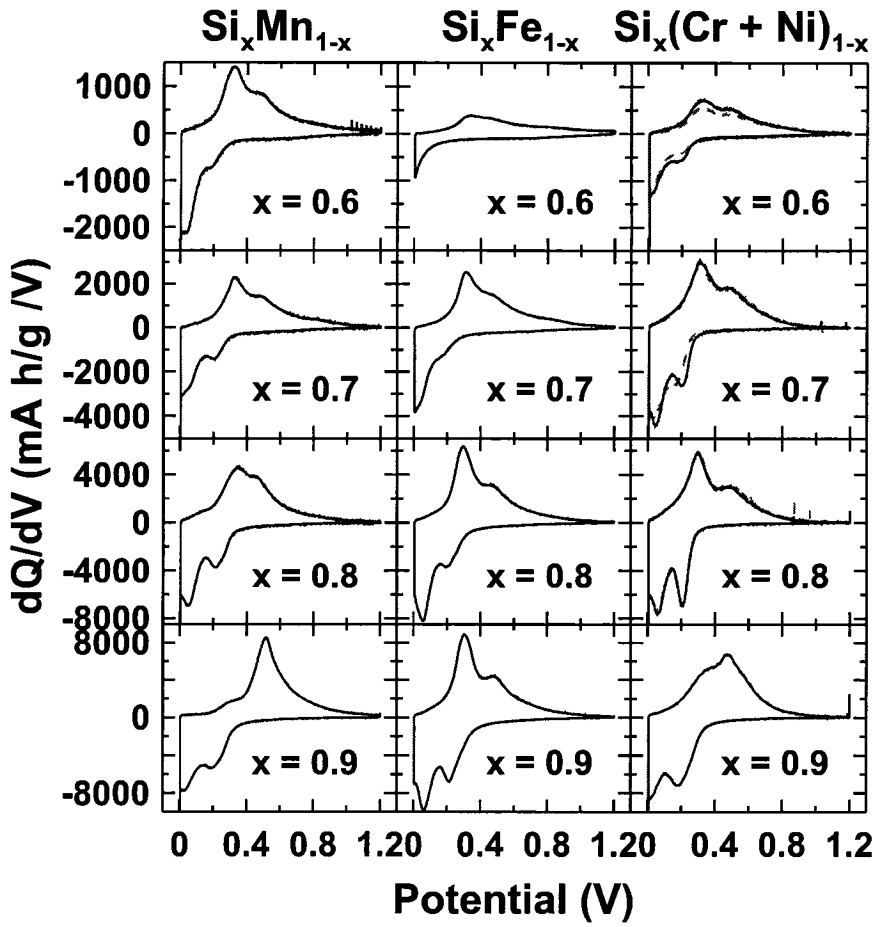

Figure 3.7: dQ/dV vs.V plots for Si_xM_{1-x} for M = Mn (left column), Fe (middle column) and Cr + Ni (right column) for various values of x. The vertical scale is consistent across rows but varies from row to row. Solid (dashed) lines in the right column correspond to high Cr (Ni) and low Ni (Cr) content; the ratio of high:low is about 3:2 Reproduced by permission of The Electrochemical Society, Inc. [86]..

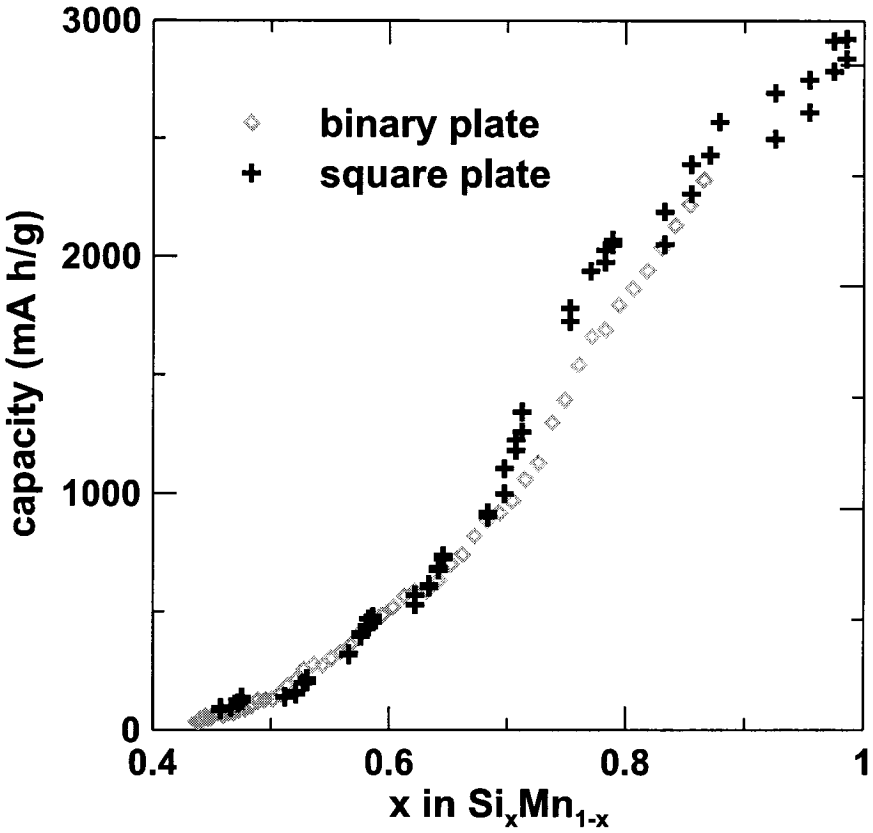

Figure 3.8: Capacity (mA h/g) vs. x in Si_xMn_{1-x}. The two sets of results are from separate sputtering runs (spj094, binary cell plates, and spj104, square cell plates).

be the next most Si-rich Si-Mn alloy, followed by SiMn. As mentioned earlier, the local structures of eg. Si_2M and $Si_{0.67}M_{0.33}$ are likely similar. However, the multiple possible Si-Mn phases may allow for more Si-Mn arrangements and make more Si accessible to Li. A higher Li diffusion co-efficient in Si-Mn (as compared to other Si-M systems) could lead to higher observed capacities for a given transition metal content.

X-ray diffraction, Mössbauer effect spectroscopy and TEM suggest amorphous Si and nanocrystalline SiM phases co-exist and grow at the expense of each other depending on composition. If this is correct, and if SiM is assumed to be electrochemically inactive, then the observed capacity should vary smoothly with composition from 3580 mA h/g for $Si_{100}Fe_0$ to zero at $Si_{0.5}Fe_{0.5}$. Figure 3.8 presents the 2^{nd} discharge capacity of Si-Mn as a function of composition. Data points from spj094 are evenly spaced in composition since they were collected with binary combinatorial

electrochemical cell plates. Data points from spj104 duplicate those from Si-Mn run 1, although clumps, not a broad range, of compositions were investigated because of the different cell plate designs used. The capacity varies from over 3000 mA h/g near pure Si to approximately zero at 50 at. % Fe (a small amount of capacity is associated with the Cu lead pattern).

The variation in capacity with composition can be modeled if a sample of composition Si_xM_{1-x} is assumed to be made up of a mole fraction of (2x-1) Si (nanoscale a-Si) and (2-2x) SiM (nanoscale SiM) for $0.5 \leq x \leq 1$. The solid lines shown in Figure 3.9 were calculated assuming Si atoms not incorporated in SiM can alloy with 3.75 Li (corresponding to $Li_{15}Si_4$). The formula used to calculate the solid lines is therefore

$$\text{capacity (mA h/g)} = \frac{3.75\,\text{Li/mol} \cdot (2x-1)}{x \cdot \text{molar mass}_{Si} + (1-x) \cdot \text{molar mass}_{M}} \cdot \frac{96500\,\text{C/mol}}{3.6\,\text{C/mA h}}. \tag{3.1}$$

Data in Figure 3.9 is shown on two vertical scales in part to emphasize the agreement between the model and the Si-Mn data for all compositions.

Data presented in Figure 3.9 for the Si-Fe and Si-Cr-Ni systems follows the model for compositions with less than 30 at. % M. The two vertical axes in Figure 3.9 show a clear difference between the capacity of Si-Mn and either Si-Fe or Si-Cr-Ni for compositions with more than 30 at. % Fe. Si-Fe data points are evenly spread in composition because the binary cell plate design was used. Si-Cr-Ni capacity vs Si content data points were collected with ternary plates. The increased scatter for this system could be due to uncertainties related to composition determination. Since there was only one axis (radial) of composition variation for the Si-Mn and Si-Fe systems, only one line of 10 composition data points was collected to determine the composition as a function of radial position. Errors in the composition determination may exist, but serve only to shift the data to lower or higher Si content. Features in Figure 3.9 are only said to occur at approximate compositions to reflect this uncertainty. Determining the composition for a ternary thin film library like Si-Cr-Ni is more complicated. A 10 x 10 grid of data points is collected using the electron microprobe. Contour plots of composition vs. position for the three components (i.e x, y, and $1-x-y$ in $A_xB_yC_{1-x-y}$) are produced using Surfer software (Golden Software Inc, Golden, CO USA). An image of the lead pattern is superimposed on the contour plots and the composition components are manually determined. Uncertainty related

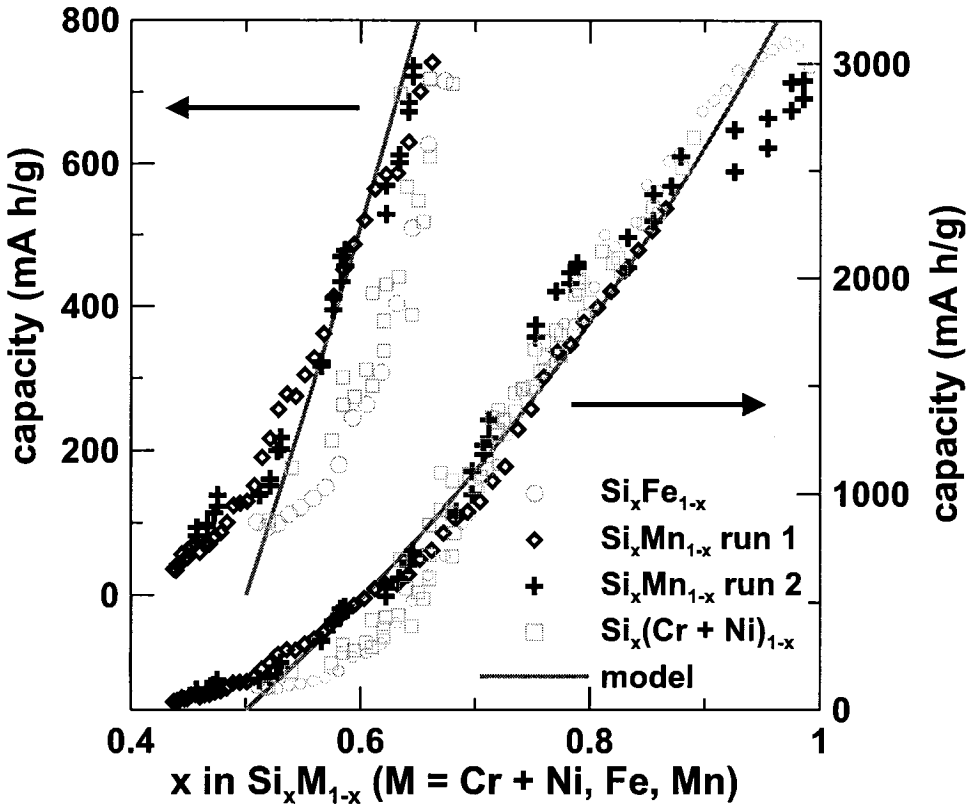

Figure 3.9: Capacity (mA h/g) vs. x (Si content) in Si_xM_{1-x} (M = Mn, Fe, Cr + Ni). Data points for the range 50 to 70 at. % Si are shown on two vertical scales to emphasize the difference between Si-Mn and either Si-Fe or Si-Ni-Cr. The solid line was calculated using Eq. 3.1, which assumed a sample composition Si_xM_{1-x} is made up of a mole fraction of (2x-1) Si (nanoscale a-Si) and (2-2x) SiM (nanoscale SiM) for $0.5 \leq x \leq 1$. Reproduced by permission of The Electrochemical Society, Inc. [86].

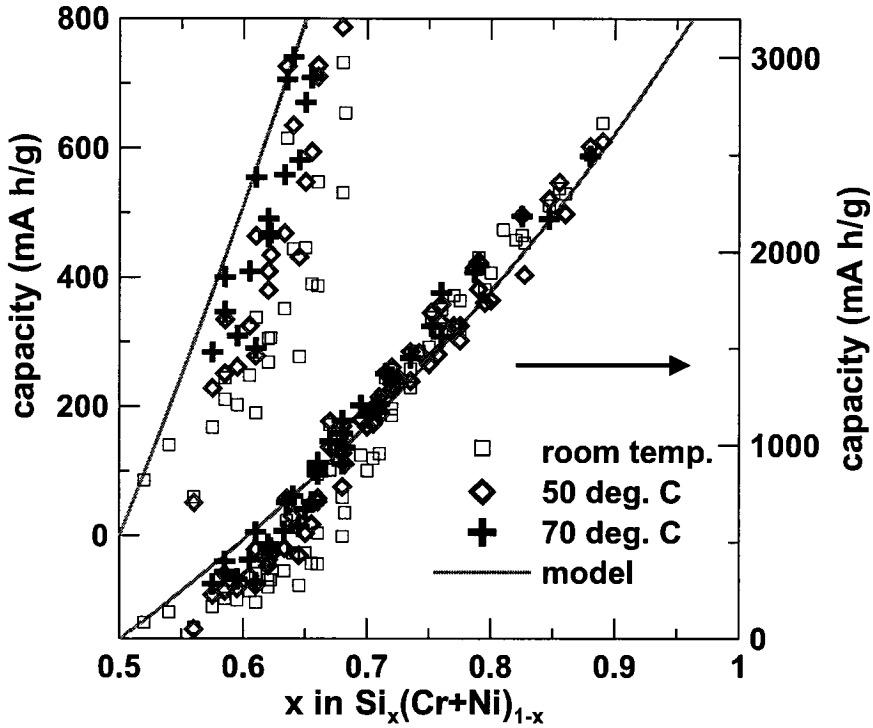

Figure 3.10: Capacity of $Si_x(Cr+Ni)_{1-x}$ as a function of cycling temperature.

to reading the contour plots is small (less than one at. %). However, two composition gradients that may shift the Si content up or down are present. Samples reported as $Cr_{0.15}Ni_{0.15}Si_{0.7}$ could feasibly be as high and low in Si content as $Cr_{0.14}Ni_{0.14}Si_{0.72}$ and $Cr_{0.16}Ni_{0.16}Si_{0.68}$, respectively.

The capacity increases smoothly from 1000 mA h/g at 70 at. % Si to over 3000 mA h/g approaching pure Si, and does not depend on the material system. Differences between Si-Mn and Si-Fe or Si-Cr-Ni appear below 70 at. % Si. The capacity of Si-Fe and Si-Cr-Ni continues to decrease smoothly and approaches zero around 55 or 60 at. % Si, which is still consistent with the idea of co-existing amorphous Si and nanocrystalline SiM phases.

Capacity increases can be realized for Si-Cr-Ni compositions with less than 70 at. % Si by performing the electrochemical testing at elevated temperature. Three cycles were performed at room temperature, then 50 and finally 70 °C by placing the combinatorial electrochemical cell in a VWR oven. Figure 3.10 presents the capacity of Si-Cr-Ni as a function of Si content and cycling temperature. Measured capacities for compositions with less than 70 at. % Si become closer to the model as the cycling

temperature is increased from room temperature to 70 °C. Diffusion effects obviously play a large role in the measured capacities and could lead to some of the uncertainty in the previously published data.

Many conclusions can be drawn from the data presented in this chapter. First, combinatorial methods can produce a higher quantity and quality of data and can therefore lead to better scientific insight. Second, the capacity of sputtered Si-M thin films can be modeled assuming a sample of composition Si_xM_{1-x} is composed of (2x-1) moles of active amorphous Si and (2-2x) moles of inactive nanocrystalline SiM for $0.5 \leq x \leq 1$. Although nanocrystalline Si_2Fe was not observed, it is feasible to suggest the inactivity of Si_2M observed by, e.g., Lee and Lee [109], was related more to diffusion effects than the fundamental capacity of the material. Weydanz *et al.* [106] note the uptake of Li by transition metal silicides is very slow at room temperature. Elevated temperature studies are therefore important before declaring an electrode material 'inactive'. Cycling temperature is limited by electrolyte breakdown (approx. 80 °C for the EC:DEC used in these studies) and the melting of Li at 180 °C. Electrolytes stable at higher temperatures (ca. 100 °C) are available (eg. dimethyl sulfone [118–120]), but would be used for studies of scientific, rather than practical, importance since cells operating at 100 °C are not likely to be included in, for example, laptop computers and digital cameras. The studies of Si-M, Al-M, Al-Si and Si-Al-M described in this thesis are important because of the relatively unexplored science and the strong likelihood of commercial cells based at least in part on these material systems. Investigations of the Al-M (M = Cr, Fe, Mn, Ni) system will now be described.

Chapter 4

Al-M (M = Cr, Fe, Mn, Ni)

The active amorphous Si - inactive nanocrystalline SiM model described in the previous chapter can be used to explain almost all of the variation in published Si-M results. The purpose of this chapter is to explain the observed capacity of Al-M alloys. Larcher *et al.* [121] investigated various isostructural A_2B alloys, where A alloys with Li and B does not. Al_2Cu, and also Al_6Mn, were found to be almost completely inactive (ca. 50 mA h/g). Larcher *et al.* issued a challenge to theorists to explain why Al_6Mn, which has 84 at. % Al, is essentially inactive. Their challenge has received little response: one questionable paper by Lindsay *et al.* [122] and the work described in this chapter [87][1]. The electrochemistry of the Al-M system is likely more complex than that of the Si-M system because of the large and varied number of equilibrium Al-M phases. Figure 4.1 presents equilibrium phase diagrams for the high Al content portions of the Al-Cr, Al-Fe, Al-Mn and Al-Ni systems. Al_7M and Al_6M exists for M = Cr and M = Mn, respectively, followed by $Al_{11}M_2$ (M = Cr), Al_4M (M = Cr), Al_3M (M = Fe, Ni) and Al_5M_2 (M = Fe) with increasing transition metal content.

Masui *et al.* produced non-equilibrium phase diagrams for sputtered thin films of Al-M (M = Fe, Ni [123] and M = Cr, Mn [124]). Nanocrystalline fcc (Al) is present in all four systems up to 5-10 at. % M followed by a region of co-existing fcc (Al) and an amorphous phase, and then an amorphous phase above 10-15 at. % M. These results suggest it is possible to develop a general model for the capacity of sputtered thin films of Al-M.

The macroscopic atom model of de Boer *et al.* [90] can be used to accurately predict the heat of formation of various Al-M alloys with low (less than 20 at. %) transition metal content. Consider the known reaction of Li with Sn-Fe as an example. Lithiation of Sn-Fe alloys results in the formation of metallic Fe and Li-Sn alloys [125]. This can be understood thermodynamically by considering the reaction of lithium

[1]Large portions of this chapter are reproduced from [87] with permission from The Electrochemical Society.

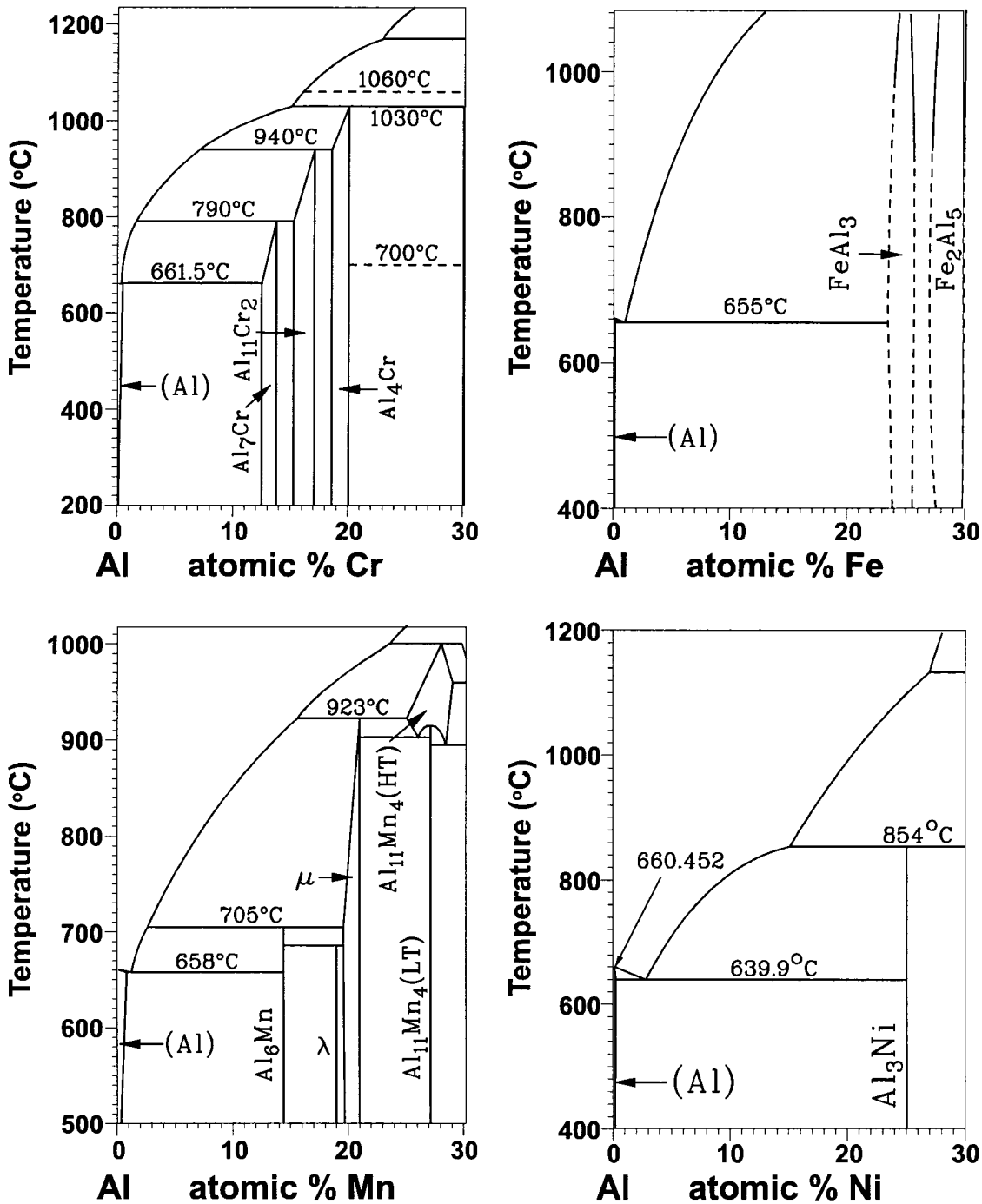

Figure 4.1: Partial equilibrium phase diagrams for Al-Cr, Al-Fe, Al-Mn and Al-Ni (data from [115]).

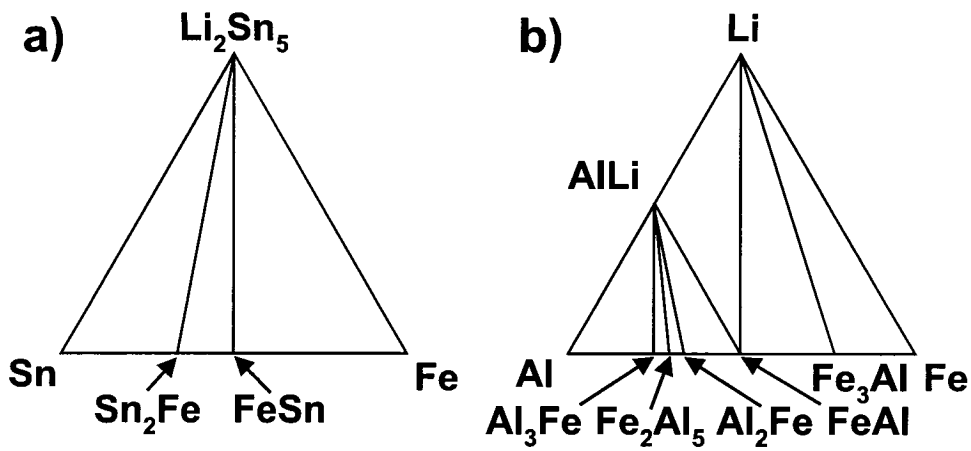

Figure 4.2: Partial Fe-Li-Sn (a) and Al-Li-Fe (b) phase diagrams based on the macroscopic atom model. Reproduced by permission of The Electrochemical Society, Inc. [87].

with FeSn, the most iron rich Sn-Fe intermetallic compound:

$$\mathrm{Li} + \frac{5}{2}\mathrm{FeSn} \longrightarrow \frac{1}{2}\mathrm{Li_2Sn_5} + \frac{5}{2}\mathrm{Fe}. \quad (1)$$

The macroscopic atom model predicts the heat of formation of FeSn to be only -4 kJ/mol, which indicates a very weak association between Fe and Sn. Using this value as an estimation of the FeSn free energy of formation (they are equal at zero temperature) and an experimental value of -145 kJ/mol for the free energy of formation of Li_2Sn_5 [126], Reaction 1 has an estimated reaction free energy of -63 kJ/mol. Based on the above calculation, then, all equilibrium Sn-Fe alloys are expected to be electrochemically active (which is in fact the case for Sn_2Fe [125] and SnFe [127]). A partial Fe-Li-Sn phase diagram is provided as Figure 4.2a.

Al-Fe alloys have a much higher free energy of formation than Sn-Fe alloys, indicating a much stronger association between Al and Fe atoms. A hypothetical displacement reaction between an Al-M alloy and Li can be considered using the same approach as above:

$$(1 - \mathrm{x})\mathrm{Li} + \mathrm{Al_{1-x}M_x} \longrightarrow (1 - \mathrm{x})\mathrm{AlLi} + \mathrm{xM}. \quad (2)$$

Once again, the free energy of formation is assumed to be approximately equal to the heat of formation so that the model of de Boer *et al.* can be used. The heat of formation for $Al_{1-x}M_x$ and (1-x) moles of AlLi is shown schematically in Figure 4.3. An experimental value of ΔH = -35 kJ/mol is used for AlLi since the macroscopic

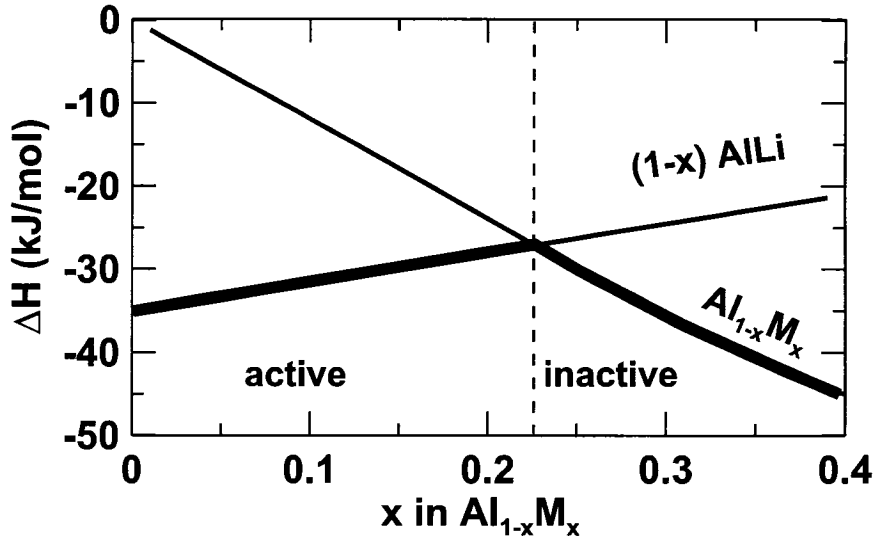

Figure 4.3: Schematic of heat of formation of (1-x) moles of AlLi and 1 mole of $Al_{1-x}M_x$ to illustrate the energetics of Reaction 2. The thick line indicates the most stable Al alloy as a function of M content. A dashed line separates the region where the formation of AlLi is favorable from the region where $Al_{1-x}M_x$ will not react with Li. Reproduced by permission of The Electrochemical Society, Inc. [87].

atom model is most accurate for alloys involving at least one transition metal. Larcher *et al.* [121] assumed ΔG = -35 kJ/mol based on thermochemical data (see references 14-17 of [121]). The parameters for Fe were used in the calculations to represent a typical transition metal M. A common oxidation state of +3 was used for Al and Fe. A thick solid line is used to indicate the Al alloy with the lowest free energy. According to Figure 4.3, the displacement reaction with lithium is not favourable for $Al_{1-x}M_x$ alloys with more than 23 at. % M. This means Reaction 2, the simple displacement reaction, does not occur for any of the known equilibrium Al-Fe phases. However, it will be shown that the reaction of Li with sputtered thin films of Al-M follows Reaction 2 over certain composition ranges.

In order to determine which Al-M phases are active, the reactivity of Li with each Al-M phase must be considered individually. Again using Fe as a model transition metal and the macroscopic atom model to determine the heats of formation of the Al-Fe alloys, the possible reactions of lithium with Al-Fe intermetallics in the Al-Fe-Li system and their estimated reaction free energies are as follows:

$$\mathrm{Li} + 2\mathrm{FeAl_3} \longrightarrow \mathrm{Fe_2Al_5} + \mathrm{LiAl} \qquad (-35\,\mathrm{kJ/mol}) \qquad (3)$$

$$Li + Fe_2Al_5 \longrightarrow 2FeAl_2 + LiAl \qquad (-31\,kJ/mol) \tag{4}$$

$$Li + FeAl_2 \longrightarrow FeAl + LiAl \qquad (-24\,kJ/mol) \tag{5}$$

$$Li + \frac{3}{2}FeAl \longrightarrow \frac{1}{2}Fe_3Al + LiAl \qquad (17\,kJ/mol). \tag{6}$$

Reactions 3-6 predict that all Al-Fe intermetallics with up to 33 at. % Fe should be active with respect to lithiation. The corresponding Al-Fe-Li phase diagram is shown in Figure 4.2b.

The above calculations only involve stoichiometric phases. Rapid quenching techniques, such as sputtering, sometimes produce metastable nonstoichiometric phases. Furthermore, room temperature lithiation of both stoichiometeric and nonstoichiometric Al-M alloys may also result in the formation of metastable phases. To take into account the formation of nonstoichiometric Al-M alloys the more general lithiation reaction:

$$yLi + Al_zM \longrightarrow yAlLi + Al_{z-y}M \tag{7}$$

should be considered. If y is an infinitely small number then change of heat of formation of Reaction 7 will be zero at the value of z for which Al_zM is inactive. The value of z required to inactivate Al_zM can be determined according to

$$y\Delta H_{AlLi} + \Delta H_{Al_{z-y}M} - \Delta H_{Al_zM} = 0$$

$$\Delta H_{AlLi} = -\lim_{y\to 0} \frac{\Delta H_{Al_{z-y}M} - \Delta H_{Al_zM}}{y} = \frac{\partial H_{Al_zM}}{\partial z}. \tag{4.1}$$

If ΔH_{AlLi} = -35 kJ/mol as assumed above and M = Fe, Eq. 4.1 is satisfied when z = 0.54 (i.e. 65 at. % Fe). Based on the all of the above thermodynamic calculations, Al-M alloys should be active towards lithiation at M contents below about 33 to 65 atomic percent.

Very little is known about the experimental electrochemical performance of Al-M alloys. Larcher *et al.* found that both bulk Al_6Mn and ball-milled Al_2Cu had very little activity with respect to Li [121]. This is surprising, since based on the thermodynamic calculations above, Al_6Mn should be active, and would have a capacity of at least 620 mA h/g. The ca. 30 mA h/g observed for Al_6Mn at both room temperature and 55 °C was attributed to the carbon black additive used during coin-cell testing.

run label	elements	at. % M	thickness	focus
spj007	Al, Fe, Mn	$0 \leq x \leq 40$	0.9-1.2 μm	electrochemistry
spj109	Al, Mn	$0 \leq x \leq 55$	0.6-1.2 μm	electrochemistry
spj114	Al, Mn	$0 \leq x \leq 29$	1.0-1.2 μm	electrochemistry
spj117	Al, Fe	$0 \leq x \leq 26$	0.4-0.5 μm	electrochemistry
spj125	Al, Ni	$0 \leq x \leq 26$	0.7-0.9 μm	electrochemistry
spj127	Al, Cr	$0 \leq x \leq 26$	0.6-0.7 μm	electrochemistry
spj140	Al, Mn	$0 \leq x \leq 26$	1.1-1.5 μm	electrochemistry
spj151	Al, Fe	$0 \leq x \leq 19$	0.8-1.0 μm	Mössbauer effect
spk026	Al, Fe	$0 \leq x \leq 20$	0.8-0.9 μm	electrochemistry / DSC
spk063	Al, Fe	$0 \leq x \leq 16$	1.3-1.5 μm	Mössbauer effect
spk128	Al, Fe	$0 \leq x \leq 22$	0.9-1.2 μm	electrochemistry
spl010	Al, Ni	$0 \leq x \leq 22$	1.0-1.2 μm	electrochemistry
spl018	Al, Cr	$0 \leq x \leq 23$	0.8-1.0 μm	electrochemistry

Table 4.1: Brief summary of Al-M sputtering runs.

Although thermodynamically Al_6Mn should be active, the strong Al-M bonds in Al-M alloys (compared to Sn-M alloys) may be responsible for poor kinetics that result in the inability to lithiate these compounds. Larcher *et al.* [121] mentioned each Al in Al_6Mn has at least one Mn nearest-neighbour and speculated the strong Al-Mn bond was the cause of the inactivity.

The approach described in this chapter involved investigating the structure and electrochemical performance of broad composition ranges of Al_xM_{1-x} for four different varieties of M (M = Cr, Fe, Mn, Ni). Approximately 64 different compositions within the range of $0.75 < x < 1$ were tested for each value of M. Transition metals were selected based on local availability. Thin film libraries of Al-M (M = Cr, Fe, Mn, Ni) were deposited on a variety of substrates using the method described in Section 2.1 and [80]. A summary of Al-M sputtering runs is provided in Table 4.1. Al was deposited using a DC power supply set to 100 W. All transition metals were deposited using a DC power supply set to approximately 25 W. All other methods were identical to those used during the Si-M analysis, except that the potential sweep rate during electrochemical testing was 0.0415 mV/s, the potential was held at 5 mV for four hours, all XRD data was collected using the Inel detector and no films were deposited on TEM grids.

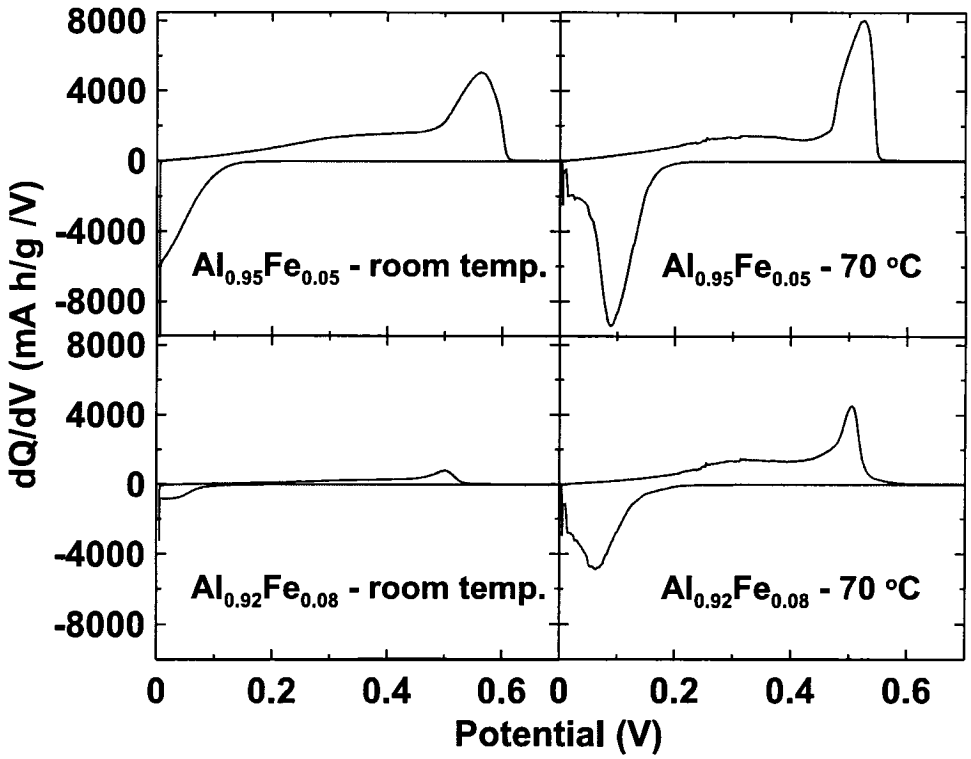

Figure 4.4: dQ/dV vs. V for $Al_{0.95}Fe_{0.05}$ and $Al_{0.92}Fe_{0.08}$ at room temperature and 70 °C. Reproduced by permission of The Electrochemical Society, Inc. [87].

4.1 Results

A dQ/dV vs. V plot for pure Al is characterized by a large peak at 0.1 V on Li insertion and at 0.5 V on Li removal. The same features can be found in the dQ/dV vs. V plots for $Al_{0.95}Fe_{0.05}$ and $Al_{0.92}Fe_{0.08}$ provided as Figure 4.4. Although the insertion (removal) capacity shifts to higher (lower) potential as the cycling temperature is increased from room temperature to 70 °C, all four plots of Figure 4.4 suggest the alloys are reacting with Li according to Al + Li $\leftrightarrow$ AlLi. A temperature of 70 °C is high enough to minimize the impact of diffusion effects but too low to cause electrolyte breakdown. It is clear that a small change in composition, or a change in cycling temperature, can have a dramatic effect on capacity.

Figure 4.5 illustrates the capacity as a function of composition for Al_xFe_{1-x} ($0.85 < x < 1$) as a function of cycle number and cycling temperature. A maximum of 900 mA h/g of Li was inserted (and removed) during the first cycle. The reversible capacity

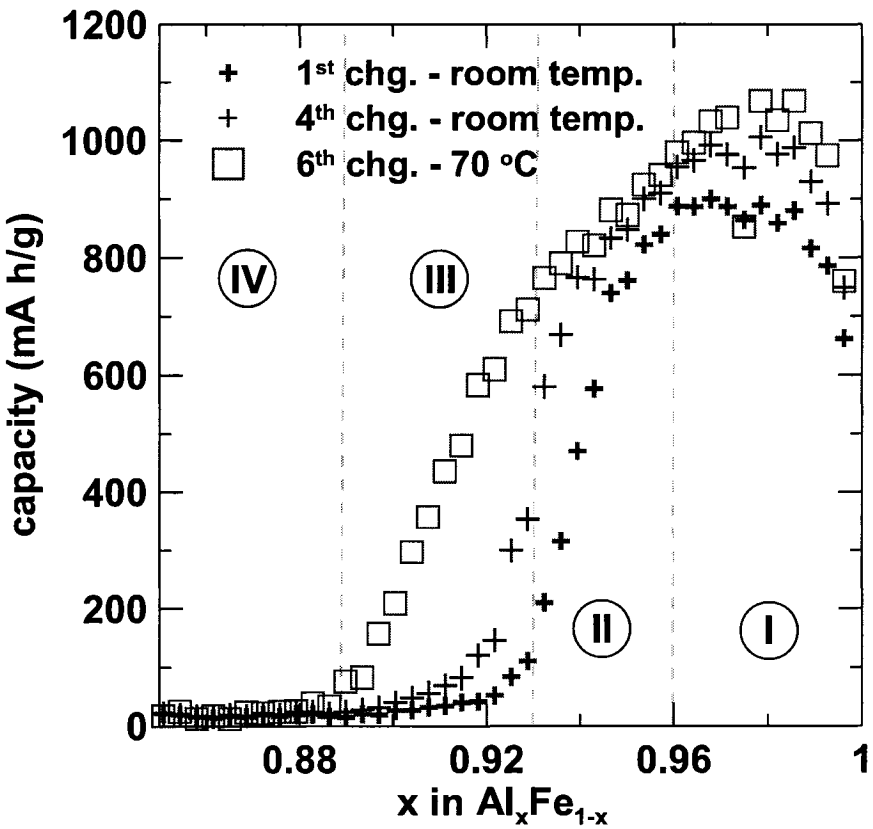

Figure 4.5: Capacity vs. x for Al_xFe_{1-x}. The four regions labeled with roman numerals are discussed in the text. Dashed lines separate the regions. Reproduced by permission of The Electrochemical Society, Inc. [87].

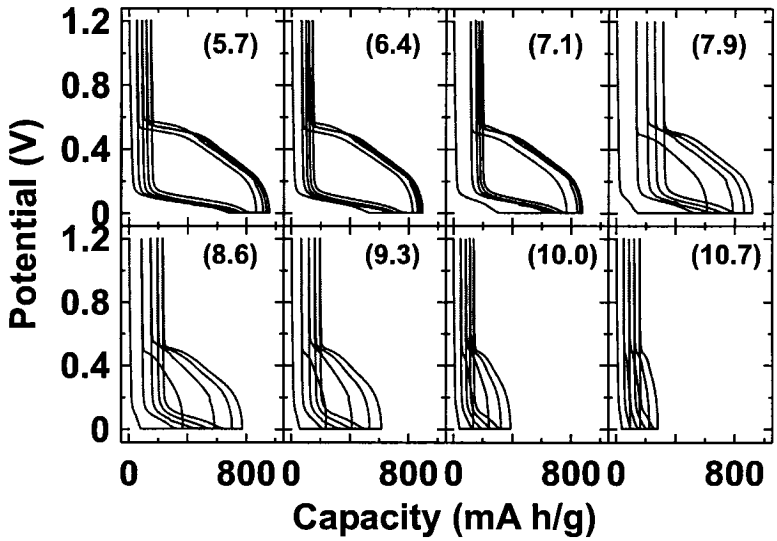

Figure 4.6: Voltage vs. capacity plots for selected low-Fe content Al_xFe_{1-x} alloys. Atomic percent Fe values for each plot are shown in brackets. Reproduced by permission of The Electrochemical Society, Inc. [87].

increased to the expected value of 1000 mA h/g for pure Al by the fourth charge-discharge cycle. Large increases in capacity with cycle number occurred for Al_xFe_{1-x} alloys in the range of $0.93 < x < 0.95$ (e.g. from 450 to 750 mA h/g for $Al_{0.94}Fe_{0.06}$). This capacity increase is probably related to changes in electrode morphology (i.e. channels / cracks developing during cycling). A larger surface area would expose more of the electrode to the electrolyte and thereby speed Li diffusion throughout the electrode. Further increases in capacity occurred for compositions with more than 5 at. % Fe as the cycling temperature was increased from room temperature to 70 °C. The most dramatic increases occurred over the region of $0.89 < x < 0.93$. Alloys in this region were essentially inactive at room temperature. This and the three other regions of capacity vs. composition are marked in Figure 4.5.

Voltage vs. capacity plots collected at room temperature for a series of eight compositions in the range of 5.7 to 10.7 at. % Fe are provided in Figure 4.6. Compositions with Fe content below 7.5 at. % Fe show relatively little change in capacity with cycle number. Diffusion and composition effects play a larger role at higher Fe contents, as illustrated by the steady increase in capacity with cycle number for alloys with more than 7.5 at. % Fe. The proportion of the capacity associated with the trickle discharge (constant potential of 5 mV vs. Li/Li^+) increases with Fe content and decreases with

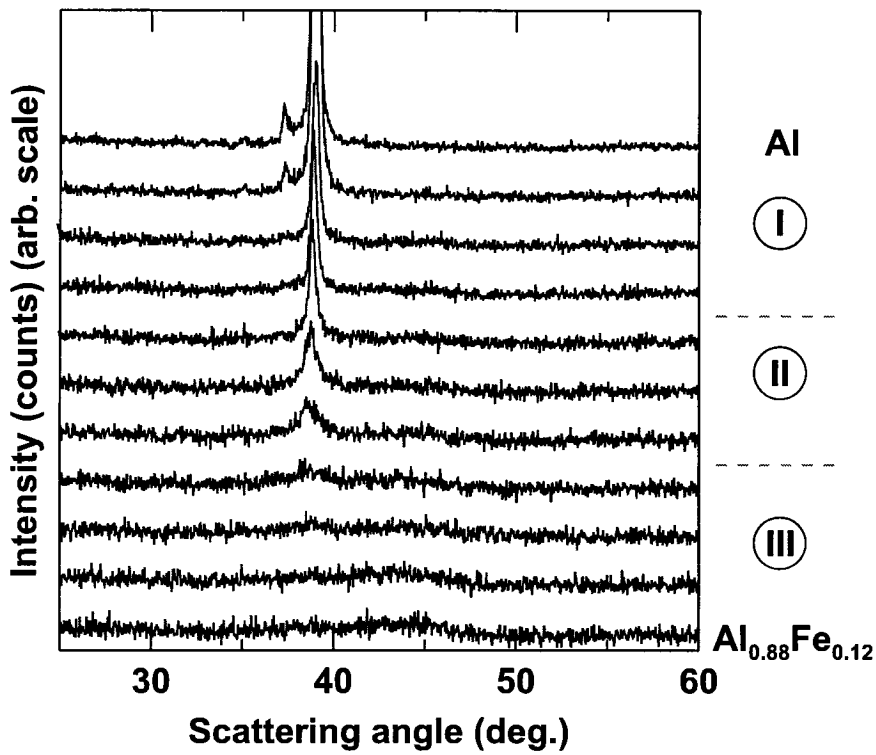

Figure 4.7: XRD patterns for Al_xFe_{1-x} ($0 < x < 0.12$). Regions, corresponding to those shown in Figure 4.5, are marked. Reproduced by permission of The Electrochemical Society, Inc. [87].

cycle number. The capacity decreases to essentially zero at 89 at. % Al.

Electrochemical measurements suggest our alloys consist of an active component (Al) and an inactive component whose composition and/or structure affects the capacity of the active component. XRD patterns from an Al-Fe library are presented as Figure 4.7. Patterns with less than 4 at. % Fe are dominated by the (111) peak of fcc (Al). Additional peaks characteristic of fcc (Al) were not observed, likely due to preferential film orientation ('texturing'). The fcc (Al) (111) peak then decreases in intensity and disappears by 7 at. % Fe. A broad hump corresponding to an amorphous phase appears at 4 at. % Fe and persists to at least 20 at. % Fe. It should be noted that the compositions at which the amorphous phase appears and the fcc (Al) phase disappears correspond to the boundaries of some of the regions shown in Figure 4.5. This comparison will be discussed shortly.

Mössbauer effect measurements were performed to characterize the unidentified amorphous phase. Spectra from the six lowest Fe contents are presented as Figure

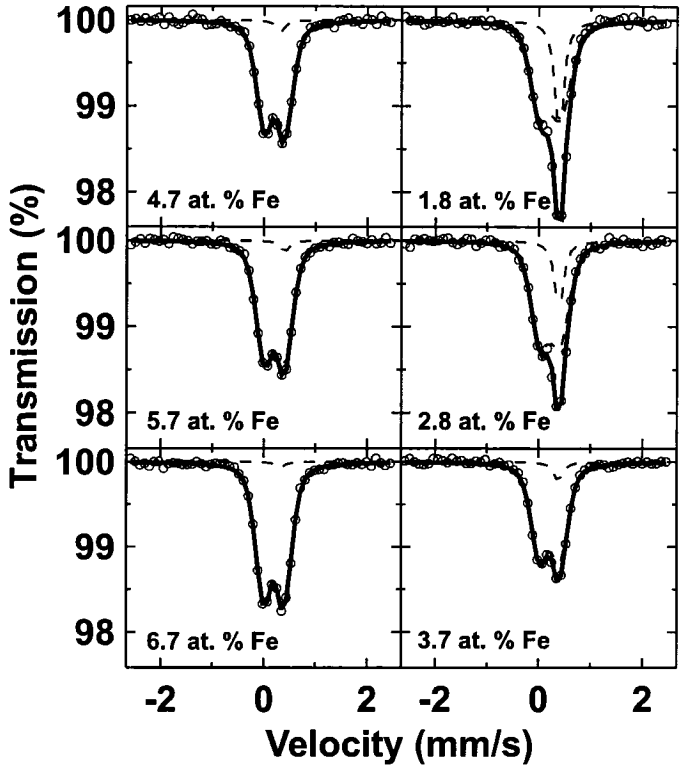

Figure 4.8: Mössbauer effect spectra collected from various Al_xFe_{1-x} alloys. at. % Fe values are provided for each panel. Circles, dashed lines and solid lines represent the raw data, site contributions and the total fit, respectively. Reproduced by permission of The Electrochemical Society, Inc. [87].

4.8. Singlet and doublet components are present in the fits up to 7 at. % Fe, followed by only a doublet component with increasing Fe content. Singlet components are characteristic of isolated Fe atoms in a symmetric environment. Doublet components are characteristic of Fe atoms in close proximity to one or more other Fe atoms in an asymmetric environment. Singlet and doublet sites were fit to Voigt-based functions [98]. The doublet centre shift decreases linearly from 0.22 mm/s to 0.195 mm/s from 2 to 7 at. % Fe, is constant at 0.195 mm/s up to 11 at. % Fe and then increases to 0.21 mm/s by 14 at. % Fe. The doublet quadrupole splitting is roughly constant at 0.395 mm/s up to 10 at. % Fe, and then linearly increases to 0.48 mm/s by 14 at. % Fe.

These results are similar to published fits for rapidly quenched Al_xFe_{1-x} alloys with low Fe content [128–130]. Doublet sites are the result of Fe-Fe interactions and might be unexpected in an intimately mixed alloy with very low Fe content. If the

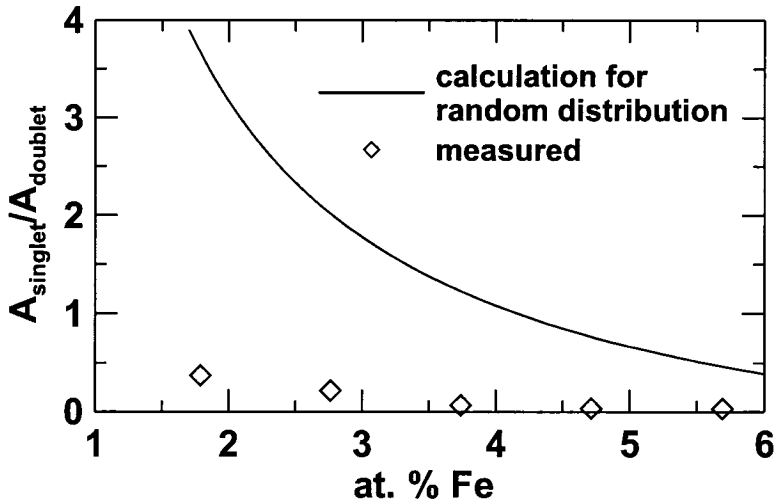

Figure 4.9: $\text{Area}_{\text{singlet}}$ / $\text{Area}_{\text{doublet}}$ for the data shown in Figure 4.8 and that expected from a random distribution of Fe in Al. Reproduced by permission of The Electrochemical Society, Inc. [87].

Fe atoms were uniformly distributed on fcc lattice sites, the probability of no Fe-Fe nearest neighbours is given by $(1-x)^{12}$ where x is the at. % Fe and 12 is the fcc co-ordination number. The probability of at least one Fe nearest neighbour is thus $1-(1-x)^{12}$. If a Taylor series expansion is used to simplify $(1-x)^{12}$ to $(1-12x)$ for small x, the ratio of singlet to doublet sites can be approximated with $(1-12x)/12x$. This expression is plotted as a function of Fe content (x) in Figure 4.9. Data points based on the spectra shown in Figure 4.8 are also presented. It is clear from Figure 4.9 that the Fe atoms are not uniformly distributed throughout the sample. Isolated and clustered Fe atoms are present in samples with less than 7 at. % Fe. Singlet components only make significant contributions to fits for samples with less than 4 at. % Fe.

Results from higher Fe content alloys may be compared with reports in the literature for samples that have been quenched from the melt [129, 130]. While melt spun samples show the presence of long range icosahedral or decagonal quasicrystalline order in XRD patterns, the sputtered samples prepared here are nanostructured or amorphous. The centre shift of the doublet observed for the present alloys is similar to that reported in the literature [129] for the quasicrystalline phase, which, in turn is very nearly the same as for crystalline Al_6Fe. The quadrupole splitting observed here is only slightly larger than that in quasicrystalline phase or Al_6Fe and may indicate

the presence of a slightly greater degree of disorder. In general these results suggest that the local structure and Fe co-ordination in the sputtered samples is similar to that in the melt spun samples and may be based on local clusters similar to those found in crystalline Al_6Fe.

4.2 Discussion

Transitions appear to be present at 4, 7 and 11 at.% Fe in elevated temperature electrochemical results, x-ray diffraction spectra and Mössbauer effect spectra. Results from these three techniques will now be discussed for each of the four regions outlined in Figure 4.5. XRD patterns in region I are characteristic of fcc (Al). The isolated and clustered Fe sites suggested by Mössbauer effect results do not have a significant effect on the crystal structure. It is therefore reasonable to assume that, although the Fe sometimes clusters, the Fe sites are spread throughout the sample. Measured capacities are equal to those expected from a combination of active Al and inactive Fe. Thus, in region I, the capacity follows the prediction of Reaction 2 presumably because the Fe content is so small that isolated Fe atoms or pairs of Fe atoms surrounded by LiAl result.

Capacities drop more rapidly with Fe content in region II than in region I. XRD peaks corresponding to fcc (Al) are still present, but decrease in intensity with increasing Fe content. A broad hump characteristic of an amorphous phase has also appeared. Isolated and clustered Fe sites probably contribute to the disordered phase. Isolated Fe sites are not present in region III. XRD spectra are characterized by broad humps corresponding to the amorphous alloy. The capacity drops rapidly with increasing Fe content, to zero at 11 at.% Fe. Region IV is an amorphous alloy with clustered Fe and no electrochemical activity.

Structural changes with composition can be explained by changes in the relative amounts of isolated and clustered Fe sites. Isolated Fe sites are less likely than clustered Fe to disrupt the long-range fcc structure. Changes in electrochemical behaviour are not as simple to describe. Larcher *et al.* [121] mention that all Al atoms in Al_6Mn are involved in at least one Al-M bond. The structure of Al_6Mn is shown in Figure 4.10 [39]. Twelve Al atoms surround each pair of Mn atoms. The main proposal of this chapter is that the clusters of Al_6Fe (or equivalently $Al_{12}Fe_2$), suggested by

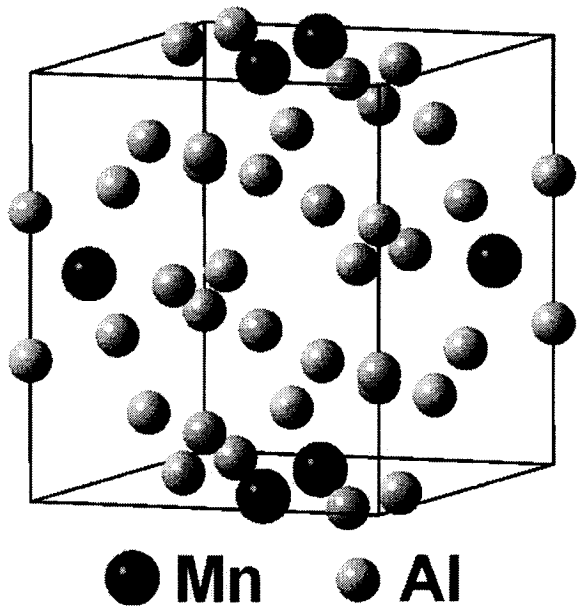

Figure 4.10: Unit cell of Al_6Mn [39]. Mn and Al atoms are dark and light grey, respectively. Reproduced by permission of The Electrochemical Society, Inc. [87].

Mössbauer measurements and schematically shown in Figure 4.11, are present and have a large impact on the electrochemical behaviour of our alloys. Note that Al_6Fe is not an equilibrium phase, although Al_6Mn is. To model the electrochemical data it was assumed that, like Al_6Mn [121], the $Al_{12}Fe_2$ regions formed in the sputtered Al-Fe films are also inactive. This does not necessarily mean that the Al on the surface of these regions is not active, since these Al have fewer Fe neighbors than Al in the bulk of the $Al_{12}Fe_2$ regions. It has also been observed that other inactive alloys containing active elements have active grain boundaries [131]. It was determined that assuming the surface Al of $Al_{12}Fe_2$ is active most satisfactorily fits the electrochemical results. For isolated Fe or isolated clusters all or most of the Al in the cluster phase is present on the surface. This means that such isolated clusters do not render any Al inactive, but only lower the specific capacity of the alloy on a gravimetric basis, due to the mass of Fe in the alloy. As the clusters begin to coalesce and increase in size, each additional Fe atom incorporates 12 surface Al into large regions of $Al_{12}Fe_2$. That is, for large clusters, each additional Fe atom renders 12 Al atoms inactive.

All Fe in region I is either isolated or part of an isolated cluster, which means all Al is at the surface and is able to alloy with Li. Isolated Fe sites become clustered and clustered sites join together in region II as some surface Al is incorporated into larger

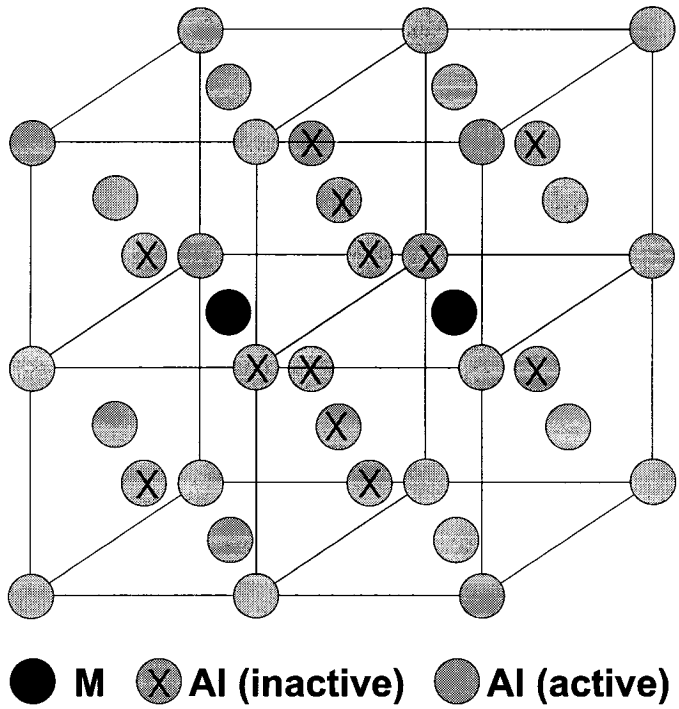

Figure 4.11: Schematic of $Al_{12}M_2$ in fcc (Al). M atoms are black. Al deactivated by the M atoms are dark grey and marked with a cross. Active Al atoms are light grey. Lines indicate the fcc unit cells. Reproduced by permission of The Electrochemical Society, Inc. [87].

regions of $Al_{12}Fe_2$. Each additional Fe joins clustered sites together in region III. Al is only present in large regions of $Al_{12}Fe_2$ or at the boundaries between these regions. The rapid capacity decrease in region III is thought to correspond to each additional Fe incorporating 12 surface Al atoms into inactive $Al_{12}Fe_2$. All $Al_{12}Fe_2$ regions are joined together in region IV and the alloy is completely inactive. The capacity of Al_xFe_{1-x} can be modeled as follows. Fe does not deactivate any Al below the fcc solubility limit (region I, 0-4 at. % Fe). The capacity decreases on a gravimetric basis in all regions with some capacity because of the increasing mass with increasing Fe content. Each additional Fe inactivates 12 Al after all singlet sites have disappeared (7 at. % Fe) until the alloy is completely inactive (11 at. % Fe). It will be shown that the disappearance of singlet sites often corresponds to the disappearance of Al (111) peaks in XRD spectra. The capacity of region II is a linear interpolation of the capacities at the end of region I (4 at. % Fe) and the beginning of region III (7 at. % Fe). The capacity of region IV is zero.

A comparison of this model to $Al_{1-x}Fe_x$ capacity data collected at room temperature and 70 °C is provided as Figure 4.12. There is excellent agreement between the model and the data collected at 70 °C. Edge effects related to imperfections in combinatorial cell sealing and non-linearities in the masks used during sputter-deposition are noticeable for compositions with less than 2 at. % Fe.

The model as described does not include anything related to diffusion effects. Electrochemical testing was performed at 70 °C to minimize the impact of diffusion effects because it is clear they play a large role at room temperature for some compositions. Large clusters of Al-Fe start to form and the room temperature capacity starts to decrease with increasing transition metal content at roughly the same composition. It is possible that these clusters impede Li diffusion throughout the electrode and lower the observed capacity.

The discussion up to this point has focused on Al-Fe so that Mössbauer effect results could be included. However, the purpose of this chapter is to understand the capacity of all Al-transition metal systems. Results for the Al-Cr, Al-Mn and Al-Ni systems were similar to those already presented for Al-Fe. Slight differences, such as the fcc solubility limit and composition at which peaks from fcc (Al) are no longer visible in XRD spectra, were present. Figure 4.13 presents non-equilibrium phase

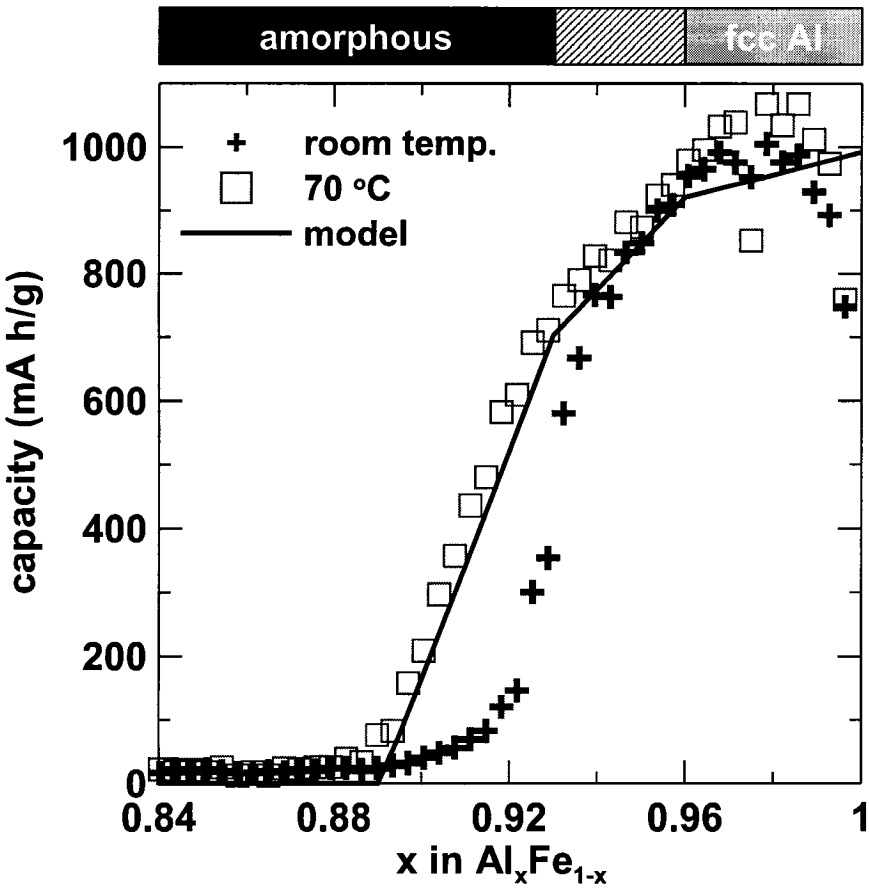

Figure 4.12: Capacity vs. x in Al_xFe_{1-x}. Crosses and squares indicate the maximum Li removal capacity during room temperature (4^{th} cycle) and 70 °C (6^{th} cycle, first four cycles at room temperature) cycling, respectively. The solid line indicates capacities predicted by the model described in the text. The non-equilibrium phase diagram as determined by XRD is provided for comparison. Reproduced by permission of The Electrochemical Society, Inc. [87].

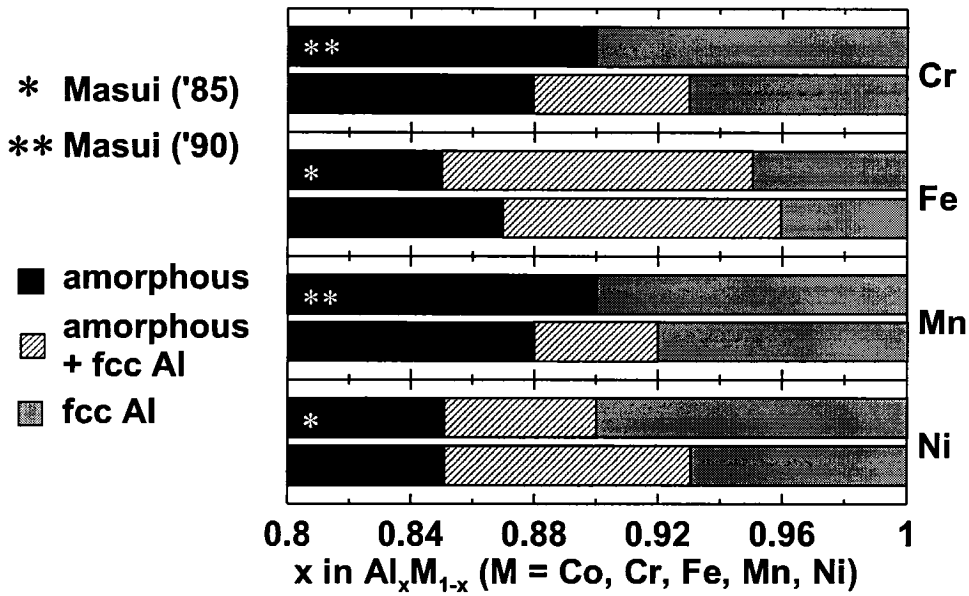

Figure 4.13: Summary of measured Al-M non-equilibrium phase diagrams. Results from Masui *et al.* for Al-Fe and Al-Ni [123], and Al-Cr and Al-Mn [124], are indicated by * and **, respectively. Reproduced by permission of The Electrochemical Society, Inc. [87].

diagrams for all four sputtered Al-M systems. Results are consistent with those of Masui *et al.* [123, 124].

The capacity of region III was modeled slightly differently for Al-M (M = Cr, Mn, Ni) because Mössbauer effect spectra were not collected for these systems. The composition limits of region III are easily read from a plot of capacity vs. composition. The capacity was modeled by assuming 12 Al were activated each time 1 M was removed (instead of 12 Al becoming inactive after the addition of 1 M). Comparisons of the modified model to data collected at room temperature and 70 °C are presented for the Al-Cr, Al-Mn and Al-Ni systems as Figures 4.14, 4.15 and 4.16, respectively. There is excellent agreement between the model and data collected at 70 °C for all three systems. The onset of region III coincides with the disappearance of fcc (Al) peaks in XRD spectra for all but the Al-Ni system.

Room temperature results are consistent with the model presented above for all four systems investigated. A rapid decrease in capacity with increasing M content starts within 2 at. % M of the fcc solubility limit for all four systems. It is possible the clusters of $Al_{12}M_2$ impede Li diffusion throughout the alloy. Clusters of $Al_{12}M_2$ joined together by additional M atoms are likely to surround small regions of otherwise

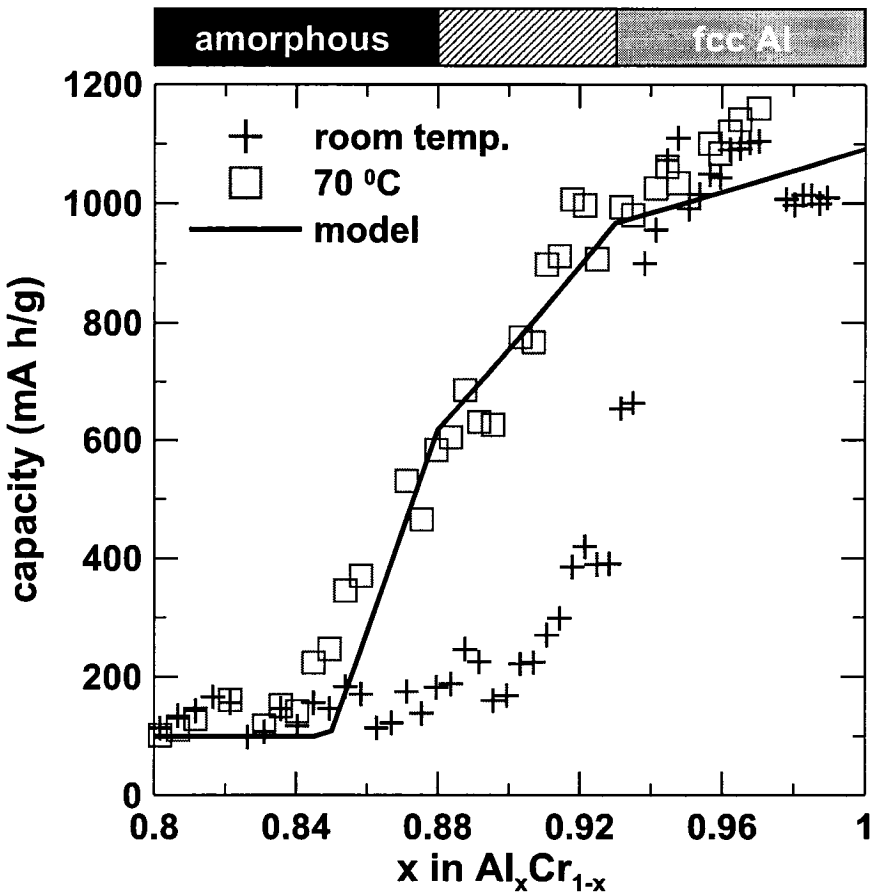

Figure 4.14: As in Figure 4.12 but for Al_xCr_{1-x}. Room temperature and 70 °C data corresponds to the second cycle and eighth cycle (cycles 1-3 at room temperature, cycles 4-6 at 50 °C, cycles 7-8 at 70 °C) of one cell, respectively. Reproduced by permission of The Electrochemical Society, Inc. [87].

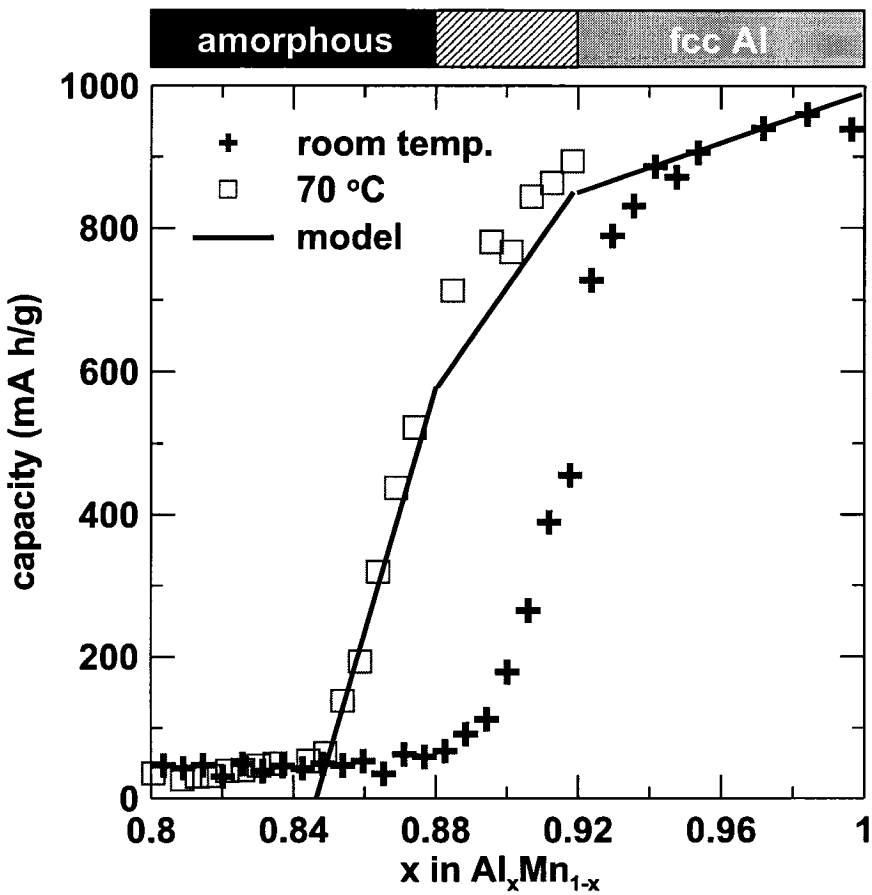

Figure 4.15: As in Figure 4.12 but for Al_xMn_{1-x}. Room temperature and 70 °C data corresponds to the fifth and third cycle of different cells cycled at the quoted temperature, respectively. Reproduced by permission of The Electrochemical Society, Inc. [87].

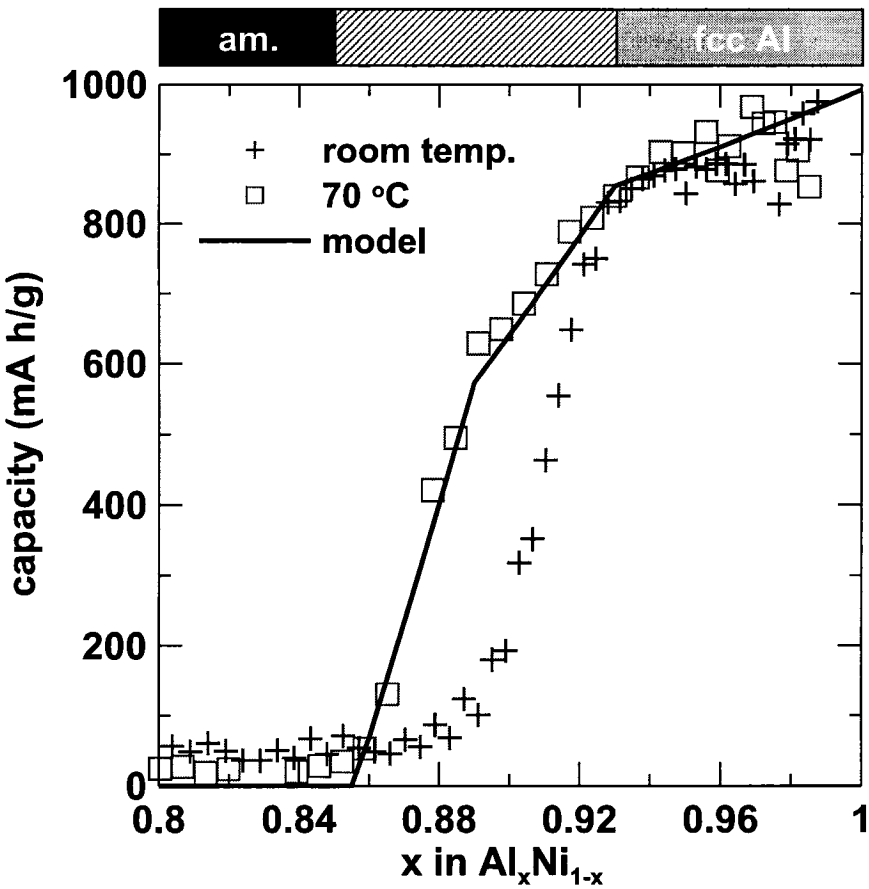

Figure 4.16: As in Figure 4.12 but for Al_xNi_{1-x}. Room temperature and 70 °C data corresponds to the second and third cycle of different cells cycled at the quoted temperature, respectively. Reproduced by permission of The Electrochemical Society, Inc. [87].

active Al and further reduce the capacity. The capacity associated with the isolated regions of Al might only become accessible after cracks develop in the electrode after repeated cycling.

The results presented above consistently show that only 15 at. % transition metal is required to render Al-M alloys completely inactive. This is far less than is predicted from thermodynamic considerations (33-65 at. % M). Larcher *et al.* [121] found bulk Al_6Mn (15 at. % M) and ball-milled Al_2Cu (33 at. % M) were inactive when cycled at room temperature and 55 °C, but were predicted to be active based on thermodynamic considerations. It is therefore possible that some kinetic limitations involving embedded $Al_{12}M_2$ clusters may be the actual cause of inactivity over the composition ranges investigated. Experiments to test the activity of Al-M alloys with more than 15 at. % M at temperatures higher than 70 °C would be impeded by liquid electrolyte breakdown (approx. 80 °C) and the melting of Li (180 °C).

It is quite apparent the macroscopic atom model can be useful to predict the electrochemical activity in systems, such as Sn-M, where kinetics do not apparently play a strong role. However, the results presented in this chapter and elsewhere [87] demonstrate Al-M alloys, materials which are active based on thermodynamic considerations, may nevertheless have kinetic barriers that impede their electrochemical activity entirely. The macroscopic model may still provide a way to further speed combinatorial investigations of advanced electrode materials by eliminating thermodynamically inactive materials from the search.

Chapter 5

Al-Si

The previous two chapters can be summarized by saying models were presented to describe the electrochemical activity of various equilibrium or metastable intermetallic phases. Figure 5.1 presents the Al-Si equilibrium phase diagram. No Al-Si equilibrium phases are present, which, along with the lack of a transition metal, prevents the proper application of the macroscopic atom model of de Boer *et al.* [90]. Some experimental work has been performed on the metastable Al-Si system. Konno *et al.* [132] determined the metastable co-sputtered Al-Si phase diagram to consist of three regions: a crystalline fcc phase extending from pure Al to the eutectic composition (12 at. % Si), an amorphous phase extending from pure Si to 60 at. % Si, and a two phase region in between. Radnoczi *et al.* [133] demonstrated Al content has a large impact on the crystallization temperature of Si-rich thin films. Crystallization first occurred between ca. 200 and 600 °C as the Si content was increased from ca. 80 to 100 at. %. Methods to predict the temperature at which this so-called metal induced crystallization occurs are described in [134].

Analysis of the electrochemistry of Al-Si may be more complicated than that of the Si-M and Al-M systems because of ternary Al-Li-Si phases. LiAlSi is the only Al-Li-Si phase agreed upon in the literature ([135–137]). Goel *et al.* [135] reviewed work on high Al-content alloys presumably of interest for high-strength alloys. Kevorkov *et al.* [136] determined AlLiSi, $Al_{2.1}Li_{5.3}Si_2$, and $Al_3Li_8Si_5$ to be the equilibrium ternary phases at 250 °C. Spina *et al.* [137] demonstrated $Al_3Li_8Si_5$ is more correctly identified as $Al_3Li_7Si_4$ after annealing near 1000 °C for hours and cooling slowly. Three other ternary phases were identified: AlLiSi, $Al_3Li_{15}Si_6$ and $Al_2Li_{18}Si_6$. $Al_3Li_{15}Si_6$ was demonstrated to have no reversible capacity when used as a battery electrode material [137]. This is one of only two published accounts[1] of

[1] S.S. Misra presented a talk [138] on the Li-Al-Si alloy/iron disulfide molten salt battery system at the 164^{th} meeting of The Electrochemical Society, but no proceedings volume was published.

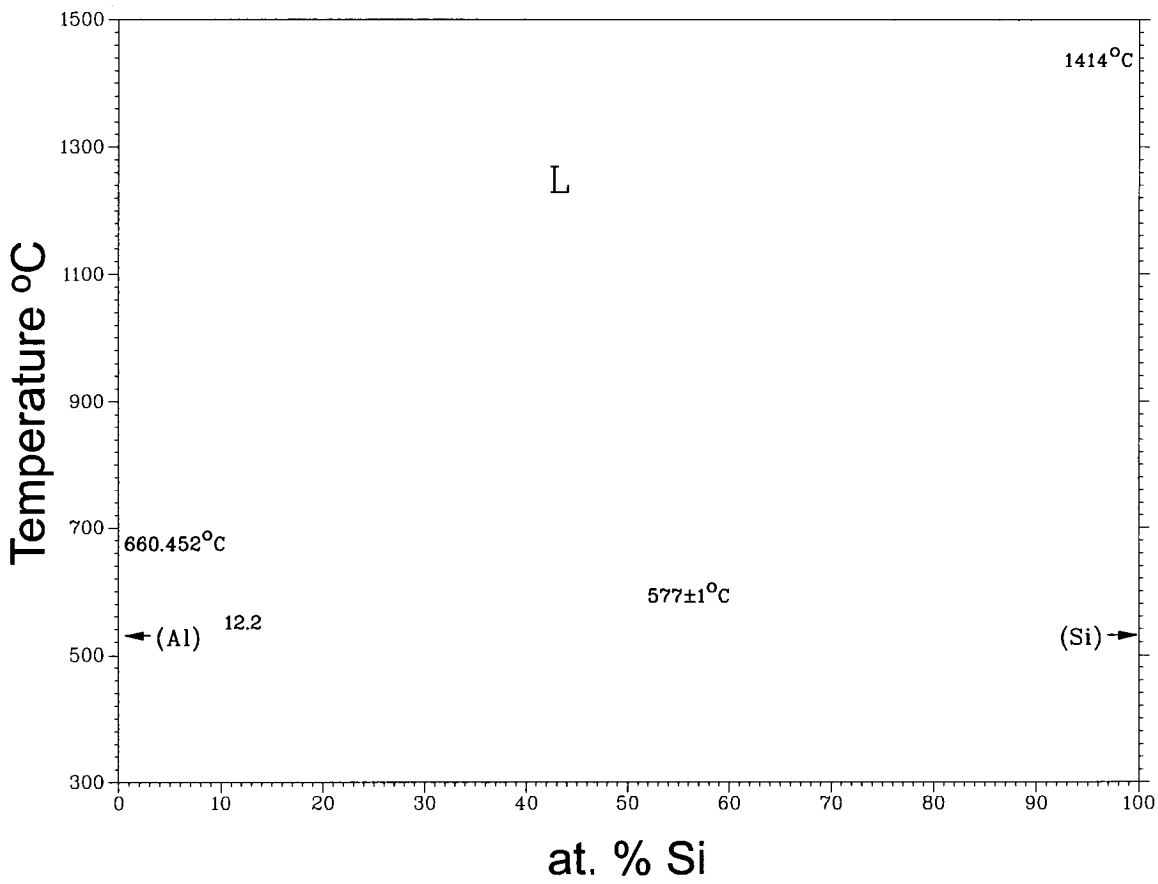

Figure 5.1: Al-Si equilibrium phase diagram (data from [115]).

run label	at. % Si	thickness	power (W) DC Al	Si	sweep rate (mV/s)
spk002	$0 \leq x \leq 100$	0.8-1.3 μm	78	128	0.0185
spk029	$0 \leq x \leq 100$	1.0-1.7 μm	78	128	0.0185
spk066	$0 \leq x \leq 35$	0.6-1.0 μm	85	100	0.0276
spk149	$55 \leq x \leq 95$	0.5-0.8 μm	40	99	0.0185
spl033	$60 \leq x \leq 100$	1.0-1.6 μm	70	200	0.0185

Table 5.1: Brief summary of Al-Si sputtering runs.

the electrochemical activity of Al-Si alloys known to the author[2], which is especially surprising since both Al and Si have been individually investigated for use as high capacity negative electrode materials, and Si suffers from poor conductivity, which the addition of Al should alleviate.

Five sputtering runs were performed to investigate the structure and electrochemistry of the Al-Si binary system. Details of each run are listed in Table 5.1. Two runs spanned the entire Al-Si system, followed by one and two runs for the Al and Si- rich ends, respectively. Al and Si were deposited using a DC power supply. Deposition powers are listed in Table 5.1. All other methods used were identical to those described in Chapter 4, except that films were deposited on to DSC pans instead of kapton film, and potential sweep rates during electrochemical testing varied from run to run (values are listed in Table 5.1). All cells cycled at 0.0185 mV/s were held at 1.2 V and 5 mV for 1 and 12 hours, respectively. Cells cycled at 0.0276 mV/s were held at 1.2 V and 5 mV for 1 and 4 hours, respectively.

5.1 Results

XRD patterns spanning most of the Al-Si binary system are presented in Figure 5.2. The sharp peak at 62.2° is due to the diffraction of Cu K_β x-rays by the Si substrate, not the deposited film. Patterns from compositions with high Si contents contain a broad hump centred at 28°, typical of amorphous Si. This hump first appears near 20 at. % Si and increases in area with increasing Si content. Peaks associated with fcc (Al) appear below 40 at. % Si and dominate patterns from compositions with high Al contents. A more detailed analysis of high Al content patterns reveals peaks at 38.8,

[2]Some work on the Al-Si system was performed by Bob Turner of 3M Co. (Woodbury, MN USA), and Dominique Larcher while at Dalhousie, but was not published.

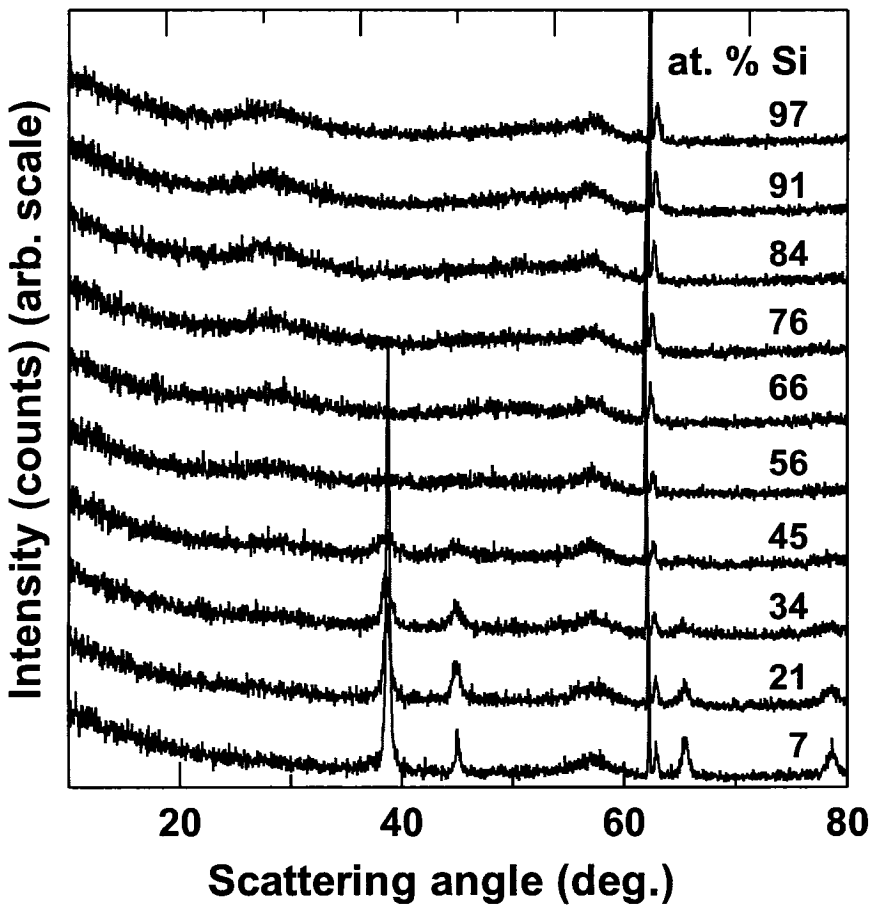

Figure 5.2: XRD patterns for $Al_{1-x}Si_x$ ($0.07 < x < 0.97$).

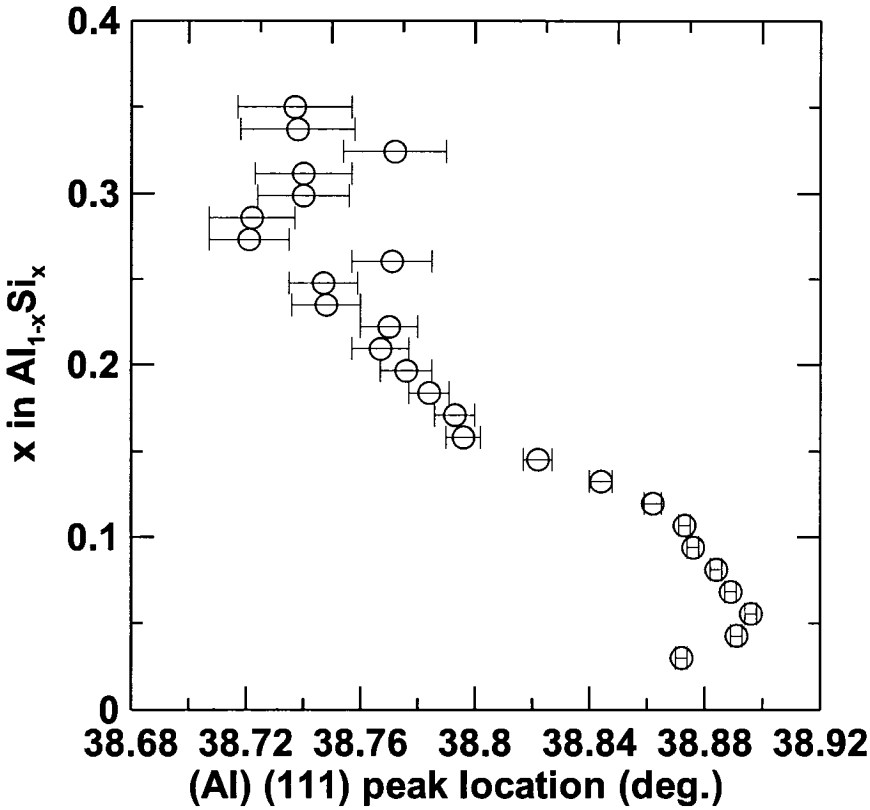

Figure 5.3: (Al) (111) peak location as a function of composition for $Al_{1-x}Si_x$ ($0 \leq x \leq 35$).

44.9, 65.5, and 78.5°, close to the four strongest peaks of fcc Al [139]. All four peaks broaden quickly as the Si content increases, and disappear completely near 40 at. % Si, suggesting Al crystallite size decreases with increasing Si content. The presence of a phase transition at 20 at. % Si can be confirmed by considering the location of the (Al) (111) peak near 38°. Figure 5.3 presents peak location (determined by fitting a Gaussian function to the peak near 38 ° using the gfit program) as a function of composition for the spk066 data set. The (Al) (111) peak shifts to lower angle (larger lattice spacing) as the composition increases to 20 at. % Si, and then remains roughly constant. Si is therefore incorporated in the fcc lattice until 20 at. % Si, at which point the amorphous phase appears and the composition of the fcc phase remains fixed. These results are summarized in the non-equilibrium phase diagram presented at the top of Figure 5.4, which is similar to the diagram presented by Konno *et al.* [132].

XRD results suggest the presence of only two single phase regions: (nano)crystalline

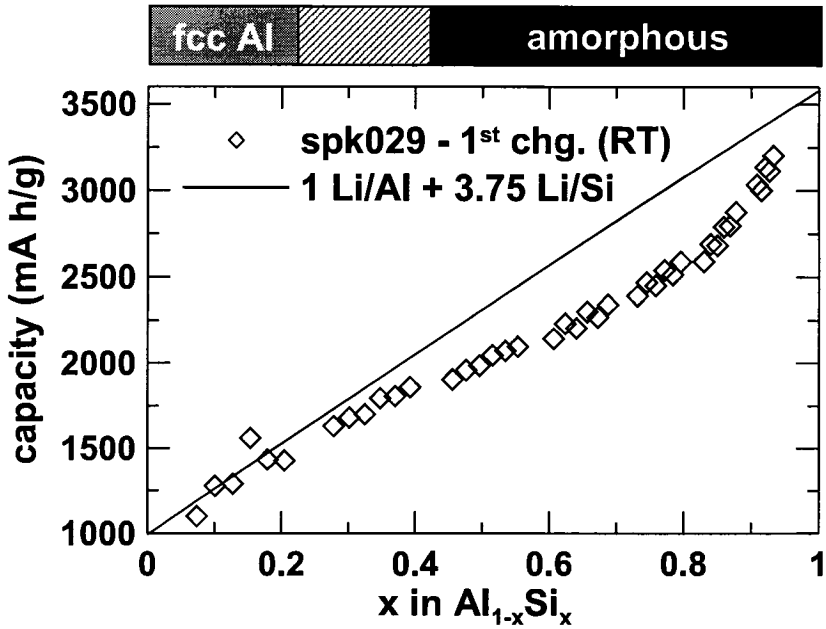

Figure 5.4: Capacity of Si_xAl_{1-x} (mA h/g) as a function of composition (x). The nonequilibrium phase diagram as determined by XRD is also shown.

Al and amorphous $Al_{1-x}Si_x$. Based on these results, attempts were made to model the electrochemical performance of the Al-Si system as the sum of separate reactions of Li with Al and Si (i.e. ignoring the possible presence of Al-Li-Si phases). The approximately straight line in Figure 5.4 indicates the capacity expected if each Al and Si reacts with 1 and 3.75 Li, corresponding to LiAl and $Li_{15}Si_4$, respectively. Capacity data points collected at room temperature (from sputtering run spk029) indicate this is apparently not the case. The capacity appears to follow the model of 1 Li/Al + 3.75 Li/Si up to about 20 at. % Si, after which the capacity increases with Si content, but not as fast as predicted by the simple model, up to about 80 at. % Si. A rapid increase in capacity occurs over the range 80-100 at. % Si, and extrapolates to the capacity expected from pure a-Si (ca. 3600 mA h/g). It is possible there is some reaction between Al and Si atoms that lowers the room temperature capacity near 80 at. % Si.

Figure 5.5 presents dQ/dV vs. V curves for three compositions ($Al_{0.25}Si_{0.75}$, $Al_{0.21}Si_{0.81}$ and $Al_{0.16}Si_{0.84}$) collected at both room and elevated temperature. All data presented in Figure 5.5 is from library spl036. A sharp peak at 0.4 V on removal, associated with crystalline $Li_{15}Si_4$, dominates the elevated temperature curve

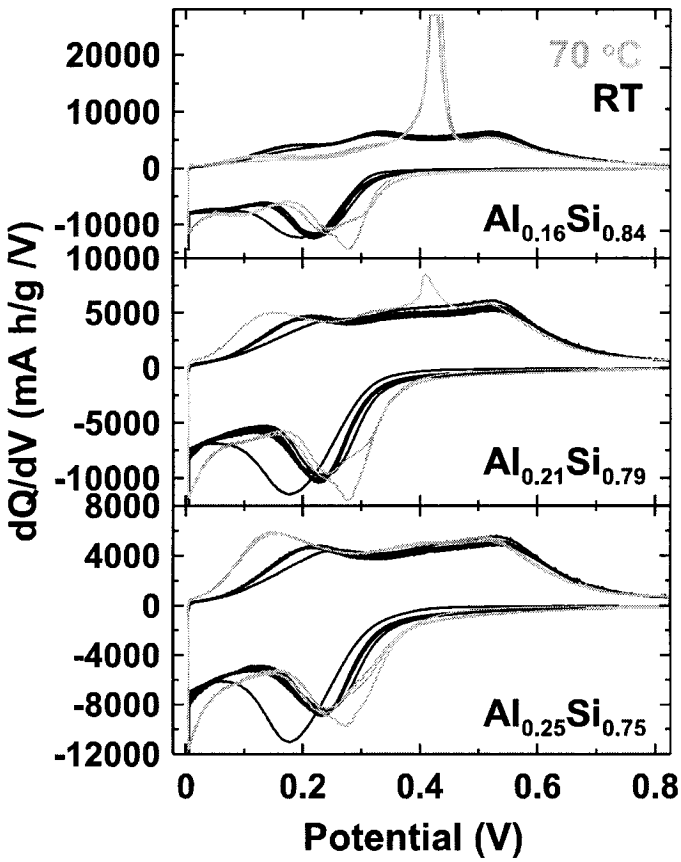

Figure 5.5: dQ/dV vs. V curves around 80 at. % Si. Grey and black curves were collected at 70 °C and room temperature, respectively. Compositions are indicated.

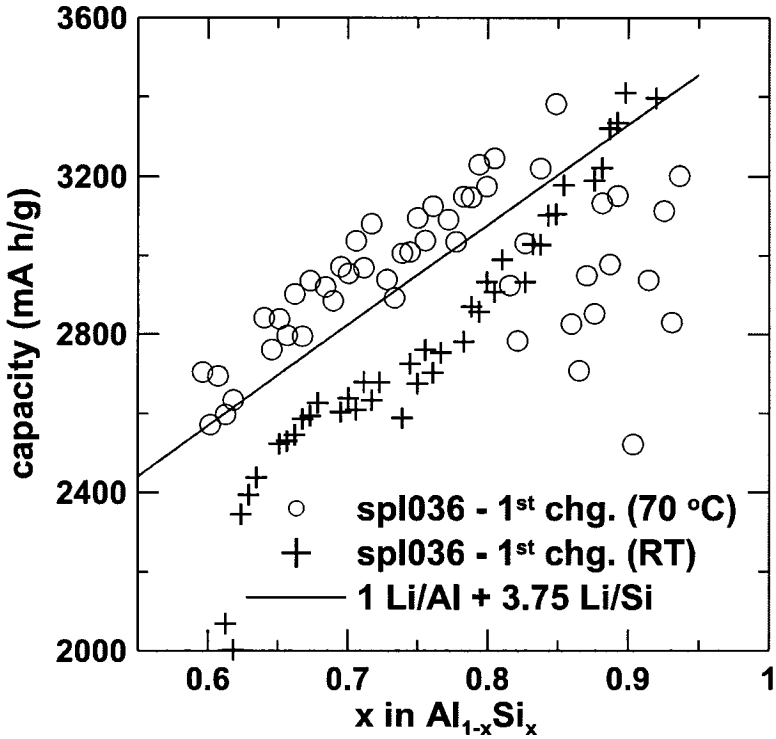

Figure 5.6: Capacity vs. composition for spl036 data set. Two cycling temperatures are shown, as well as the capacity predicted if 1 and 3.75 Li alloy with each Al and Si, respectively.

of $Al_{0.16}Si_{0.84}$. Only a small peak at 0.4 V on removal is present for the elevated temperature $Al_{0.21}Si_{0.79}$ data, and no peak is observed for $Al_{0.25}Si_{0.75}$. No sharp peaks are observed in any of the data collected at room temperature. This demonstrates the formation of crystalline $Li_{15}Si_4$ occurs only at elevated temperature and for compositions with more than 80 at. % Si.

The effect of cycling at elevated temperature on a wide range of compositions is shown in Figure 5.6. Two identical cell plates from sputtering run spl036 were cycled, one at room temperature and one at 70 °C. Cycling conditions were otherwise identical. Once again, a 'bend' is present near 80 at. % Si in the room temperature data. Capacities measured at 70 °C are hundreds of mA h/g higher than the room temperature results. The difference between the elevated temperature data and the simple model is quite small, on the order of 100 mA h/g or a few percent. The simple model of 1 Li/Al + 3.75 Li/Si may in fact be correct, although diffusion effects might play a role for certain compositions at room temperature. Room temperature capacities shown in Figure 5.6 appear higher, or at least more consistent, near 90 at. %

Si. Variation in the elevated temperature capacity data is related to the presence of crystalline $Li_{15}Si_4$. Obrovac and Christensen showed $Li_{15}Si_4$ crystallizes below 50 mV relative to Li. Although the combinatorial electrochemical cells are held at 5 mV for many hours, there is no guarantee crystalline $Li_{15}Si_4$ will form, especially at room temperature, because the electrodes are not at perfect equilibrium. Formation of $Li_{15}Si_4$ is more likely at higher temperatures because of the higher atom mobility. Removing all the inserted Li from crystalline $Li_{15}Si_4$ can be more difficult because of the uneven volume expansions, loss of electrical contact and loss of capacity associated with crystalline electrodes. The smooth drop in room temperature capacity data below 65 at. % Si will be discussed shortly.

The data presented in Figure 5.6 suggests $Li_{15}Si_4$ is more likely to crystallize at higher cycling temperature. Crystallization dynamics also depend on composition. As noted above, Radnoczi *et al.* [133] determined the crystallization temperature of Al-Si films varied from 200 to 600 °C over the range 86 to 98 at. % Si. These results were later confirmed by Konno *et al.* [132]. DSC results from library spk149 are shown in Figure 5.7. All DSC samples were swept from 50 to 550 °C after being held at 50 °C for 5 minutes. A second identical test was performed after the sample cooled to 50 °C. Data from the second test was subtracted from the first so that features associated with the pan, and not the sample, could be removed.

Konno *et al.* [132] attribute the first main DSC peak to the separation of Al and Si, and the second peak near 500 °C for compositions near 80 at. % Si to the secondary growth of Si nanocrystals. This is consistent with the earlier findings of Radnoczi *et al.* [133], who claimed Al crystal nucleation occurred before the metal induced crystallization of a-Si for compositions with less than 88 at. % Si. The relative ease with which Al and Si can be separated also gives support to the simple electrochemical model of separate reactions of Li with Al and Si. However, this model does not explain the capacity at 80 at. % Si.

The room temperature $Al_{0.16}Si_{0.84}$ data presented in Figure 5.5 is characteristic of amorphous Si (humps at 0.3 and 0.5 V on removal), with the exception of the hump at 0.2 V. This hump is clearly present in the other room temperature curves, as well as the $Al_{0.19}Si_{0.81}$ and $Al_{0.25}Si_{0.75}$ elevated temperature data (shifted to 0.15 V). The hump at 0.55 V on removal could be associated with the 0.5 V removal peak

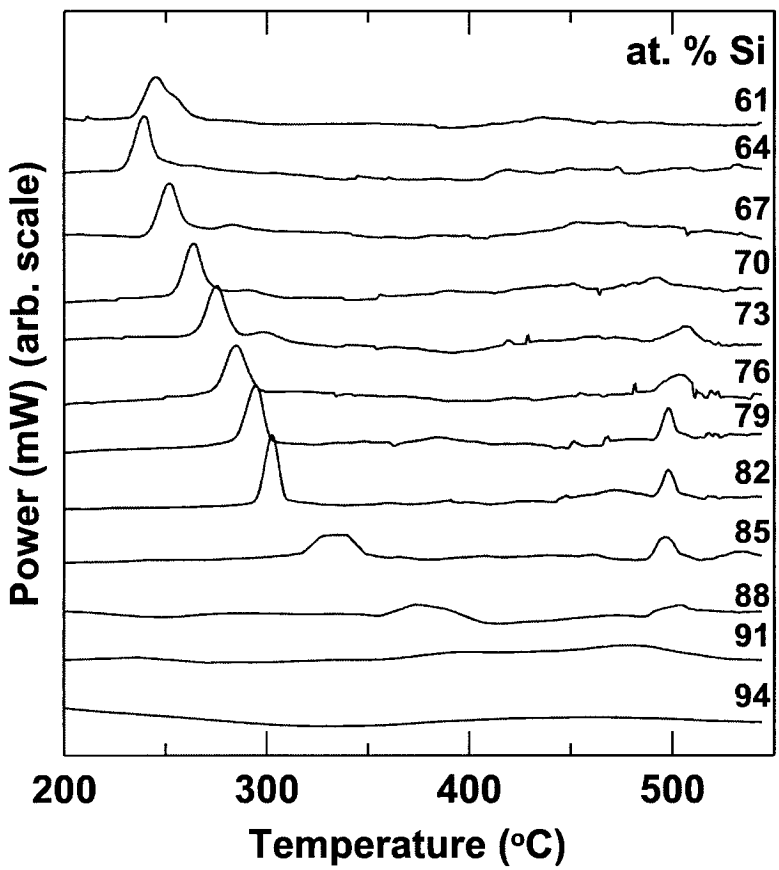

Figure 5.7: DSC curves of $Al_{1-x}Si_x$ ($61 < x < 94$). Atomic percent Si is indicated. Cycling parameters are listed in the text.

of Li from Al or Si, and does not therefore indicate the presence of a Al-Li-Si phase. However, the hump at 70 °C at 0.15 V on removal, when coupled with the observed capacity, can only be explained by the presence of $Li_{13}Si_4$ (equilibrium potential of 0.155 V) [140] or an unidentified Al-Li-Si phase. Although $Li_{13}Si_4$ could be used to justify the room temperature capacity (consider $Al_{0.2}Si_{0.8}$, $0.8 \cdot Li_{13}Si_4 + 0.2 \cdot AlLi = 2700$ mA h/g, close to observed), there is no reason for bend near 80 at. % Si. The dQ/dV vs. V curves do not change dramatically even though the capacity increases by up to 20 %; most of the extra capacity occurs at potentials below 0.1 V on insertion.

Figure 5.8 presents dQ/dV vs. V curves similar to those of Figure 5.5 for compositions with 20 to 70 at. % Si. All data is from library spk002, except the elevated temperature data at 20 and 30 at. % Si, which is from spk066. The hump at 0.15-0.2 V on removal is present at 70 at. % Si, but decreases in intensity with decreasing Si content and is no longer distinguishable at 20 at. % Si. The peak at 0.6 V on removal associated with AlLi appears near 60 at. % Si and increases in intensity as the Al content is increased. Curves from compositions between 20 and 50 at. % Si appear to be a combination of the unidentified phase and AlLi. Note the room temperature profile for $Al_{0.60}Si_{0.40}$ is essentially flat from 0.2 to 0.6 V on removal.

The grey curves in Figure 5.8 for compositions near 50 at. % Si appear smaller than the room temperature curves. The first three cycles of spk002 were performed at room temperature, followed by three cycles at 50 °C, and then two at 70 °C. Three cycles at room temperature were followed by two at 70 °C for the spk066 data. Some of the capacity fade can be associated with comparing the first and ninth cycle. However, capacity fade also seems to be associated with the relative area of an unexpected hump at 1.1 V on removal, which is present only in the elevated temperature data near 50 at. % Si. The data for $Al_{50}Si_{50}$ and $Al_{60}Si_{40}$ is shown again in Figure 5.9 as a function of cycle number (and cycling temperature). No hump is present for either composition for any of the three room temperature cycles (1-3). The hump at 1.05 V sharpens and shifts to higher potential during the three cycles performed at 50 °C. A sharp peak is present in both the 70 °C cycles (7-8).

The peak at 1.1 V corresponds to the removal of Li from a relatively stable compound, and is unexpected based on the known dQ/dV vs. V curves associated with

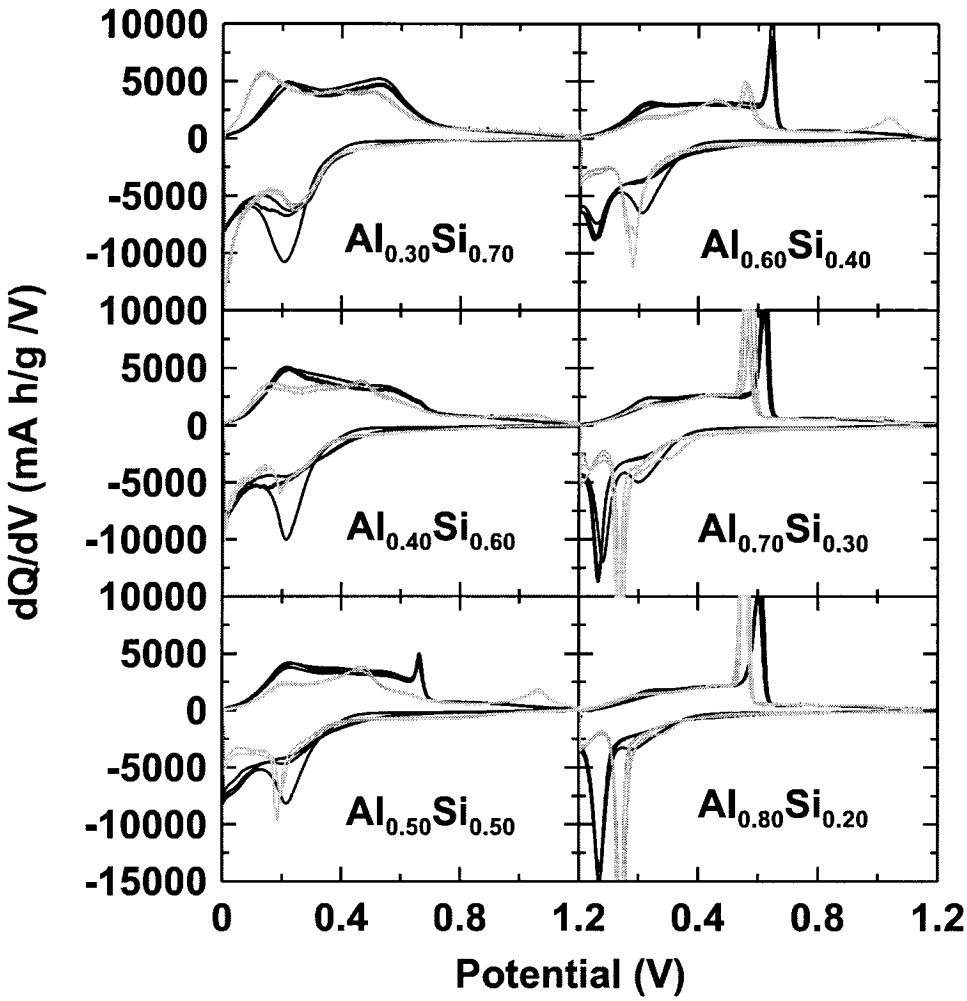

Figure 5.8: dQ/dV vs. V curves for compositions from 20 to 70 at. % Si. Grey and black curves were collected at 70 °C and room temperature, respectively. Compositions are indicated. See the text for cycle number / library information.

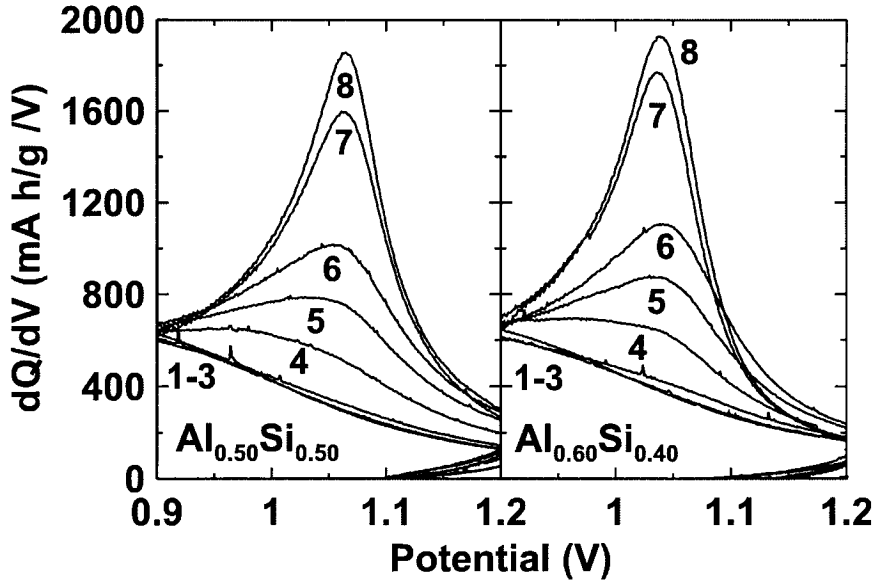

Figure 5.9: dQ/dV vs. V curves for $Al_{50}Si_{50}$ and $Al_{60}Si_{40}$. Numbers indicate cycle numbers. Cycles 1-3, 4-6 and 7-8 were cycled at room temperature, 50 °C and 70 °C, respectively.

LiAl and $Li_{15}Si_4$. A fourth phase (in addition to LiAl, $Li_{15}Si_4$ and the unidentified phase) likely forms at all temperatures, but dissociates only at elevated temperature (i.e. the dissociation is kinetically limited). Formation of this phase appears to be kinetically limited as well, as the features shown in Figure 5.9 grow with increasing cycle number. This phase is probably AlLiSi, based on both the Al-Li-Si equilibrium phase diagram and the composition (roughly 50 at. % Si), although $Al_3Li_7Si_4$ is also a possibility. A plot of charge capacity between 0.9 and 1.2 V is provided as Figure 5.10. Capacity increases over the room temperature data occur over the range of 20-70 at. % Si, but do not occur at Al- or Si- rich compositions. The largest capacity increases occur near 50 at. % Si. Precise identification of this fourth phase is not critical since the uneven volume changes (if dissociation proceeds) or irreversible capacity (if dissociation does not proceed) associated with either alloy would negatively impact the capacity retention.

Cycles 1-3 in both panels of Figure 5.9 appear to be stable. Figure 5.11 demonstrates capacity losses associated with AlLiSi appear only after multiple room temperature cycles. Differences in charge capacities with cycle number first appear between the 2^{nd} and 3^{rd} cycles. The 4^{th} charge capacity is up to 1000 mA h/g lower than the

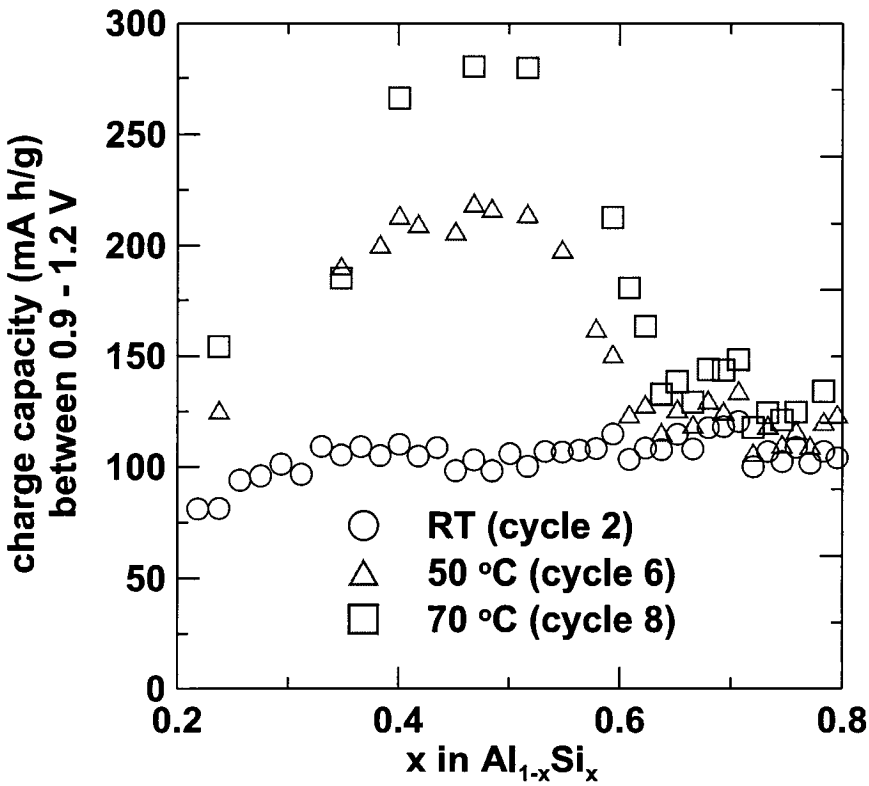

Figure 5.10: Charge capacity between 0.9-1.2 V as a function of cycle number / temperature for spk002 data set.

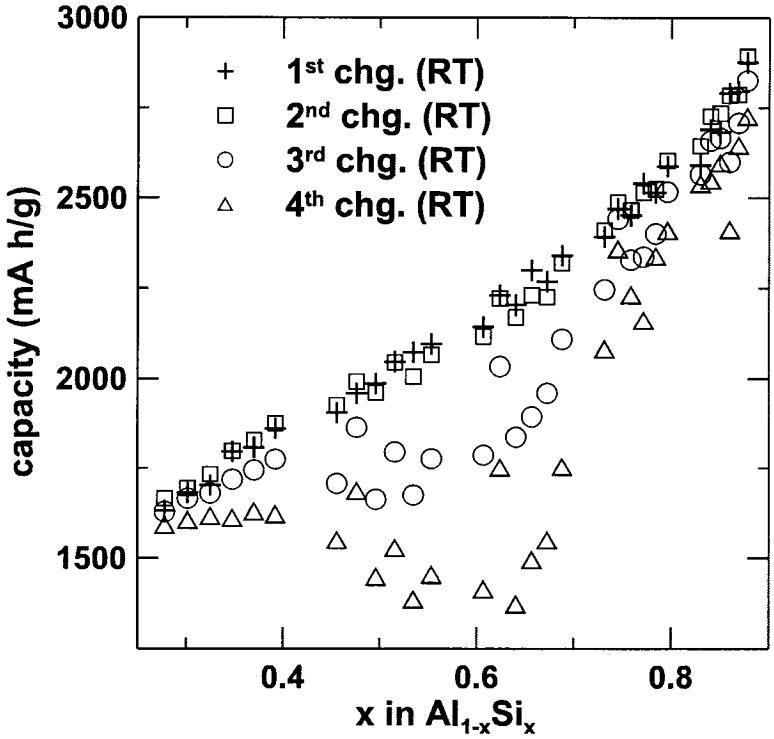

Figure 5.11: 1^{st}, 2^{nd}, 3^{rd} and 4^{th} charge capacity at room temperature (spk029).

1^{st} charge capacity for certain compositions near 60 at. % Si. Decreases in capacity are even more apparent when the 2^{nd}, 3^{rd} and 4^{th} charge capacities are plotted as a percentage of the 1^{st} charge capacity, as shown in Figure 5.12. The sputtered electrodes are metastable when deposited; the insertion and removal of large quantities of Li may allow for sufficient atom mobility for the production of equilibrium phases. Capacity fade in Figures 5.9 and 5.12 is centred about ca. 58 at. % Si, rather than 50 at. % Si as expected if AlLiSi was being formed. This may be because the so-called AlLiSi phase is actually $Al_3Li_7Si_4$, or because of small composition determination errors. Distinction between AlLiSi and $Al_3Li_7Si_4$ would be possible if all of the irreversible capacity could be associated with Li consumption by a known amount of this phase. However, the amount of the fourth phase (AlLiSi or $Al_3Li_7Si_4$) is not known, nor is the impact of this fourth phase on the other active phases. For reasons of simplicity the fourth phase will be identified as the AlLiSi phase although this may not be strictly correct. In-situ XRD experiments on sputtered Al-Si powder (produced using the method described in Section C.1.3) would probably allow for a proper identification.

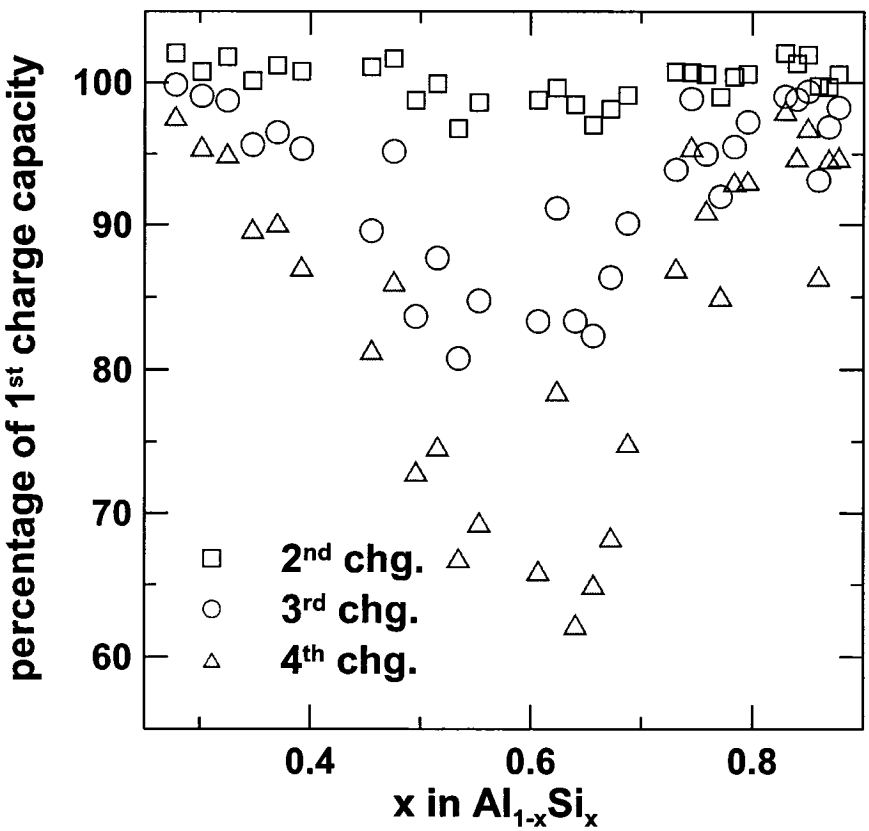

Figure 5.12: Data shown in Figure 5.11 as a percentage of 1^{st} charge capacity.

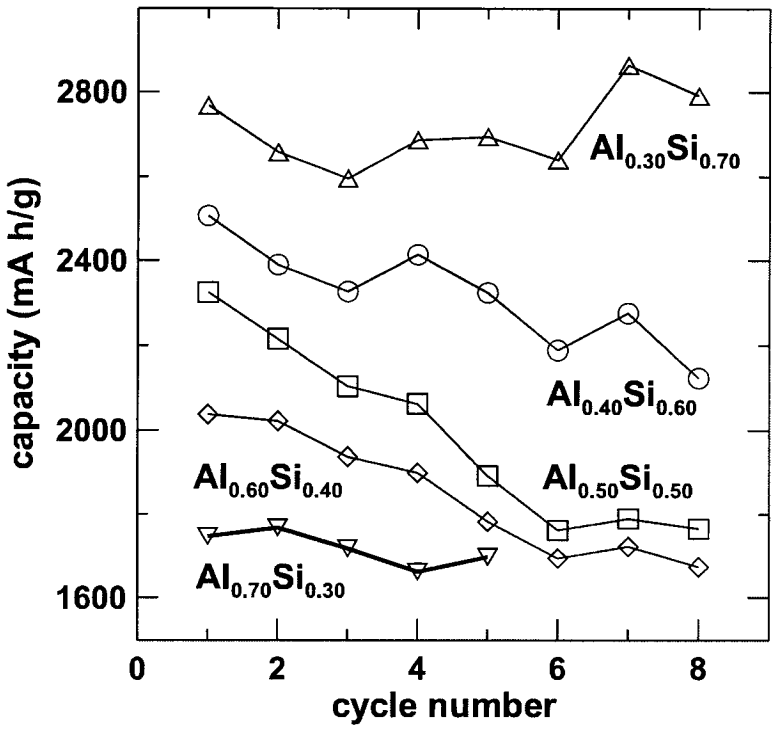

Figure 5.13: Capacity retention of various Al-Si alloys at various temperatures. Cycles 1-3 were performed at room temperature. Cycles 4-6 and 7-8 were performed at 50 and 70 °C for all compositions except $Al_{0.30}Si_{0.70}$, where cycles 4-5 were performed at 70 °C.

It has been demonstrated that Li associated with the AlLiSi phase can be removed at high temperature and high potential. The obvious question is then: can capacity 'lost' to the AlLiSi phase at room temperature be recovered by cycling at elevated temperature? Figure 5.13 presents charge capacity as a function of cycle number (and therefore cycling temperature) for five different compositions of Al-Si. Once again, cycles 1-3 were performed at room temperature. Cycles 4-6 and 7-8 were performed at 50 and 70 °C (library spk002), except for $Al_{0.70}Si_{0.30}$, where cycles 4-5 were performed at 70 °C (library spk066). The capacity of both $Al_{0.30}Si_{0.70}$ and $Al_{0.70}Si_{0.30}$ is essentially constant with cycle number, which is to be expected since the electrochemistry of both compositions is dominated by the presence of the unknown phase and AlLi, respectively. Some capacity fade is present in the $Al_{0.40}Si_{0.60}$ and $Al_{0.60}Si_{0.40}$ data. It is interesting to note capacity increases occur for $Al_{0.40}Si_{0.60}$ at the onset of each temperature increase (cycles 4 and 7), but the increased capacity is lower than the first charge capacity and decreases with subsequent cycles at the

Atom	position	x	y	z	occ. (%)
Si(1)	4a	0	3/4	1/8	100
Si(2)	4b	0	1/4	3/8	50
Al/Li(3)	16f	0.2377	0	0	12/88
Li(4)	8e	0	1/4	0.123	54

Table 5.2: Atomic positions for $Al_2Li_{18}Si_6$ as determined by Spina *et al.* [137].

new, higher, temperature. $Al_{0.50}Si_{0.50}$ and $Al_{0.60}Si_{0.40}$ experience an almost constant capacity fade from cycles 1-6, followed by a plateau during cycles 7-8. The net result is that there has been no clear demonstration that capacity 'lost' to the AlLiSi phase at room temperature can be recovered by elevated temperature cycling. This may be related to the uneven volume changes occuring in a multiple active phase electrode.

AlLiSi is the only ternary Al-Li-Si phase agreed upon in the literature ([135–137]). AlLiSi apparently forms after a few room temperature cycles, and can be pulled apart at elevated temperatures and high potential. It is clear, however, that the AlLiSi phase does not play a large role in the first few cycles, and cannot be used to explain the hump in dQ/dV vs. V curves at 0.15 V during Li removal or the bend in room temperature capacity data near 80 at. % Si. Other possible Al-Li-Si phases should thus be considered. Kevorkov *et al.* claimed $Al_{2.1}Li_{5.3}Si_2$ and $Al_3Li_8Si_5$, in addition to AlLiSi, to be the equilibrium ternary phases at 250 °C [136]. All three phases have approximately similar amounts of Al and Si, and therefore cannot be used to explain a feature most present near $Al_{0.20}Si_{0.80}$. The $Al_3Li_7Si_4$ phase claimed by Spina *et al.* [137] can be dismissed for the same reason. $Li_{15}Al_3Si_6$ is closer to the desired ratio of Si to Al, but the capacity is too low (1610 mA h/g vs. 2200 mA h/g for $Al_{0.33}Si_{0.66}$). $Al_2Li_{18}Si_6$ is the only reported Al-Li-Si phase with approximately correct Si:Al stoichiometry and capacity (2200 mA h/g vs. 2400 mA h/g for $Al_{0.25}Si_{0.75}$).

A plot of charge capacity between 0.005-0.3 V as a function of composition and cycling temperature is provided as Figure 5.14. The capacity over this potential range increases until 75-80 at. % Si, and then drops off sharply as the Si content increases. This plot, along with the data shown in Figure 5.5, provides strong evidence for a phase near 80 at. % Si. Atomic positions for $Al_2Li_{18}Si_6$ as determined by Spina *et al.* [137] are listed in Table 5.2. The occupancies listed in Table 5.2 are not all simple fractions because the actual sample composition is in fact $Al_{1.92}Li_{18.4}Si_{6.03}$ [137]. The

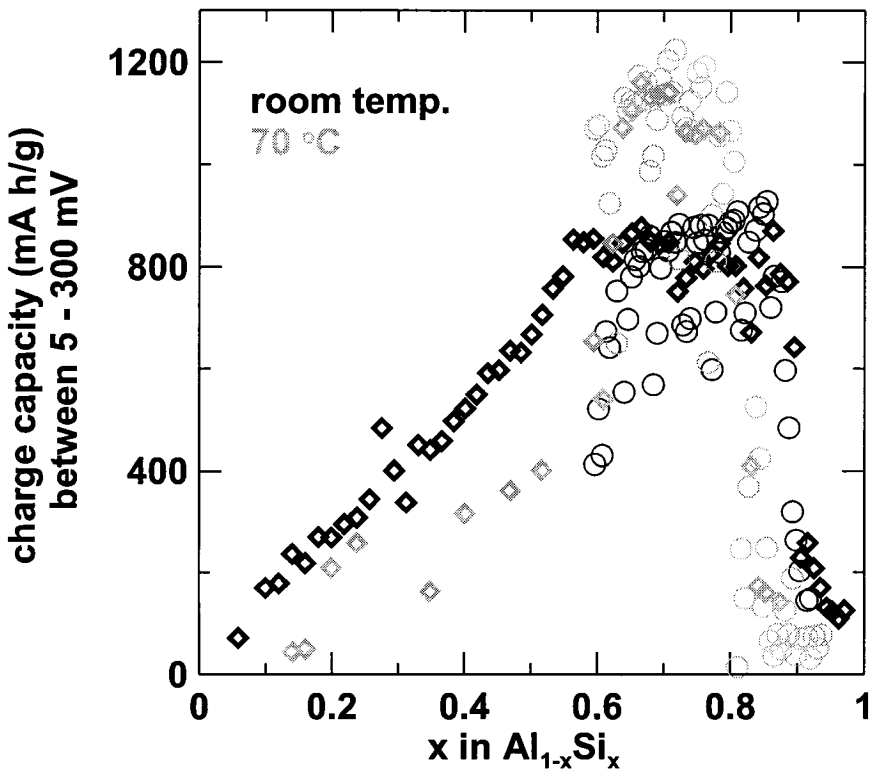

Figure 5.14: Charge capacity between 0.005-0.3 V as a function of composition for spk002 data set.

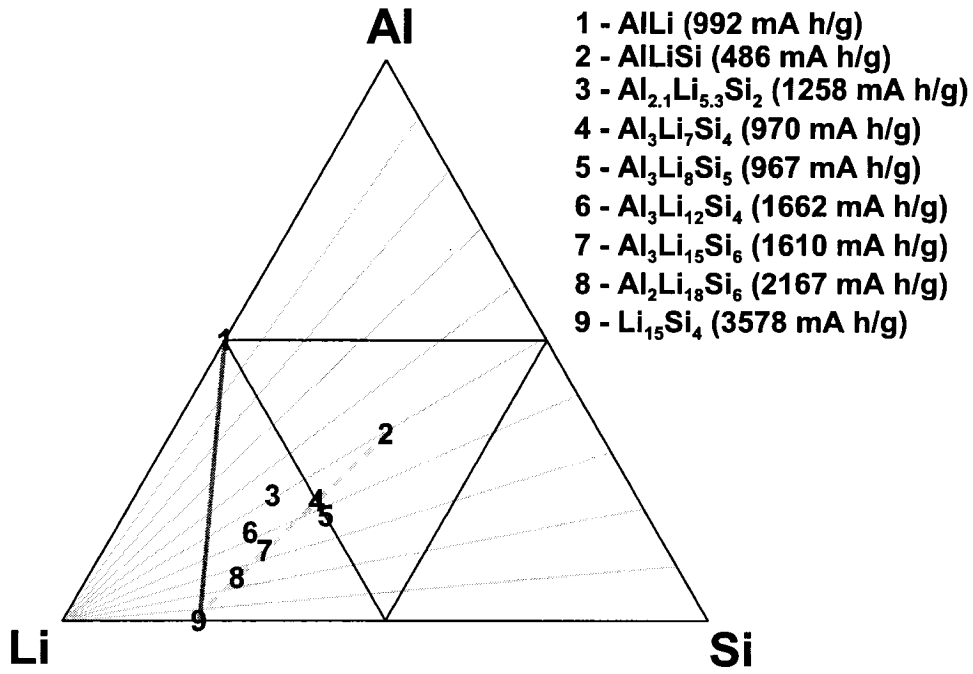

Figure 5.15: All reported Al-Li-Si ternary phases reported in the literature [135–137]. A solid line indicates the capacity expected if each Al and Si reacted with 1 and 3.75 Li, respectively. The dashed line indicates neutral compositions if charge transfer occurs between the atoms as in Zintl type phases [141] and Al, Li and Si have charges of +3, +1 and -4, respectively.

two Si sites are fully and exactly half filled. Some Li/Al substitution is possible in the third site (16f), and the dedicated Li site is only partially filled.

Precise identification of the unknown phase would be difficult for a number of reasons. None of the dQ/dV vs. V curves in Figures 5.5 and 5.8 show a sharp peak at 0.15 V, which means $Al_2Li_{18}Si_6$ is nanocrystalline or amorphous. Studies on equilibrium alloys would be complicated by the relatively low Li melting temperature of Li (180 °C). The identification of the unknown phase as $Al_2Li_{18}Si_6$ must therefore be treated with some scepticism although it fits the existing data well. All phases identified by Spina *et al.* ([137], the most recent paper on Al-Li-Si phases) can be considered neutral if there is strong charge transfer between the components as is found in Zintl type phases (e.g. [141]) and each Al, Li and Si has a charge of +3, +1 and -4, respectively. Spina *et al.* [137] note charge transfer from Al to Si is possible. Figure 5.15 presents a plot of all reported Al-Li-Si ternary phases. A thick solid line indicates the capacity expected if each Al and Si reacted with 1 and 3.75 Li,

respectively. The dashed line indicates neutral compositions if charge transfer occurs between the atoms as in Zintl type phases [141] and Al, Li and Si have charges of +3, +1 and -4, respectively. Note $Li_{15}Si_4$ does not lie along the dashed line, although it is not far from it. No evidence connected to phases 3 ($Al_{2.1}Li_{5.3}Si_2$), 5 ($Al_3Li_8Si_5$), 6 ($Al_3Li_{12}Si_4$) and 7 ($Al_3Li_{15}Si_6$) has been observed, so these phases can probably be ignored. There is substantial evidence for the existence of either phase 2 (AlLiSi) or 4 ($Al_3Li_7Si_4$), and phase 8 ($Al_2Li_{18}Si_6$). Phases 1 (AlLi) and 9 ($Li_{15}Si_4$) are clearly observed.

The complicated electrochemistry of the Al-Si system is surprising, and may have contributed to the lack of published accounts. The presence, or lack thereof, of the AlLiSi phase in the lithiated Si-Al-M systems will likely have a large impact on the suitability of these alloys systems for commercial application. Kinetic limitations may once again play a role. Details of the Si-Al-M (M = Cr, Fe, Mn, Ni) system will now be presented.

Chapter 6

Si-Al-M (M = Cr, Fe, Mn, Ni)

Discussion of the Si-M and Al-M systems in Chapters 3 and 4 was focused on the electrochemical activity of various equilibrium and metastable phases. This approach was not as applicable to the Al-Si system, since no binary Al-Si equilibrium phases exist and the proper identification of ternary Al-Li-Si phases is ongoing. Broad features in dQ/dV vs. V curves made active phase identification impossible in some cases.

Equilibrium phase diagrams for the Si-Al-Cr, Si-Al-Fe, Si-Al-Mn and Si-Al-Ni systems are presented in Figures 6.1, 6.2, 6.3, and 6.4, respectively. Binary phase diagrams of Al-M and Si-M are available in Figures 4.1 and 3.1, respectively. Equilibrium ternary phases of Si-Al-M according to Pearson's Handbook of Crystallographic Data for Intermetallic Phases (1991) [39] are labeled with circles; phases according to the more recent review papers [142–145] are labeled with triangles. Si-Al-Ni is the only system without conflicting reports; no paper on the Si-Al-Cr system not included in the Pearson data set was available.

The only trend apparent from Figures 6.1, 6.2, 6.3, and 6.4 is that equilibrium ternary phases of Si-Al-M tend to contain more than 15-20 at. % M at high Al contents, and less than 50 at. % Si. Note almost no capacity was observed over these regions for the Al-M and Si-M systems. Previous work by the author [83] is the only published account describing the electrochemistry of the Si-Al-M system[1], and prompted the additional investigations described in this thesis. Figure 1.3 illustrates the room temperature capacity of the Si-Al-Mn system. Lines of constant capacity are roughly parallel with the Al-Si axis up until about 60 at. % Si, at which point they bend towards the Si-M axis. Sputtering runs used to characterize the Si-Al-M system are summarized in Table 6.1. The purpose of the first two runs was to investigate

[1] A significant amount of work on various Si-Al-M alloys was performed by Leif Christensen, Mark Obrovac, and Robert Turner of 3M Co. (Woodbury, MN USA), but was not published. Some details of their work are available in U.S. Patent Application 20050031957 and U.S. Patent 6,699,336 [146].

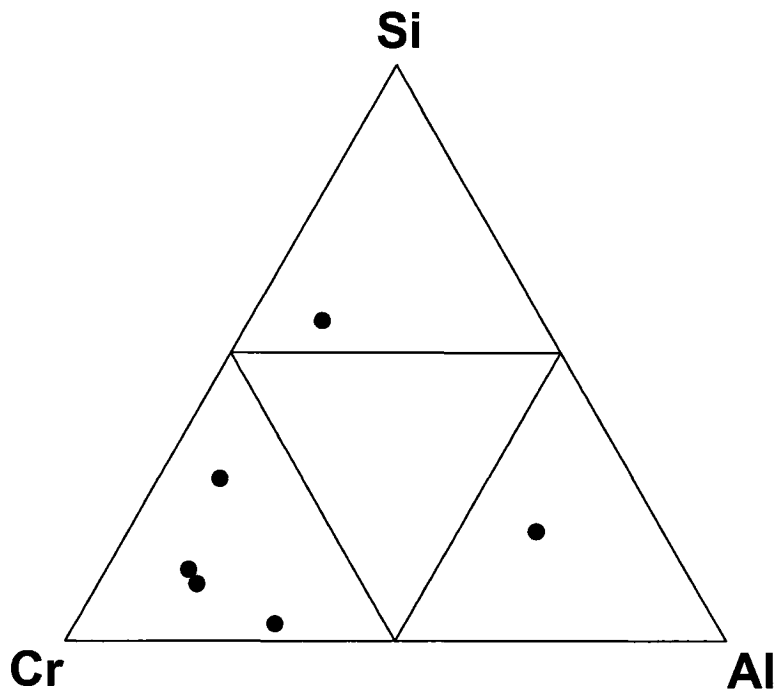

Figure 6.1: Al-Cr-Si equilibrium phases according to [39].

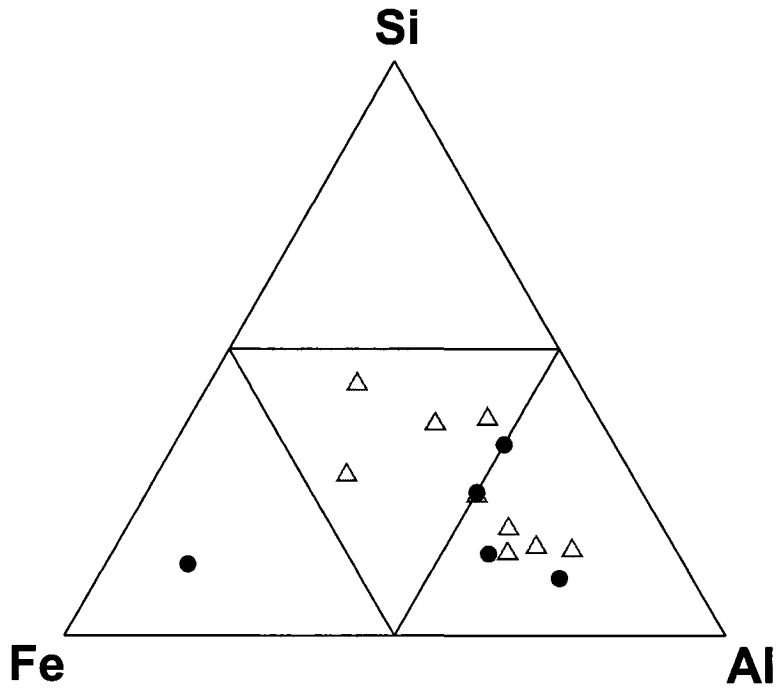

Figure 6.2: Al-Fe-Si equilibrium phases according to [39] (circles) and [142] (triangles).

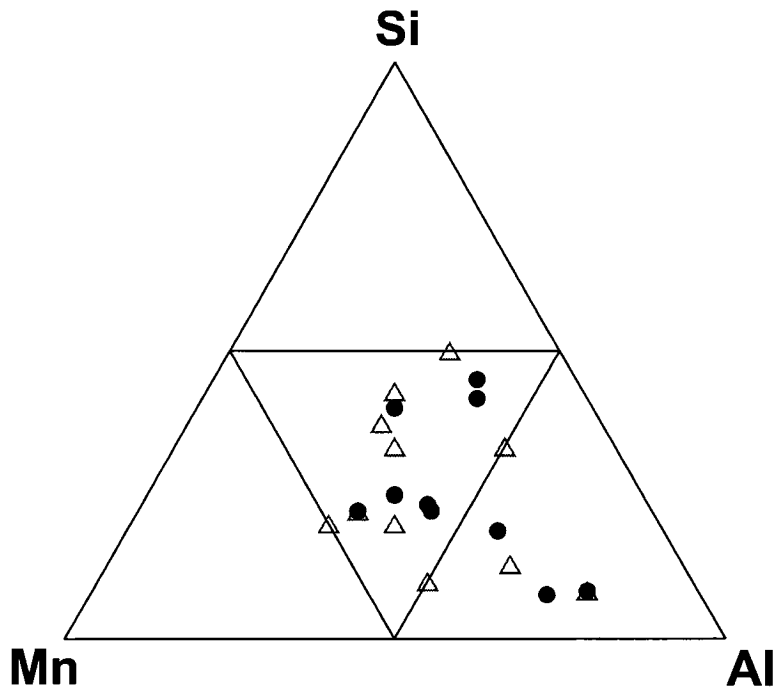

Figure 6.3: Al-Mn-Si equilibrium phases according to [39] (circles) and [143] (triangles).

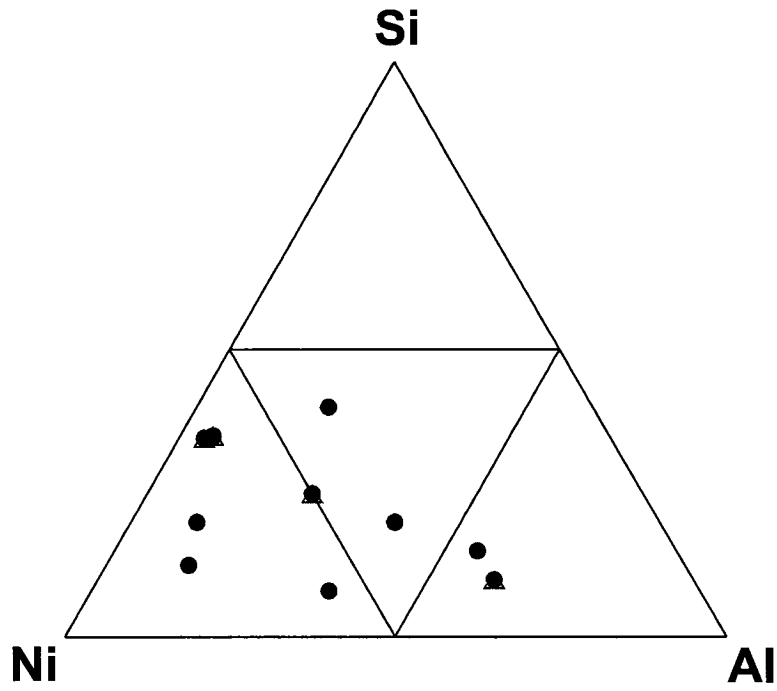

Figure 6.4: Al-Ni-Si equilibrium phases according to [39] (circles) and [144, 145] (triangles).

run label	system	at. % M	thickness (μm)	power (W) Al	Si	M	sweep rate (mV/s)
spk091	$(Al_{0.73}Si_{0.27})_{1-x}Fe_x$	$0 \leq x \leq 20$	1.1-1.6	80	60	21	0.0276
spl025	$(Al_{0.31}Si_{0.69})_{1-x}Fe_x$	$0 \leq x \leq 23$	1.1-1.3	34	140	34	0.0185
spl036	$Si_{1-x-y}Al_xFe_y$	$0 \leq y \leq 32$	0.6-1.2	80	202-7	30	0.0185
spl066	$Si_{1-x-y}Al_xCr_y$	$0 \leq y \leq 34$	0.9-1.4	83	202-7	31	0.0185
spl080	$Si_{1-x-y}Al_xMn_y$	$0 \leq y \leq 41$	0.8-1.2	83	202-7	34	0.0185
spl083	$Si_{1-x-y}Al_xNi_y$	$0 \leq y \leq 42$	0.7-1.3	83	202-7	30	0.0185

Table 6.1: Brief summary of Si-Al-M sputtering runs. The range of x for all ternary runs was approximately from 0 to 1.

compositions before and after the bend in constant capacity. Binary cell plates were used to study the impact of Fe addition on a fixed ratio of Si:Al. Ternary cell plates were used for the remaining four runs, with the intent of evenly spanning the Si-Al composition range out to approximately 35 at. % M. Al and all transition metals were deposited using a DC power supply. Deposition powers are listed in Table 6.1. Si was deposited using a DC power supply for the two binary runs and an RF power supply for the four ternary runs. Si deposition powers listed as 202-7 refer to forward and reflected powers of 202 and 7 W, respectively. Target purity / fabrication method was as described in Sections 3 and 4. Thin film libraries were deposited on electrochemical cell plates, Cu foil, Si wafers and Cu disks for all six runs. All cells cycled at 0.0185 mV/s were held at 1.2 V and 5 mV for 1 and 12 hours, respectively. Cells cycled at 0.0276 mV/s were held at 1.2 V and 5 mV for 1 and 4 hours, respectively. Additional Si-Al-Mn runs are described in the author's M. Sc. thesis [91].

6.1 Si-Al-Fe Binary Runs

Figure 6.5 indicates the range of compositions tested for the two binary Si-Al-Fe sputtering runs (spk091 and spl025). Fe was chosen as a representative transition metal for consistency with the Si-M and Al-M chapters.

XRD patterns for the spk091 library are presented in Figure 6.6. XRD patterns indicate the presence of nanocrystalline Al only at low Fe content. No evidence of any of the Si-Al-Fe ternary intermetallic phases with ca. 16 at. % Fe (eg. $Al_5Fe_2Si_5$, $Al_8Fe_2Si_9$, $Al_9Fe_2Si_1$ [39] or $Al_{2.7}Fe_1Si_{2.3}$, $Al_{4.5}Fe_1Si_1$ [142]) is visible.

Figure 6.7 presents the 1^{st}, 5^{th} and 6^{th} charge capacity of $(Al_{0.73}Si_{0.27})_{1-x}Fe_x$ as

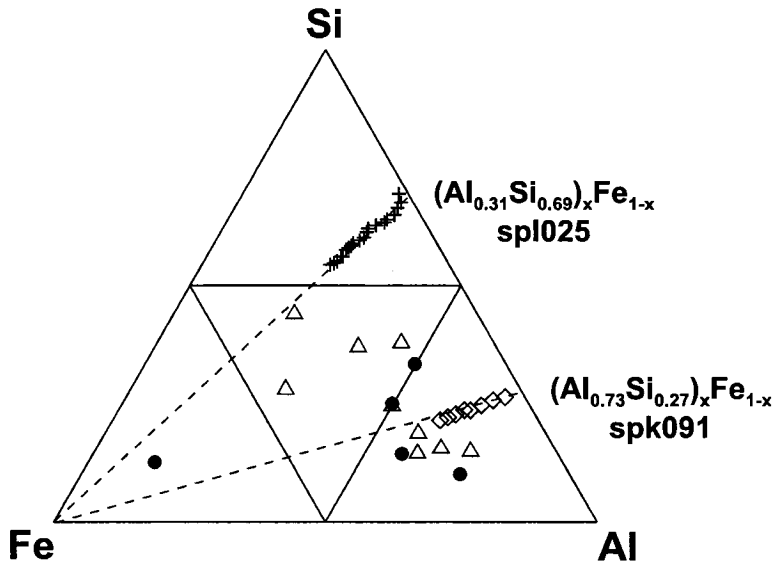

Figure 6.5: Crosses and diamonds indicate the range of compositions tested for spl025 and spk091, respectively. The dashed lines are guides to the eye. Ternary Si-Al-Fe phases are reproduced from Figure 6.2.

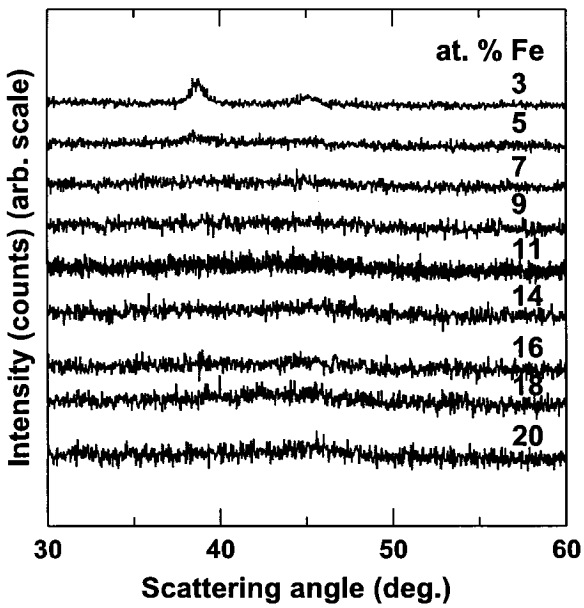

Figure 6.6: XRD patterns for $(Al_{0.73}Si_{0.27})_{1-x}Fe_x$ $(0 \leq x \leq 0.2)$ (spk091). Numbers indicate at. % Fe.

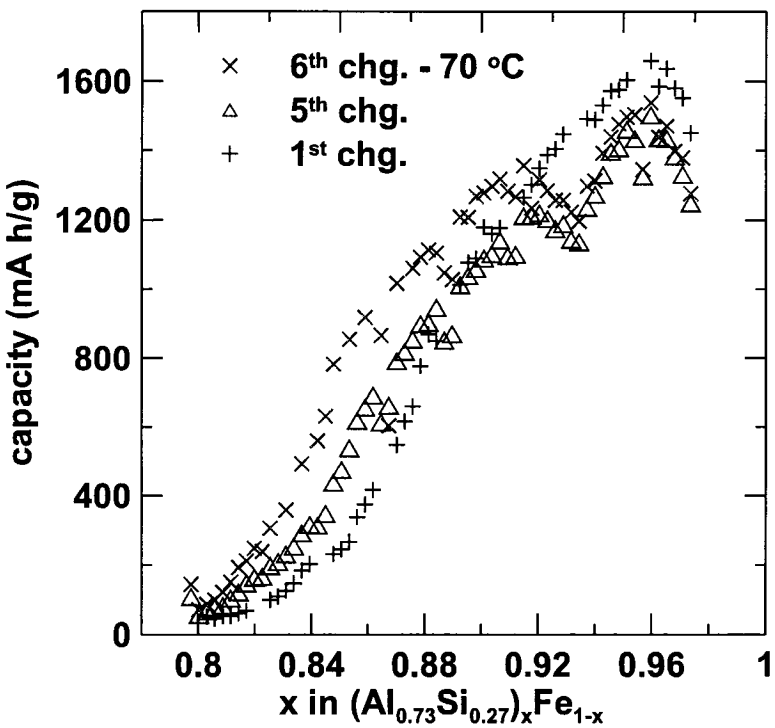

Figure 6.7: Charge capacity (mA h/g) vs. x for $(Al_{0.73}Si_{0.27})_{1-x}Fe_x$ $(0 \leq x \leq 0.2)$ (spk091).

a function of composition. Cycles 1-5 and 6-8 were performed at room temperature and 70 °C, respectively. The first charge capacity drops off rapidly from 1600 mA h/g for $(Al_{0.73}Si_{0.27})_{0.95}Fe_{0.05}$ to zero at $(Al_{0.73}Si_{0.27})_{0.8}Fe_{0.2}$. The first charge capacity appears to be roughly linear over the range 4-10 at. % Fe, followed by steep and then shallow decreases over the ranges 10-14 and 14-20 at. % Fe. By the fifth cycle the room temperature capacity has increased over these two ranges, reminiscent of Al-M data. A sharp capacity decrease has also developed at 7 at. % Fe. Cycling at 70 °C increased the capacity most near 14 at. % Fe, but did not extend the range of active compositions beyond 20 at. % Fe. Each of these features (capacity decrease at 7 at. % Fe, increased capacity at 14 at. % Fe, inactive by 20 at. % Fe) warrants further discussion.

Selected dQ/dV vs. V plots collected at both room temperature and 70 °C from the spk091 library are presented in Figure 6.8. The peak at 0.6 V attributed to the removal of Li from Al is only visible in curves with less than 10 at. % Fe. dQ/dV vs. V curves with 10 at. % Fe or more are of a similar shape to those of amorphous Si in an inactive matrix (see $Si_{0.6}Fe_{0.4}$ in Figure 3.7), although the 70 °C peak is at 0.2,

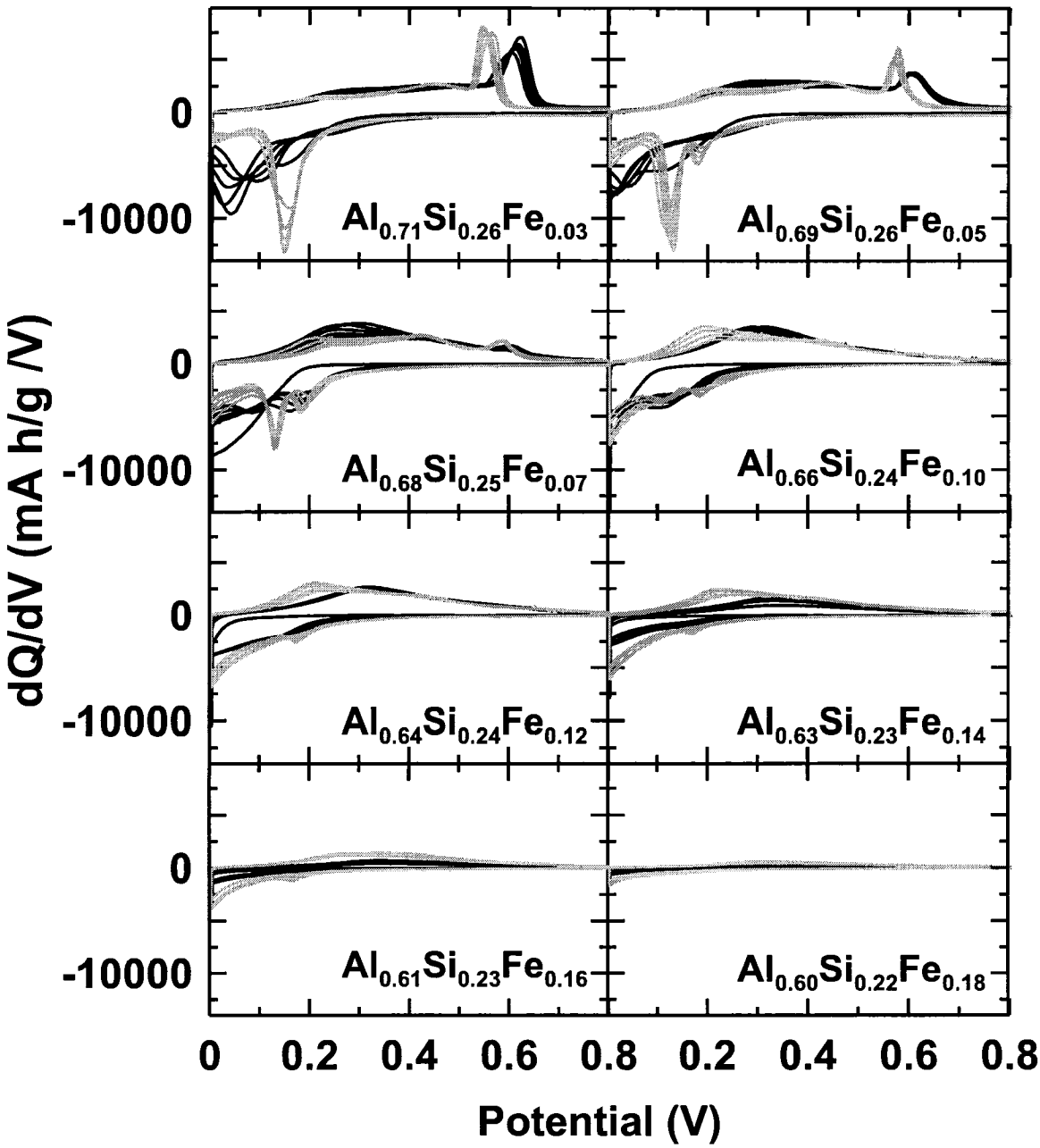

Figure 6.8: dQ/dV vs. V curves for various compositions of spk091. Black and grey curves were collected at room temperature (cycles 1-5) and 70 °C (cycles 6-8), respectively. Compositions are indicated.

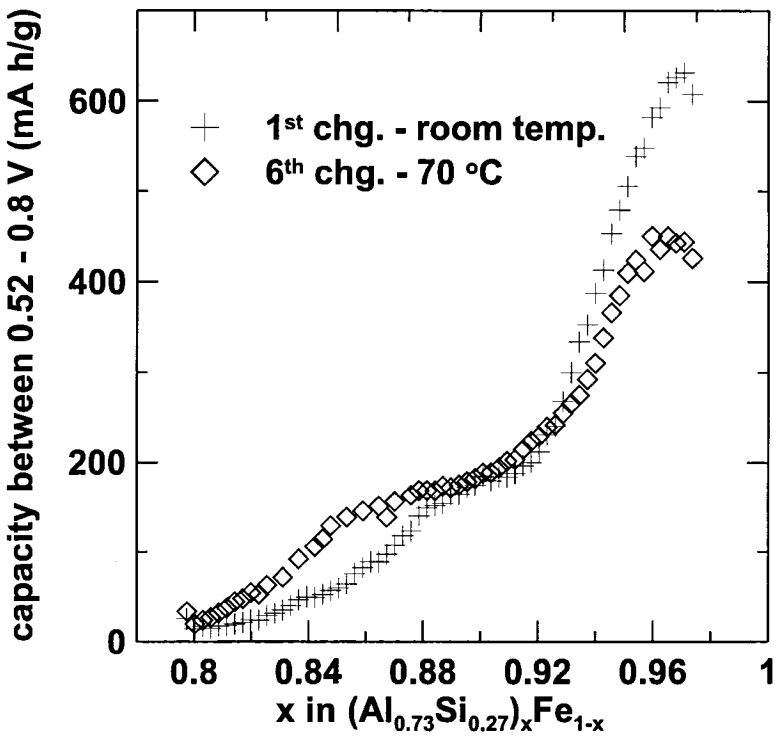

Figure 6.9: Charge capacity between 0.52-0.8 V for $(Al_{0.73}Si_{0.27})_{1-x}Fe_x$ $(0 \leq x \leq 0.2)$ (spk091).

rather than 0.3, V. No changes in peak location were observed in any of the elevated temperature Si-M studies, so these curves can not be attributed to the capacity of a-Si. In addition, if all the capacity at 15 at. % Fe were attributed to Si, the rapid decrease in capacity (800 mA h/g over 5 at. % Fe) could not be explained by the established Si-M model presented in Chapter 3. The 70 °C peak at 0.2 V seems to fade faster than the overall capacity above 10 at. % Fe and is difficult to distinguish above 14 at. % Fe. Transitions appear to occur at 7 and 14 at. % Fe (capacity fade and increased rate of capacity loss with increasing transition metal content, respectively), although the nature of the transition, and whether it can be attributed to Si-M, Al-M, or Si-Al-M interactions, is unclear.

Plots of capacity over limited potential regions will again be used to attempt to separate features in dQ/dV vs V plots. The charge capacity of $(Al_{0.73}Si_{0.27})_{1-x}Fe_x$ between 0.52-0.8 V is presented in Figure 6.9. Three regions are present in both the room temperature and 70 °C data. The rapid decrease in capacity up to 8 at. % Fe can be associated with the removal of Li from AlLi, which disappears at 8 at. %

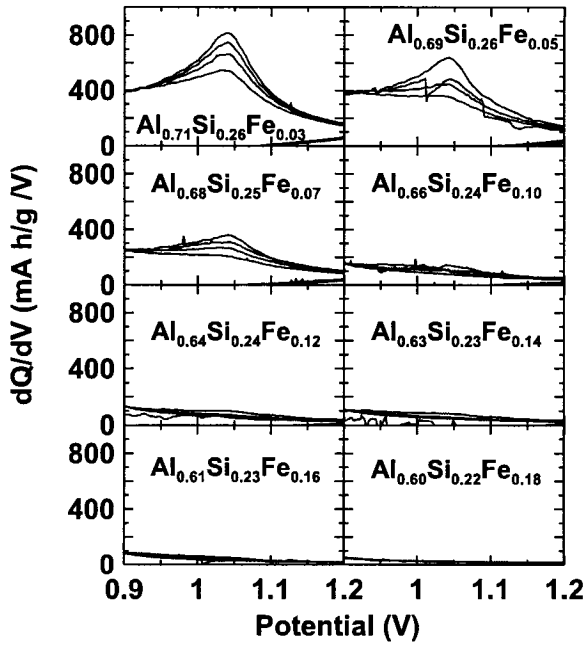

Figure 6.10: dQ/dV vs. V curves for various compositions of spk091 collected at 70 °C showing the dissociation of the AlLiSi phase. Compositions are indicated.

Fe. Regions with slowly decreasing capacity (8-12 at. % Fe at room temperature, 8-15 at. % Fe at 70 °C) and a sharper decrease (12-20 and 15-20 at. % Fe for room temperature and 70 °C, respectively) follow. Although this is similar to features in the overall capacity (shown in Figure 6.7) and the activity of Al-M alloys with ca. 5-10 at. % M, the physical origin of these two regions is not known.

The high potential features shown in Figure 6.10 can be attributed to the dissociation of the AlLiSi phase. The AlLiSi phase dissociates over a range of 20-70 at. % Si in the Al-Si system so the presence of these features at a Si:Al ratio of 27:73 is not unexpected. The peak at 1.1 V grows with increasing cycle number but decreases in intensity with increasing Fe content. Charge capacities between 0.9-1.2 V shown in Figure 6.11 indicate the dissociation of the AlLiSi phase does not occur above 8 at. % Fe. The formation of the AlLiSi phase was associated with capacity fade in the Al-Si system and can be used to explain the decreased capacity at 7 at. % Si shown in Figure 6.7. It is interesting to note the (formation and) dissociation of the AlLiSi phase and the removal of Li from AlLi occur over the same range of compositions. The reason why both reactions only take place out to 8 at. % Fe, when all Si-Al-Fe ternary intermetallic phases have at least 15 at. % Fe, is unclear. Based on Figure

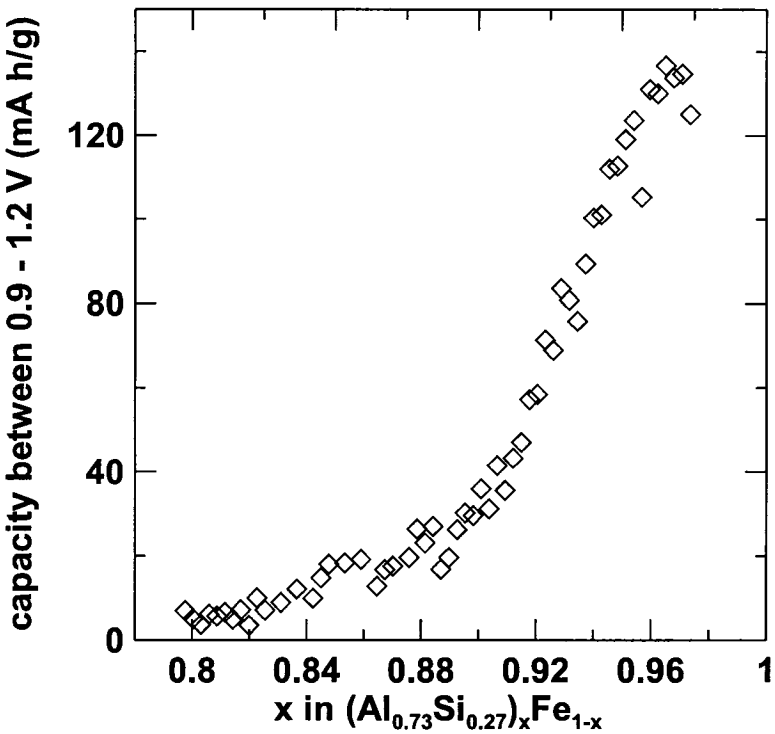

Figure 6.11: 6^{th} charge capacity between 0.9-1.2 V for the spk091 data set.

6.5, $(Al_{0.73}Si_{0.27})_{0.85}Fe_{0.15}$ should be composed of two Si-Al-Fe ternary phases, Al, and Si. No evidence of active Al or Si at this composition is available, which means the Si-M and Al-M models developed in Chapters 3 and 4 cannot be applied.

Library spl025 samples an entirely different composition range than library spk091, as shown in Figure 6.5. No Al-Fe-Si ternary intermetallic phases are in close proximity - $Al_2Fe_3Si_4$ has a similar Si:Al ratio but 10 at. % more Fe than the highest Fe content composition of spl025. XRD patterns shown in Figure 6.12 indicate no crystalline phases in the as-deposited film.

Figure 6.13 presents the first charge capacity of $(Al_{0.31}Si_{0.69})_{1-x}Fe_x$ as a function of composition at room temperature and 70 °C. Separate cells were cycled at room temperature and 70 °C so the effect of composition and cycle number could be separated. Capacities from the cell cycled at 70 °C were about 250 and 500 mA h/g higher than from the room temperature cell for compositions with less and more than 20 at. % Fe, respectively. Capacity decreases are roughly linear over the two regions (above and below 20 at. % Fe). It should be noted additional features in the capacity vs. composition plot may be present at higher Fe contents than were tested, although the

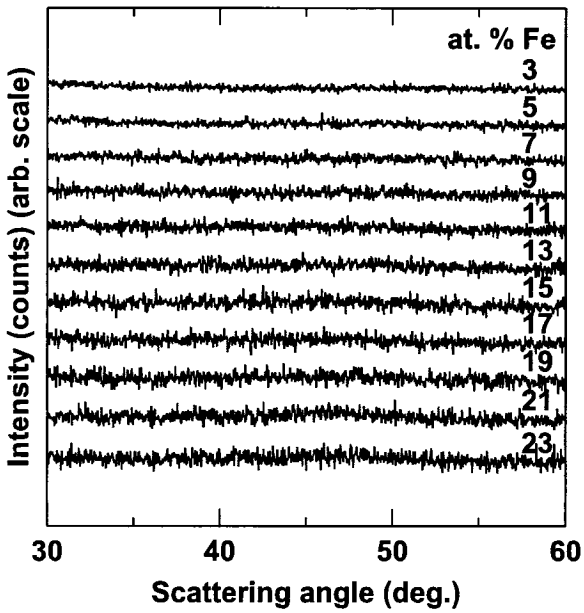

Figure 6.12: XRD patterns for $(Al_{0.31}Si_{0.69})_{1-x}Fe_x$ $(0 \leq x \leq 0.23)$ (spl025). Numbers indicate at. % Fe.

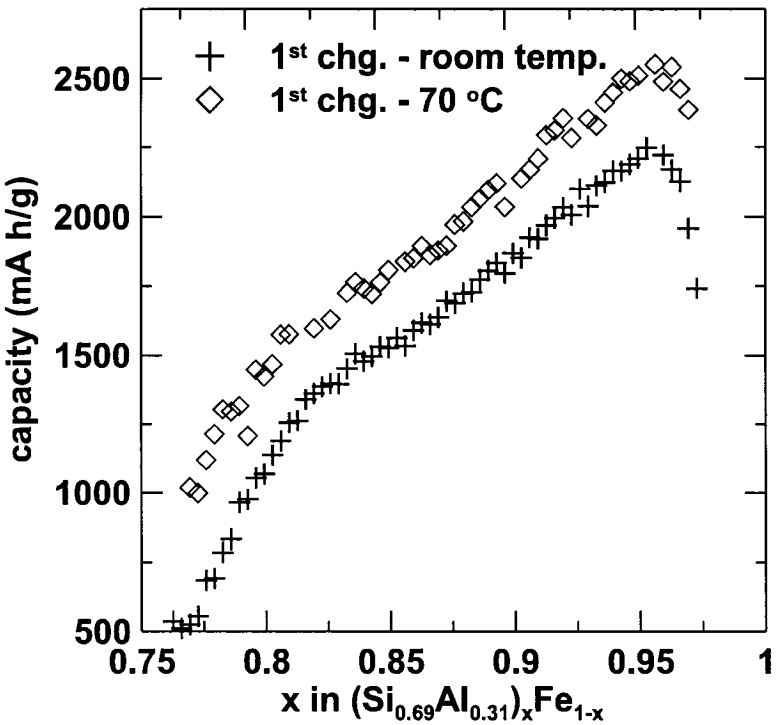

Figure 6.13: Capacity (mA h/g) vs. x for $(Al_{0.31}Si_{0.69})_{1-x}Fe_x$ $(0 \leq x \leq 0.25)$ (spl025).

slope of the 70 °C data at high Fe content suggests compositions with approximately 30 at. % Fe would be inactive (which is very close to the Fe content of $Al_2Fe_3Si_4$).

dQ/dV vs. V curves of various compositions of $(Al_{0.31}Si_{0.69})_{1-x}Fe_x$ collected at room temperature and 70 °C are provided in Figure 6.14. The hump at 0.15 V on removal at 70 °C, presumably associated with $Al_2Li_{18}Si_6$, is clearly present to at least 12 at. % Fe. A plot of capacity between 0.005 and 0.3 V has the same shape as Figure 6.13 and is therefore not shown. dQ/dV vs. V plots from compositions of $(Al_{0.31}Si_{0.69})_{1-x}Fe_x$ with higher Fe content are difficult to characterize based on the shape of the removal curve. Changes in the shape of dQ/dV vs. V curves with composition during Li insertion are suggestive of a-Si in an inactive matrix (eg. see Figure 3.6), but this cannot be confirmed during Li removal. Differences between the shape of the first and subsequent insertion curves are not yet understood.

Once again the shape of dQ/dV vs. V curves at high Fe content cannot be explained based on results from the Si-M or Al-M systems. Features assumed to be associated with $Al_2Li_{18}Si_6$ are clearly present for compositions with low Fe content, but cannot be used to explain features in the plot of capacity as a function of composition. Results from all four (Si/Al)-Fe binary systems (Al_0Si_1, $Al_{0.31}Si_{0.69}$, $Al_{0.73}Si_{0.27}$ and $Al_{100}Si_0$) are summarized in Figure 6.15. Three regions of capacity vs composition are present in the Al-Fe and $(Al_{0.73}Si_{0.27})$-Fe data, but do not have the same physical origin since features characteristic of the removal of Li from AlLi do not appear for $(Al_{0.73}Si_{0.27})$-Fe beyond 8 at. % Fe. $(Al_{0.73}Si_{0.27})$-Fe data beyond 15 at. % Fe appears to decrease in a manner similar to the Al-Fe room temperature data above 8 at. % Fe. Increased Al-Fe capacities over this region were achieved by increasing the cycling temperature; cycling at 70 °C may not provide enough mobility to surpass kinetic barriers. The nearly uniform capacity increase with increased cycling temperature found in $(Al_{0.31}Si_{0.69})$-Fe can be attributed to capacity changes with temperature for $Al_{0.31}Si_{0.69}$. It is possible to envision a model where each transition metal deactivated a certain amount of $Al_{0.31}Si_{0.69}$, similar to the situation for Si-Fe (one Fe deactivates one Si because of the growth of SiFe nanocrystals at the expense of amorphous Si). However, the increased rate of capacity loss with increasing Fe content above 20 at. % Fe could not be explained by this simple model. Active grain boundary arguments such as that found in Chapter 4 would also fail because of the pronounced changes

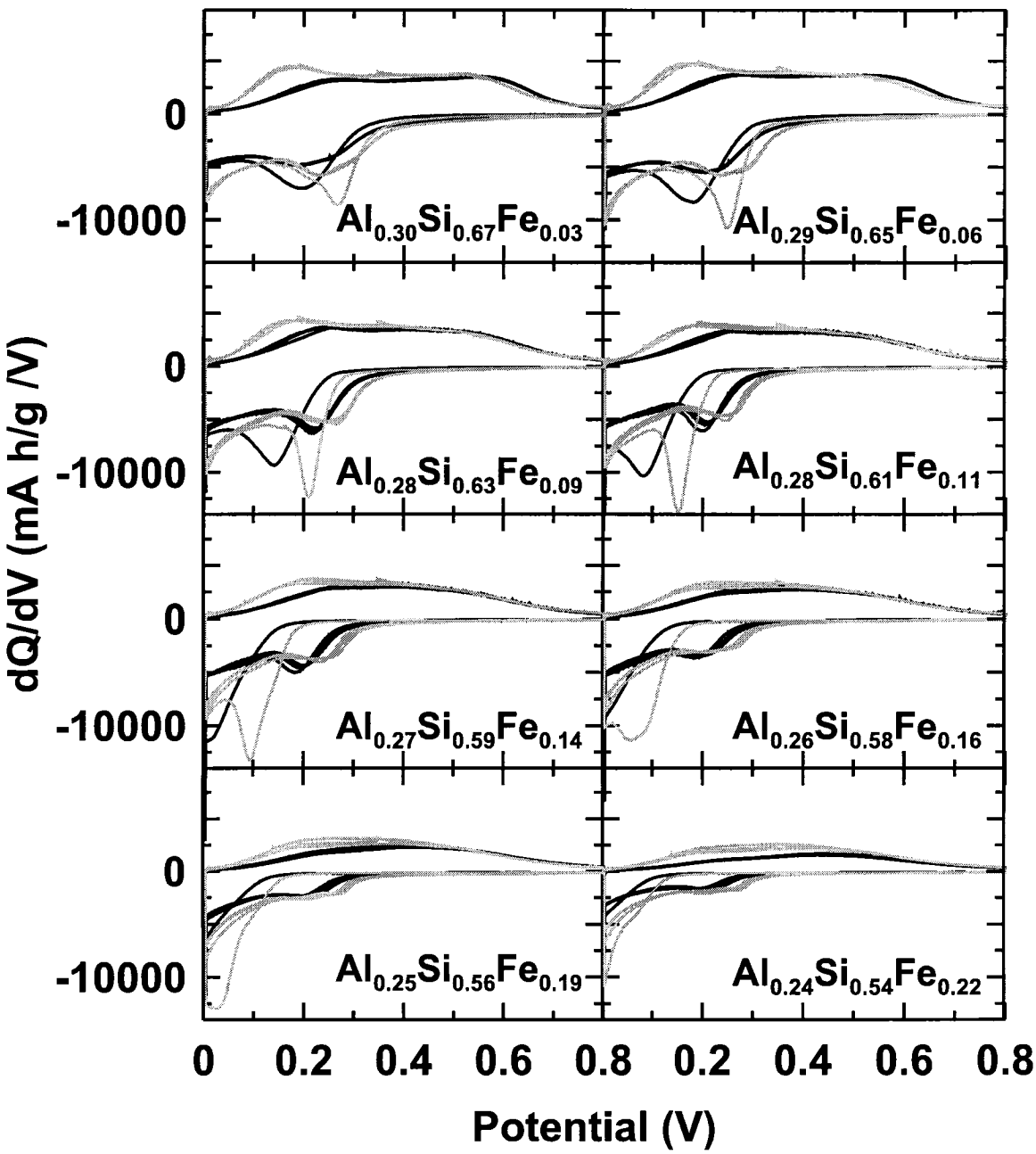

Figure 6.14: dQ/dV vs. V curves for various compositions of spl025. Black and grey curves were collected at room temperature and 70 °C, respectively. Compositions are indicated.

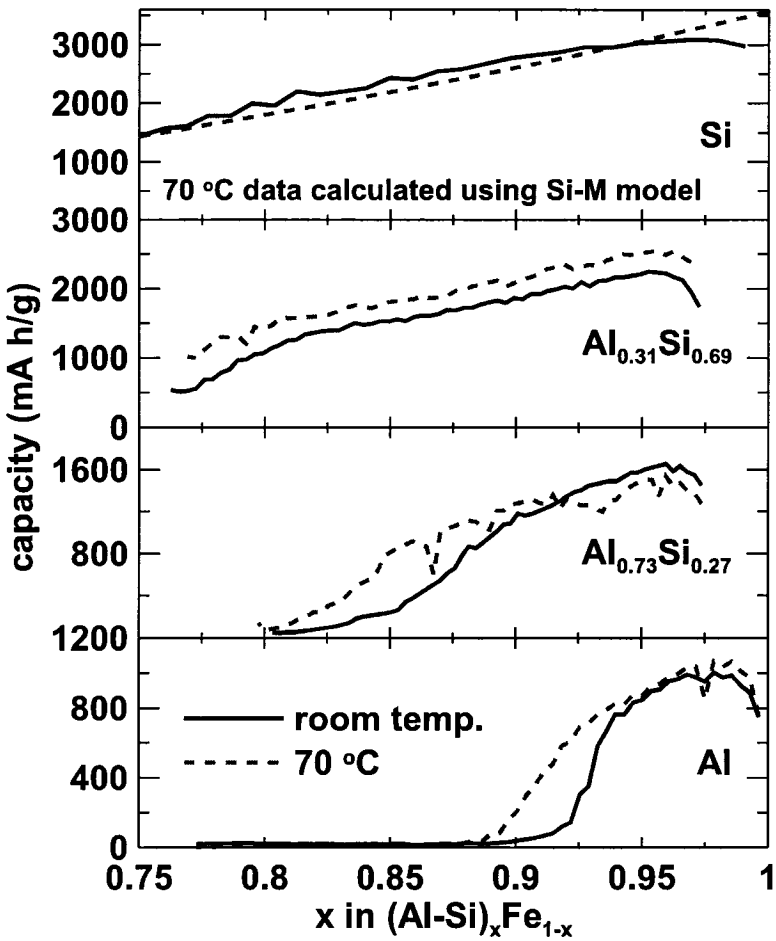

Figure 6.15: Capacity as a function of Fe content spanning the range of Si:Al. The relative ratio of Si:Al is provided.

in dQ/dV vs. V curves above 20 at. % Fe.

Mössbauer effect measurements could be used in attempts to identify the phases in the as-deposited film. *In-situ* XRD on single compositions of Si-Al-Fe could also be used to associate features in dQ/dV vs. V curves with the appearance / disappearance of various phases.

Although dQ/dV vs. V curves with more than 10-20 at. % Fe could not be associated with a known reaction, they are characteristic of an electrode material that starts and remains amorphous during cycling. Capacities along the $(Al_{0.31}Si_{0.69})$-Fe line are also quite high (1000 mA h/g at room temperature for $(Al_{0.31}Si_{0.69})_{0.8}Fe_{0.2}$), and there is no evidence for the formation of the AlLiSi phase. Results from large composition ranges of the Si-Al-M (M = Cr, Fe, Mn, Ni) will now be presented.

6.2 Si-Al-M (M = Cr, Fe, Mn, Ni) Ternary Runs

One ternary run for each of the four values of M is listed in Table 6.1. Each run spanned approximately the same composition range. XRD patterns from Si-Al-Fe, typical of all values of M, are provided in Figure 6.16. Fe content, and the background counts associated with Fe fluorescence, increases from right to left. Si (Al) content increases (decreases) from bottom to top. The composition represented by each panel can be determined by comparing panel number with the compositions of the first and last columns in the 10 x 10 grid shown in Figure 6.17. Additional numbers / compositions were not indicated for the sake of clarity. Compositions along rows can be determined by interpolating between the end members. There are no sharp diffraction peaks in the data of Figure 6.16. Some evidence of crystalline / nanocrystalline phases may have been expected, especially at the high Al / low Fe corner (i.e. panel 10). The lack of crystalline Al can be understood by recalling the range of crystalline Al extended from 0-8 at. % Fe along the Al-M axis and from 0-40 at. % Si along the Al-Si axis. The composition of panel 10 ($Al_{0.85}Fe_{0.08}Si_{0.06}$) is not within this range. Evidence for nanocrystalline SiFe is lacking because of the composition range (the composition of panel 91 is $Al_{0.05}Fe_{0.22}Si_{0.73}$), the signal to noise ratio (low), and the broadness of the expected peak ($Si_{0.70}Fe_{0.30}$ has a FWHM of approximately 8°, as shown in Figure 3.2).

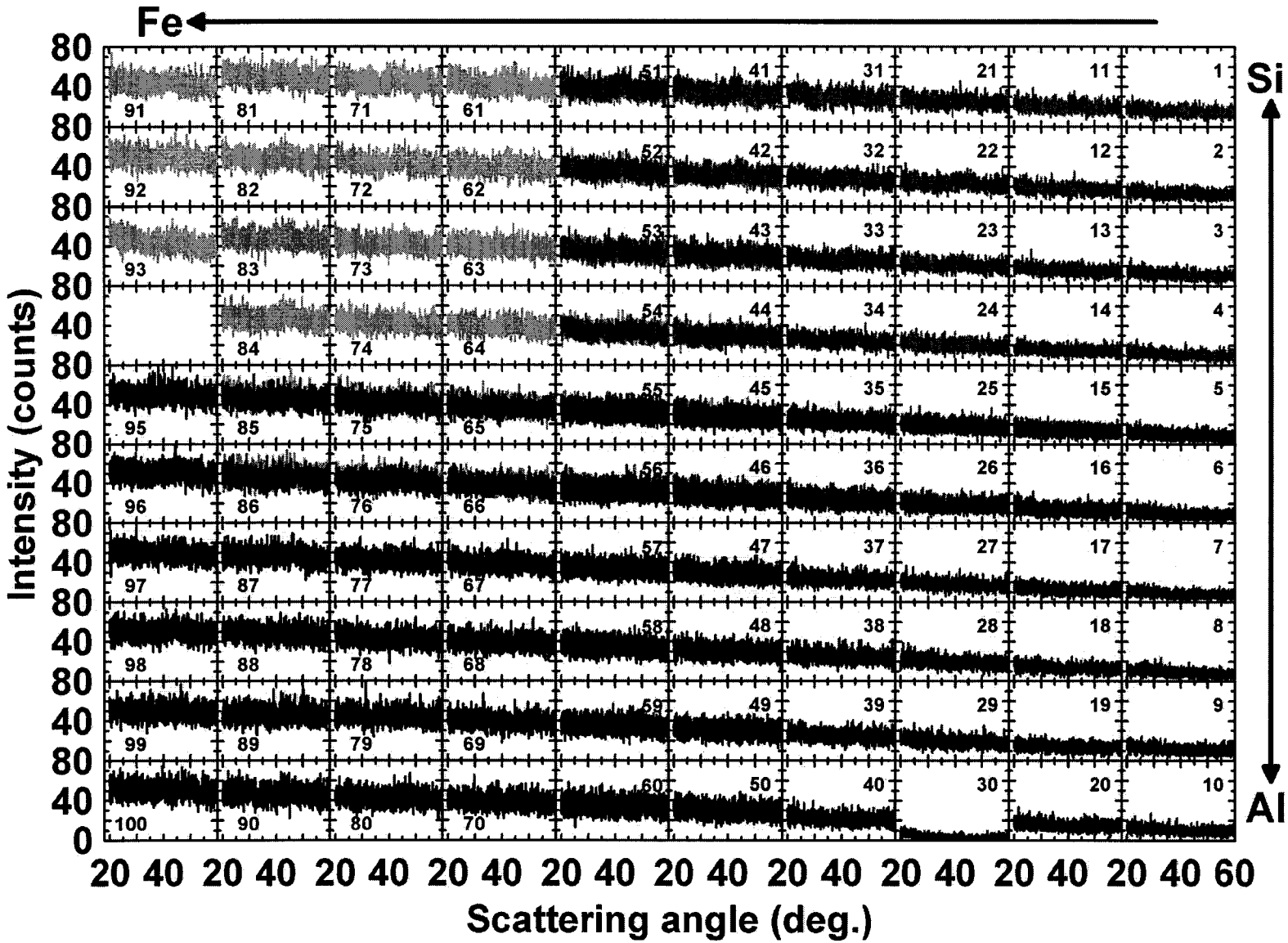

Figure 6.16: XRD patterns from Si-Al-Fe (spl036). Fe content increases from right to left. Compositions can be estimated from the numbers in Figure 6.17.

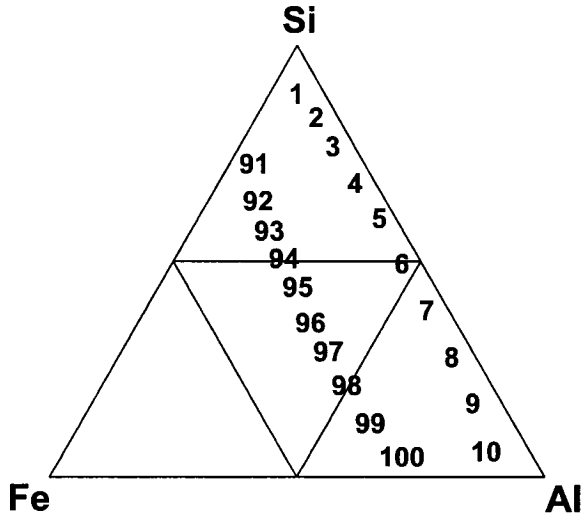

Figure 6.17: High and low Fe-content edges of spl036 composition range. Numbers correspond to those of Figure 6.16.

Contour plots of charge capacity (mA h/g) as a function of composition are provided for the Si-Al-Cr, Si-Al-Fe, Si-Al-Mn and Si-Al-Ni systems at room temperature and 70 °C as Figures 6.18, 6.19, 6.20, and 6.21, and 6.22, 6.23, 6.24, and 6.25, respectively. Separate cells were cycled at room temperature and 70 °C for each value of M. Solid circles are used to indicate compositions tested throughout this series of figures. Contour plots were produced using Surfer 7 (Golden Software Inc., Golden CO USA) using the default Kriging method. Sharp curves between neighbouring dots should be attributed to artifacts of the contour plot method rather than data trends. Curves far outside of the range of dots should be ignored.

Summarizing the data in Figures 6.18 to 6.25 is a daunting task. Capacities along the Si-M, Al-M, and Al-Si axes are as expected from the respective binary systems. Cycling temperature has a relatively minor effect on contour position because of the small changes at a given composition (ca. 200 mA h/g) relative to the highest capacities observed (ca. 3000 mA h/g). Bends in lines of constant capacity occur at a Si:Al ratio of approximately 2:1. The onset of capacity fade with increasing transition metal content first occurs for Fe, then at roughly the same composition for Mn and Cr. A similar trend is present in the Al-M data. No rapid capacity fade is observed for Si-Al-Ni. Compositions of Si-Al-Fe are first to reach negligible capacity at a fixed ratio of Si:Al, followed by Mn and Cr at roughly the same composition, and then, by

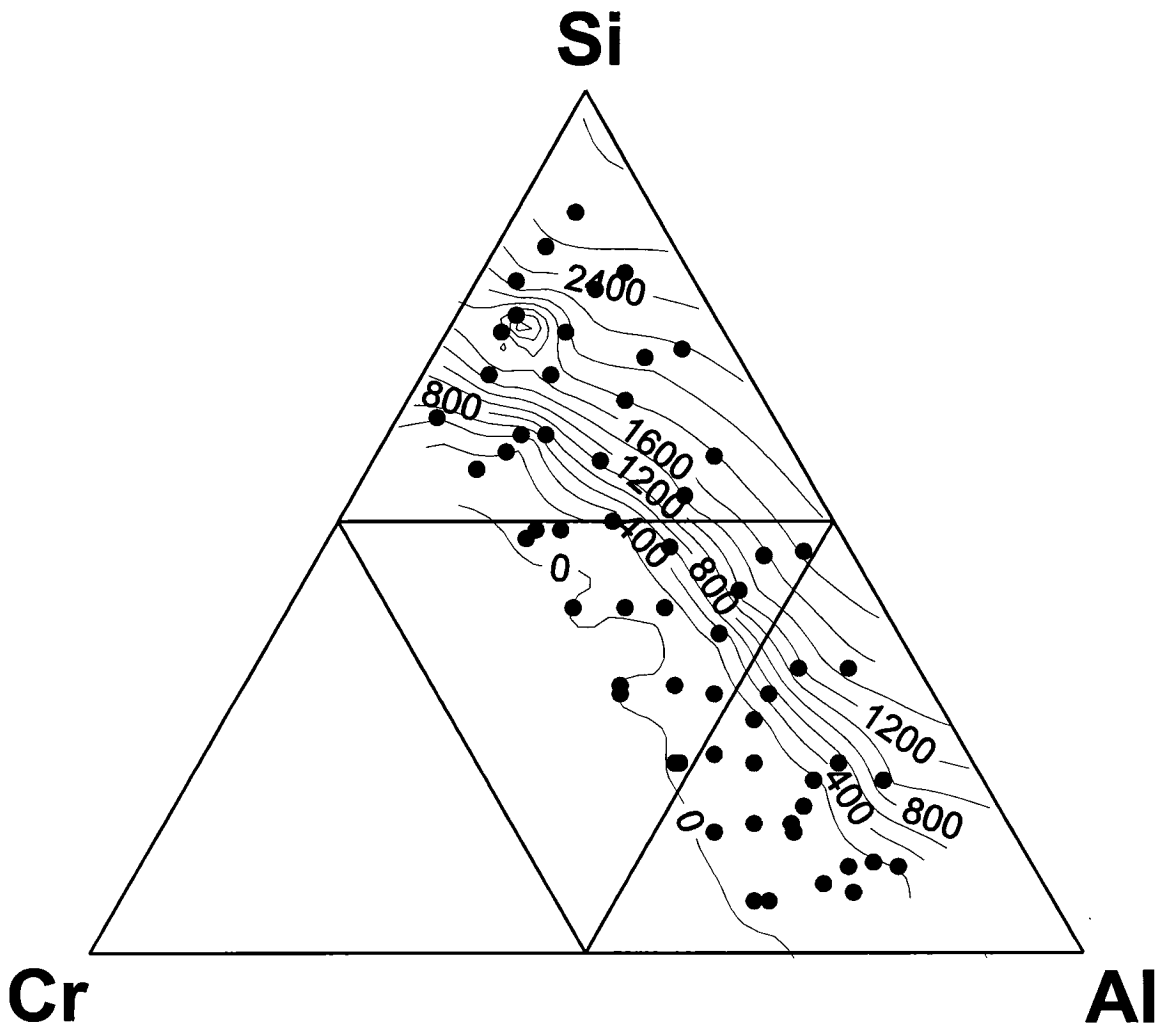

Figure 6.18: 1^{st} charge capacity (mA h/g) as a function of composition for Al-Cr-Si cycled at room temperature. Dots indicate compositions used to form the contours.

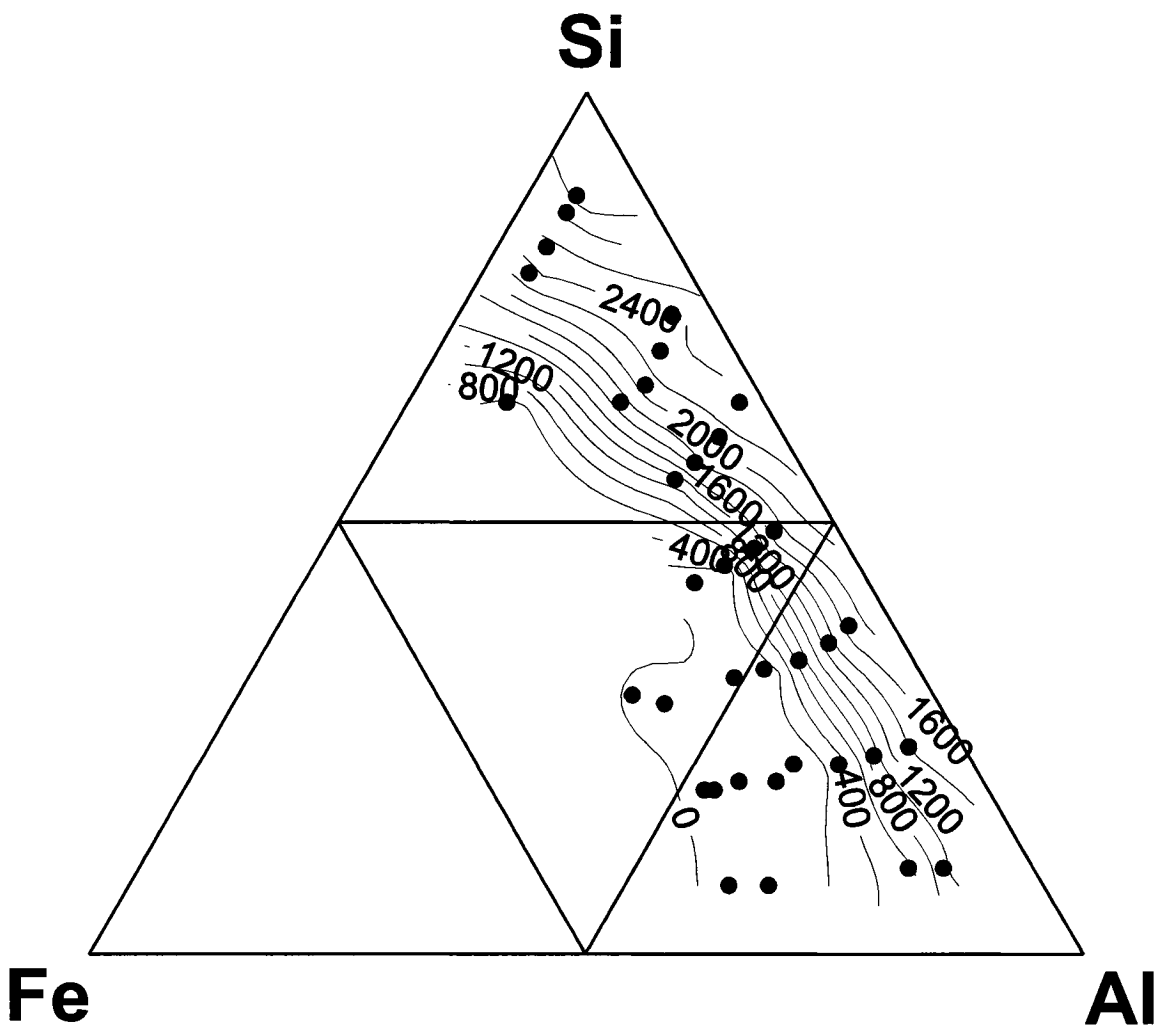

Figure 6.19: 1^{st} charge capacity (mA h/g) as a function of composition for Al-Fe-Si cycled at room temperature. Dots indicate compositions used to form the contours.

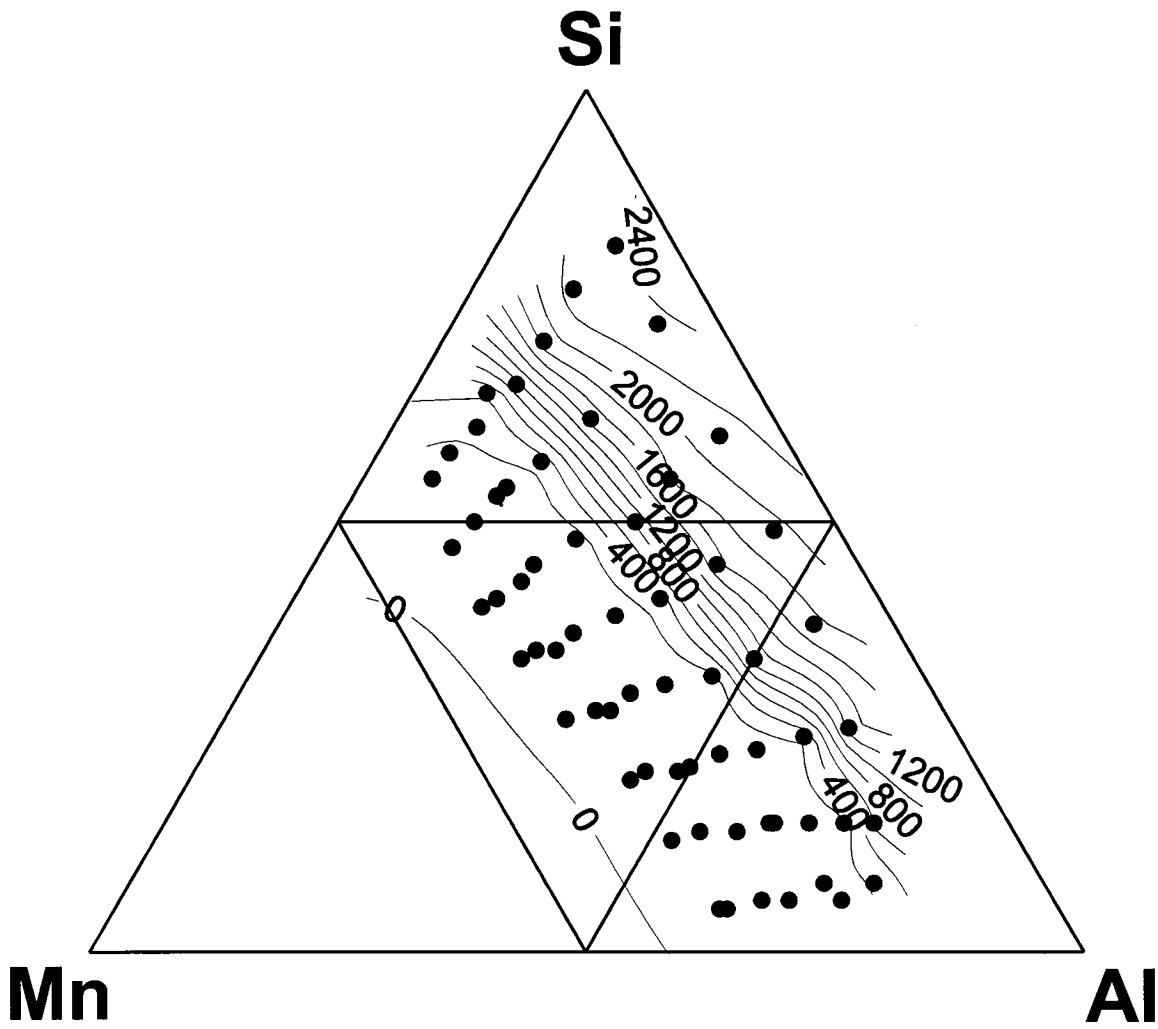

Figure 6.20: 1^{st} charge capacity (mA h/g) as a function of composition for Al-Mn-Si cycled at room temperature. Dots indicate compositions used to form the contours.

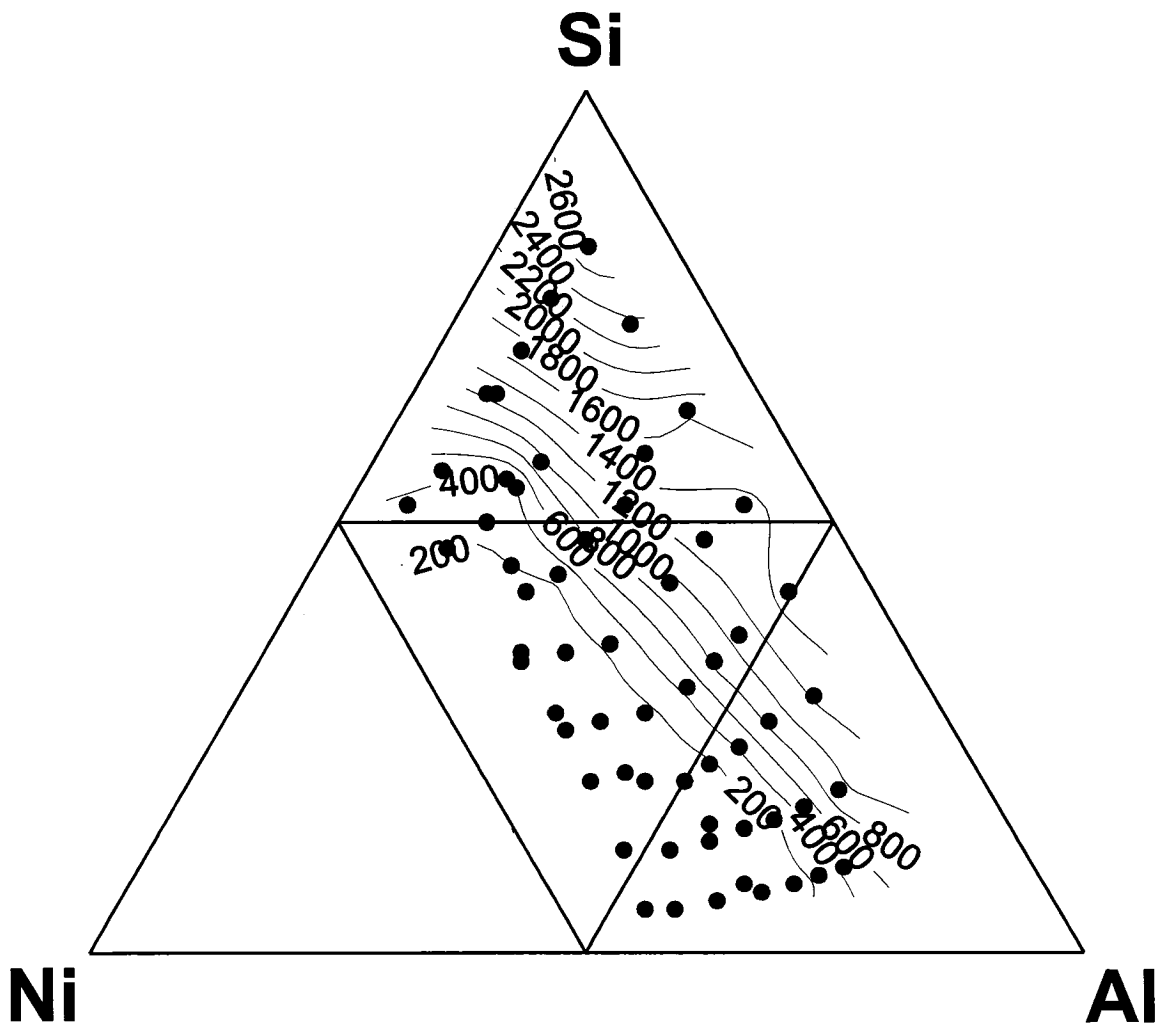

Figure 6.21: 1^{st} charge capacity (mA h/g) as a function of composition for Al-Ni-Si cycled at room temperature. Dots indicate compositions used to form the contours.

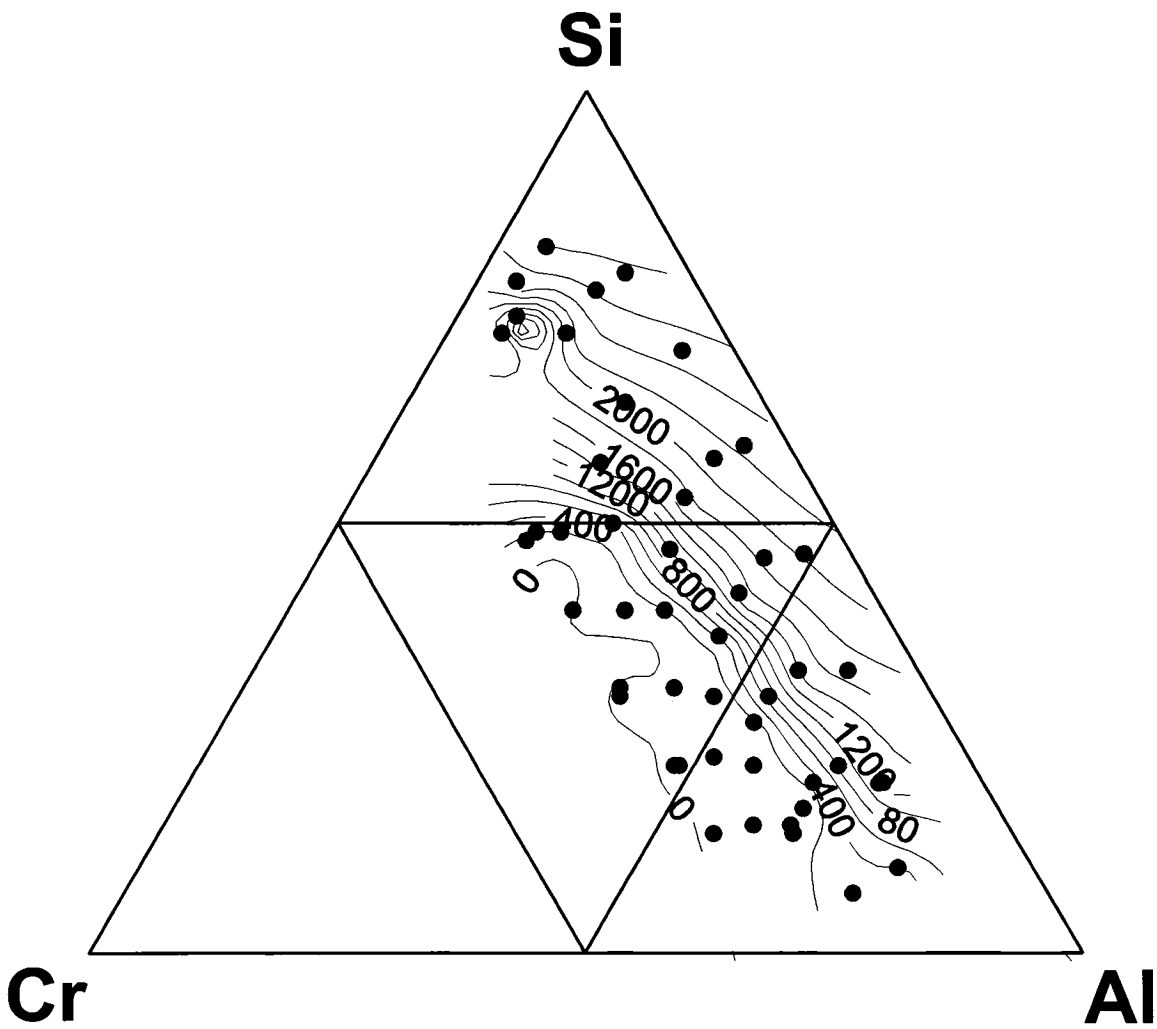

Figure 6.22: 1^{st} charge capacity (mA h/g) as a function of composition for Al-Cr-Si cycled at 70 °C. Dots indicate compositions used to form the contours.

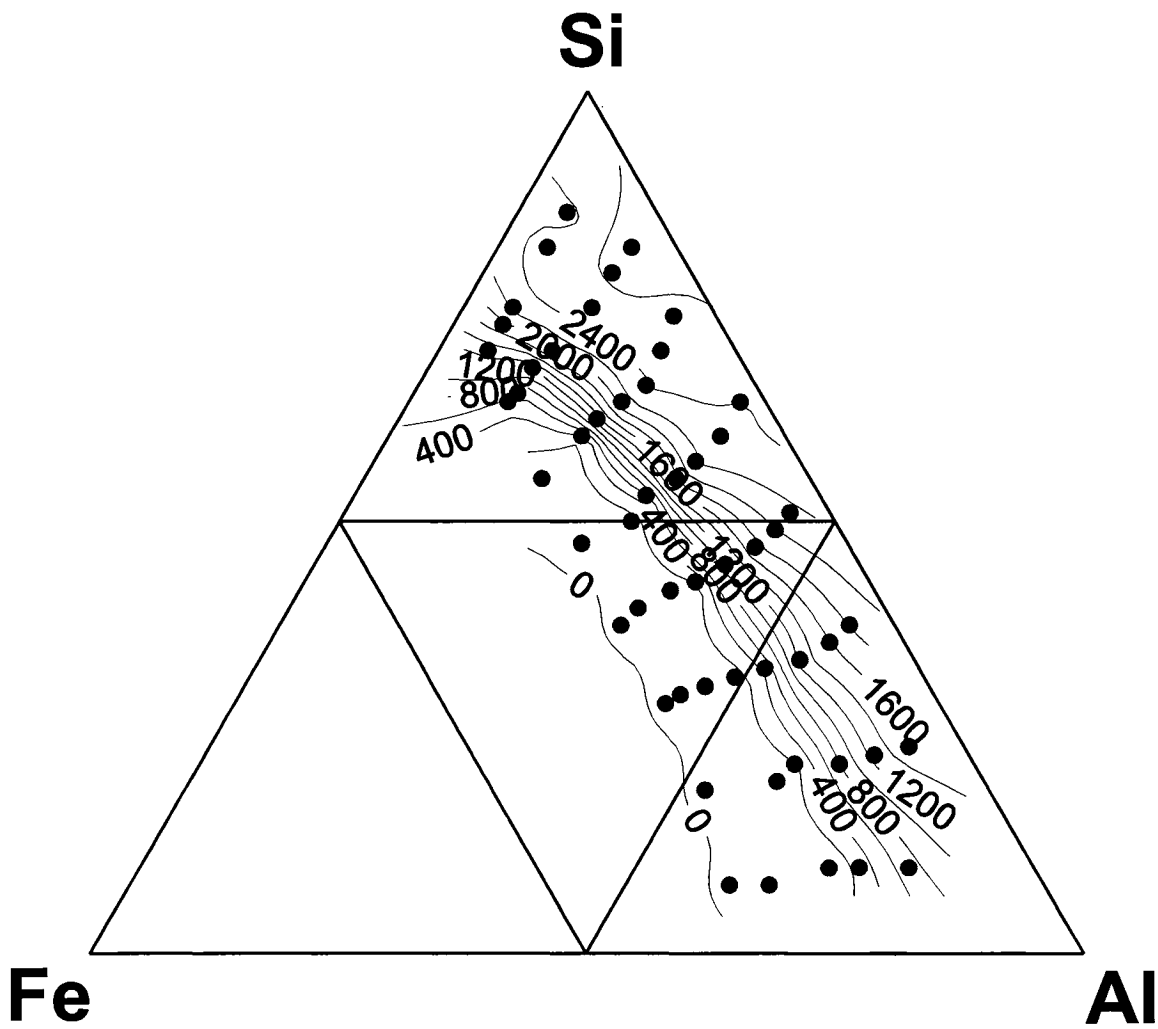

Figure 6.23: 1^{st} charge capacity (mA h/g) as a function of composition for Al-Fe-Si cycled at 70 °C. Dots indicate compositions used to form the contours.

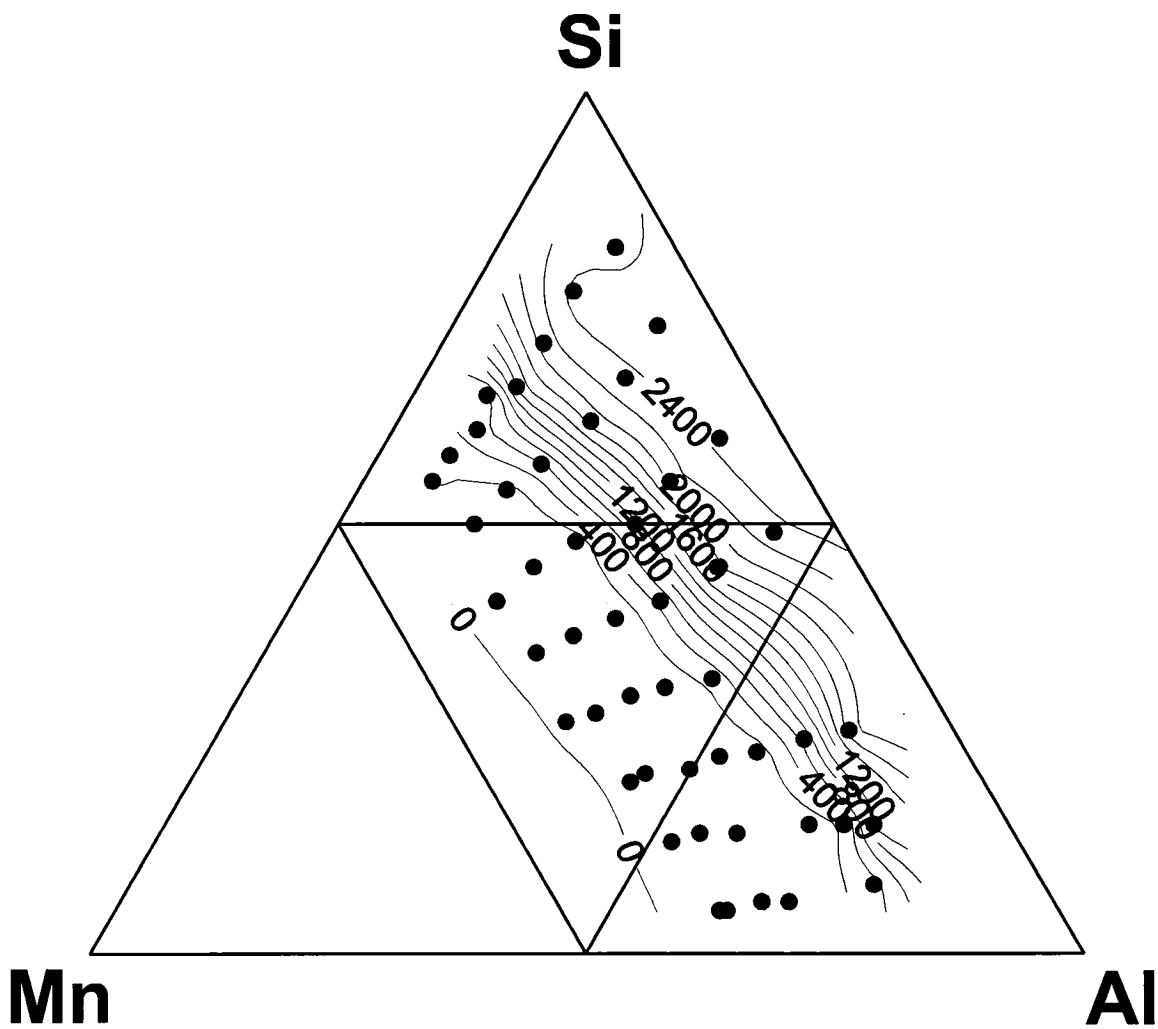

Figure 6.24: 1^{st} charge capacity (mA h/g) as a function of composition for Al-Mn-Si cycled at 70 °C. Dots indicate compositions used to form the contours.

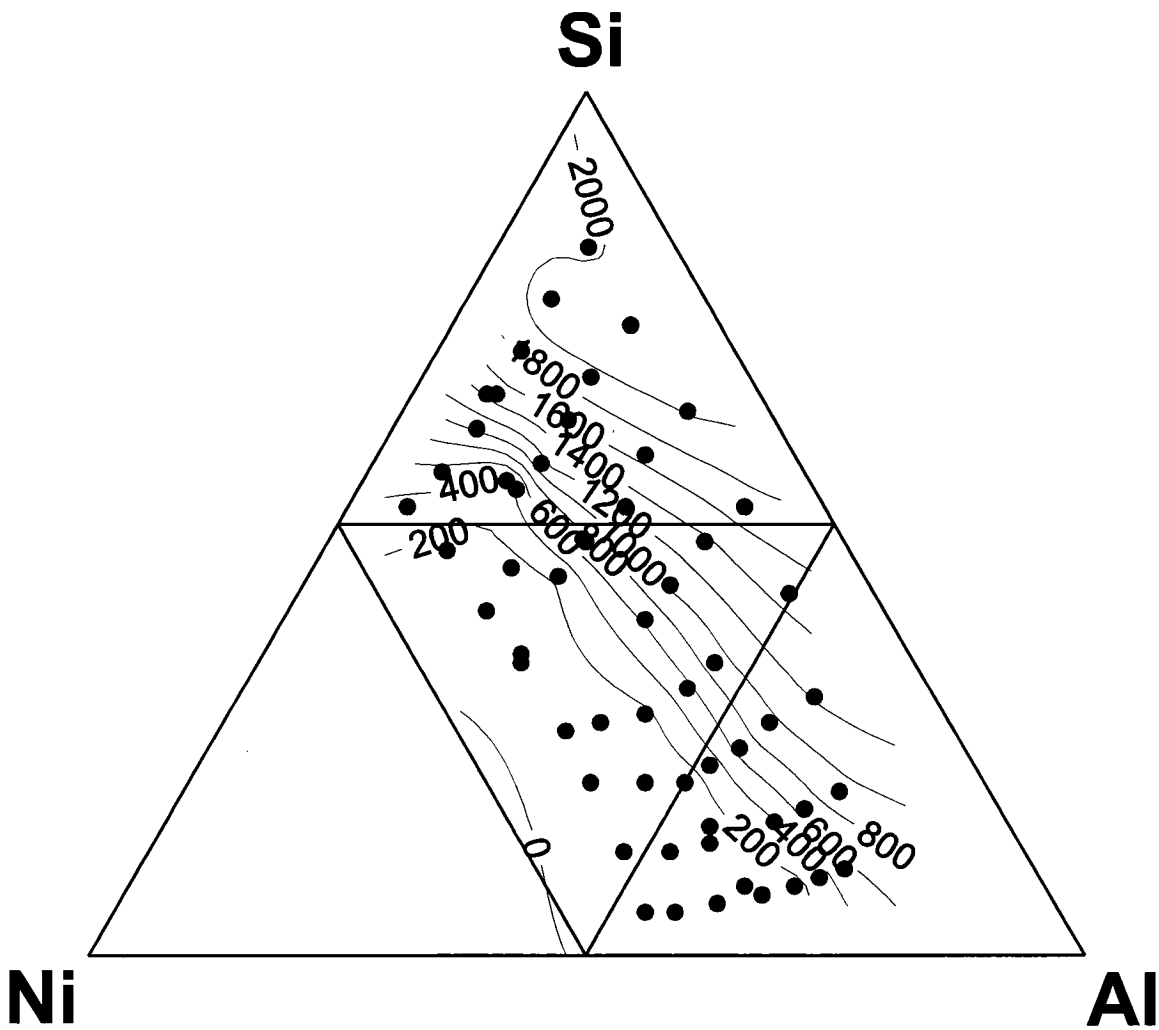

Figure 6.25: 2^{nd} charge capacity (mA h/g) as a function of composition for Al-Ni-Si cycled at 70 °C. Dots indicate compositions used to form the contours.

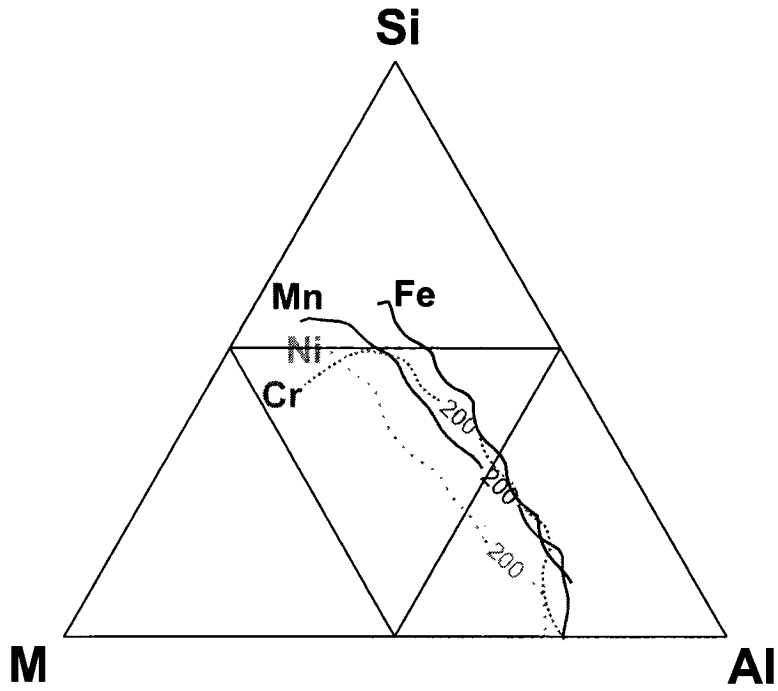

Figure 6.26: Contour lines of 200 mA h/g for Si-Al-M (M = Cr, Fe, Mn, Ni) reproduced from Figures 6.22, 6.23, 6.24, and 6.25, respectively.

a wide margin, Ni. The difference between Ni and the other transition metals is clear when contours of constant capacity (200 mA h/g) as a function of composition for M = Cr, Fe, Mn, and Ni are superimposed, as shown in Figure 6.26.

dQ/dV vs. V curves along $(Al_{0.22}Si_{0.78})_{1-x}Ni_x$ exhibit some of the features found in the $(Al_{0.27}Si_{0.73})_{1-x}Fe_x$ data (i.e. hump at 0.15 V, decrease of said hump with increasing Fe content) but are more characteristic of the reaction of Li with amorphous Si in an inert matrix. The physical reason behind this difference is unknown. Recall the behaviour of Al-Ni was also different from the other Al-M systems. Al-Ni was the only system investigated in which the fcc (Al) phase and the capacity went to zero at the same composition (see Figure 4.16). No differences between Ni, Cr and Fe were observed while investigating the Si-M system.

These results suggest that models developed from investigations of the various binary systems can be applied to most, but not all, of the ternary systems. A few general rules can still be considered. Various features in dQ/dV vs. V plots were attributed to specific reactions, such as a peak at 0.6 V on removal being connected with the removal of Li from AlLi. dQ/dV vs. V curves collected at 70 °C for each

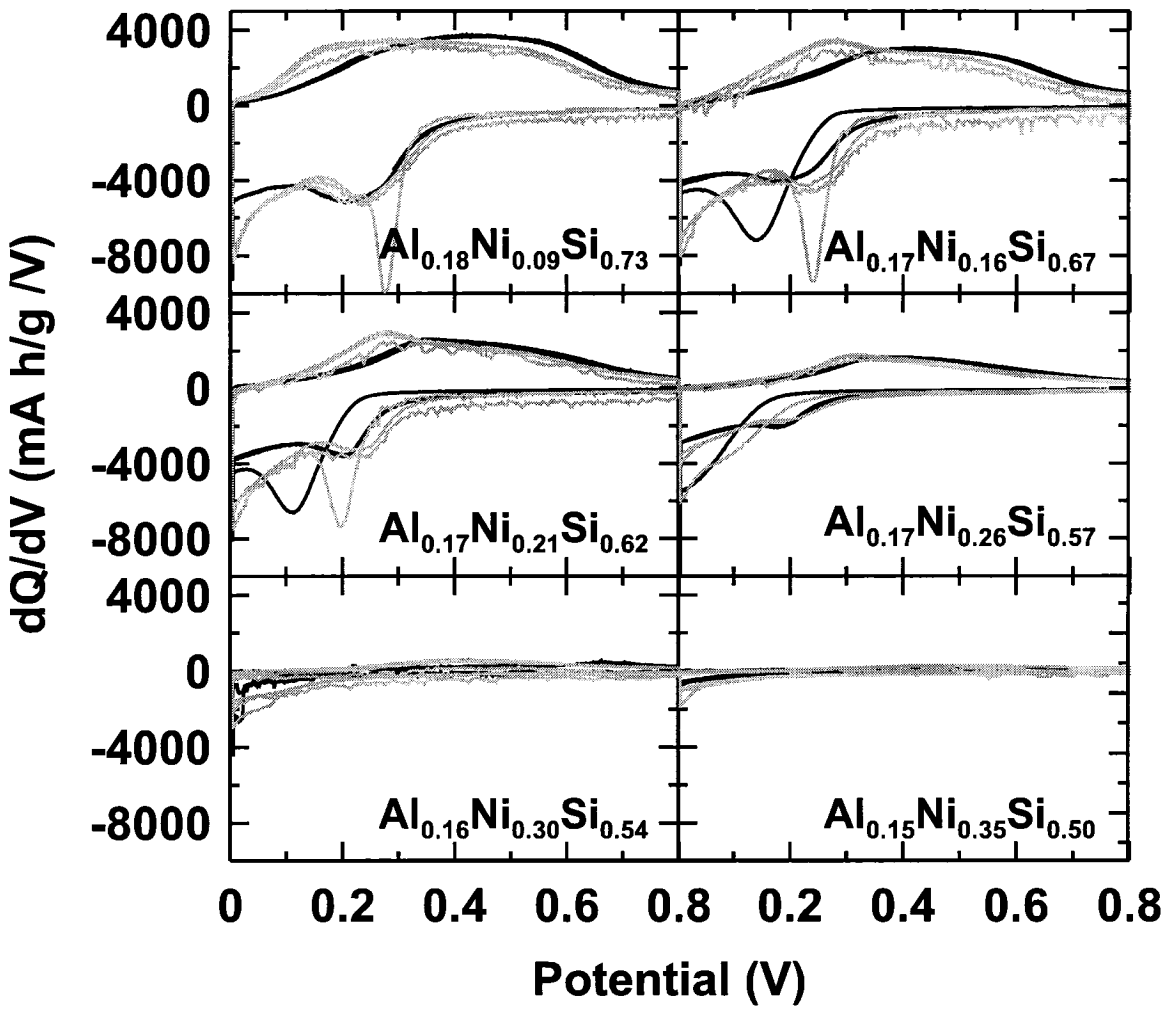

Figure 6.27: dQ/dV vs. V curves for various compositions approximately along $(Al_{0.22}Si_{0.78})_{1-x}Ni_x$. Black and grey curves were collected at room temperature and 70 °C, respectively. Compositions are indicated.

of the more than 200 Si-Al-M compositions were inspected for features associated with $Li_{15}Si_4$ (sharp peak at 0.4 V during removal), $Al_2Li_{18}Si_6$ (hump at 0.15 V during removal), AlLi (peak at 0.6 V during removal), and the dissociation of the AlLiSi phase (peak at 1.1 V during removal). Data collected from spk002 (Al-Si) at 70 °C was also included in this analysis. Results for the aforementioned features are provided in Figures 6.28, 6.29, 6.30, and 6.31, respectively. Grey areas are used in each figure as a guide to the eye, to separate compositions marked with an 0 (feature present) from compositions marked with an X (feature not present).

The grey area in Figure 6.28 extends from Si to approximately $Al_{.20}Si_{0.80}$ along the Al-Si axis. This could presumably be extended to SiM along the Si-M axis in order to be consistent with the model for Si-M thin films developed in Chapter 3, although features characteristic of crystalline $Li_{15}Si_4$ were not observed for compositions outside the grey area. The grey area of Figure 6.29 is approximately centred about $Al_{0.25}Si_{0.75}$, and extends out to 10-15 at. % M. Results from investigations of the Al-M and Al-Si systems in Chapter 4 and 5 can be used to explain most of the shape of the grey area in Figure 6.30. The peak associated with the removal of Li from AlLi decreased in intensity with increasing cycle number for compositions of Al-Si with more than 30 at. % Si (see Figure 5.8) and was not observed during cycling at 70 °C. No evidence of the dissociation of the AlLiSi phase was observed for compositions of Si-Al-M with more than 8 at. % M, as shown by the grey area in Figure 6.31. The physical mechanism behind this, and the reason why this 8 at. % M limit is not consistent for a range of Si:Al ratios, is not known.

The shapes of the 200 mA h/g contour lines shown in Figure 6.26 become less of a mystery when the contour line for each value of M is superimposed on the appropriate Al-M / Si-M / Si-Al-M binary and ternary phase diagram, as demonstrated in Figures 6.32, 6.33, 6.34, and 6.35 for M = Cr, Fe, Mn, and Ni, respectively. Si-Al-Mn is the only system where non-zero capacities are observed for any composition at which a ternary phase occurs, and these capacities are small (a few hundreds of mA h/g).

The results shown in Figures 6.32, 6.33, 6.34, and 6.35 contain a great deal of information. The 200 mA h/g lines, which represent compositions with little to no capacity, approximately connect the various lowest M content Si-Al-M phases. No evidence of Si_2M (M = Cr, Fe, Ni) or $Si_{0.63}Mn_{0.37}$ was observed during investigations

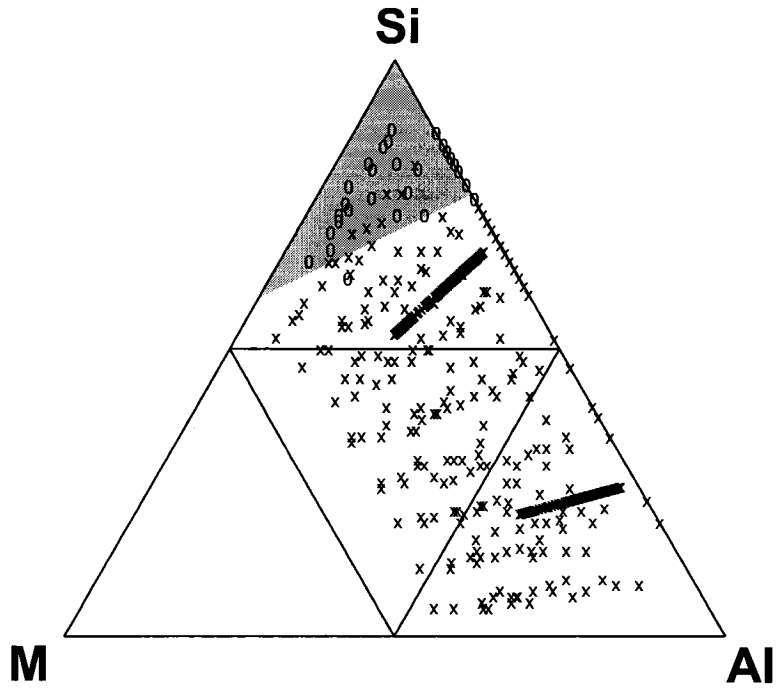

Figure 6.28: Formation range of $Li_{15}Si_4$ as determined by the presence of a peak in dQ/dV vs. V curves at 0.4 V on removal. Compositions with and without said peak are labeled with an 0 and X, respectively. The shaded region is a guide to the eye.

of the Si-M system. It is possible that the other Si-Al-M binary and ternary room temperature phases (e.g. Al_7Cr, Al_9Mn_3Si) occurring at compositions with non-zero capacities were not actually formed. No binary or ternary Si-Al-M phases were observed that alloy with Li. If the short-range atomic order of an amorphous alloy is not very different than that of an equilibrium phase with the same composition, then it could be said that all Si-Al-M binary and ternary phases are inactive. Tests on various crystalline Si-Al-M phases (e.g. Si_2Fe) would obviously be required to back up this hypothesis.

Additional insight might be gained by turning the hypothesis inside out: previously unknown equilibrium phases of Si-Al-M might be identified based on regions that do not alloy with Li. Only four transition metal varieties were tested, and of those, the recent literature conflicted with earlier results or did not exist. Relatively straightforward electrochemical testing may have something to offer. These and other conclusions are developed further in the next chapter.

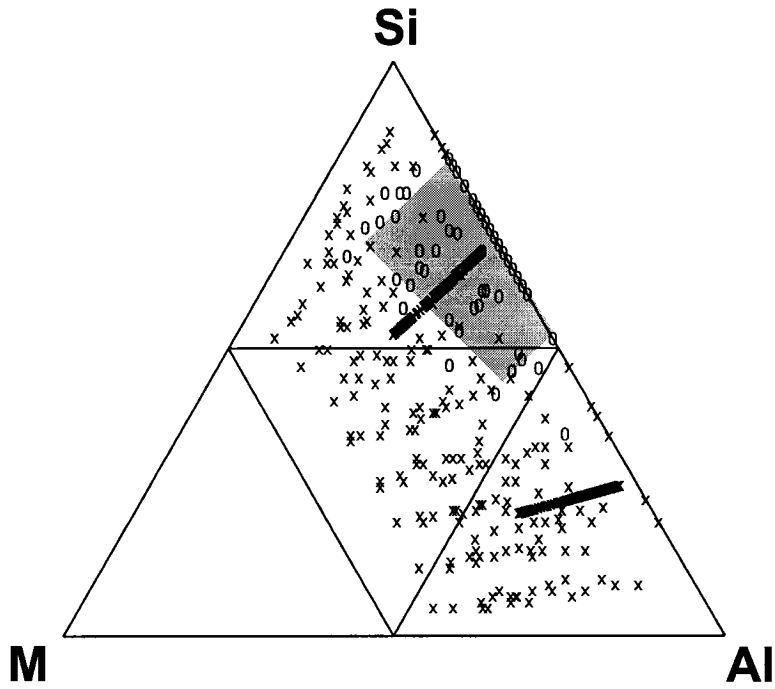

Figure 6.29: Formation range of $Al_2Li_{18}Si_6$ as determined by the presence of a peak in dQ/dV vs. V curves collected at 70 °C at 0.15 V on removal. Compositions with and without said peak are labeled with an 0 and X, respectively. The shaded region is a guide to the eye.

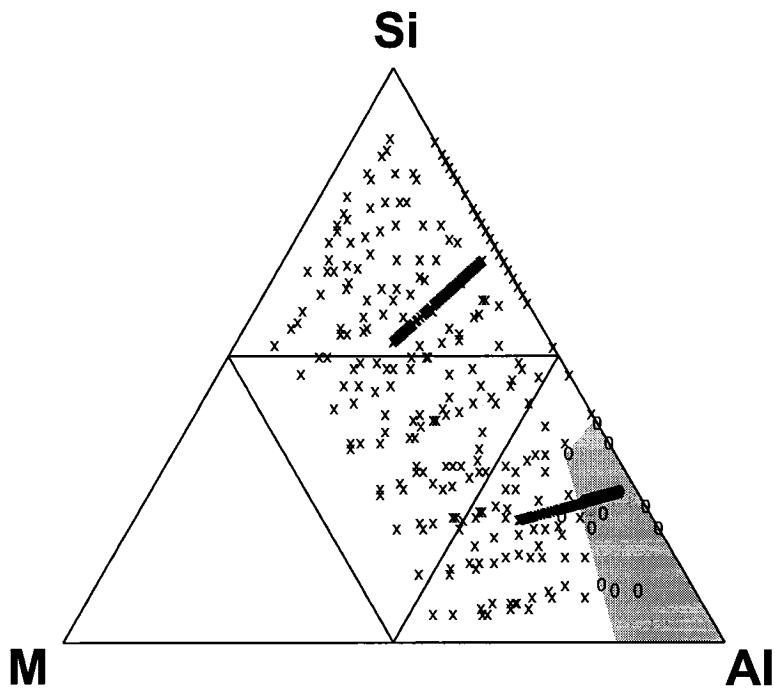

Figure 6.30: Formation range of AlLi as determined by the presence of a peak in dQ/dV vs. V curves between 0.5-0.7 V on removal. Compositions with and without said peak are labeled with an 0 and X, respectively. The shaded region is a guide to the eye.

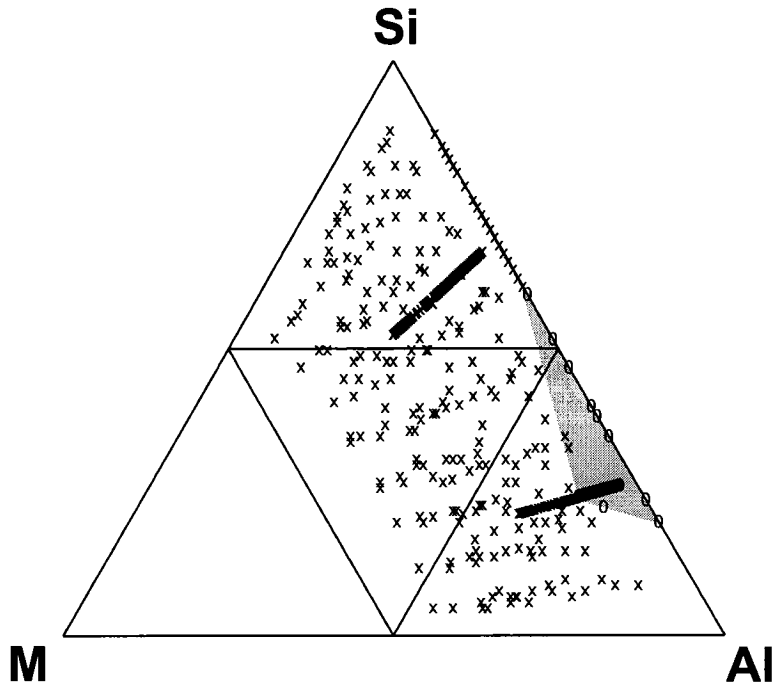

Figure 6.31: Dissociation range of the AlLiSi phase as determined by the presence of a peak in dQ/dV vs. V curves collected at 70 °C between 1.0-1.2 V on removal. Compositions with and without said peak are labeled with an 0 and X, respectively. The shaded region is a guide to the eye.

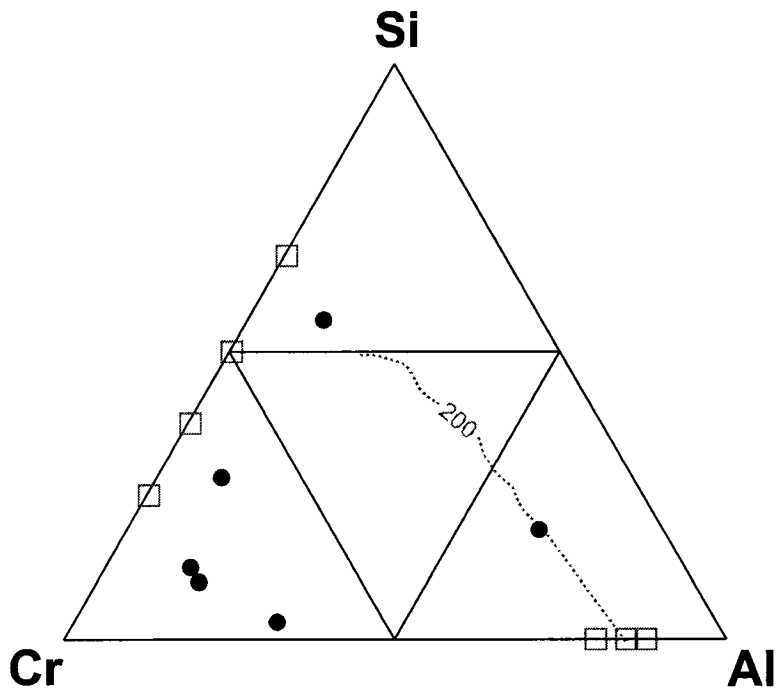

Figure 6.32: Equilibrium binary (squares [115]) and ternary (circles [39]) Al-Cr-Si phases, and the 200 mA h/g line from Figure 6.26 extrapolated to 0 at. % Si according to Figure 4.14.

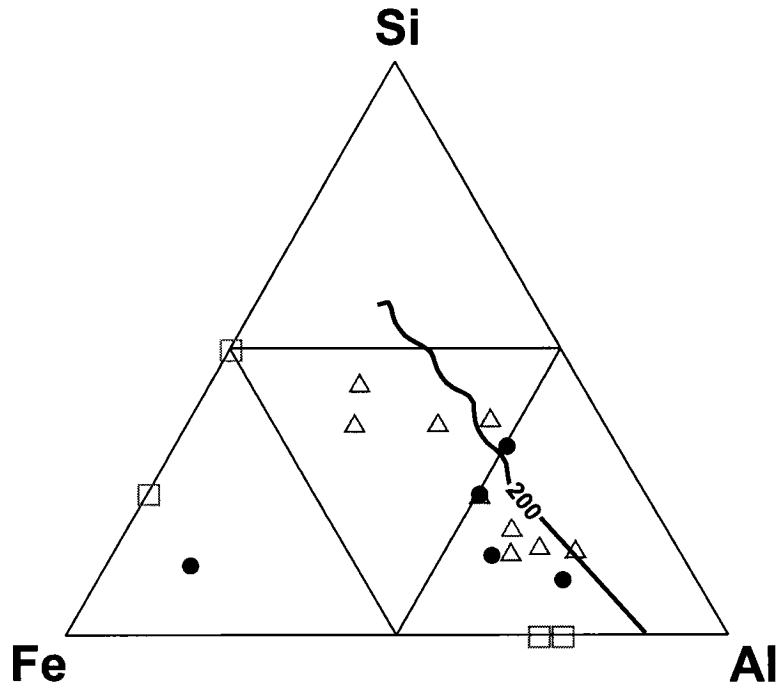

Figure 6.33: Equilibrium binary (squares [115]) and ternary (circles [39], triangles [142]) Al-Fe-Si phases, and the 200 mA h/g line from Figure 6.26 extrapolated to 0 at. % Si according to Figure 4.12.

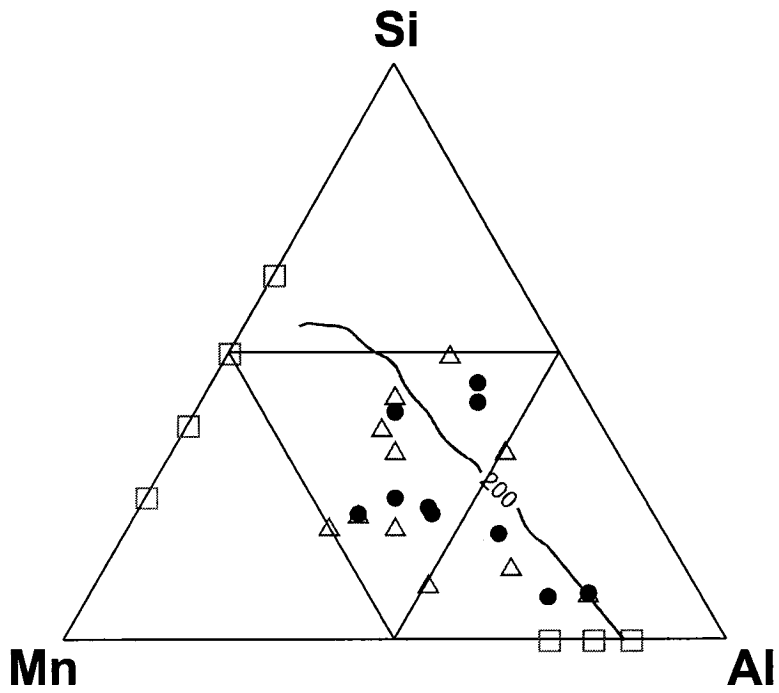

Figure 6.34: Equilibrium binary (squares [115]) and ternary (circles [39], triangles [143]) Al-Mn-Si phases, and the 200 mA h/g line from Figure 6.26 extrapolated to 0 at. % Si according to Figure 4.15.

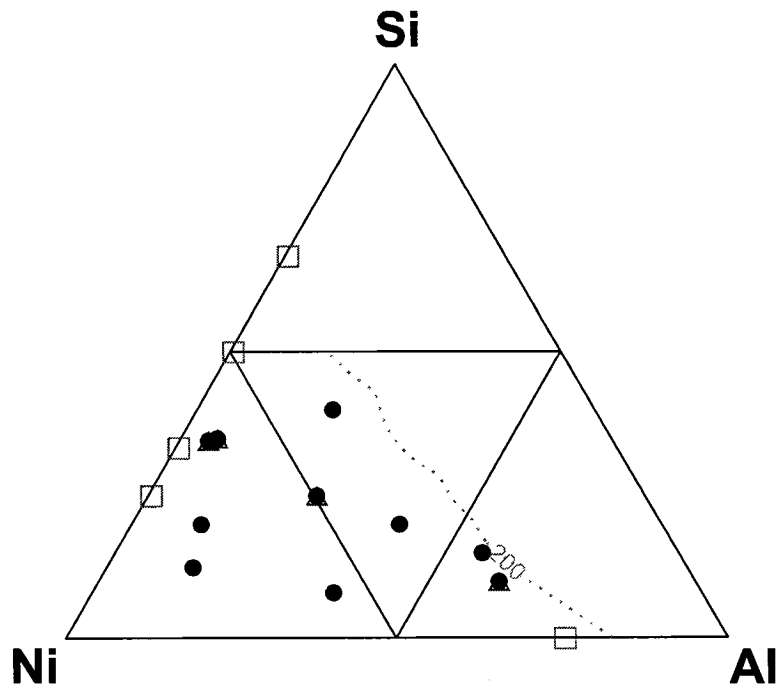

Figure 6.35: Equilibrium binary (squares [115]) and ternary (circles [39], triangles [144, 145]) Al-Ni-Si phases, and the 200 mA h/g line from Figure 6.26 extrapolated to 0 at. % Si according to Figure 4.16.

Chapter 7

Conclusions And Future Work

The work described in the previous four chapters provides considerable insight on the electrochemical performance of the Si-M, Al-M, Al-Si and Si-Al-M (M = transition metal) systems. Capacities in the Si-M system can be understood by assuming the presence of co-existing active amorphous Si and inactive nanocrystalline SiM. Diffusion effects dominate all but the Si-Mn system below 70 at. % Si when cycling at room temperature, and can be used to explain the lower capacities observed by some authors (e.g. [109]).

Mössbauer and XRD measurements suggest M atoms are not randomly distributed throughout Al-M samples, but instead occur in isolated and clustered sites. A phenomenological model based on the relative amounts of isolated and clustered sites was presented to explain the capacities observed at room and elevated temperature.

Interactions between Si, Al, and Li complicate the electrochemistry of the Si-Al system. Measurements suggest the presence of AlLi, either AlLiSi or $Al_3Li_7Si_4$, $Al_2Li_{18}Si_6$, and $Li_{15}Si_4$ in certain compositions of fully-lithiated films. The presence of the so-called AlLiSi phase has a negative impact on capacity retention.

Results from the Si-Al-M system were not as clear-cut. Features from the Si-M, Al-M, and Al-Si systems were present, but could not be used to completely explain the rapid drop in capacity that occurred between ca. 10-25 at. % M for intermediate ratios of Si:Al for M = Fe, Cr, and Ni. The rapid capacity fade associated with the formation (and dissociation) of the AlLiSi phase was not observed for any compositions of Si-Al-M with more than 8 at. % M. This range may extend further upon extended cycling, but was not observed.

Elements of the electrochemical performance of each of the four systems described in this thesis are still not understood. *In-situ* XRD and Mössbauer effect spectroscopy could be used to investigate the differences between the first and subsequent dQ/dV vs. V curves during Li insertion in the Si-M system, which change with transition

metal variety and content. *In-situ* XRD measurements could also probably distinguish between the formation of AlLiSi and $Al_3Li_7Si_4$ in the Si-Al and Si-Al-M systems.

The rapid capacity drop with increasing transition metal content in the Al-M system was not predicted by the macroscopic atom model of de Boer *et al.* [90]. Larcher *et al.* [121] performed free energy calculations for the reaction of Li with Al_2Cu using established literature values and reached the same conclusion: $Al_{1-x}M_x$ alloys with low M content should alloy with Li based on thermodynamics. Very high temperature (ca. 100 °C or higher) cycling would likely indicate if kinetic barriers lead to the apparent inactivity at room temperature and 70 °C.

Results from the Al-Ni and Si-Al-Ni systems differed somewhat from those of the other Al-M and Si-Al-M systems investigated. The reason does not seem to be related to the equilibrium phase diagrams since the diagrams for Al-Ni and Al-Fe are almost identical below 25 at. % M and 800 °C (see Figure 4.1). A comparision of *in-situ* XRD measurements on thin films of Si-Al-M (M = Fe or Ni) with identical compositions (approximately $Si_{0.30}Al_{0.65}M_{0.15}$ and separately $Si_{0.60}Al_{0.15}M_{0.25}$) might allow for identification of the phases present during Li insertion and removal. This information might then be used to explain the dQ/dV vs. V curves of Si-Al-M without distinguishable features.

Cr, Fe, Mn, and Ni were the only transition metals investigated during the course of this thesis. Investigations of the other top-row transition metals (Sc, Ti, V, Co, Cu, and Zn) should also be performed. Very recently (September 2005), R. Mar, J. Dahn and the author started to investigate the Si-Co system. A plot of first charge capacity as a function of composition at both room temperature and 70 °C is provided as Figure 7.1. The room temperature capacity drops rapidly at approximately 80 at. % Si, as opposed to 70 at. % Si as found in the Si-Fe and Si-Cr-Ni systems. Higher capacities over the range 70-80 at. % Si were realized in the cell cycled at 70 °C, but no compositions with less than 70 at. % Si had any appreciable capacity. This strongly suggests that nanocrystalline Si_2Co, rather than nanocrystalline SiCo, is present in the deposited film and is inactive.

XRD patterns collected from $Si_{0.60}Co_{0.40}$ and $Si_{0.45}Co_{0.55}$ after deposition and after annealing to 400 °C in 45 seconds using a rapid thermal annealer are presented in Figure 7.2. XRD patterns from the as-deposited film are similar to those collected

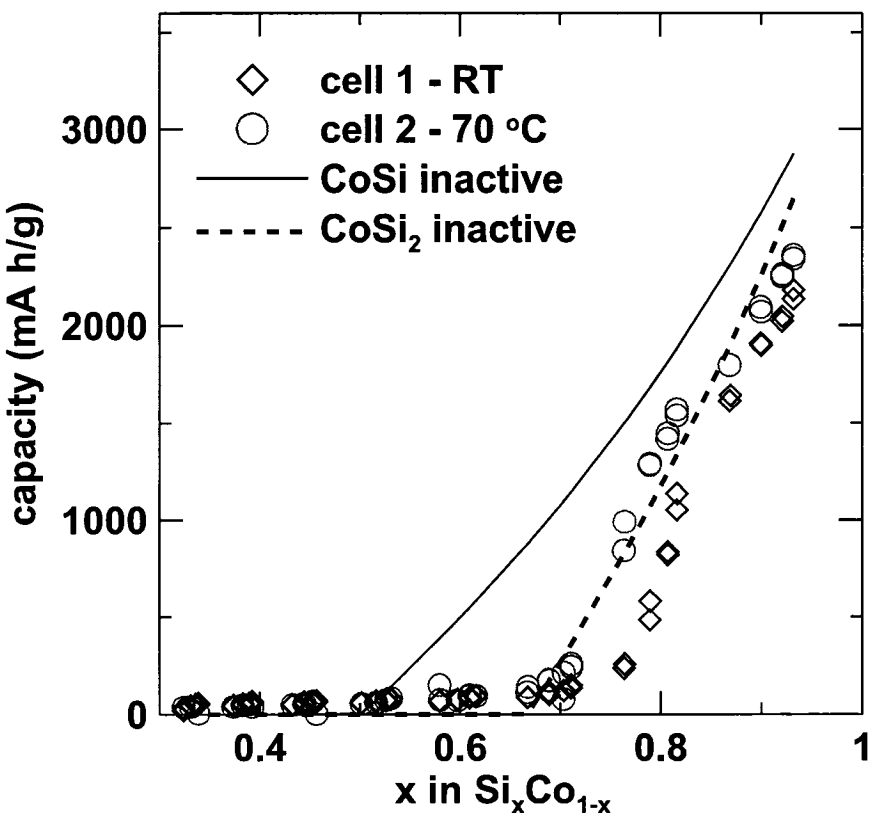

Figure 7.1: 1^{st} charge capacity as a function of composition for Si_xCo_{1-x} at room temperature (diamonds) and 70 °C (circles). Dashed and solid lines indicate the expected capacity if SiCo and Si_2Co are inactive.

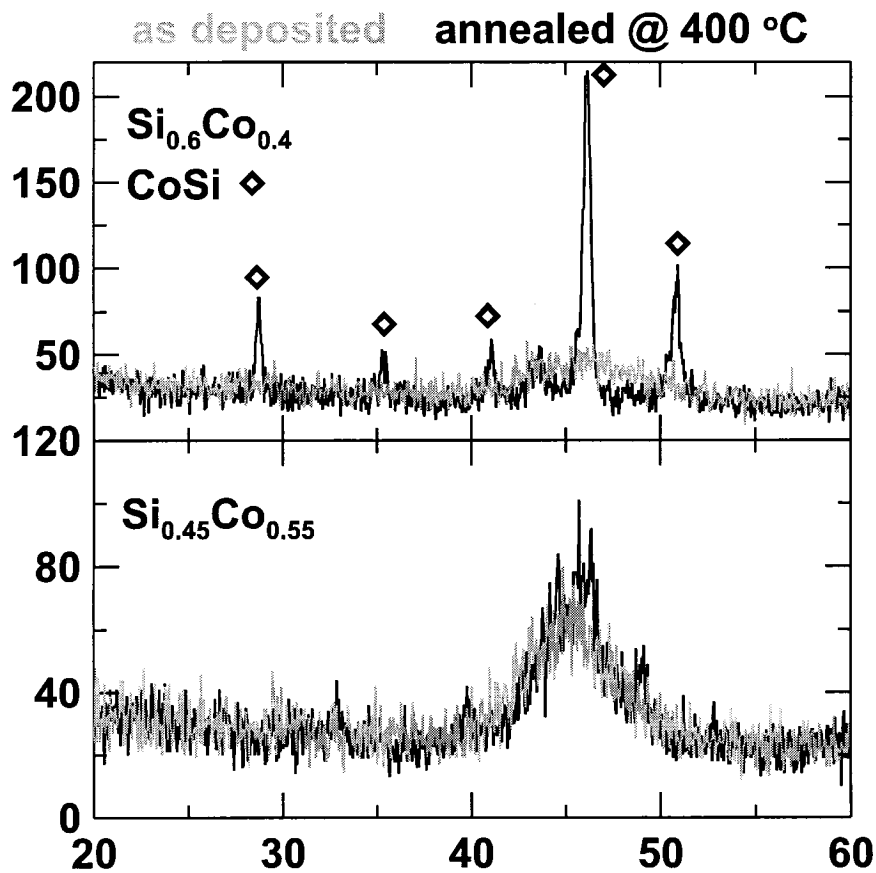

Figure 7.2: XRD patterns of as-deposited (grey) and annealed to 400 °C in 45 seconds using a rapid thermal annealer (black) $Si_{0.60}Co_{0.40}$ and $Si_{0.45}Co_{0.55}$.

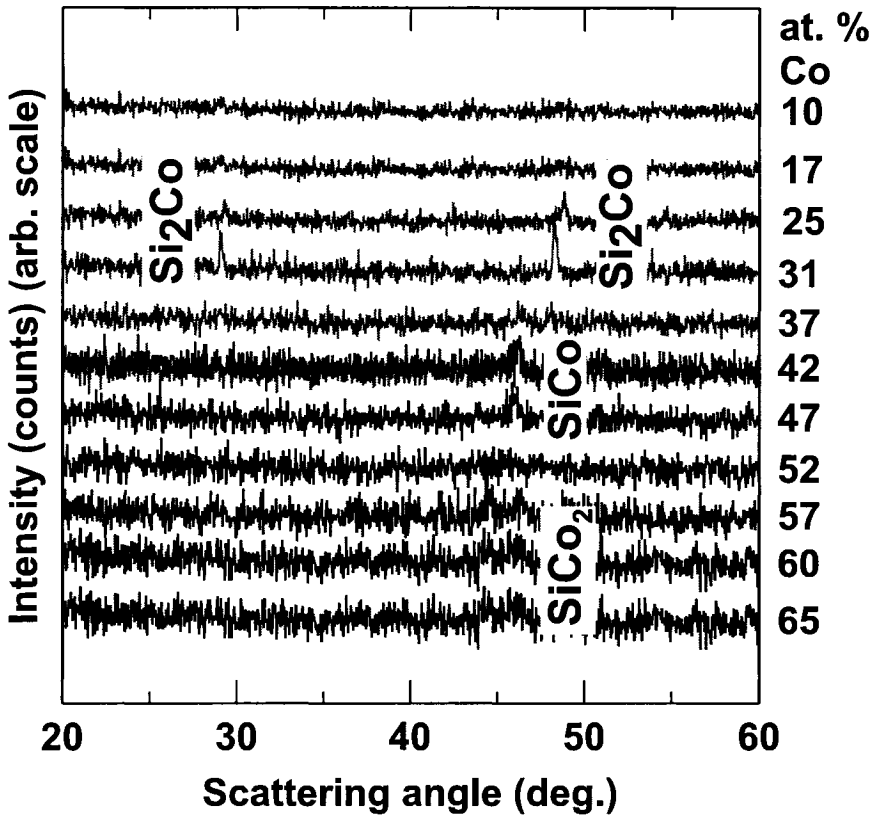

Figure 7.3: XRD patterns of annealed Si_xCo_{1-x}.

from Si-Fe and Si-Mn, although the identification of SiCo based on one 5-10° wide peak is unwise. Peaks in annealed $Si_{0.60}Co_{0.40}$ can be attributed to SiCo. XRD patterns collected from a broad range of annealed Si-Co compositions are provided in Figure 7.3. Peaks associated with Si_2Co, SiCo, and $SiCo_2$ are present over the expected composition ranges.

The Co-Si equilibrium phase diagram (not shown) is very similar to the equilibrium phase diagram for Si-Cr (see Figure 3.1), especially above 50 at. % Si. 400 °C is well below all relevant eutectic temperatures (ca. 1200 °C). Metal induced crystallization is only expected to decrease the crystallization temperature of Si-M alloys between 10-30 at. % M, not near 50 at. % M [134]. This could indicate that the local atomic ordering in sputtered Si-Co is similar to that found in the phase diagram - i.e. nanocrystalline Si_2Co may be present in the deposited film. While this would differ from the other transition metals investigated, it would be consistent with the idea that all Si-Al-M equilibrium crystalline phases are inactive. Further investigations of

the Si-Co system, including DSC measurements and more detailed electrochemical testing, are required before any additional conclusions can be drawn.

Electrochemical testing of various crystalline Si-Al-M phases such as Si_2Fe and Al_2Ni_2Si should be performed to strengthen the hypothesis that all crystalline Si-Al-M equilibrium room temperature phases are inactive. This hypothesis could lead to a new method to identify Si-Al-M equilibrium phases, but more importantly, could also offer a connection between the electrochemical performance of sputtered thin films and bulk samples. Results suggest that a) if a sputtered composition is active, the corresponding crystalline phase is active; and b) if the crystalline phase is inactive, the corresponding sputtered composition is also inactive (e.g. Al_6Mn). This does not fall apart for the case of Si_2M because sputtered films of $Si_{0.66}M_{0.33}$ are actually composed of amorphous Si and nanocrystalline SiM.

The original motivation for studying the Si-Al-M system was that large composition ranges with significant amounts of Si and Al could be prepared in an amorphous state by melt-spinning. The melt-spun amorphous range of Si-Al-Mn is shown in Figure 1.3 (approximately 10-20 at. % Mn and 50-80 at. % Al). Within this composition region, there is no evidence of the formation / dissociation of the AlLiSi phase, $Al_2Li_{18}Si_6$, $Li_{15}Si_4$, or SiM. Features associated with the removal of Li from AlLi were present for compositions along the low M, high Al corner of the melt-spun amorphous range of Si-Al-Mn. This region, along with compositions just beyond the onset of rapid capacity decreases at higher Si content, appears ideal from an 'amorphous equals excellent capacity retention' standpoint. Although the focus of this thesis was to understand, rather than optimize, the performance of Si-Al-M electrode materials, the ideal composition of Si-Al-M can be identified and appears to be at the high-Si, low M composition of the amorphous range. It is encouraging to note that this same conclusion was reached in the author's M. Sc. thesis [91], before any of the work described in this thesis was performed, which demonstrates the efficiency of the methods described herein for rapid screening.

There can be no doubt the combinatorial methods described here have proven to be worth the considerable investment. Subtle and not-so subtle trends in data from the Si-M (M = Cr + Ni, Fe, Mn), Al-M (M = Cr, Fe, Mn, Ni) and Al-Si systems lead to models / non-equilibrium phase diagrams for each, which in turn were used

to understand some of the performance of the industrially relevant Si-Al-M (M = Cr, Fe, Mn, Ni) system. One can only imagine how difficult it would be to understand the performance of the Al-M alloys looking at one composition at a time, especially in composition regions where the capacity changes by close to 1000 mA h/g over two or three at. % M. These powerful combinatorial and high throughput tools will provide significant insight to future electrode material development. The big question, however, should not be on the ability of the testing method but in the way it was applied, especially considering there are some similarities and some differences between the materials described within and the (presumed) focus of future research, the Sony Nexelion amorphous Sn-Co-Sn-In-Ti negative electrode. Sony's new electrode represents the first major development in commercialized negative electrode materials since the convertible Sn oxides introduced by Fuji in 1997.

Courtney and Dahn were the first to explain the physical mechanisms responsible for the increased Li storage capacity and excellent capacity retention of Sn-based oxides [23, 24]. References [23] and [24] are just two of the numerous accounts of amorphous material investigations described by 3M scientists and the Dahn group in the peer-reviewed and patent literature over the past eight years (e.g. [21, 147]). Amorphous materials can provide high capacities and excellent capacity retention. The fact the Sony electrode is based on Sn, rather than Si, is probably related to the larger amount of research on Sn based alloys. Sony's Sn-Co-C-In-Ti negative electrode is very similar to the Sn-Fe-C work of Mao, Dahn *et al.* [26], which was published seven years ago. Significant work on Si-based multicomponent alloys has only been published to date by the groups of Dahn, Huggins (e.g. [104, 106, 148, 149]), and Lee (e.g. [105, 108, 109, 113]). One can assume the higher gravimetric and volumetric capacity of Si relative to Sn, and the demonstration that Sn based amorphous alloys perform well, will lead to additional Si-based alloy research.

Si-based alloys can be difficult to produce in an amorphous state by melt-spinning in part because of the high melting point of Si (ca. 1400 °C) relative to that of other elements of interest (eg. Sn, melting point ca. 230 °C). Some of these problems could be alleviated by mass producing amorphous alloys via (presumably room temperature) ball milling, as Sony apparently did. The relative strengths and weaknesses of ball milling relative to melt spinning should be investigated before any new research

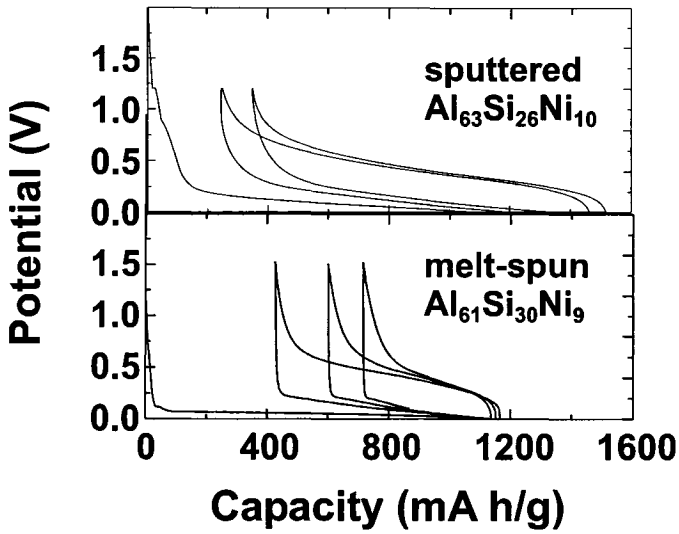

Figure 7.4: Capacity vs. potential plots of melt-spun $Al_{61}Si_{30}Ni_9$ and sputter deposited thin film $Al_{63}Si_{26}Ni_{10}$.

direction is attempted. However, leaders in the field of amorphous alloy production such as A. Inoue tend to focus on quenching from the melt. This focus may be related to attempts to produce large volume amorphous samples rather than a large amount of amorphous sample.

Powders prepared from ground melt-spun ribbons or ball milling do not lend themselves to high throughput methods. A combinatorial battery research method designed by Owens *et al.* [70] to handle powders works 'so well' that the the operators have resorted to loading their 'high-throughput' cell by hand [150]. Sputter deposited films are far easier to characterize using high-throughput methods, but do not always yield the same results as powders prepared by melt-spinning for a given composition. Capacity vs. potential curves for melt-spun $Al_{61}Si_{30}Ni_9$ (unpublished data collected by Dominique Larcher) and sputter deposited thin film $Al_{63}Si_{26}Ni_{10}$ are provided in Figure 7.4. The sputter deposited thin film has a higher capacity, lower irreversible capacity and better capacity retention. Similar results are found for most other compositions of Si-Al-M. Some of the difference may be related to film thickness, but a large portion could be associated with the quench rate. Electrochemical results from sputtered $Si_{0.66}Sn_{0.34}$ are identical for films 1 μm and 6 mm thick (and then ground in to a powder with pieces less than 30 μm to a side) [151,152]. XRD patterns from melt-spun powders of Si-Al-M (not shown) typically contain more defined features than

those shown in Figure 6.16, which suggests melt-spun ribbons are 'less' amorphous than sputtered thin films of the same composition. Many melt-spinning parameters such as wheel speed, diameter, and temperature, nozzle diameter, and overpressure could be varied to attempt to reproduce results from sputtered films. Control over the quench rate may be easier with ball milling (variable shaking strength, ball size, milling time).

Work on predicting the ability to produce amorphous alloys is already underway within the lab. These directions could be complimented by an expanded implementation of the methods of de Boer *et al.* [90]. The main restrictions of the macroscopic atom model involve limited composition ranges and the requirement of at least one transition metal in a two component alloy. Transition and / or rare earth metals are likely to be found in most amorphous alloys because of the size difference between most transition metals and the active materials of interest. The composition range limitation could be removed if expressions that more accurately predict the number of (dis)similar neighbours at a particular composition were developed. Emperical fits for various sizes of atoms would be suitable for the fully computerized calculations. It should also be possible to expand the macroscopic atom model to ternary systems over large composition ranges using Chapter 4, Sections 1.2-1.4 in Ref. [90] as a starting point. Other approaches to model the activity of various phases, such as CALPHAD [153], should also be considered.

The macroscopic atom model was used to predict Al-M alloys with, e.g. 20 at. % M, would alloy with Li. This prediction was not verified experimentally, and this discrepancy needs to be understood. Higher cycling temperatures are one possible answer. Cycling at 70 °C pushed the design limits of the combinatorial electrochemical cells. Electrolyte breakdown can start to occur near 80 °C. The higher temperature also encourages evaporation of the electrolyte, which can only be prevented by tight cell seals. Higher (and uneven) sealing pressures were often too much for the glass cell plates to bear which lead to cracked glass plates and ruined experiments. Electrolytes designed for higher temperatures (ca. 100 °C) exist, but would not solve the sealing problem. Efforts by the author to even out the sealing pressure through better cell design (adding the polypropylene liner, deepening the o-ring groove) and assembly procedure (see Section C.4) reduced the cracking but did not eliminate it completely.

Thicker glass plates and modified connectors would likely go a long way to solving the cracking problem.

Something must be said about the relative benefits of the combinatorial methods of Whitacre *et al.* [71, 79]. Although these methods are complex and expensive, as they involve extensive microfabrication work and rely on a solid electrolyte, they appear at first glance to eliminate most temperature / sealing concerns, and apparently can be used to produce hundreds to thousands of different compositions on a single substrate. Advanced designs would permit for the galvanostatic testing of each channel in parallel. One must consider that after a certain point, all the so-called 'low hanging fruit' in the combinatorial environment will be picked and more complicated methods, for instance something combining the microfabrication method of Whitacre *et al.* with the composition spread techniques described in this thesis, will be required for work in the distant future. Many interesting studies can be performed with the existing system.

Sony's Nexelion Sn-Co-C-In-Ti negative electrode is likely based in large part on the earlier Sn-Fe-C work by Mao *et al.* [26]. Co is more expensive and toxic than Fe. One must assume that these costs are balanced by better performance. Transition metal varieties are not completely indistinguishable, as demonstrated by the performance differences between Si-Mn and Si-M (M = Cr, Fe, Ni) at higher transition metal contents, the different solubilities of the various M values in Al, and the difference between Si-Al-Ni and the other Si-Al-M systems. Detailed studies of (Si, Al, Si+Al)-M_1-M_2-M_3 (-M_i ...), where each M_x is either a transition or a rare-earth metal, would probably reveal subtle trends with inactive metal variety and lead to an optimized electrode composition, but would be entirely impractical using traditional methods and laborious to perform using the combinatorial methods described here. One must also consider the relative costs and benefits of performing this type of experiment, especially since the bulk of the science is (hopefully) reported in this thesis. Experiments performed by the author indicate the Si-M model developed for transition metals is directly applicable to rare earth metals as well. It would probably be more informative to study the influence of Sn and / or C additions on the electrochemistry of one representative Si-Al-M system with the aim of reducing the impact of diffusion limitations.

It is also useful to consider the role of the negative electrode in the complete cell. Si has the highest gravimetric and volumetric capacity of all known materials, with the exception of pure Li metal. If the negative electrode were pure Si, the capacity of a standard 18650-sized cell would be about 4100 mA h, significantly more than the current state-of-the art 2800 mA h, and yet not even double. Further advances require advanced positive electrodes. Although sputtering has been shown to be a very versatile tool for composition exploration, difficulties in producing bulk oxide phases in thin films have prevented widespread application. Only two combinatorial studies of sputtered positive electrode materials have been reported to date [79, 82]. High capacity nanostructured positive electrodes such as the carbon metal fluoride nanocomposites investigated by Badway *et al.* [154] offer high capacities (ca. 600 mA h/g) that are thought to depend more on crystal size rather than structure. Combinatorial investigations of metal variety and carbon loading seem like a natural fit between materials and methods with high potential. In any case, the combinatorial infrastructure described and applied within this thesis will help speed investigations and allow better scientific insight of advanced battery electrode materials.

Bibliography

[1] J.J. Auborn, K.W. French, S.I. Lieberma, V.K. Shah, and A. Heller. Lithium anode cells operating at room-temperature in inorganic electrolytic solutions. *Journal of The Electrochemical Society*, 120(12):1613–1619, 1973.

[2] M.S. Whittingham. The hydrated intercalation complexes of the layered disulfides. *Materials Research Bulletin*, 9(12):1681–1689, 1974.

[3] J.L. Tirado. Inorganic materials for the negative electrode of lithium-ion batteries: state-of-the-art and future prospects. *Materials Science and Engineering Reports*, 40:103–136, 2003.

[4] W.R. Mckinnon. *Physical mechanisms of intercalation batteries.* PhD thesis, University of British Columbia, 1980.

[5] M Lazzari and B Scrosati. Cyclable lithium organic electrolyte cell based on 2 intercalation electrodes. *Journal of The Electrochemical Society*, 127(3):773–774, 1980.

[6] B. Di Pietro, M. Patriarca, and B. Scrosati. On the use of rocking chair configurations for cyclable lithium organic electrolyte batteries. *Journal of Power Sources*, 8(2):289–299, 1982.

[7] T. Nagaura and K. Tozawa. Lithium ion rechargeable battery. *Progress in Batteries & Solar Cells*, 9:209–217, 1990.

[8] Zhonghua Lu, D. D. MacNeil, and J. R. Dahn. Layered Cathode Materials $Li[Ni_xLi_{1/3-2x/3}Mn_{2/3-x/3}]O_2$ for Lithium-Ion Batteries. *Electrochemical and Solid-State Letters*, 4(11):A191–A194, 2001.

[9] Zhonghua Lu, D. D. MacNeil, and J. R. Dahn. Layered $Li[Ni_xCo_{1-2x}Mn_x]O_2$ Cathode Materials for Lithium-Ion Batteries. *Electrochemical and Solid-State Letters*, 4(11):A200–A204, 2001.

[10] A.K. Padhi, K.S. Nanjundaswamy, and J.B. Goodenough. Phospho-olivines as positive-electrode materials for rechargeable lithium batteries. *Journal of The Electrochemical Society*, 144(4):1188–1194, 1997.

[11] M.M. Thackeray, W.I.F. David, P.G. Bruce, and J.B. Goodenough. Lithium insertion into manganese spinels. *Materials Research Bulletin*, 18:461–472, 1983.

[12] Jürgen O. Bessenhard, editor. *The Structural Stability of Transition Metal Oxide Insertion Electrodes for Lithium Batteries*, chapter 3.1, pages 293–317. Wiley-VCH, Toronto, 1998.

[13] Zonghai Chen, Vincent Chevrier, L. Christensen, and J. R. Dahn. Design of Amorphous Alloy Electrodes for Li-Ion Batteries A Big Challenge. *Electrochemical and Solid-State Letters*, 7(10):A310–A314, 2004.

[14] Walter A. van Schalkwijk and Bruno Scrosati, editors. *Carbon Anodes*, chapter 2, pages 79–102. Kluwer Academic / Plenum Publishers, Boston, 2002.

[15] Martin Winter and Jürgen O. Besenhard. Electrochemical lithiation of tin and tin-based intermetallics and composites. *Electrochimica Acta*, 45:31–50, 1999.

[16] A.N. Dey. Electrochemical alloying of Li with inorganic electrolytes. *Journal of The Electrochemical Society*, 118(10):1547–1549, October 1971.

[17] B.M.L. Rao, R.W. Francis, and H.A. Christopher. Lithium-aluminum electrode. *Journal of The Electrochemical Society*, 124(10):1490, October 1977.

[18] W. Weppner and R. A. Huggins. Electrochemical Investigation of the Chemical Diffusion, Partial Ionic Conductivities, and Other Kinetic Parameters in Li_3Sb and Li_3Bi. *Journal of Solid State Chemistry*, 22(3):297–308, 1977.

[19] Jovan Antula and Bernhard F. Becker. Investigation of the cathodic reduction of lithium and arsenic ions on monocrystalline silicon by cyclic voltammetry. *Journal of Physical Chemistry*, 79(23):2470–2474, 1975.

[20] C. John Wen and Robert A. Huggins. Chemical diffusion in intermediate phases in the lithium-tin system. *Journal of Solid State Chemistry*, 35(3):376–384, 1980.

[21] L.Y. Beaulieu, K.W. Eberman, R.L. Turner, L.J. Krause, and J.R. Dahn. Colossal reversible volume changes in lithium alloys. *Electrochemical and Solid-State Letters*, 4(9):A137–A140, 2001.

[22] Yoshio Idota, Tadahiko Kubota, Akihiro Matsufuji, Yukio Maekawa, and Tsutomu Miyasaka. Tin-based amorphous oxide: A high-capacity lithium-ion-storage material. *Science*, 276:1395–1397, 30 May 1997.

[23] Ian A. Courtney and J.R. Dahn. Electrochemical and *In Situ* x-ray diffraction studies of the reaction of lithium with tin oxide composites. *Journal of The Electrochemical Society*, 144(6):2045–2052, 1997.

[24] Ian A. Courtney and J.R. Dahn. Key Factors Controlling the Reversibility of the Reaction of Lithium with SnO_2 and Sn_2BPO_6 Glass. *Journal of The Electrochemical Society*, 144(9):2943–2948, 1997.

[25] J.C. Jumas. How can Mössbauer Spectroscopy help us to study Li-ion insertion mechanisms? Talk K8 at Lithium Battery Discussion 3, 2005.

[26] O. Mao, R. L. Turner, I. A. Courtney, B. D. Fredericksen, M. I. Buckett, L. J. Krause, and J. R. Dahn. Active/inactive nanocomposites as anodes for li-ion batteries. *Electrochemical and Solid-State Letters*, 2(1):3–5, 1999.

[27] Robert A. Huggins. Materials science principles related to alloys of potential use in rechargeable lithium cells. *Journal of Power Sources*, 26:109–120, 1989.

[28] J. Yang, M. Winter, and J.O. Besenhard. Small particle size multiphase Li-alloy anodes for lithium-ion-batteries. *Solid State Ionics*, 90(1-4):281–287, September 1996.

[29] E. Ferg, R.J. Gummow, A. DeKock, and M.M. Thackeray. Spinal anodes for lithium-ion batteries. *Journal of The Electrochemical Society*, 141(11):L147–L150, 1994.

[30] P. Poizot, S. Laruelle, S. Grugeon, L. Dupont, and J-M. Tarascon. Nano-sized transition-metaloxides as negative-electrode materials for lithium-ion batteries. *Nature*, 407:496–499, 2000.

[31] D. C. S. Souza, V. Pralong, A. J. Jacobson, and L. F. Nazar. A reversible solid-state crystalline transformation in a metal phosphide induced by redox chemistry. *Science*, 296:2012–2015, 2002.

[32] C.S. Wang, G.T. Wu, X.B. Zhang, Z.F. Qi, and W.Z. Li. Lithium insertion in carbon-silicon composite materials produced by mechanical milling. *Journal of The Electrochemical Society*, 145(8):2751–2758, August 1998.

[33] D.Billaud, L. Balan, A. Dailly, and P. Willmann. Novel graphite-metal materials as high specific charge negative electrodes for Li-ion batteries. Talk 53 at Lithium Battery Discussion 3, June 2005.

[34] L.Y. Beaulieu, T.D. Hatchard, A. Bonakdarpour, M.D. Fleischauer, and J.R. Dahn. Reaction of Li with Alloy Thin Films Studied by *In-Situ* AFM. *Journal of The Electrochemical Society*, 150(11):A1457–A1464, 2003.

[35] M. N. Obrovac and Leif Christensen. Structural changes in silicon anodes during lithium insertion/extraction. *Electrochemical and Solid-State Letters*, 7(5):A93–A96, 2004.

[36] T.D. Hatchard and J.R. Dahn. *In Situ* xrd and electrochemical study of the reaction of lithium with amorphous silicon. *Journal of The Electrochemical Society*, 151(6):A838–A842, 2004.

[37] Pimpa Limthongkul, Young-Il Jang, Nancy J. Dudney, and Yet-Ming Chiang. Electrochemically-driven solid-state amorphization in lithium-silicon alloys and implications for lithium storage. *Acta Materialia*, 51:1103–1113, 2003.

[38] Pimpa Limthongkul, Young-Il Jang, Nancy J. Dudney, and Yet-Ming Chiang. Electrochemically-driven solid-state amorphization in lithiummetal anodes. *Journal of Power Sources*, 119-121:604–609, 2003.

[39] P. Villars and L.D. Calvert. *Pearson's Handbook of Crystallographic Data for Intermetallic Phases.* ASM International, Inc., Materials Park, OH USA, 2^{nd} edition, 1991.

[40] A. Inoue and K. Hashimoto (Eds.). *Amorphous and Nanocrystalline Materials*, volume 3 of *Advances In Materials Research.* Springer, New York, 2001.

[41] H.-J. Güntherodt and H. Beck, editors. *Glassy Metals I Ionic Structure - Ionic Structure, Electronic Transport and Crystallization*, volume 46 of *Topics in Applied Physics.* Springer-Verlag, New York, 1981.

[42] H. Beck and H.-J. Güntherodt, editors. *Glassy Metals II Atomic Structure - Dynamics, Electronic Structure and Magnetic Properties*, volume 53 of *Topics in Applied Physics.* Springer-Verlag, New York, 1983.

[43] Ryusuke Hasegawa, editor. *Glassy Metals: Magnetic, Chemical and Structural Properties.* CRC Press, Boca Raton, FL, 1983.

[44] A. Calka, M. Madhava, D.E. Polk, B.C. Giessen, H. Matyja, and J. Vander Sande. A transition-metal-free amorphous alloy: $Mg_{.70}Zn_{.30}$. *Scripta Metallurgica*, 11(1):65–70, 1977.

[45] A. Inoue, M. Yamamoto, H.M. Kimura, and T. Masumoto. Ductile aluminum-base amorphous alloys with two separate phases. *Journal of Materials Science Letters*, 6:194–196, 1987.

[46] A. Inoue, Y Bizen, H. M. Kimura, T. Masumoto, and M. Sakamoto. Compositional range, thermal stability, hardness and electrical resistivity of amorphous alloys in Al-Si (or Ge)-transition metal systems. *Journal of Materials Science*, 23:3640–3647, 1988.

[47] R.A. Dunlap and K. Dini. Amorphization of rapidly quenched quasicrystalline Al-transition metal alloys by the addition of Si. *J. Mater. Res.*, 1(3):415–419, May/Jun 1986.

[48] R.O. Suzuki, Y. Komatsu, K.F. Kobayashi, and P.H. Shingu. Formation and crystallization of Al-Fe-Si amorphous alloys. *Journal of Materials Science*, 18:1195–1201, 1983.

[49] K. Dini and R.A. Dunlap. The relationship of the quasicrystalline icosahedral phase to the amorphous structure in rapidly quenched Al-Mn-Si and Al-Fe-Si alloys. *J. Phys. F: Met. Phys.*, 16:1917–1925, 1986.

[50] H.S. Chen and C.H. Chen. Structural relaxation in the $Al_{86}Mn_{14}$ quasicrystal. *Physical Review B*, 33(1):668–671, 1986.

[51] D.V. Louzguine, A. Takeuchi, and A. Inoue. New Amorphous Alloys in Al-Si-Fe-Ni and Al-Si-Fe-Co Systems and Their Crystallization Behaviour. *Materials Transactions, JIM*, 38(7):595–598, 1997.

[52] D.V. Louzguine, A. Takeuchi, and A. Inoue. New amorphous alloys in Al-Si-Fe-TM (TM = Cr, Mn, V) systems and their crystallization behavior. *Journal of Materials Science Letters*, 17(17):1439–1442, 1998.

[53] D.V. Louzguine and A. Inoue. Multicomponent si-based amorphous alloys produced by melt spinning and their crystallization behaviour. *Materials Transactions, JIM*, 38(12):1095–1099, 1997.

[54] D.V. Louzguine and A. Inoue. *Amorphous and Partially Crystalline Alloys Produced by Rapid Solidification of The Melt in Multicomponent (Si,Ge)-Al-Transition Metal Systems*, chapter 5, pages 133–165. Volume 3 of *Advances In Materials Research* [40], 2001.

[55] J.Q. Wang, C.F. Qian, M.G. Tseng, and M.Q. Lü. Crystallization behaviour of new amorphous Al-Fe-V-Si-Mm alloy. *Scripta Metallurgica et Materialia*, 32(5):663–668, 1995.

[56] Japan Sony Corp. Sony's new nexelion hybrid lithium ion batteries to have thirty-percent more capacity than conventional offering. Sony Press Release 05-006E, February 15 2005.

[57] L. Y. Beaulieu, K. C. Hewitt, R. L. Turner, A. Bonakdarpour, A. A. Abdo, L. Christensen, K. W. Eberman, L. J. Krause, and J. R. Dahn. The electrochemical reaction of Li with amorphous Si-Sn alloys. *Journal of The Electrochemical Society*, 150(2):A149–A156, 2003.

[58] T.D. Hatchard, J.M. Topple, M.D. Fleischauer, and J.R. Dahn. Electrochemical performance of SiAlSn films prepared by combinatorial sputtering. *Electrochemical and Solid-State Letters*, 6(7):A129–A132, 2003.

[59] K. Kennedy, T. Stefansky, G. Davy, V.F. Zackay, and E.R. Parker. Rapid method for determining ternary-alloy phase diagrams. *Journal of Applied Physics*, 36(12):3808–3810, 1965.

[60] J.J. Hanak. The 'multiple-sample concept' in materials research: Synthesis, compositional analysis and testing of entire multicomponent systems. *Journal of Materials Science*, 5:964–971, 1970.

[61] Eric W. McFarland and W. Henry Weinberg. Combinatorial approaches to materials discovery. *Trends In Biotechnology*, 17:107–115, March 1999.

[62] X.-D. Xiang, Xiaodong Sun, Gabriel Briceño, Yulin Lou, Kai-An Wang, Hauyee Chang, William G. Wallace-Freedman, Sun-Wei Chen, and Peter G. Schultz. A combinatorial approach to materials discovery. *Science*, 268:1738–1740, June 23 1995.

[63] C.J. Warren, R.C. Haushalter, and L. Matsiev. Method for creating and testing a combinatorial array employing individually addressable electrodes. US patent office, February 13, 2001. US Patent 6,187,164.

[64] P.G. Schultz, X. Xiaodong, and I. Goldwasser. Combinatorial synthesis of novel materials. US patent office, December 4, 2001. US Patent 6,326,090 B1.

[65] Erik Reddington, Anthony Sapienza, Bogdan Gurau, Rameshkrishnan Viswanathan, S. Sarangapani, Eugene S. Smotkin, and Thomas E. Mallouk. Combinatorial electrochemistry: A highly parallel, optical screening method for discovery of better electrocatalysts. *Science*, 280:1735–1737, 12 June 1998.

[66] Melani G. Sullivan, Henry Utomo, Paul J. Fagan, and Michael D. Ward. Automated electrochemical analysis with combinatorial electrode arrays. *Analytical Chemistry*, 71(19):4369–4375, October 1 1999.

[67] M.D. Fleischauer, T.D. Hatchard, G.P. Rockwell, J.M. Topple, S. Trussler, S.K. Jericho, M.H. Jericho, and J.R. Dahn. Design and testing of a 64-channel combinatorial electrochemical cell. *Journal of The Electrochemical Society*, 150(11):A1465–A1469, 2003.

[68] Rongzhong Jiang and Deryn Chu. A combinatorial approach toward electrochemical analysis. *Journal of Electroanalytical Chemistry*, 527(1):137–142, 2002.

[69] Kazunori Takada, Kenjiro Fujimoto, Takayoshi Sasaki, and Mamoru Watanabe. Combinatorial electrode array for high-throughput evaluation of combinatorial library for electrode materials. *Applied Surface Science*, 223:210–213, 2003.

[70] A.D. Spong, G. Vitins, S. Guerin, B.E. Hayden, A.E. Russell, and John R. Owen. Combinatorial arrays and parallel screening for positive electrode discovery. *Journal of Power Sources*, 119-121:778–783, 2003.

[71] W.C. West, J.F. Whitacre, V. White, and B.V. Ratnakumar. Fabrication and testing of all solid-state microscale lithium batteries for microspacecraft applications. *Journal of Micromechanics and Microengineering*, 12(1):58–62, 2002.

[72] Ikuo Yanase, Takugo Ohtaki, and Mamoru Watanabe. Application of combinatorial process to $LiCo_{1-X}Mn_XO_2$ ($0 \leq X \leq 0.2$) powder synthesis. *Solid State Ionics*, 151:189–196, 2002.

[73] A. Spong, G. Vittens, and J. Owen. Combinatorial arrays and parallel screening for positive electrode discovery. Poster 267 at International Meeting on Lithium Batteries 11, June 2002.

[74] T.D. Hatchard, A. Bonakdarpour, M. Fleischauer, J. Mueller-Neuhaus, S. Trussler, K. Hewitt, and J.R. Dahn. A Combinatorial Materials Science Study of the Si-Al-Sn Ternary System. Poster 256 at International Meeting on Lithium Batteries 11, June 2002.

[75] J. Whitacre, W. West, and R. Bugga. A Combinatorial Study Of $LiMn_xNi_{2-x}O_4$ Cathode Materials. Talk 149 at 202^{nd} meeting of The Electrochemical Society, October 2002.

[76] M. Devenney, S.W. Donne, and S. Gorer. Application of combinatorial methodologies to the synthesis and characterization of electrolytic manganese dioxide. *Journal of Applied Electrochemistry*, 34:643–651, 2004.

[77] M.D Fleischauer, T.D. Hatchard, A. Bonakdarpour, and J.R. Dahn. Combinatorial investigations of advanced Li-ion rechargeable battery electrode materials. *Measurement Science and Technology*, 16:212–220, 2005.

[78] R.B. van Dover, L.F. Schneemeyer, and R. M. Fleming. Discovery of a useful thin-film dielectric using a composition-spread approach. *Nature*, 392:162–164, 12 March 1998.

[79] J.F. Whitacre, W.C. West, and B.V. Ratnakumar. A combinatorial study of $LiMn_xNi_{2-x}O_4$ cathode materials using microfabricated solid-state electrochemical cells. *Journal of The Electrochemical Society*, 150(12):A1676–A1683, 2003.

[80] J.R. Dahn, S. Trussler, T.D. Hatchard, A. Bonakdarpour, J.N. Meuller-Neuhaus, K.C. Hewitt, and M. Fleischauer. Economical sputtering system to produce large-size composition-spread libraries having linear and orthogonal stoichiometry variations. *Chemistry of Materials*, 14(8):3519–3523, 2002.

[81] T.D. Hatchard, J.R. Dahn, S. Trussler, M. Fleischauer, A. Bonakdarpour, J.R. Mueller-Neuhaus, and K.C. Hewitt. The amorphous range in sputtered Si-Al-Sn films as determined by Combinatorial Materials Science. *Thin Solid Films*, 443:144–150, 2003.

[82] A. Bonakdarpour, K.C. Hewitt, T.D. Hatchard, M.D. Fleischauer, and J.R. Dahn. Combinatorial Synthesis and Rapid Characterization of $Mo_{1-x}Sn_x$ ($0 \leq x \leq 1$) Thin Films. *Thin Solid Films*, 440:11–18, 2003.

[83] M.D. Fleischauer and J.R. Dahn. Combinatorial Investigations of the Si-Al-Mn System for Li-Ion Battery Applications. *Journal of The Electrochemical Society*, 151(8):A1216–A1221, 2004.

[84] A. Bonakdarpour and J.R. Dahn. Combinatorial synthesis of $Li[Ni_xCo_{1-2x}Mn_x]O_2$. Poster 144 at 202^{nd} Meeting of The Electrochemical Society, October 2002.

[85] M.D. Fleischauer, J.M. Topple, T.D. Hatchard, and J.R. Dahn. Understanding the effect of composition on amorphous alloy electrochemical performance. Poster 354 at 204^{th} Meeting of The Electrochemical Society, October 2003.

[86] M. D. Fleischauer, J. M. Topple, and J. R. Dahn. Combinatorial Investigations of Si-M (M = Cr + Ni, Fe, Mn) Thin Film Negative Electrode Materials. *Electrochemical and Solid-State Letters*, 8(2):A137–A140, 2005.

[87] M.D. Fleischauer, M.N. Obrovac, J.D. McGraw, R.A. Dunlap, J.M. Topple, and J.R. Dahn. Al-M (M = Cr, Fe, Mn, Ni) thin film negative electrode materials. *36 pages, 15 figures submitted July 10 to Journal of The Electrochemical Society*, 2005.

[88] A. Van der Ven and G. Ceder. Ordering in $Li_x(Ni_{0.5}Mn_{0.5})O_2$ and its relation to charge capacity and electrochemical behavior in rechargeable lithium batteries. *Electrochemical Communications*, 6:1045–1050, 2004.

[89] D. Morgan, G Ceder, MY Saidi, J Barker, J Swoyer, H Huang, and G Adamson. Experimental and computational study of the structure and electrochemical properties of monoclinic $Li_xM_2(PO4)_3$ compounds. *Journal of Power Sources*, 119-121:755–759, 2003.

[90] F.R. de Boer, R. Boom, W.C.M. Mattens, A.R. Miedema, and A.K. Niessen. *Cohesion in Metals*, volume 1 of *Transition Metal Alloys*. North-Holland, New York, 1988.

[91] M.D. Fleischauer. Combinatorial investigations of silicon-aluminum-manganese films for lithium-ion battery applications. Master's thesis, Dalhousie University, Halifax, Nova Scotia CANADA, April 2003.

[92] Donald M. Mattox. *Handbook of Physical Vapor Deposition (PVD) Processing Film Formation, Adhesion, Surface Preparation and Contamination Control.* Noyes Publications, Park Ridge, NJ USA, 1998.

[93] John L. Vossen and Werner Kern, editors. *Thin Film Processes.* Academic Press, Inc., 1978.

[94] Kenjiro Fujimoto, Kazunori Takada, Takayoshi Sasaki, and Mamoru Wantanabe. Combinatorial approach for powder preparation of pseudo-ternary system $LiO_{0.5}XTiO_2$ (X: $FeO_{1.5}$, $CrO_{1.5}$ and NiO). *Applied Surface Science*, 223:49–53, 2004.

[95] J. Ballon, V. Comparat, and J. Pouxe. The blade chamber: a solution for curved gaseous detectors. *Nuclear Instruments and Methods in Physics Research*, 217:213–216, 1983.

[96] N.N. Greenwood and T.C. Gibb. *Mössbauer Spectroscopy.* Chapman and Hall Ltd., London, 1971.

[97] Harry J. Lipkin. Some simple features of the Mössbauer effect. *Annals of Physics*, 9(2):332–339, 1960.

[98] D.G. Rancourt and J.Y. Ping. Voigt-based methods for arbitrary-shape static hyperfine parameter distributions in Mössbauer spectroscopy. *Nuclear Instruments and Methods in Physics Research*, B58:85–97, 1991.

[99] Ken Lagarec and Denis G. Rancourt. Recoil Mössbayer Spectral Analysis Software for Windows version 1.0. Department of Physics, University of Ottawa, 1998.

[100] J.D. McGraw, M.D. Fleischauer, J.R. Dahn, and R.A. Dunlap. A mössbauer effect study of fe-si prepared by combinatorial materials science methods. 11^{th} Canadian Forces / Defence Research and Development Canada International Meeting on Naval Applications of Materials Technology, Dartmouth, NS., June 7-9 2005.

[101] David B. Williams and C. Barry Carter. *Transmission Electron Microscopy : A Textbook for Materials Science.* Plenum Press, New York, 1996.

[102] Joseph I. Goldstein, Dale E. Newbury, Patrick Echlin, David C. Joy, A.D. Romig, Jr., Charles E. Lyman, Charles Fiori, and Eric Lifshin. *Scanning Electron Microscopy and X-Ray Microanalysis.* Plenum Press, New York, 1992.

[103] V.K. Cumyn, M.D. Fleischauer, T.D. Hatchard, and J.R. Dahn. Design and testing of a low-cost multichannel pseudopotentiostat for quantitative combinatorial electrochemical measurements on large electrode arrays. *Electrochemical and Solid-State Letters*, 6(6):E15–E18, 2003.

[104] Andreas Netz, Robert A. Huggins, and Werner Weppner. The formation and properties of amorphous silicon as negative electrode reactant in lithium systems. *Journal of Power Sources*, 119-121:95–100, 2003.

[105] Young-Lae Kim, Heon-Young Lee, Serk-Won Jang, Sung-Hwan Lim, Seung-Joo Lee, Hong-Koo Baik, Young-Soo Yoon, and Sung-Man Lee. Electrochemical characteristics of Co/Si alloy and multilayer films as anodes for lithium ion microbatteries. *Electrochimica Acta*, 48:2593–2597, 2003.

[106] W.J. Weydanz, M. Wohlfahrt-Mehrens, and R.A. Huggins. A room temperature study of the binary lithiumsilicon and the ternary lithiumchromiumsilicon system for use in rechargeable lithium batteries. *Journal of Power Sources*, 81-82:237–242, 1999.

[107] H. Dong, X.P. Ai, and H.X. Yang. Carbon/BaFeSi alloy composite as high capacity anode materials for Li-ion batteries. *Electrochemical Communications*, 5:952–957, 2003.

[108] Jae-Bum Kim, Heon-Young Lee, Kawn-Soo Lee, Sung-Hwan Lim, and Sung-Man Lee. Fe/Si multi-layer thin film anodes for lithium rechargeable thin film batteries. *Electrochemical Communications*, 5:544–548, 2003.

[109] Heon-Young Lee and Sung-Man Lee. Graphite FeSi alloy composites as anode materials for rechargeable lithium batteries. *Journal of Power Sources*, 112:649–654, 2002.

[110] G.X. Wang, L. Sun, D.H. Bradhurst, S. Zhong, S.X. Dou, and H.K. Liu. Innovative nanosize lithium storage alloys with silica as active centre. *Journal of Power Sources*, 88:278–281, 2000.

[111] G.X. Wang, L. Sun, D.H. Bradhurst, S. Zhong, S.X. Dou, and H.K. Liu. Nanocrystalline NiSi alloy as an anode material for lithium-ion batteries. *Journal of Alloys and Compounds*, 306:249–252, 2000.

[112] Seung-Joo Lee, Hong-Koo Baik, and Sung-Man Lee. An all-solid-state thin film battery using LISIPON electrolyte and SiV negative electrode films. *Electrochemical Communications*, 5:32–35, 2003.

[113] Seung-Joo Lee, Heon-Young Lee, Hong-Koo Baik, and Sung-Man Lee. SiZr alloy thin-film anodes for microbatteries. *Journal of Power Sources*, 119-121:113–116, 2003.

[114] Robert A. Huggins. Alternative materials for negative electrodes in lithium systems. *Solid State Ionics*, 152-153:61–68, 2002.

[115] ASM International The Materials Information Society. Binary alloy phase diagrams second edition plus updates.

[116] R. Hultgren, P.D. Desai, D.T. Hawkins, M. Gleiser, and K.K. Kelly. *Selected Values of Thermodynamic Properties of Binary Alloys.* American Society for Metals, Ohio, 1973.

[117] J. Desimoni and F.H. Sánchez. Overview of the Mössbauer results obtained on silicon-rich iron silicide epitaxial phases on Si. *Hyperfine Interactions*, 122:277–307, 1999.

[118] J.P. Pereira-Ramos, R. Messina, and J. Perichon. Sulfone-based electrolytes for lithium intercalation batteries. *Journal of Power Sources*, 16(3):193–204, 1985.

[119] A. Tranchant, R. Messina, and J. Perjchon. Electrochemical behaviour of copper oxide in molten dimethyl sulfone at 150 °C. *Journal of Electroanalytical Chemistry*, 233:189–198, 1987.

[120] A. Tranchant, R. Messina, and J. Perichon. Electrochemical Behaviour Of CuO + V_2O_5 Systems In Molten Dimethyl Sulfone At 150 °C. *Journal of Electroanalytical Chemistry*, 242:181–190, 1988.

[121] D. Larcher, L. Y. Beaulieu, O. Mao, A. E. George, and J. R. Dahn. Study of the Reaction of Lithium with Isostructural A_2B and Various Al_xB Alloys. *Journal of The Electrochemical Society*, 147(5):1703–1708, 2000.

[122] M.J. Lindsay, G.X. Wang, and H.K. Liu. Al-based anode materials for Li-ion batteries. *Journal of Power Sources*, 119-121:84–87, 2003.

[123] K. Masui, S. Maruno, S. Sakakibara, and T. Kawaguchi. Formation of amorphous Al-transition metal (TM: Fe, Co, Ni) binary alloy films by RF-sputtering. *Journal of Non-Crystalline Solids*, 74:271–284, 1985.

[124] K. Masui, H. Nakamoto, S. Maruno, T. Kawaguchi, and S. Sakakibara. Formation of amorphous Al-Cr and Al-Mn alloy films by rf sputtering. *Journal of Non-Crystalline Solids*, 124:121–130, 1990.

[125] Ou Mao, R.A. Dunlap, I.A. Courtney, and J.R. Dahn. In Situ Mössbauer Effect Studies of the Electrochemical Reaction of Lithium with Mechanically Alloyed Sn_2Fe. *Journal of The Electrochemical Society*, 145(12):4195–4201, 1998.

[126] I.A. Courtney, J.S. Tse, Ou Mao, J. Hafner, and J.R. Dahn. *Ab initio* calculation of the lithium-tin voltage profile. *Physical Review B*, 58(23):15583–15588, 1998.

[127] Ou Mao, R.A. Dunlap, and J.R. Dahn. In situ ^{57}Fe and ^{119}Sn Mössbauer effect studies of the electrochemical reaction of lithium with mechanically alloyed SnFe. *Solid State Ionics*, 118:99–109, 1999.

[128] R.A. Dunlap, J.R. Dahn, D.A. Eelman, and G.R. MacKay. Microstructure of supersaturated fcc AlFe alloys: A comparison of rapidly quenched and mechanically alloyed $Al_{98}Fe_2$. *Hyperfine Interactions*, 116:117–126, 1998.

[129] R A Dunlap, D J Lloyd, I A Christie, G Stroink, and Z M Stadnik. Physical properties of rapidly quenched Al-Fe alloys. *J. Phys. F: Met. Phys.*, 18:1329–1341, 1988.

[130] S. Nasu, U. Gonser, P. H. Shingu, and Y Murakami. ^{57}Fe Mössbauer spectra in splat quenched Al-0.5, 1, 3 and 5 at % Fe alloys. *J. Phys. F: Met. Phys.*, 4(2):L24–L28, 1974.

[131] L. Y. Beaulieu, D. Larcher, R. A. Dunlap, and J. R. Dahn. Reaction of Li with Grain-Boundary Atoms in Nanostructured Compounds. *Journal of The Electrochemical Society*, 147(9):3206–3212, 2000.

[132] Toyohiko J. Konno and Robert Sinclair. Crystallization and decomposition of co-sputtered amorphous silicon-aluminum thin films. *Materials Chemistry and Physics*, 35:99–113, 1993.

[133] G. Radnoczi, A. Robertsson, H.T.G. Hentzell, S.F. Gong, and M.-A. Hasan. Al induced crystallization of a-Si. *Journal of Applied Physics*, 69(9):6394–6399, 1991.

[134] J. R. A. Carlsson, J.-E. Sundgren, X.-H. Li, L. D. Madsen, and H. T. G. Hentzell. Predicting the crystallization temperature variation with composition for amorphous silicon-based binary alloy thin films. *Journal of Applied Physics*, 81(3):1150–1156, 1996.

[135] N.C. Goel and J.R. Cahoon. The Al-Li-Si System (Aluminum-Lithium-Silicon). *Journal of Phase Equilibria*, 12(2):225–230, 1991.

[136] D. Kevorkov, J. Gröbner, and R. Schmid-Fetzer. The Al+Li+Si System 1. A New Structure Type $Li_8Al_3Si_5$ and the Ternary Solid-State Phase Equilibria. *Journal of Solid State Chemistry*, 156:500, 2001.

[137] Laurent Spina, Yong Zhong Jia, Bernard Ducourant, Monique Tillard, and Claude Belin. Compositional and structural variations in the ternary system Li-Al-Si. *Zeitschrift fur Kristallographie*, 218(11):740–746, 2003.

[138] S.S. Misra. Investigations on the Li-Al-Si Alloy/Iron Disulfide Molten Salt Battery System. *Journal of The Electrochemical Society*, 130(8):C309, 1983.

[139] Joint Committee on Powder Diffraction Standards. Associateship at the National Bureau of Standards. *Powder diffraction data : from the Joint Committee on Powder Diffraction Standards Associateship at the National Bureau of Standards : data book / by JCPDS Associateship at the National Bureau of Standards, Marlene C. Morris ... [et al.].* The Committee, Swarthmore, Pa, 1976.

[140] C. John Wen and Robert A. Huggins. Chemical diffusion in intermediate phases in the lithium-silicon system. *Journal of Solid State Chemistry*, 37:271–278, 1981.

[141] Herbert Schäfer, Brigitte Eisenmann, and Wiking Müller. Zintl phases: transitions between metallic and ionic bonding. *Angewandte Chemie-International Edition*, 12(9):694–712, 1973.

[142] V. Raghavan. Al-Fe-Si (Aluminum-Iron-Silicon). *Journal of Phase Equilibria*, 23(4):362–366, 2002.

[143] Nataliya Krendelsberger, Franz Weitzer, and Julius C. Schuster. On the Constitution of the System Al-Mn-Si. *Metallurgical and Materials Transactions*, 33A:3311–3319, November 2002.

[144] Klaus W. Richter and Herbert Ipser. The AlNiSi phase diagram between 0 and 33.3 at. % Ni. *Intermetallics*, 11:101–109, 2003.

[145] Klaus W. Richter, Karthik Chandrasekaran, and Herbert Ipser. The AlNiSi phase diagram. Part II: phase equilibria between 33.3 and 66.7 at. % Ni. *Intermetallics*, 12:545–554, 2004.

[146] Robert L. Turner, Brian D. Fredericksen, Larry J. Krause, Jeffrey R. Dahn, Dominique C. Larcher, Ian A. Courtney, and Ou Mao. Amorphous electrode compositions. US patent office, March 2, 2004. US Patent 6,699,336.

[147] Robert L. Turner, Donald J. McClure, Larry J. Krause, Mary M. Buckett, Jeffrey R. Dahn, and Ou Mao. Electrode for a lithium battery. US patent office, March 26, 1998. US Patent 6,203,944.

[148] A. Anani and R.A. Huggins. Multinary alloy electrodes for solid state batteries I. A phase diagram approach for the selection and storage properties determination of candidate electrode materials. *Journal of Power Sources*, 38:351–362, 1992.

[149] A. Anani and R.A. Huggins. Multinary alloy electrodes for solid state batteries II. A new Li-Si-Mg alloy negative electrode material for use in high energy density rechargeable lithium cells. *Journal of Power Sources*, 38:363–372, 1992.

[150] M. Roberts, G. Vitins, A. Spong, and J. Owen. High Throughput Investigations of Battery Electrodes. Talk K2 at Lithium Battery Discussion 3, June 2005.

[151] T.D. Hatchard and J.R. Dahn. Study of the electrochemical performance of sputtered $si_{1-x}sn_x$ films. *Journal of The Electrochemical Society*, 151(10):A1628–A1635, 2004.

[152] Zonghai Chen, L. Christensen, and J.R. Dahn. Large-volume-change electrodes for li-ion batteries of amorphous alloy particles held by elastomeric tethers. *Electrochemical Communications*, 5:919–923, 2003.

[153] N. Saunders and A.P. Miodownik. *CALPHAD Calculation of Phase Diagrams A comprehensive guide.* Pergamon, London, 1998.

[154] F. Badway, F. Cosandey, N. Pereira, and G. G. Amatucci. Carbon metal fluoride nanocomposites high-capacity reversible metal fluoride conversion materials as rechargeable positive electrodes for li batteries. *Journal of The Electrochemical Society*, 150(10):A1318–A1327, 2003.

[155] J.R. Chelikowsky and J.C. Philips. Quantum-defect theory of heats of formation and structural transition energies of liquid and solid simple metal alloys and compounds. *Physical Review B*, 17(6):2453–2477, 1978.

Appendix A

Macroscopic Atom Model Details

The macroscopic atom model considers interactions between one atom of metal A surrounded by atoms of metal B. de Boer *et al.* [90] assume the bulk of the interaction between atoms A and B can be described by the electron density at the boundary of the Wigner-Seitz cell n_{ws} and the electric charge chemical potential ϕ^*. Energy is required to remove discontinuities in electron density and released when two dissimilar metals are brought in to contact. n_{ws} can be closely approximated using the relationship

$$(n_{ws})^2 = \frac{K}{V}$$

where K is the bulk modulus and V is the molar volume of a pure metal. Values of ϕ^* were experimentally determined from the work function of pure metals, adjusted for experimental uncertainty. The heat of formation can therefore be described as

$$\Delta H^{for} \propto \Big[- P(\Delta\phi^*)^2 + Q(\Delta n_{ws}^{1/3})^2 \Big] \tag{A.1}$$

where $\Delta n_{ws}^{1/3}$ and $\Delta\phi^*$ are the differences in electron density and chemical potential, respectively. The proportionality constants P and Q will be discussed shortly. Chelikowsky and Philips noted the use of $n_{ws}^{1/3}$ instead of Δn_{ws} leads to a more accurate representation of electron density and units compatible with ϕ^* [155]. Further improvements to the predictive ability of the macroscopic atom model are achieved when an additional negative term, R^*, is added to the expression above.

A numerical expression for heat of formation can be determined by following the arguments of Chapter 2 of [90]. The adhesion energy of two van der Waals substances A and B in contact is given by

$$-\Delta\gamma_{A-B}^{\text{adhesion, } T} = \gamma_A^T + \gamma_B^T - \gamma_{A-B}^{\text{interface, } T}$$

where

$$\Delta\gamma_{A-B}^{\text{adhesion, } T} = -2\sqrt{\gamma_A^T \gamma_B^T}.$$

The interfacial energy per unit contact area is thus

$$\gamma_{A-B}^{\text{interface, } T} = \left[\sqrt{\gamma_A^T} - \sqrt{\gamma_B^T}\right]^2.$$

γ_i^T is the surface energy of atom i at temperature T. All temperature superscripts can be dropped because all calculations assume a temperature of 0 K. γ_i is proportional to $\Delta H^{vap}/V^{2/3}$ which is in turn proportional to n_{ws}. The interfacial energy $\Delta H_{\text{A in B}}^{\text{interface}}$ is then given by

$$\Delta H_{\text{A in B}}^{\text{interface}} = V_A^{2/3} Q'' \left[(n_{ws}^{1/2})_A - (n_{ws}^{1/2})_B\right]$$

where $V_A^{2/3}$ is the molar surface area of element A and Q'' is a proportionality constant. This expression can be re-written as

$$\Delta H_{\text{A in B}}^{\text{interface}} = V_A^{2/3} Q \frac{\left[(n_{ws}^{1/3})_A - (n_{ws}^{1/3})_B\right]^2}{(n_{ws}^{-1/3})_A + (n_{ws}^{-1/3})_B}$$

for small differences in n_{ws}.

The total heat of formation is the result of van der Waals and ionic interactions. $\Delta H_{\text{A in B}}^{\text{interface (ionic)}}$ is given by

$$\Delta H_{\text{A in B}}^{\text{interface (ionic)}} = -P \frac{V_A^{2/3}}{(n_{ws}^{-1/3})_{av}} [\phi_A^* - \phi_B^*]^2.$$

P has a numerical value of 14.2 for alloys of two metals each with a valence larger than two and 10.7 otherwise [90]. The value of Q is 9.4 P [90].

The total heat of formation is then given by

$$\Delta H_{\text{A in B}}^{\text{interface}} = \frac{V_A^{2/3}}{(n_{ws}^{-1/3})_{av}} [-P(\Delta\phi^*)^2 + Q(\Delta n_{ws}^{1/3})^2]$$

which bears a remarkable resemblance to Eq. A.1.

Additional model refinements include the ability to deal with non-dilute alloys and semiconductor-metal transitions. The above discussion assumes an atom of element A is completely surrounded by atoms of element B. The term f_B^A describes the degree to which atoms of element A are surrounded by atoms of element B. ($f_B^A = 1$ indicates dilute A in B). The heat of formation per mole of A is then

$$\Delta H_{\text{per mole A}}^{\text{for}} = f_B^A \Delta H_{\text{A in B}}^{\text{interface}}.$$

The degree of coverage depends on the relative sizes and concentrations of A and B. The surface concentration of element A, c_S^A, is given by

$$c_A^S = \frac{c_A V_A^{2/3}}{c_A V_A^{2/3} + (1 - c_A) V_B^{2/3}}$$

where c_A is the molar concentration of A. f_B^A is then given by

$$f_B^A = c_B^S = 1 - c_A^S, \quad \text{or} \quad f_B^A = c_B^S[1 + 8(c_A^S c_B^S)^2]$$

for the cases of statistical (random) and actual ordering, respectively.

Molar volume changes can also be expected for non-dilute alloys. The molar volume of an alloy of element A can be approximated using

$$\left(V_A^{2/3}\right)_{\text{alloy}} = \left(V_A^{2/3}\right)_{\text{pure A}} [1 + a f_B^A (\phi_A^* - \phi_B^*)]$$

where a is a parameter corresponding to experimentally measured volume contractions. $a = 0.14$ for alkaline metals, 0.10 for divalent metals, 0.07 for noble and trivalent metals and 0.04 for all other metals [90].

Finally, semiconductor-metal and gas-solid transitions can be dealt with by including a transition heat term $\Delta H_{\text{A}}^{\text{trans}}$ so that the total calculated heat of formation is given by

$$\Delta H_{\text{calc}}^{\text{for}} = c_A \left(\Delta \bar{H}_{\text{A in B}}^{\text{interface}} + \Delta H_{\text{A}}^{\text{trans}} \right).$$

Values of $\Delta H_{\text{A}}^{\text{trans}}$ are listed in Table II-2 of [90] (reproduced as Table A.1 A).

In summary, the heat of formation for an alloy $\text{A}_{c_A}\text{B}_{c_B}$ can be estimated knowing only the electron density at the boundary of the Wigner-Seitz cell n_{ws}, the work function ϕ^*, the molar volume V, the common oxidation state, transition heat ΔH^{trans} and fit parameter R^* using

$$\frac{\Delta \bar{H}_{\text{A in B}}^{\text{interface}}}{V_{\text{A}}^{2/3}} = \frac{[-P(\Delta\phi^*)^2 + Q(\Delta n_{ws}^{1/3})^2 - R^*]}{(n_{ws}^{-1/3})_{\text{av}}}. \tag{A.2}$$

Tables A.1, A.3 and A.2 [90] list all values required to perform calculations. Agreement between calculated and experimental values is generally within 5 - 10 kJ/mol. Predictions are more accurate for compositions not far from unity (out to approximately $\text{A}_{0.8}\text{B}_{0.2}$) and for alloys involving at least one transition metal.

Element	ΔH^{trans}
Hydrogen	100
Boron	30
Carbon	180
Nitrogen	310
Silicon	34
Phosphorus	17
Germanium	25

Table A.1: ΔH^{trans} values for those elements that undergo a gas-solid or semiconductor-metal transition [90].

The computer program listed in Table V-3 of [90] was translated to the C++ programming language by Mark Obrovac of 3M Co. He pointed out line 9 of the code in Table V-3 should include the expression `z=31` rather than `a=31`. The author built a user interface around Obrovac's code so that the heat of formation for all compositions any two metals listed in the tables of Cohesion of Metals [90] can be calculated with the press of a button. A second option permits the direct calculation and display of the heat of formation for any alloy A_xB_{1-x}. This program is available from the author and on the main Dahn lab computer server under the name `MacroscopicAtomModel.exe`.

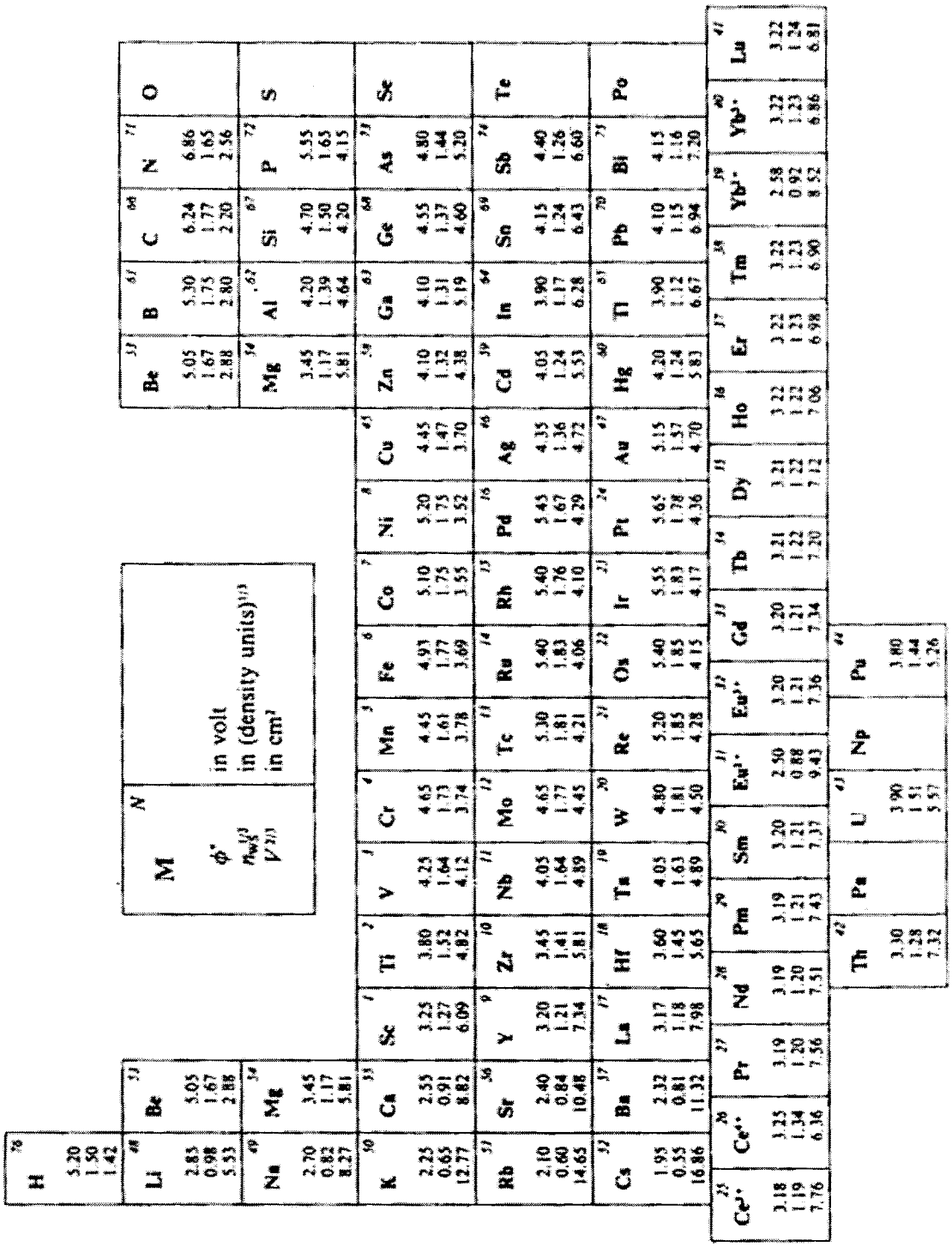

Table A.2: Fig. 2.4 from deBoer *et al.* [90]. Values of ϕ^* (chemical potential, units of volts), $n_{ws}^{1/3}$ (electron density at boundary of Wigner-Seitz cell, units of density$^{1/3}$), and $V^{2/3}$ (molar surface area, units of cm^2) are listed for most elements.

Transition metals

Ca 0.4	Sc 0.7	Ti 1.0	V 1.0	Cr 1.0	Mn 1.0	Fe 1.0	Co 1.0	Ni 1.0	Cu 0.3
Sr 0.4	Y 0.7	Zr 1.0	Nb 1.0	Mo 1.0	Tc 1.0	Ru 1.0	Rh 1.0	Pd 1.0	Ag 0.15
Ba 0.4	La 0.7	Hf 1.0	Ta 1.0	W 1.0	Re 1.0	Os 1.0	Ir 1.0	Pt 1.0	Au 0.3
	Th 0.7	U 1.0	Pu 1.0						

Non transition metals

Li 0	Be 0.4	B 1.9	C 2.1	N 2.3
Na 0	Mg 0.4	Al 1.9	Si 2.1	P 2.3
K 0	Zn 1.4	Ga 1.9	Ge 2.1	As 2.3
Rb 0	Cd 1.4	In 1.9	Sn 2.1	Sb 2.3
Cs 0	Hg 1.4	Tl 1.9	Pb 2.1	Bi 2.3

Table A.3: Fig. 2.28 from deBoer *et al.* [90]. The value of R^*/P used in Eq. A.2 for an alloy of A and B is the product of the values listed for each.

Appendix B

Mask Profile Calculation Routine

The deposition flux profile $J(\vec{q})$ opposite a sputtering target can be approximated as a Gaussian function, given by

$$J(\vec{q}) = A \exp -(\vec{q}/\omega)^2. \tag{B.1}$$

$\vec{q}$ is the vector from the point where the axis of the target meets the substrate to the point on the substrate where the deposition occurs, as shown in Figure B.1. ω is the width of the Gaussian. $\vec{q}$ in Eq. B.1 can be considered in terms of the rest of the sputtering machine as shown in Figure 2.5. R and s are the radial distances from the centre of the sputtering machine to the centre of the target and the point of deposition, respectively. $|\vec{q}|$ is then given by

$$|\vec{q}| = \sqrt{R^2 + s^2 - 2sR\cos\theta} \tag{B.2}$$

where θ is the angle between $\vec{s}$ and $\vec{R}$. The total deposition $D(s)$ at a given radius s (mass per unit length) is calculated by integrating the flux along the arc with radius s, as shown in Figure B.2. This is given by

$$D(s) = 2A \int_0^{\theta_{max}} \exp -(\vec{q}/\omega)^2 s d\theta. \tag{B.3}$$

θ_{max} defines the arc length and is the angular limit of the mask at radius s.

$D(s)\,ds$ calculates the total number of atoms that pass through a slit of width ds and length $s\,d\theta$. This amount of material is deposited on an area $2\pi s\,ds$ when the table is rotated. The mass per unit area B as a function of radius s is then given by

$$B(s) = \frac{D(s)\,ds}{2\pi\, s\, ds}, \tag{B.4}$$

where $B(s)$ is the desired deposition profile (mass per unit area). Thick dashed lines in Figure 2.4 indicate 'constant', 'linear in' and 'linear out' profiles. Mask openings are determined by numerically solving the system of Eqn's B.2, B.3 and B.4.

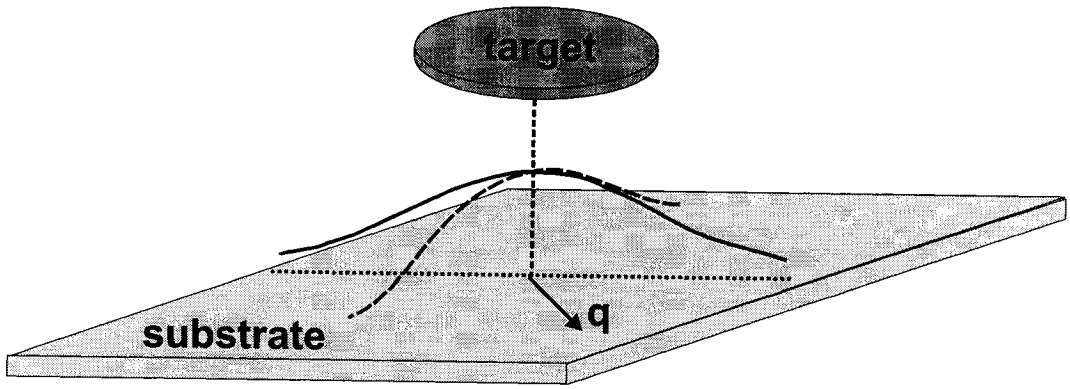

Figure B.1: Deposition profile opposite a target. The solid line is a projection of the deposition amount along the dotted line. Deposition is largest directly opposite the target.

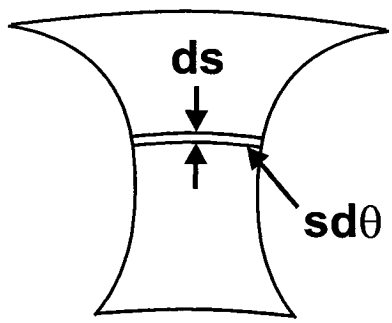

Figure B.2: Arc and angles used in mask design calculation.

Appendix C

Tricks Of The Combinatorial Trade

Many of the high-throughput techniques described within this thesis were developed and refined by the author, T. Hatchard and J. Topple. Subtle details in sample fabrication and testing methods that can have a large impact on data quality are at risk of being forgotten. This appendix includes all the so-called 'tricks of the trade' known by the author so that future generations of students will be able to focus on science rather than re-designing proven experimental methods.

C.1 Thin Film Library Deposition

This section includes proper operating procedures for the sputtering machine located in Room B9. While many of the steps / procedures can also be used when operating the sputtering machine in Room 316, instructions specific to the upstairs sputtering machine should take precedence. Instructions related to sputtering machine operation are also available in the five-page document written by R. Mar and edited by the author and R. Sanderson.

C.1.1 Defrost The Polycold

The machine should be under vacuum (turbo full speed, throttle open) and heated (heater on, 120 V, set to '40') at all times except right before and during deposition. Make note of all changes to the status of the machine (ion gauge on/off, table position, throttle position etc.) in the log book at all times. The polycold should be defrosted and / or turned off before opening the chamber. If the polycold is off, ensure the main water valve (on the wall, to the right of the polycold) is closed and proceed to the next paragraph. Otherwise, open the throttle and set the turbo to full speed. Wait until the turbo power has subsided to approximately 35 W, or whatever power the turbo runs at under high vacuum (between 25-35 W). Ensure the mag water is off. Set the polycold to 'defrost'. Set the polycold back to 'cool' if no hissing noise is

heard and follow the instructions written on the polycold to fix the defrost function. Watch the fore pressure (ForeP), chamber pressure (ChamP) and pump power. The pump power should peak a few minutes after the defrost procedure is started. Record the peak values for the pump power, ForeP and ChamP in the log book. Switch the polycold to standby when the pump power returns to approximately 35 W or the hissing stops. The polycold should be turned off unless the user is in a tremendous rush. Turn the main water off a few minutes after the polycold is turned off.

C.1.2 Vent The Chamber

To vent the chamber, turn off the turbo and open the needle valve on top of the turbo very slightly (approximately 1/16 of a turn). Opening the valve further will cause the turbo to slow faster than desired and could lead to reduced turbo lifetime. Remove the two brass bolts and shear pin holder from the table rotator assembly and open all three of the latch clamps while waiting for the chamber pressure to reach 3.00E+2 torr. The latches need to be opened before the chamber reaches atmospheric pressure. A slight overpressure on the large door could cause the door to open suddenly. The pressure will plateau at approximately 2.98E+2 torr for a few minutes - be patient. Wait until ChamP reads 3.00E+2 torr or higher, then open the valve on the upper left hand side of the chamber until a hissing noise is heard. The handle should be approximately 135° from vertical. Close this valve once the chamber door opens to prevent overpressure situations. Close the needle valve. The substrate table may need to be rotated to the same position it was inserted at in order to open the door easily. Never force the chamber door open or closed. Although throttle position does not have a large impact on vent time, the throttle should be closed when the chamber is open to prevent flakes of material from interfering with the turbo pump vanes. Check that the heater (actually heating tapes plugged in to a power bar / variac) is on and set to '40'.

C.1.3 Substrate / Mask Removal

Remove the three / four (ternary / binary table, respectively) bolts holding the substrate table to the water cooled table mount. Place the substrate table on the bench and remove all substrates. Apiezon 'M' grease should be removed from all

fingers associated with the five subtable table. Substrates can crack if forced off the table - careful use of the tip of a scalpel blade and acetone/methanol will weaken the tape and allow all samples to be removed intact. Substrates with a photolithographic mask should be set to soak in a covered baking dish. Place a glass microscope slide in the centre of a 9 x 13" baking dish if masks are to be removed from two substrates - set the microscope slide to the edge of an 8 x 8" baking dish for a single substrate. Place the substrate(s) photoresist side down in the baking dish so that the microscope slide props up one side of the substrate. In a fume hood, pour in enough acetone to cover the sides of the substrate (but not the top) and seal the baking dish with one of the Al foil covers. Let this sit for approximately half an hour and perform some of the other clean-up steps described below. Remove the Al cover and turn one of the substrates over using a plastic rod. Prop the substrate up against the side of the baking dish. Soak the tip of a cotton-tipped applicator in acetone and gently rub the cotton tip over the substrate. A small amount of acetone may be required to loosen the deposited film, especially if all the acetone evaporated. The deposited film should separate from the substrate easily. If not, return the substrate to the acetone bath, re-cover with Al foil, and soak for another 15 minutes. All of the deposited film should be removed from undesired areas. Small amounts of film can be removed by rubbing an acetone-soaked Kim-wipe over the substrate. Clean Scotch-brite can also be used sparingly. Rinse the substrate with clean acetone (into the baking dish) and place inside an appropriately labeled plastic bag. Repeat for all other substrates and place each in a separate plastic bag. A large plastic bag can be used to gather all substrates from a sputtering run. Clean bags should be re-used.

Flakes of deposited film should be removed from the acetone / photoresist mixture before disposal. Filter the acetone / photoresist / deposited film mixture using a funnel and 8" filter paper into a beaker. Film pieces stuck to the baking dish can be removed with an acetone soaked kim wipe or scotchbrite. Rinse the flakes with acetone until it runs clear. Dispose of the filter paper, kimwipes / scotchbrite (if required), and flakes in the regular garbage unless the deposited film contains a significant amount of heavy and / or toxic metals (in which case see H. Fortier for further instruction). Place the acetone / photoresist mixture in the appropriate waste jug and wash all glassware.

'Powder' Method

Some sputtering runs are performed with the intention of flaking off almost all of the deposited film. The idea is that large (ca. 100 μg) amounts of a single composition material can be produced for specific types of experiments (eg. *in-situ* XRD and Mössbauer effect spectroscopy). Up to six[1] 4.5 x 4.5" glass plates can be coated with a layer of photoresist. Areas of the plates that are not coated with photoresist after spin-coating can be covered by spreading an extra drop of photoresist over the relevant areas with a gloved finger. Remove any excess photoresist with another, clean, gloved finger. Two of the six glass plates can be cut (remove two of the corners) after spin-coating so that all six plates lie flat on the substrate table, if desired. Do not make any other marks on the plates as extra chemicals (eg. marker ink) might become incorporated with the sample. Hold the glass plates down using a small amount of scotch tape. After the desired film has been deposited, remove the plates from the substrate table and stack them, spaced my microscope slides, in a baking disk. Soak in acetone as before. The film should separate from the glass plate in a few large pieces. Clean the baking dish as before. Flakes in the filter paper should be directed towards the bottom of the filter to minimize sample loss and ensure proper rinsing occurs. Remove the filter paper from the funnel after a few minutes and fold in half (along the axis of the cone) twice. The deposited film should be removed from the filter paper while it is clumped up for ease of handling.

C.1.4 Clean-Up

Make sure the throttle is closed. Remove the masks, tunnels and ground shields from the chamber. The fingers in the centre of the chamber should also be removed if present, unless the five subtable table will be used in the subsequent run. Replace and tighten the screw used to hold the fingers in completely. Remove all flakes of deposited film from the chamber using the shop vac located in B9. The empty chamber should be pumped down (throttle open, turbo on, heater on) unless the next user is ready to load.

Separate the masks, tunnels and ground shields and re-tighten the screws used to hold the masks in place. All pieces should be sandblasted. The sand blaster in the

[1]Four glass plates normally allow for a sufficient amount of material to be collected.

student shop is a relatively simple instrument. There are only two important rules: close the door before turning on the power and don't sandblast the window. Place all items to clean in the chamber and close the door. Turn on the air (the valve is behind and to the left of the sandblaster) and then the power. It is a good idea to wear gloves inside the sandblaster gloves because holes sometimes appear in the fingers. Keep the item being sandblasted in contact with the metal grid to prevent shocks. Sometimes the sand flow is slower than expected. If this is the case, first check that there is enough sand in the hopper. If not, check the dust trap. Clean out the dust trap if the sand level is anywhere close to the maximum fill line. Do not throw out the dessicant bag that is inside the dust trap. Dump the sand in the dust trap into a doubled garbage bag and throw this bag in the dumpster - don't just dump the sand into the dumpster. The filter should also be removed and cleaned out (bang it against the sides of the emptied dust trap or roll it up and down the loading area driveway until very little dust comes out). Make sure to put everything back together the way it was found. Next, add some sand to the hopper. Extra sand (glass beads, actually) should be to the right of the sandblaster, or available from the shop. Dessicant bags should be in the hopper and dust trap. Finally, remove the hose from the bottom of the sand hopper and make sure nothing is trapped - coin cell parts tend to get caught in here.

Blow all sandblasted items off with the air line and close the air valve. These parts can be returned to Room B9 as is. It is the responsibility of each person sputtering to ensure the cleanliness of everything that goes in to the sputtering chamber.

C.1.5 Loading The Chamber

Details of substrate preparation methods are provided in Sections C.2 and C.3. Attention to detail in substrate preparation and placement can have a large impact on final data quality.

Start each binary run by replacing the Al foil according to the following steps. Remove the Al foil from the substrate table and cut a suitable amount of foil from the roll. Place the foil over top of the substrate table. Press the foil against the the table using a crumpled kimwipe. Work the kimwipe over the substrate table while keeping the unattached foil under tension. There should not be any creases in the Al

foil. Cut the excess Al from the outer edge of the table using a scalpel. Substrate position on the binary tables can be understood relatively easily. The table is 16.5" in diameter, with a 1.5" dia. hole in the centre. The centres of the sputtering targets are along a circle 5.25" from the centre of the sputtering table. Substrates that are 3" in length should be placed 3.75 to 6.75" from the centre, the extension to other sizes is trivial.

Small variations in lead pattern position on the glass plate (on the order of a mm or so) can occur, which means the position of the contact pads, rather than the position of the glass plate, should be measured. Draw a line from the centre to the edge of the substrate table. Place the cell plate so that the two centre columns of contact pads are evenly spaced along this line. The 64 contact pads on the binary plates are 5 mm in diameter and span 76 mm. The centre of the closest contact pad should be 3.75" (9.52 cm) + 2.5 mm = 9.8 cm from the centre of the substrate table. The center of the furthest contact pad should be 16.9 cm from the centre of the table.

Position all other substrates on the table. Use enough tape to hold the substrates in place, but no more (extra tape can lead to higher base pressures). Holding substrates down on the five subtable table can be tricky, especially in humid air. Cell plates masked using the photolithographic method tend to fall off less frequently than the heavier rigid Al-masked cell plates. A triple layer of double sided tape can be used for a high degree of success. Apply a layer of the normal double sided tape to both the substrate and the subtable. Remove any air / dust bubbles. Place either two strips of carpet tape or one piece of extra sticky double sided tape on the subtable, again without forming any air bubbles. Place the substrate in position. Note that substrate position should always be measured relative to the centre of the table as the subtables are not perfectly positioned. Press down evenly on the substrate (as if punching it, albeit very slowly) with as much weight as possible for about 10 seconds.

Attach the substrate table to the cooled table mount using the appropriate number of bolts. Marks on the back of the substrate tables and table mount indicate the proper orientations. Attach the shear pin holder and rotate the substrate table so that the empty portion of the table (used for sputter cleaning) is at the top. The five subtable table will need to be rotated 135° from this position to allow the door to close. A small amount (ca. 0.3 ml) of Apiezon 'M' grease should be applied to the

contact area of all fingers of the five subtable table, and the centre fingers. Change gloves after applying the grease.

Be careful when replacing targets. Make sure the mag water is off. Put on a clean set of gloves. Loosen the target ring approximately 1/2 turn using the appropriate tools. Hold the target in place with the thumb of one hand while unscrewing the target ring with the other. Remove the target ring but keep the target in place. Place a plastic beaker underneath the magnetron, then push the target up. Approximately 30 ml of water should pour into the beaker. Replace the beaker with 2' of wadded paper towel once the water flow has stopped. Arrange the paper towel so that any water coming out of the magnetron does not simply run down the paper towel to the bottom of the chamber. There is no excuse for water spills in the chamber, period. Clean off the back of the target using another piece of paper towel and put the target away. Sandblast the top and sides of the target ring (do not sandblast the threads), and then clean the entire target ring with methanol-soaked kimwipes. Spread approximately 0.2 ml of vacuum grease over the backing plate of the new target (clean off any existing grease beforehand). Carefully pry the target o-ring out of its groove. Remove grease from both the magnetron o-ring and o-ring groove using dry kimwipes. Spread approximately 0.2 ml of vacuum grease uniformly over the o-ring, and replace it in the groove. Put on a clean set of gloves. Hold the new target in place with one hand while tightening the target ring with the other. Tighten the target ring using the appropriate tool. Turn the main water and mag water on. Check the water flow has not been restricted by the magetron / target position. If the flow has weakened, turn off the mag and main water, remove the target using the method mentioned above, clean out the magnet set using tweezers, kimwipes, water pressure and air flow, and repeat. Repeat this method for all required target changes. It is obviously better to perform all target changes in parallel to reduce the glove consumption. Vacuum the bottom of the chamber once all targets have been changed.

Clean off all required ground shields, tunnels and masks using methanol-soaked kimwipes. Install the ground shields by tightening against the back wall of the chamber and then loosening by 3/4 of a turn. Ground shields can get stuck to the chamber on the top magnetron. Loosen the ground shield using only a strap wrench, not a

hammer. Place the tunnels over the ground shield and re-tighten one or two of the set screws. Install the appropriate masks so that a line through the two guide holes intersects the centre of the chamber (centre of the bolt in the centre post). Ideally the mask screws will also fall along this line. While it is possible to fine-tune the distance between the masks and the substrates - see R. Mar for details - the routine described here will not cause any of the substrates to be stripped from the substrate table by the masking hardware.

Make note of target and substrate positions in the log book. Close the chamber door and clamp shut with the three latch clamps. Mark the table position. Make sure both the needle valve and main vent valve are closed. Open the throttle. Turn the turbo on full speed. Make note of the time the turbo was turned on and when ChamP reaches 1.00E-3 torr. The elapsed time should be less than 3 minutes. Turn on the main water, switch the polycold to 'cool' and turn it on after half an hour or when the ForeP reads less than 1.00E-3 torr. Commence the sputtering run once the IonP is less than 5E-7 torr (the ion gauge sometimes needs half an hour or so to warm up). Make note of all changes to the status of the machine (ion gauge on/off, table position, throttle position etc.) in the log book at all times.

C.2 Non-Photolithographic Substrate Preparation

A total of seven different types of substrates were used during the course of this thesis. The following five subsections describe instructions specific to the six types of substrates that do not require any photolithographic steps. Details of the various photolithography procedures are available in Section C.3.

C.2.1 Cu/Al Disks and Foil

Cu and Al disks are used for mass determination. Cu and Al are generally used for negative and positive electrode materials, respectively, because they are conductive and stable over the range of potentials appropriate to each application. The 'thick' Cu foil (24 μm thick) is also more durable than either the 'thin' Cu (11 μm thick) or Al foil. Cut a piece of Cu foil from the roll attached to the sputtering machine. Nine disks are required for each binary run, 25 for each ternary run. All substrates for binary runs should be marked 'in' and 'out' in appropriate places. Scrub one side

of the foil with Scotch-brite until the Cu/Al is shiny. Place the foil scrubbed side up on a sheet of paper on the bench in Room 217 and clean with methanol-soaked kimwipes. Place the foil between a folded piece of weigh paper and punch out the appropriate number of disks using the large punch.

Weigh the disks using the Cahn 29 electrobalance in Room 314. Make sure to calibrate every time the balance is used. The calibration mass and a pair of plastic tweezers should be located in the top drawer to the right of the balance. It is a good idea to place the disks on the glass substrate (covered on both sides with double sided tape) as they are weighed - shiny side up. Disks are easier to place and pick up if they are slightly curved (but not creased). Flatten each disk completely before placing it on the substrate.

Disks are most easily removed from a substrate by slowly separating the disk from the tape with a scalpel. Do not crease the weigh disk as this can cause the deposited film to peel off. Lift the disk from the substrate using a set of plastic tweezers without any texturing on the tips. Metal tweezers with textured tips tend to cause wrinkles in the disk which in turn can lead to poor film adhesion. Place the disk film side down on a kimwipe. Gently rub a methanol-soaked cotton tip applicator against the back of the disk until all the tape residue is removed. Weigh the disk as before.

Cu foil is also used as a substrate for composition determination. Place double sided tape on both sides of a cleaned glass substrate. Cut a piece of Cu foil that is at least 1 cm wider and longer than the glass substrate. Smooth the Cu foil in to the glass substrate using a crumpled kimwipe and then cut the Cu foil to fit. Only the long sides should be cut for binary substrates so that the 'wings' can be used to hold the substrate down. Si wafers can also be used for runs without Si deposition, although the wafers are relatively expensive ($12 buys one wafer or approximately 25 m^2 of Al foil).

C.2.2 DSC Pans

DSC pans can be loaded and unloaded using a similar method to the Cu disks. Pans need not be weighed before and after deposition. V. Chevrier should be consulted for details of pan cleaning routines. Pan height can be an issue. DSC pan bottoms should go on a Si substrate or pan tops on a glass substrate. Use scrap Si whenever

possible. Twelve / forty-nine pans are used for binary / ternary runs. Consider the cost of each pan is on the order of $1 before including additional pans.

C.2.3 Kapton Film

Scrap pieces of Kapton film are available from D. Stevens in Room 316. Cut approximately fifteen 1.25 x 4" pieces using either a sharp pair of scissors or a new scalpel blade and clean corrugated cardboard. Consistency in substrate size is important. Locate the centre of the substrate table (the inner hole is 1.5" in diameter) and mark with a dot. Draw a line to the outer edge of the table. Make marks every 2" along the circumference of the table. Draw lines between the marks and the centre dot. Place each piece of Kapton foil along a line, starting 3.25" from the centre of the table. Hold down the narrow edges of the kapton foil using small amounts of scotch tape. The kapton films will overlap slightly at inner radii. This can be used to keep track of library orientation. Do not tape down both ends of those pieces of Kapton foil that overlap a bolt hole until the table is mounted in the chamber. Scrub mounted pieces of Kapton with scotch brite and clean off with a methanol-soaked kimwipe. Do not expose the scotch tape to methanol. Punch the Al foil through the centre of the table and tape the foil down against the back of the table after all substrates have been positioned.

Strips of Kapton film are easy to remove after deposition. Lift each piece of Kapton from the substrate one edge at a time without removing the scotch tape. Do not allow the film to roll. Stack half of the strips directly on top of each other and set aside. Stack the remaining strips on top of one another, then tape the two stacks together back-to-back.

C.2.4 Si Wafers

Si wafer substrate preparation requires a delicate touch. Obtain a piece of clean Si that is at least 8.5 x 8.5 cm or 1.5 x 8.5 cm in size for ternary or binary runs, respectively. Draw a rectangle on the unpolished side of the Si wafer, making sure the rectangle sides are parallel to the notches in the wafer. Place the Si wafer on either a clean, padded section of bench in Room 316 or on one of the cleaned glass blocks. Make sure there are no loose particles between the wafer and the support surface.

Clean off both sides of a clear plastic ruler with alcohol or between the fingers of a glove. Hold the ruler against the Si with one hand while making strokes with either the scribe or a glass cutting tool until a definite groove is present. Support the bottom of the Si wafer up to the inner edge of the groove with the glass block. Press the ruler down on the inner edge of the Si wafer and slowly drop something flat and heavy (i.e. the edge of the Al foil box) on the portion of the wafer to be removed. Adjust the line positions if the wafer cleaved at an angle to the groove and repeat along the other three sides. Mark Si wafers for binary runs with lines indicating the 76 mm spacing, and 'in' and 'out' labels, using the glass scribe. Si wafers for ternary runs should be attached to a cleaned 76 x 76 mm glass plate using double sided tape. The Si wafer can be scrubbed using scotch-brite and then cleaned using methanol-soaked kimwipes to increase film adhesion. The 'pumpkin' in B9 can also be used to increase film adhesion. Operating instructions are attached to the fume hood in B9.

C.2.5 TEM Grids

A technique for depositing thin films directly on to TEM grids is being developed by the author and Prof. Craig Bennett of Acadia University. V. Chevrier can be consulted for current details of this technique. TEM grids are very delicate and should be handled carefully. Three to four layers of scotch tape should be placed on the clean side of a scrap Si wafer. Use a scalpel to remove any air bubbles in the tape. Cut diamonds small enough to surround a TEM grid out of the tape using a scalpel. Place the TEM grid inside said diamond and cover with a piece of coarse wire mesh. Tape the sides of the mesh down. The TEM grids can be carefully removed after deposition, or remain attached to the substrate until right before analysis.

C.3 Photolithography

Photolithographic masking methods used at Dalhousie were originally developed by G. Rockwell. Fortunately, the time required to produce a cell plate / mask has since been reduced from 2 hours to approximately 30 minutes.

All pieces of glass destined to be combinatorial cell plates should be cleaned in the 'pumpkin' according to the instructions attached to the fume hood in Room B9.

Failure to clean cell plates using the pumpkin can lead to poor adhesion / poor data quality. Use the pumpkin.

Cu is often deposited directly on to glass plates before any photolithography process occurs. Deposition rates / durations are available from R. Mar, but are typically in the range of 130 W DC for about 2 hours. Glass plates should be held to the substrate table using scotch tape. The tape should be positioned such that only 1 mm of the plate is covered at the inner and outer edges. Smaller or larger coverages can lead to dead channels in assembled combinatorial electrochemical cells. Do not trap air bubbles.

Place Prof. Jericho's hot plate in the fume hood, turn on to setting '2'. Put on two layers of gloves and a lab coat. Clear the stopwatch timer. Do not set the photoresist bottle right beside the heater - it should be at the opposite end of the fume hood. Move cleaned substrates directly from the pumpkin to the spin coater. Tighten all four of the latches. Latches that are stuck can be loosened using lineman's pliers. The screws used to tighten the latches could be replaced by hex-head bolts for better ease of use. Dump any photoresist in the 10 ml graduated cylinder to the side of the substrate holder. Pour 4 ml of photoresist in to the graduated cylinder, close the photoresist bottle and put it back in the insulated box. Pour all 4 ml of photoresist on to the centre of the glass plate in one quick motion. Slowly rotate the substrate holder to spread the photoresist over most of the substrate. Rotate the substrate so that most of the photoresist is in the centre and then plug the spin coater in. Put the cardboard lid over the spin coater. Wait until the spin coater is up to full speed (based on the noise), wait for 30 seconds, then unplug the spin coater. It will take two or three minutes for the spin coater to stop. If the photoresist does not cover all of the desired areas the existing photoresist should be removed with acetone and disposed of in the appropriate waste bottle. Otherwise, return the photoresist bottle to the refrigerator and heat the substrate on the hot plate photoresist side up for 30 seconds. Shift the substrate around for even heating. Place the substrate to the side to cool for a few minutes.

A variety of mask designs exist. Users can produce new masks by printing the desired pattern on to two overhead transparencies and stapling them together. Two overheads are required for proper exposure contrast. The substrate corners should

be indicated. Small amounts of double sided tape placed on both sides of the transparencies prevent the mask from shifting during UV exposure. Clean any dust off the mask using a glove. Clean off the top glass plate using methanol-soaked kim wipes. Align the mask using the indicated corners for cell plate production or the contact pads for photolithographic masking. Position the substrate, mask and top glass plate on the plastic holder and slide under the UV lamp. The lamp window should be centred on the support ring. Four 2-3 minute exposures, focused on each corner, are required for each cell plate etch; one 5 minute exposure in the middle is sufficient for each photolithographic mask. Only touch the plastic holder when repositioning the substrate between exposure steps. Heat the exposed substrate for 30 seconds, as before. Place the cooled substrate in a baking dish and bathe in developer. Exposed, dissolved photoresist appears red in developer. Wait for 10+ minutes while most of the exposed photoresist is removed. Shake the baking dish once or twice to disperse the dissolved photoresist. Wait until no more 'red' appears, then rinse the substrate with water into the baking dish. With practice the user will be able to tell when all the exposed photoresist has been dissolved.

The next steps depend on what type of substrate is being produced. Cu-coated glass plates should be etched in ammonium persulfate[2] to dissolve the Cu in unwanted areas, rinsed with water into the etch bath, then rinsed with acetone and water into a beaker or second baking dish to remove the unexposed photoresist. Etchant details are available in either of the photolithography documents written by G. Rockwell (stored in `//queen/data/share/photolithography`). Dry the substrate using the compressed air line in the student shop.

Ti-coated glass plates and photolithographic masks are ready for use after blow drying (using the air line in the student shop). Methods for other types of cell plates (eg. stainless steel) are also under development. All liquid wastes should be disposed of properly.

[2]Ammonium persulfate dissolved in water should not be stored in a sealed container since the pressure will build up and could cause the container to explode.

C.4 Combinatorial Electrochemical Cell Assembly

Combinatorial electrochemical cell assembly is an evolving art. A great deal can be learned by disassembling cycled cells. Place the cell and a 0.5 l beaker filled with water in the fume hood in Room 217. Loosen all eight pressure bolts a couple of turns, then remove the four corner bolts. Remove the pressure plate and lift the cell top up. The cell plate should be stuck to the cell top so the base can be removed. Clean off any salt residue on the base using slightly moistened kimwipes, then dry completely. Do not disturb the tape holding the polypropylene liner in place. Remove any corrosion from the two guide posts using scotch brite. It is a good idea to bolt the pressure and base plates back together.

Put on goggles when attempting to separate the cell plate and cell top. Flip the cell top over so that the cell plate is visible, then take note of the position of any cracks or broken electrical contacts (especially underneath the o-ring). Press up on one side of the cell plate with both thumbs until the seal is broken. Set the cell plate aside then pry the o-ring out with a set of tweezers (starting in a corner). Put the separator and o-ring in the water. Cut three horizontal and three vertical lines in the Li foil so that no piece is larger than a couple of cm^2. Use the tweezers to place each piece of Li in the water separately. Do not crumple the Li foil or put in too much Li foil at once - don't play with fire in fume hoods containing organic solvents. Slowly scrape away the bulk of the remaining Li using a dry scalpel blade. Position the cell top underneath the tap in the fume hood and slowly turn on the water. It is best to only allow one corner or edge of the cell plate to get wet at once to minimize the fire risk. Turn on the tap and slowly pour the contents of the beaker down the drain. Refill the beaker twice and pour down the drain. Keep the tap running for a few more minutes. Rinse the cell top off in the main sink, dry completely and place in the oven to the left of the sink.

The cell top and o-ring should be in the oven for at least a few hours. It also takes a few hours for the cell top to cool down to room temperature in the glove box antechamber. Ensure the cell plate is clean while the cell top and o-ring cool. Remove all tape residue from the back of the cell plate and make sure there is not a thin line of metal connecting all the leads on one side. Said line can be removed using a fraction of a ml of undiluted nitric acid and cotton-tipped applicators. Put

the cell plate in an open plastic bag when bringing it and the cell hardware in to the glovebox. It is a good idea to record in the glove box book how many times the antechamber has been purged during sample insertion or removal.

Replace the o-ring in its groove. Spread the o-ring out uniformly so that it does not stick out on any one side. The o-ring groove should probably be widened so that the o-ring has more room for lateral expansion.

Microporous separators should be approximately 76 x 85 mm in size. Put the separator to be used in a separate bag. Use this separator as a size guide when cutting the Li foil. Clean off any Li stuck to the scissor blades using a scoopula. Cut two ca. 80 mm pieces of Li foil from the roll. One of these pieces should then be cut nearly in half along the roll direction. Position the two pieces of Li foil on top of the bag containing the separator to make sure of the sizes. The pieces will lengthen slightly when they are scrubbed with the nail brush. Scrub until the Li foil is shiny (two or three strokes), but be careful not to pit or fold the foil. Place the cell plate on the cleaned cell base. Lead 1 should be aligned with the `I` scratched in the cell base. Draw 0.4 ml of electrolyte (normally 1 M $LiClO_4$ in EC:DEC 1:2 vol:vol) up into a syringe. Put enough pressure on the syringe piston to cause a steady stream of electrolyte to flow. Spread electrolyte over all of the contact pads, working from the left hand column over to the right. Do not worry if the contact pads on the right hand side have no electrolyte when the syringe is empty. Draw the microporous separator over the left hand edge of the cell plate at an angle so that the left edge of the separator is the first to wet. There should be about 2 mm of separator overhang relative the left hand contact pads. Slowly lower the separator on to the cell plate so that the separator is wet by one continuous front. There should be no air bubbles between the separator and cell plate and all contact pads should be wet. Lift up the separator and try again if this is not the case. Flatten then press each piece of Li foil into the separator so that there are no air bubbles. Make sure the pieces of Li foil do not overlap.

The cell plate should be properly seated and positioned. Position the cell top and the pressure plate. Loosen all eight pressure bolts. Tighten all four corner bolts until there is a very small gap between the top of the pressure plate and the bottom of the bolt head. Torque all corner bolts to about 20"-lbs (this is lower than the lowest

setting on the torque wrench, just don't crank it) in a star pattern, then torque to 25"-lbs. Finger tighten all eight pressure bolts. Torque the four pressure bolts over the leads to 25"-lbs in a star pattern followed by the top, bottom and then the middle bolts. Repeat this pattern on the pressure bolts two more times until each bolt rotates very little when torqued to 25"-lbs. Remove the assembled cell from the glove box and blow the gaps between the cell plate and cell top dry with the air line line room 217.

Test all connectors used to cycle the cell using one of the resistor test boards. Remember that some of the motherboard connector contacts will not have the same contact pressure when holding the thinner glass plates. Clean off any salt residue using a scalpel. It is best to setup the desired test before connecting the cell if using either Scribner. While the Medusa connectors are generally decent, the original Scribner connectors have lost much of the clamping pressure and should probably be replaced. Place a sheet of paper between the cell base and any metallic shelf. Connect the cell so that connector 1 and lead 1 come together, and start the desired test. If using the oven, place the cell in the oven before connecting the cables, and spread the cables out over the door seal. Run the reference voltage wire out the top of the oven - make sure the vent is open only far enough to pass the wire through. The user should reread the assembly section if more than one or two channels are dead. Cracks in the glass are generally caused by improper o-ring position. The assembly procedure would probably be more tolerant if the cell top o-ring groove was widened slightly (a second time).

Appendix D

Copyright Releases

D.1 The Electrochemical Society, Inc.

09/26/2005 MON 09:30 FAX 001/001

09/15/2005 14:04 FAX 8024845191 DALHOUSIE PHYSICS DEPT 002

Department of Physics and Atmospheric Science
Dalhousie University
6300 Coburg Rd.
Halifax, NS B3H 2J3
CANADA
Tel: (902) 494-2991
Fax: (902) 494-5191

September 15, 2005

Permissions Request
The Electrochemical Society (ECS)
65 South Main Street
Pennington, NJ 08534, USA
Fax: (609) 737-2743

I am preparing my Ph. D. thesis for submission to the Faculty of Graduate Studies at Dalhousie University, Halifax, Nova Scotia Canada. I am seeking your permission to include portions of the following papers in the thesis:

a) M.D. Fleischauer *et al.*, Journal of the Electrochemical Society, **150** (11) A1465-A1469 (2003)
b) M.D. Fleischauer and J.R. Dahn, Journal of the Electrochemical Society, **151** (8) A1216-A1221 (2004)
c) M.D. Fleischauer *et al.*, Electrochemical and Solid-State Letters, **8** (2) A137-A140 (2005)
d) M.D. Fleischauer, M.N. Obrovac, J.D. McGraw, R.A. Dunlap, J.M. Topple, and J.R. Dahn Al-M (M = Cr, Fe, Mn, Ni) thin film negative electrode materials. 36 pages including 18 figures submitted July 10 to Journal of the Electrochemical Society (manuscript JES-05-1144).

Revision Under Review

Specifically, I would like permission to reproduce Figures 1 and 3 of paper a), Figure 12 of paper b), Figures 1-4 of paper c) and Figures 1-15 of paper d). I would also like permission to reproduce the bulk of the text of paper d) (all the text, excluding the experimental and acknowledgement sections). I am the principal author of all four papers, and am still a student under Prof. Jeff Dahn, the contact author for all four papers.

Canadian graduate theses are reproduced by the Library and Archives of Canada (formerly National Library of Canada) through a non-exclusive, world-wide license to reproduce, loan, distribute, or sell theses. I am also seeking your permission for the material described above to be reproduced and distributed by the LAC(NLC). Further details about the LAC(NLC) thesis program are available on the LAC(NLC) website (www.nlc-bnc.ca).

Full publication details and a copy of this permission letter will be included in the thesis. I would appreciate a completed version of this letter to be faxed to (902) 494-5191 Attn: Michael Fleischauer or mailed to the address above before September 25, 2005. Thank you for considering this request.

Yours sincerely,

TO.

Michael D. Fleischauer

Permission is granted to include the above-referenced paper in your thesis, provided that you obtain permission of the other individual authors. In the thesis, please acknowledge the authors and the citation given above, and include the words: "Reproduced by permission of The Electrochemical Society, Inc."

24 Sept. 2005
Date

Mary E. Yess, Deputy Executive Director

Faxed 9/26/05

D.2 IOP Publishing, Ltd.

Department of Physics and Atmospheric Science
Dalhousie University
6300 Coburg Rd.
Halifax, NS B3H 2J3
CANADA
Tel: (902) 494-2991
Fax: (902) 494-5191

August 23, 2005

Institute of Physics Publishing
Dirac House
Temple Black
Bristol BS1 6BE, UK

I am preparing my Ph. D. thesis for submission to the Faculty of Graduate Studies at Dalhousie University, Halifax, Nova Scotia Canada. I am seeking your permission to include portions of the following paper in the thesis:

M D Fleischauer, T D Hatchard, A Bonakdarpour and J R Dahn *Combinatorial investigations of advanced Li-ion rechargeable battery electrode materials* Measurement Science & Technology **16** (2005) 212–220.

Specifically, I would like permission to reproduce Figures 2, 3, 6 and 14. I am the principal author of this paper and am still a student under Prof. Jeff Dahn, the contact author for this paper.

Canadian graduate theses are reproduced by the Library and Archives of Canada (formerly National Library of Canada) through a non-exclusive, world-wide license to reproduce, loan, distribute, or sell theses. I am also seeking your permission for the material described above to be reproduced and distributed by the LAC(NLC). Further details about the LAC(NLC) thesis program are available on the LAC(NLC) website (www.nlc-bnc.ca).

Full publication details and a copy of this permission letter will be included in the thesis. I would appreciate a completed version of this letter to be mailed to the address above or faxed to 1 (902) 494-5191 Attn: Michael Fleischauer before September 15, 2005. A scanned version could also be e-mailed to mike@dahn.phys.dal.ca. Thank you for considering this request.

Yours sincerely,

Michael D. Fleischauer

Permission is granted for:

a) the inclusion of the material described above in your thesis.

b) for the material described above to be included in the copy of your thesis that is sent to the Library and Archives of Canada (formerly National Library of Canada) for reproduction and distribution.

Name: _____

Signature: _____

PERMISSION TO REPRODUCE AS REQUESTED
IS GIVEN PROVIDED THAT:

(a) ~~the consent of the author(s) is obtained~~.
(b) the source of the material including author/editor, title, date and publisher is acknowledged.

IOP Publishing Limited
Dirac House
~~Temple Back~~
BRISTOL

BS1 6BE

24/8/05
Date

Rights & Permissions